Ph.D. Thesis

Automatic Detection of Ischemia in Holter Recordings and Search for New Risk Markers from the Electrocardiographic Signal

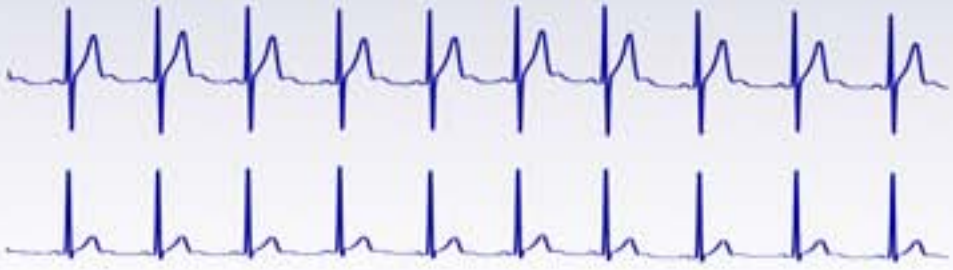

Ana Mincholé Lapuente

Supervisor: Pablo Laguna Lasaosa

March 2011

Instituto Universitario de Investigación
en Ingeniería de Aragón
Universidad Zaragoza

Instituto Universitario de Investigación
en Ingeniería de Aragón
Universidad Zaragoza

Ph.D. Thesis

Automatic Detection of Ischemia in Holter Recordings and Search for New Risk Markers from the Electrocardiographic Signal

Detección Automática de Isquemia en Registros Holter y Búsqueda de Nuevos Marcadores de Riesgo en la Señal Electrocardiográfica

Ana Mincholé Lapuente

Supervisor
Pablo Laguna Lasaosa

March 2011

Acknowledgements

This thesis would not have been possible without the help and support of many people, to whom I would very pleasantly like to thank.

First of all, I would like to express my gratitude to Pablo Laguna to rely on me and for his encouragement, support and guidance during the course of this thesis. His joy, energy and enthusiasm for research have been very motivational for me. His personal and scientific skills have built a strong, solid and joint group of which I feel very happy to be part of. For all the members of the group is my second acknowledgment. With them, Juan Pablo, Violeta, Michele, Eduardo, Rute and so on, I have had very productive discussions in the professional part and shared great times in the lab, during coffee breaks, conferences, stays and travels. Specially, I would like to thank Esther who introduced me into the cardiac modeling and simulation and helped me so much in the second part of the thesis, and Raquel who shared with me her experience in database acquisition.

To José García, the one who developed the original ischemia detector, the starting point of the present thesis, and kindly offered me his code and his help.

To Franc Jager, for very fruitful discussions and for making me feel very welcome during the stays in his laboratory at the University of Ljubljana, Slovenia.

To José Felix Rodríguez from the Structural Mechanics and Material Modeling (GEMM) group at the University of Zaragoza, for guiding me in the world of cardiac simulation and for his immediate disposition to help at any time.

To Manuel Doblaré, head of the GEMM group, for providing valuable suggestions and comments in the second part of the thesis.

To my friends at the department Isabel, Matías, Antonio, Alicia, Hans, Carol, Luis, Javi, Begoña, Juan, Pedro, Mariano, ... Thank you all for having such a nice lunch times and funny discussions. To my friends Melisa, Ana, Patricia and Isabel who are always there.

To Ernesto, my partner, love and also colleague, who has constantly relied on me and encouraged me. His curiosity about my work and his infinite questions have also helped me to see different points of view and improve my work.

My parents Angel y María Pilar deserve my highest thanks. With their unconditional and constant love and support, I have been able to complete all the different academic and personal stages. Laura, Jorge, Elisa, José Carlos, Miriam and Miguel, are my 'sisters' and confidantes, always cheering me up and supporting me. The last but not the least, my aunts, who are there whenever I need them, giving me affection.

This Ph.D. thesis has been developed in the Aragón Institute for Engineering Research (I3A) from the University of Zaragoza and in the Biomedical Research Networking center in Bioengineering, Biomaterials and Nanomedicine (CIBER-BBN), in the framework of several research projects which were financially supported by the Comisión Interministerial de Ciencia y Tecnología (CICYT) and by the Diputación General de Aragón (DGA):

- "Tratamiento de señal en el análisis del ECG y polisomnografía: procesado orientado por el modelado fisiológico", CICYT/FEDER, Ref. TEC2004-05263-C02-02/TCM, 2005-2007
- "CIBER en Ingeniería Biomédica. Análisis multimodal-multicanal e interpretación fisiológico-diagnóstica de señales biomédicas del sistema cardiorrespiratorio, autonómico y del sueño: variabilidad dinámica e interacciones.", Centro de Investigación Biomédica en Red. CB06/01/0062
- "Análisis multimodal-multicanal e interpretación fisiológico-diagnóstica de señales biomédicas del sistema cardiovascular, respiratorio, autonómico y del sueño: variabilidad dinámica e interacciones", CICYT/FEDER, Ref: TEC2007-68076-C02-02, 2008-2010
- "Ayudas destinadas a las Unidades Operativas de Investigación de la Comunidad Autónoma de Aragón", DGA, Cod. T30, Grupo de Tecnologías de las Comunicaciones (Universidad de Zaragoza), grupo consolidado reconocido por la DGA. 2005-2010

Abstract

In the present thesis, the problem of automatic ischemia detection in Holter recordings and the search for new risk markers from the surface ECG are studied.

The first part of the thesis deals with ischemia detection, which is commonly diagnosed by observing changes of the ST segment in the ECG. Despite the frequent use of ST deviation in clinical practise to diagnose ischemia, several studies have shown the limitations of using it as the only diagnostic tool due to its low specificity. Not only ischemic episodes result in ST deviations but also heart rate related events, body position changes or conduction changes. The release of the Long Term ST database, which contains a large number of human annotated ischemic and non-ischemic ST-segment events such as those mentioned before, has provided an extensive tool to evaluate ischemia detectors. In particular, in this thesis we elaborate on one detector structure which accounts for changes in the ST segment after defining a reference non ischemic ST segment. However, body position changes, which are often manifested as shifts in the electrical axis, also result in ST modifications, and thus, may be misclassified as ischemic changes during ambulatory monitoring. In order to cancel out body position changes, with a more abrupt ST signature than ischemic or heart rate related episodes, we have modelled the body position change as a step like change in the Karhunen-Loève transform coefficient series of the QRS and STT complexes. Karhunen-Loève transform series accounts for morphological changes of an specific complex with respect to a template. A generalized likelihood ratio test assuming laplacian noise has been chosen as the strategy to detect those body position changes. Two databases have been selected to assess both the performance in detection and the false alarm rate, obtaining improved results in both with respect to current techniques based on gaussian noise assumptions.

The very similar signature of ST modifications in ischemia and heart rate related events has driven us to look for other ECG indices allowing to discriminate between them. Heart rate-based indices, correlation between the absolute ST segment deviation and heart rate series, the interval between the T wave peak and the T wave end, the signal to noise ratio and changes in the upward/downward slopes of the QRS complex have been considered and shown as significant discriminant parameters. A discrimination analysis between the three types of events: ischemia, heart rate related episodes and sudden step changes, and between ischemic and non ischemic episodes, have been performed in order to select the most significant set of features in each case. The obtained set of features in each case has been analyzed and discussed.

The second part of the thesis is focused on finding ECG features which could prevent

the occurrence of life threatening arrhythmias. Recent clinical and experimental studies have suggested that abnormalities of ventricular repolarization, and specially the last part of it, the interval between the T wave peak and the T wave end (T_{pe}), play a role in the genesis of ventricular arrhythmias. Also, restitution characteristics of the tissue are very important in the occurrence of a reentry. Therefore the rate adaptation of the T_{pe} has been characterized and compared to the QT rate adaptation, using an acquired database of healthy subjects undergoing a tilt test trial. The tilt test trial results in heart rate changes and then, in modifications of the repolarization features. Results from this study confirm that T_{pe} adapts to HR changes much faster than the QT interval.

The generation of arrhythmias has been widely studied by dynamically pacing cardiac myocytes, cardiac tissue or whole hearts. In particular, dispersion of action potential duration restitution (APDR) has been suggested to act as a potent arrhythmogenic substrate. In the last chapter, a methodology is developed for its computation from the surface ECG through the T_{pe} interval dynamics. In particular, the estimate includes compensation for the T_{pe} memory lag after heart rate changes. The capability of the proposed estimate to reflect APDR dispersion has been assessed using a combination of ECG signal processing and computational modeling and simulation. Specifically, ECG control recordings are used to measure that estimate, while its capability to provide a quantification of APDR dispersion at tissue level is assessed by using a 2D ventricular tissue simulation. Our results provide evidence that the proposed estimate is a non invasive surrogate of APDR dispersion in ventricle.

Resumen y conclusiones de la tesis

En la presente tesis se estudian tanto la problemática en la detección automática de isquemia en registros ambulatorios como la búsqueda de índices de riesgo en el ECG de superficie basándonos en marcadores conocidos a nivel celular.

La primera parte de la tesis se centra en la detección de isquemia, enfermedad que se diagnostica en la práctica clínica observando cambios en segmento ST del electrocardiograma (ECG). A pesar de la frecuente utilización de la desviación del segmento ST, varios estudios han mostrado sus limitaciones como única herramienta de diagnóstico debido a su baja especificidad. La baja especificidad se debe a que no sólo los episodios isquémicos causan cambios en el segmento ST sino también episodios relacionados con el ritmo cardiaco, cambios posturales o bloqueos de rama. La base de datos Long Term ST contiene un gran número de episodios isquémicos y no isquémicos relacionados con cambios en el segmento ST como los ya mencionados, anotados por expertos. Esto proporciona una valiosa herramienta para evaluar detectores de isquemia. Específicamente, en esta tesis utilizamos una estrategia de detección, que se basa en la búsqueda de cambios en el segmento ST una vez definido un segmento ST de referencia no isquémico. Sin embargo, los cambios posturales se manifiestan a menudo como cambios bruscos en el eje eléctrico, produciendo también modificaciones en el segmento ST que pueden ser clasificados incorrectamente como episodios isquémicos durante la monitorización ambulatoria. Para cancelar estos cambios posturales, los cuales provocan un cambio más abrupto en el segmento ST con respecto a los episodios isquémicos o relacionados con cambios de ritmo, se ha modelado el cambio postural como un cambio tipo escalón en los series de coeficientes de la transformada Karhunen-Loève de los complejos QRS y STT. Las series de coeficientes de la transformada Karhunen-Loève proporcionan un seguimiento de los cambios morfológicos de un complejo específico con respecto a un patrón de referencia. Se ha elegido la técnica de detección GLRT asumiendo ruido laplaciano como estrategia para detectar cambios posturales desde el ECG. Dos bases de datos han sido seleccionadas para evaluar tanto el rendimiento del detector como la probabilidad de falsa alarma, obteniendo mejores resultados en ambas bases de datos con respecto a la técnica actual de detección que asume ruido gausiano.

Los cambios producidos en el segmento ST en episodios isquémicos y relacionados con ritmo cardiaco tienen una forma similar, lo que nos ha llevado a buscar índices que nos permitan distiguirlos. Índices relacionados son el ritmo cardiaco, la correlación entre la desviación del segmento ST y el ritmo cardiaco, el intervalo del pico al fin de la onda T, la relación señal a ruido y cambios en las pedientes ascendente y descendente del complejo

QRS, se han considerado y posteriormente mostrado como parámetros significativos en la discriminación de ambos tipos de episodios. Un análisis de discriminación entre los tres tipos de episodios: isquémicos, relacionados con cambios de ritmo y cambios posturales, y otro entre isquémicos y no isquémicos se han desarrollado para seleccionar el conjunto de variables más significativas en cada caso. El conjunto de variables en cada caso han sido analizados independientemente.

La segunda parte de la tesis tiene como objetivo la búsqueda de biomarcadores sobre el ECG de superficie que pudieran alertar de la aparición de arritmias ventriculares malignas. Recientes estudios clínicos y experimentales han sugerido que abnormalidades en la repolarización ventricular, y especialmente, en la última parte de ella, el intervalo entre el pico y el fin de la onda T (T_{pe}), tienen un papel importante a la hora de generarse una arrítmia ventricular. Además, las propiedades especificas de la restitución en el tejido cardiaco juegan un papel importante en la aparición de reentradas. Por lo tanto, la adaptación del intervalo T_{pe} ante cambios en el ritmo cardiaco se ha caracterizado y comparado con la del intervalo QT, utilizando una base de datos adquirida con sujetos sanos sometidos a una prueba de mesa basculante (tilt-test) y tres maniobras de Valsalva, causando cambios en el ritmo cardiaco y por lo tanto en los intervalos y morfología de la repolarización. Los resultados de este estudio confirman que el intervalo T_{pe} se adapta a cambios en el ritmo cardiaco mucho más rápido que el intervalo QT.

La generación de arritmias se ha estudiado normalmente excitando dinámicamente a distintos ritmos cardiacos un miocito, un tejido cardiaco o el corazón completo. En particular, se ha sugerido que la dispersión en la restitución de la duración de potencial de acción (APDR) actúa como un potente substrato arritmogénico. En el último capítulo de ésta tesis, se desarrolla una completa metodología para el cómputo de esta variable de forma no invasiva desde el ECG de superficie, a través de la dinámica del intervalo T_{pe}. Exactamente, el estimador incluye una compensación de la memoria del intervalo T_{pe} ante cambios en el ritmo cardiaco. La capacidad del estimador propuesto para reflejar dispersión en la restitución de la APD, se ha evaluado utilizando una combinación de técnicas de procesado de ECG, modelado computacional y simulación. Específicamente, se han usado registros de ECG de control para medir el estimador mientras que la capacidad de proporcionar una cuantificación de la dispersión de la APDR a nivel de tejido se ha evaluado usando una simulación de tejido ventricular 2D. Nuestros resultados evidencian que el estimador propuesto proporciona una medida no invasiva de la dispersión de APDR en ventriculo.

Contents

List of Figures

List of Tables

Chapter 1

Introduction

1.1. Cardiovascular diseases

Cardiovascular disease is the leading cause of death in industrialized countries, followed by cancer, accidents, diabetes, Alzheimer and AIDS. According to the World Health Organization, cardiovascular disease causes 12 million deaths in the world each year and will remain by far the top cause of mortality through 2030 [7]. According to the last report of the American Heart Association [8], more than 80 million people in the United States have one or more forms of cardiovascular disease (CVD) and these diseases claimed more than 830 thousand lives, 34.3% of all deaths. In Spain, CVD represented a 32.5% of the total number of deaths (4.297 deaths in Aragón, a 32.4% of the total), reported in *Instituto Nacional de Estadística* (www.ine.es). These figures do justify any effort to reduce the incidence of cardiovascular diseases, including prevention, diagnosis and treatment.

1.1.1. Coronary Artery Diseases and Arrhythmogenesis

Coronary artery diseases (CAD), which are caused by the narrowing of the coronary arteries (infarction, angina pectoris, ...), induced more than 425 thousand deaths in America [8], being the single leading cause of death in western countries, and a major cause of hospital admissions.

This narrowing of one or more coronary arteries leads to a diminution of blood in the cardiac muscle with respect to the myocardial requirements, and this imbalance cause myocardial ischemia. This transient blood flow reduction may cause chest discomfort, referred to as angina pectoris. However, in other cases, there is no pain, being referred to as silent ischemia. When ischemia is severe or lasts too long, such as in case of a totally blocked coronary artery, it can cause a heart attack or myocardial infarction, leading to the heart tissue death. Ischemia results in physiological modifications (structural and/or functional abnormalities) in the myocardial ventricle, which are associated to arrhythmias [9, 10, 11].

Some of CAD deaths occur unexpectedly and within a short time after symptoms appear and are referred to as sudden cardiac death (SCD). SCD represents approximately

20 per cent of all deaths and its incidence is similar in all western populations, where estimates indicate that 1 out of 1000 subjects dies every year due to SCD [12]. The most common sequence of SCD appears to be the degeneration of ventricular tachycardia (VT) into ventricular fibrillation (VF), during which disorganized contractions of the ventricles fail to eject blood effectively, often followed by asystole or pulseless electrical activity [13]. Reentry can be initiated even in normal and healthy hearts, but it is more common in hearts with structural and/or functional abnormalities such as ischemia. Approximately about 80% of SCD are related to ventricular fibrilations induced by ischemia [14].

1.1.2. Diagnosis

Some common methods used to diagnose CAD, for instance angiogram or coronary catheterization to determine the location and severity, to treat CAD, such as coronary angioplasty and stents to reduce narrowing in the artery, and to prevent SCD as implantable cardioverter-defibrillator to act as an instant defibrillator in the event of arrhythmia, are invasive and expensive. Therefore, developing less expensive and non-invasive tools to help diagnosis and eventual therapy of cardiopathies is of great social and technological interest. One of those is the electrocardiographic (ECG) signal which describes the electrical activity of the heart recorded from electrodes on the body surface. It is a cheap and non invasive technology, widely used to investigate and diagnose heart diseases such as ischemia or some types of arrhythmia [15, 1].

1.2. The Electrocardiographic Signal (ECG)

The electrocardiographic (ECG) signal is a recording of the heart's electrical activity over time. It is one of the main clinical tools to examine the heart's electrical activity with several advantages such as being noninvasive, simple, cheap and very useful in the study of cardiac pathologies. ECG signals are recorded from electrodes on the body surface.

According to the information needed to be extracted from the ECG, different types of recordings are chosen. The 12-lead ECG, stress test or Holter recordings provide information such as abnormalities of the electrical activity, irregular blood flow or areas of the cardiac muscle which are damaged, and therefore can be used to determine the risk of suffering infarctions or ventricular arrhythmias.

1.2.1. Electrical Activity of the Heart

Muscle cells and nerve cells (neurons) have the property of being excitable so they can be stimulated to create a tiny electric current through their membrane. The electrical membrane potentials of these cells follow a stereotyped signature which rapidly rises (depolarization) and falls (repolarization) and it is known as action potential (see Fig.1.1). The muscle cells of the wall of the heart, i.e. myocardium, are connected and allows that electrical impulse spread throughout the heart. Electrical activity occurs before the

mechanical part, and that is why electrical impulse is prior to the contraction of the cardiac cell.

The normal electrical conduction of the heart allows electrical propagation to be transmitted from the sinoatrial (SA) node (located on the upper part of the right atrium) through both atria and forward to the atrioventricular (AV) node. AV node connects atrial and ventricular chambers. After a delay, the stimulus is conducted through the bundle of His to the bundle branches and eventually to the ventricular myocardium through the Purkinje fibers. Purkinje fibers, located in the inner ventricular walls of the heart, just beneath the endocardium, conduct rapidly the electrical impulse enabling the heart to contract in a coordinated fashion. The delay in the AV node is extremely important. It ensures that the atria have ejected their blood into the ventricles before the ventricles contract [16].

Time ordered stimulation of the myocardium allows efficient contraction of all four chambers of the heart, thereby allowing selective blood perfusion through both the lungs and systemic circulation.

Electrical activity at cellular level

In order to study the surface ECG waveforms, the action potential properties of individual cardiac cells should be understood.

At rest, the membrane potential, i.e. the voltage difference between the inside and the outside of the cell, is negative. A sufficient stimulation of the myocardial cell creates an action potential (AP) representing depolarization and repolarization of the myocardial cell. During depolarization, positively charged ions cross the cell membrane through the channels to which they are permeable, into the cell, while during repolarization they are pumped out.

The myocardial action potential has 5 phases (numbered 0-4), and shown in Fig. 1.1:

- **Phase 4** corresponds to the resting membrane potential, and describes the membrane potential when the cell is not being stimulated (-85 to -95 mV in ventricular myocardium).

- **Phase 0** corresponds to the depolarization phase where an initial fast upstroke results due to the opening of the inward fast Na^+ channels. This opening causes a rapid increase in the membrane conductance to Na^+ (G_{Na}) and thus a rapid influx of Na^+ ions (I_{Na}) into the cell; that is, a Na^+ current. The ability of the cell to open the fast Na^+ channels during phase 0 is related to the membrane potential at the moment of excitation. If the membrane potential is at its baseline (about -85 mV), all the fast Na^+ channels are closed, and excitation will open them all, causing a large influx of Na^+ ions. If, however, the membrane potential is less negative, some of the fast Na^+ channels will be in an inactivated state insensitive to opening, thus causing a lesser response to excitation of the cell membrane and a lower maximum potential. For this reason, if the resting membrane potential becomes too positive,

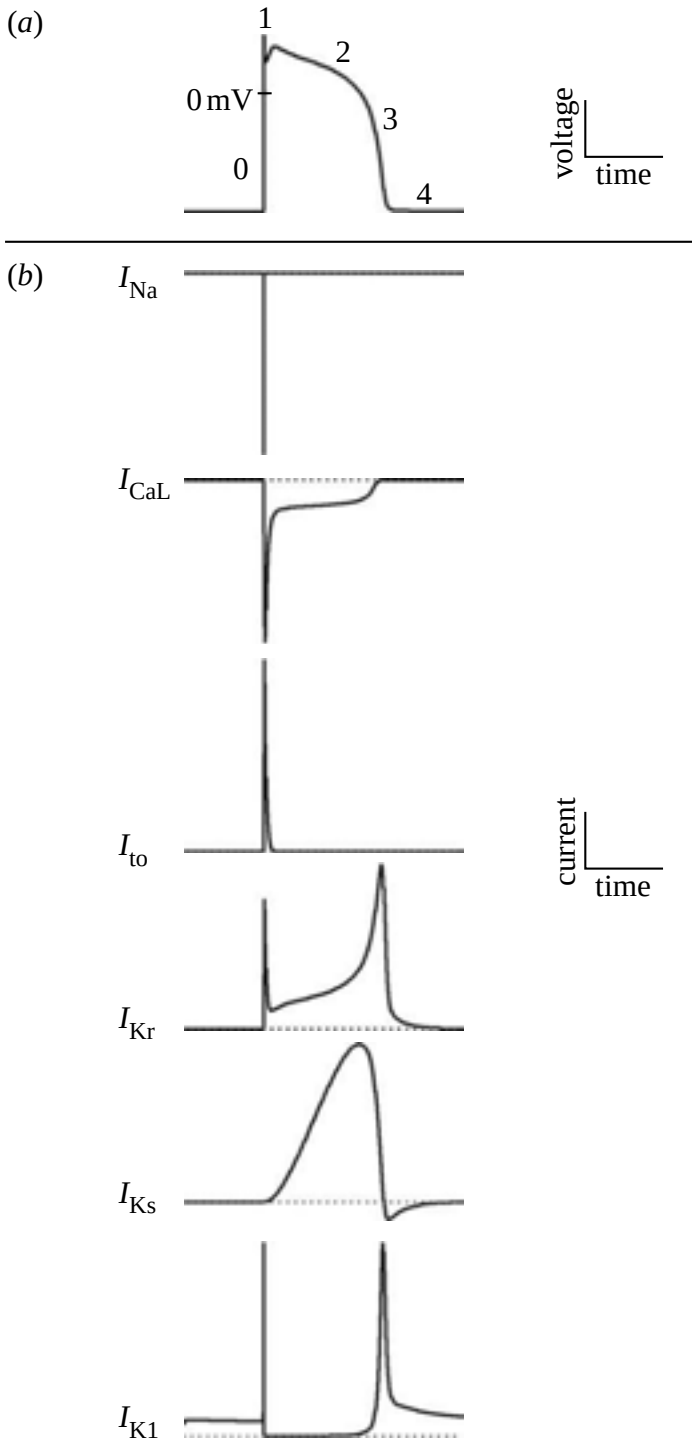

Figure 1.1: *a*) Action potential of a myocardial cell with its different phases indicated.*b*) Ionic currents underlying the different phases (Reproduced from [1])

the cell may not be excitable, and conduction through the heart may be delayed, increasing the risk for arrhythmias.

- **Phase 1** represents an initial and brief repolarization and occurs with the inactivation of the fast Na^+ channels. The transient net outward current causing the small downward deflection of the AP is mainly due to the movement of K^+ ions, carried by the transient outward potassium current I_{to1}. Particularly the transient outward potassium current I_{to1} contributes to the "notch" of some ventricular myocyte action potentials.
- **Phase 2**, also called "plateau" phase of the cardiac action potential, is sustained by a balance between inward movement of Ca^{2+} (I_{Ca}) through L-type calcium channels and outward movement of K^+ through the slow delayed rectifier potassium channels, I_{Ks}. This plateau phase prolongs the action potential duration and distinguishes cardiac action potentials from the much shorter action potentials found in nerves and skeletal muscle.
- **Phase 3**, the "rapid repolarization" phase, the L-type Ca^{2+} channels close, while the slow delayed rectifier (I_{Ks}) K^+ channels are still open. This ensures a net outward current, corresponding to negative change in membrane potential, thus allowing more types of K^+ channels to open. These are primarily the rapid delayed rectifier K^+ channels (I_{Kr}) and the inwardly rectifying K^+ current, I_{K1}. This net outward, positive current (equal to loss of positive charge from the cell) causes the cell to repolarize. The delayed rectifier K^+ channels close when the membrane potential is restored to about -80 to -85 mV, while I_{K1} remains conducting throughout phase 4, contributing to set the resting membrane potential.

Global electrical activity from the surface ECG

As the heart undergoes depolarization and repolarization, the electrical activity which is generated spreads not only within the heart, but also throughout the body. The ECG describes the different electrical phases of a cardiac cycle and represents a summation in time and space of the action potential gradients generated in the cardiac tissue.

QRS complex reflects the ventricular depolarization of the myocardium, and its duration represents to the time in which the impulse is traveling within the ventricles. On the other hand, the T wave represent the heterogeneity of ventricular repolarization. The formation of the T wave is dependent on both the sequence of ventricular activation and the heterogeneities in AP characteristics throughout the ventricular myocardium.

Ventricular depolarization, QRS complex, is shorter than repolarization T wave due to the fast conduction velocity of the electrical impulse in the ventricle. Repolarization wave of the ventricle, the T wave, is smoother than the QRS due to the dispersion in action potential durations (APD) of the different cells in the myocardium. In Fig.1.2, the morphology and timing of action potential waveforms of different parts in the atria and ventricles are shown, together with a representation of the resulting ECG measured on the body surface.

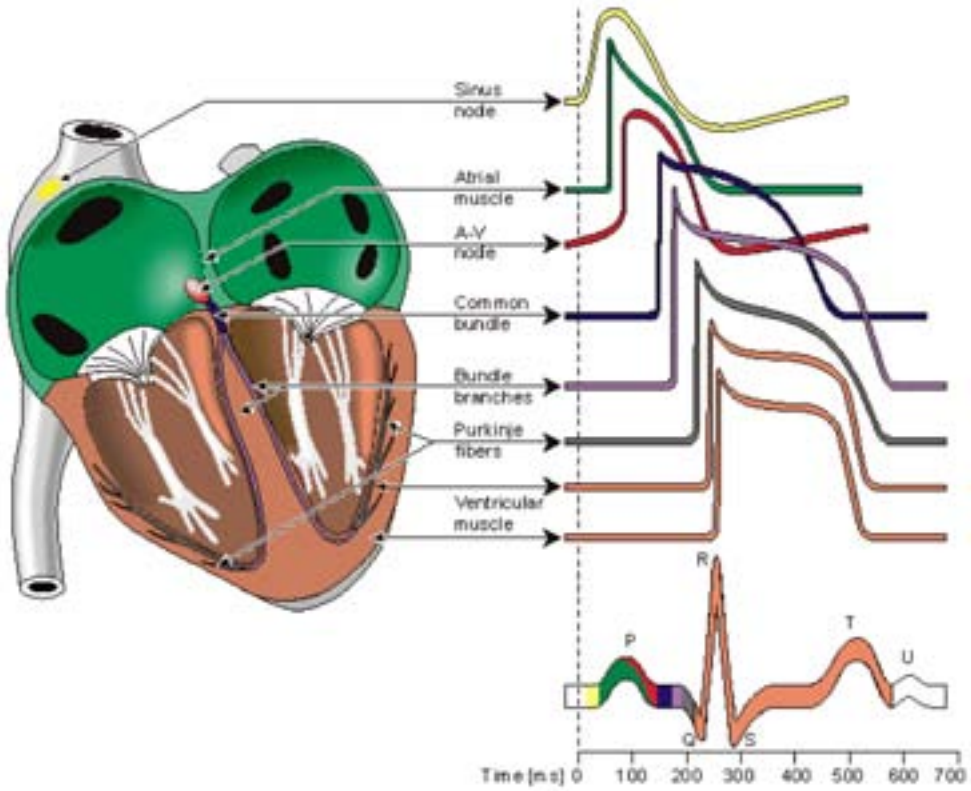

Figure 1.2: Morphology and timing of different action potentials from different regions of the heart and the related ECG measured on the body surface.

1.2.2. ECG Recording and Leads

The electric waves in the heart are recorded in millivolts by the electrocardiograph. These ECG waves are registered by electrodes placed on certain parts of the body which are usually ten in number. An ECG signal presents different characteristics depending on the location of the recording electrode. Simultaneous ECG recording in different positions of the torso (channels or leads) provides time and spatial information about cardiac events. The output from two electrodes is called lead and measures the voltage difference between both.

In 1913, Einthoven named the leads between the three limb electrodes "standard lead I, II and III" referring to the two arm electrodes and the left leg electrode. He studied the relationship between these electrodes, forming a triangle where the heart electrically constitutes the null point (see Fig. 1.3). The relationship between these standard leads which reflect the electrical activity in three different directions forming 60^o between them, is called Einthoven's triangle, and is used when determining the electrical axis of the heart.

The most commonly used lead system is the standard 12 lead ECG, that consists on eight independent leads (referred to as unipolar precordial leads $V1$-$V6$ and the bipolar limb leads I and II), and the remaining four leads (bipolar III and augmented limb

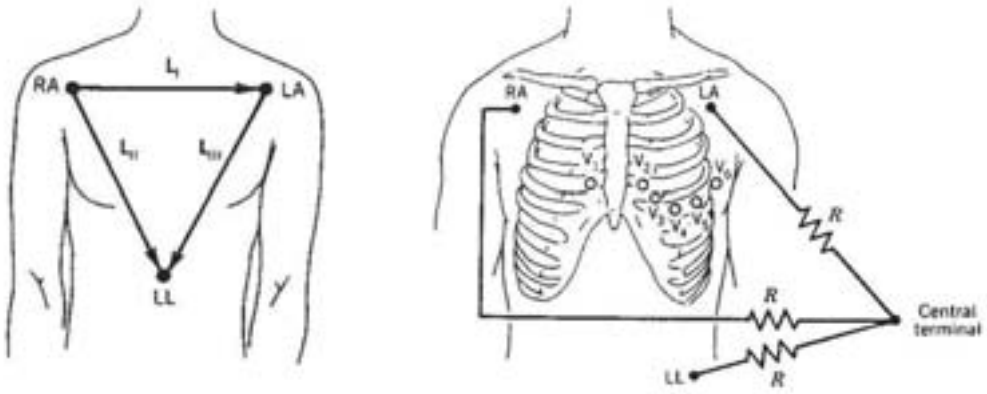

Figure 1.3: Einthoven's bipolar leads I, II and III, and precordial leads V1-V6.

leads: aVR, aVL and aVF) that can be calculated using the independent ones. Each of the 12 leads represents a particular orientation in space, as indicated below (RA = right arm, LA = left arm, LL = left leg and RL = right leg):

- Bipolar limb leads (frontal plane):
  - Lead I: RA (-) to LA (+) (Right Left, or lateral)
  - Lead II: RA (-) to left LL (+) (Superior Inferior)
  - Lead III: LA (-) to LL (+) (Superior Inferior)
- Augmented limb leads are derived from the same three electrodes as leads I, II, and III (frontal plane):
  - Lead aVR = RA $-\frac{1}{2}$(LA+LL) = $-\frac{\text{I+II}}{2}$
  - Lead aVL = LA $-\frac{1}{2}$(RA+LL) = $-\text{I}-\frac{\text{II}}{2}$
  - Lead aVF = LL $-\frac{1}{2}$(RA+LA) = $-\text{II}-\frac{\text{I}}{2}$
- Unipolar precordial leads V1-V6 (frontal plane) are placed directly on the chest as shown in Fig. 1.3. Because of their close proximity to the heart, they do not require augmentation. These unipolar leads measure voltage variations of electrodes V1-V6 with respect to the Wilson's central terminal which is the average of the three limb leads $V_W = \frac{1}{3}(RA + LA + LL)$.

The orthogonal lead system or Frank lead system (X, Y, Z) reflects the electrical activity in three orthogonal leads (see Fig. 1.4) They are calculated from electrodes placed on different points of the body (A, C, E, I, M, F, H) and a net of resistances from which X, Y and Z are generated (see Fig. 1.4). In the literature, there are transformation matrices such as Dower's matrix which allows to synthesize the standard 12 lead ECG from the three Frank leads and viceversa [17, 18].

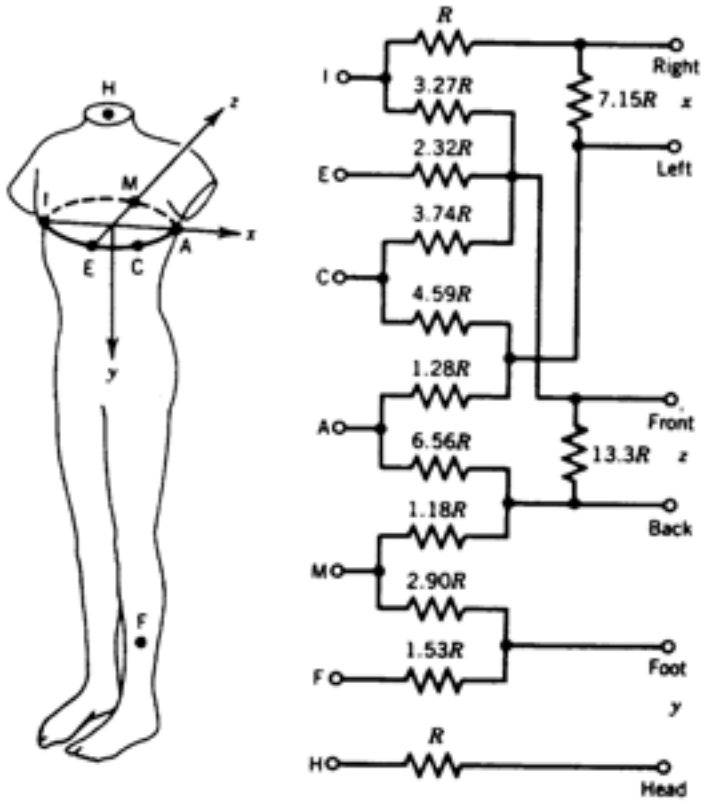

Figure 1.4: Original X, Y and Z leads, together with the resistances needed to calculate them. Reproduced from [2].

Holter Recordings

Ambulatory electrocardiography (Holter) is a continuous ECG recording during long periods (24-48 hours) using a reduced number of leads (usually two or three leads) while the patient is doing hers/his usual daily activities [19]. This tool was originally used for assessing the presence of various classes of beat abnormalities. Later applications of this tool were expanded to detection of ST displacement, documentation of therapeutic effects of anti-arrhythmic and anti-ischemic drugs, prediction of future cardiac events, heart rate variability, pacemaker analysis, multi-channel ST analysis, QT repolarization and high resolution ECG analysis for late potential and P-wave analysis. The electrodes used are similar to those used during clinical standard ECG and they are connected to a tape recorder.

This method makes it possible to study transient cardiac problems, problems that "come and go" and could be missed during physical examination and routine electrocardiography (ECG) because these procedures permit only a few seconds of observation. This kind of recordings are useful in diagnosing transient heart arrhythmias and transient ischemia.

Ischemic episodes are not always accompanied by anginal pain; in fact this so called "silent ischemic" events are even more frequent in patients with coronary artery disease than are the ones with chest pain [20]. Therefore, a non invasive tool as Holter that continuously monitors the ECG during everyday activities, allows to diagnose "come and go" ischemic episodes. The long duration and huge amount of data for these recordings require some kind of automatization by signal processing techniques in order to effectively detect potential ischemic events on the ECG signal.

Manually analyzing the data would take too long (at least the time of the recording), this is why it is essential to use signal processing in order to interpret the recordings.

Ambulatory ECG recording suffers from the influence of external noise such as electrical interferences, relative movement between the electrode surface and the skin, or extra-cardiac electrical phenomena such as muscular activity or baseline variations generated by respiration. Therefore, signal processing techniques are needed to extract relevant information from the ECG in a reliable way. Many of those signal processing techniques in cardiac applications are nicely described in [15].

1.2.3. ECG Signal Description

Temporal Characteristics

As we described before, ECG represents the heart's electrical activity over time and therefore, it presents a characteristic pattern with five characteristic waves (P, Q, R S and T), which are repeated every cardiac cycle:

P wave reflects the depolarization of the atrium (80-100 ms). During normal atrial depolarization, P wave is upright over most of the standard 12-lead ECG and the absence of the P-wave indicate diseases such as atrial fibrillation or sinoatrial node block.

Q, R and S waves compose the QRS complex that reflects the fast depolarization of the ventricles (60-100ms). QRS complex presents a larger amplitude than the P wave due to the larger muscle mass of the ventricles compared to the atria. Prolonged QRS can indicate diseases such as bundle branch blocks.

T wave represents the repolarization of the ventricles (150-350ms) [21]. It is longer in duration than depolarization (i.e., conduction of the repolarization wave is slower than the wave of depolarization) and it is very rate dependent, unlike the P wave or the QRS complex.

Some widely used repolarization indices (see Fig. 1.5) which are important in the study of ischemia and arrhythmias, object of this thesis, are:

- *QT* interval: time interval from the onset of the QRS complex (onset of the depolarization) to the end on the T wave (end of the repolarization). Therefore, the QT represents the time for both ventricular depolarization and repolarization to occur, and also roughly estimates the duration of an average ventricular action potential. It is rate dependent. Duration about 350-400 ms.

- *ST* segment: time interval from the end of the QRS complex to the onset of the T wave. It is also called the isoelectric segment because it is the time at which the

entire ventricle is depolarized and roughly corresponds to the plateau phase of the ventricular action potential. Deviations of ST level can be caused by ischemia as it will be seen later. Duration about 50-150 ms.

- RR interval: time interval between two R waves that represents the cardiac cycle. Duration about (600-1000 ms)
- T_{pe} interval : time interval from the peak to the end of the T wave.
- T_w interval: time interval comprising the width of the T wave.

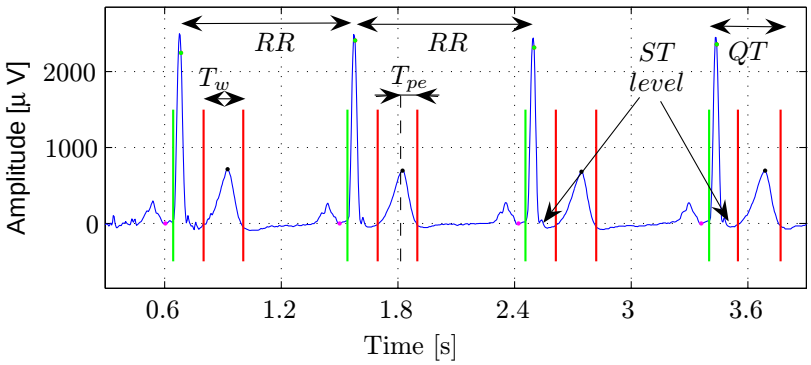

Figure 1.5: Different intervals measured on the ECG to compute the QT, T wave width (T_w), T wave peak to T wave end (T_{pe})and RR interval series. The ST level series is calculated in this thesis by averaging the first 8 ms of the ST segment.

Frequency Characteristics

In order to apply correctly signal processing techniques, the frequency components of each ECG waves should be known. In Fig. 1.6, the ECG spectrum and its components are characterized [3].

1.2.4. Pathologies reflected in the ECG

- **Ischemia:** Insufficient blood supply to the myocardium can result in myocardial ischemia, injury or infarction, or all three. Atherosclerosis of the larger coronary arteries is the most common anatomic condition to diminish coronary blood flow. The branches of coronary arteries arising from the aortic root are distributed on the epicardial surface of the heart. These in turn provide intramural branches that supply the cardiac muscle. Myocardial ischemia generally appears first and is more extensive in the sub-endocardial region since these deeper myocardial layers are farther from the blood supply, with greater intramural tension and need for oxygen.

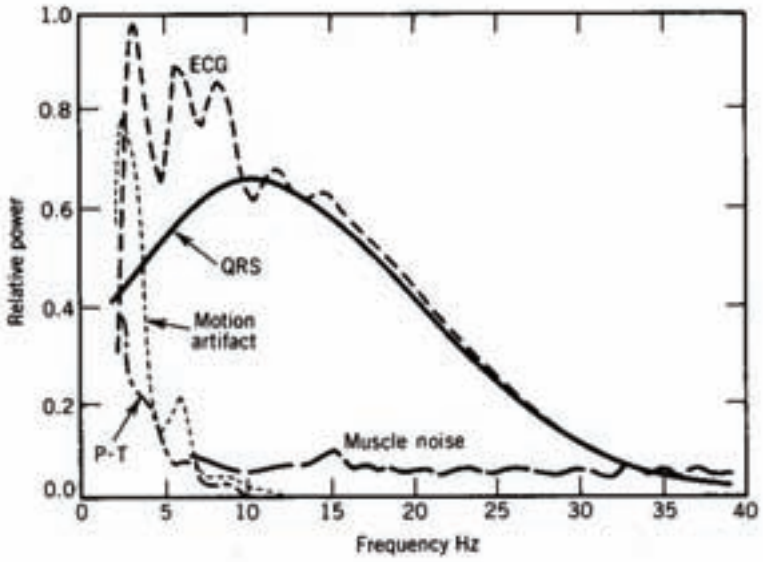

Figure 1.6: ECG power spectrum and its components. Reproduced from [3].

- **Arrhythmia:** It can be defined as an abnormal electrical activity in the heart. The most common arrhythmias are atrial tachycardia that shows a narrow QRS complex with heart rates above 100 beats/min and atrial bradycardia with a slow rhythm, less than 60 beats/min. Ventricular arrhythmia generate Premature Ventricular Contractions (PVC) and then produce shape and duration changes in the QRS complex. Ventricular tachycardia is a fast heart rhythm that originates in one of the ventricles of the heart. This is a potentially life-threatening arrhythmia because it may lead to ventricular fibrillation, asystole, and sudden death.

1.3. Ischemia and its ECG manifestations

Myocardial ischemia can be defined as the imbalance between oxygen/nutrient delivery with regard to myocardial requirements [22]. Ischemia is generally produced by a partial occlusion of a coronary artery (coronary arteries represent the only source of blood supply to the myocardium), reducing the blood flow, and consequently oxygen (hypoxia), glucose or nutrients. In this case, when a supply reduction is produced, the imbalance is referred to as "supply ischemia". The term "demand ischemia" refers to a condition where an increased oxygen demand caused by exercise, tachycardia or emotion, leads to a transitory imbalance [23, 24, 25, 26].

Myocardial ischemia affects both depolarization and repolarization, leading to changes of QRS complex, ST segment and T wave in the ECG. Study of such manifestations can help to distinguish among the different types and degrees of ischemia, localize the time in which those events occur, and identify the occluded coronary artery.

At cellular level, ischemia markedly influences the electrophysiological properties of

the myocardial cells. The increased extracellular potassium level, $[K^+]_o$, during ischemia, leads to a reduction of the resting membrane potential to less negative values (between -60 and -65 mV). This is reflected on the ECG as a change in the TQ segment (baseline). There is also a reduction in rate of rise of phase 0 (reduction of number of sodium channels opened). This is reflected on the ECG as changes in the QRS complex such as morphological changes [27], amplitude changes [28] and slope changes [29]. During ischemia, fluctuations in calcium levels during systole and diastole produce changes in the calcium currents of the membrane and in action potential durations (APD) [30, 31]. Ischemia results also in a decrease of the amplitude and duration of the AP, as shows Fig. 1.7. AP waveform changes resulting in ST displacement, include alterations in the duration, amplitude and and slope of phase 2. The ST segment displacement described in the surface ECG during ischemia corresponds to a combination of the TQ segment change (loss of resting membrane potential) and the real ST segment change (shorter APD).

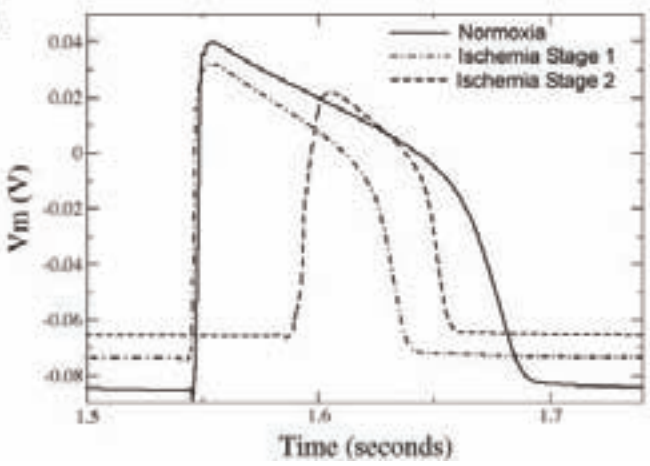

Figure 1.7: Simulation of an action potential in normoxia and two stages of ischemia, stage I and a more severe stage II. Reproduced from [4].

In the initial phase of the normal cellular repolarization (Phase 1 to 2), all the cells are in the plateau part of the transmembrane AP, and therefore a null gradient is generated. This is reflected on an isoelectric or a positive quasi-isoelectric level in ST segment of the surface ECG, which corresponds to the first part of the repolarization phase [16]. The electrocardiographic effect of myocardial ischemia is the "injury current" which results from partial depolarizations and reduced duration and amplitude of APs. When ischemia is produced at the tissue, cells surrounding the affected area reduce duration and amplitude of their AP, producing an AP gradient between normal and ischemic myocardial zones, and therefore an "injury current" between both. This is reflected on the ECG through changes in the ventricular repolarization period including the ST-T complex [25, 32, 33]. These changes in the ST segment and in the T wave are produced before the QRS complex change, indicating that a more severe ischemia is needed to produce changes in the depolarization phase [34].

In clinical practice, diagnosis of myocardium ischemia is usually performed by evaluating just the deviation of the ST segment, considered as an early ischemic marker. The recommended criteria to diagnose changes in the ST segment requires that two or more contiguous leads from the 12-lead ECG show a change in the ST segment of more than 0.1 mV [35].

The ST deviation pattern can correspond to a ST elevation or a ST depression depending on different factors related to the ischemic process such as the degree of severity or localization of the ischemic zone.

Electrocardiographic images of ischemia are different depending on whether the ischemic area affects mainly the sub-endocardium or the sub-epicardium. It should be noticed that the subendocardial layer is the most susceptible to ischemia, being the most distant from the source of blood supply. In the case of sub-endocardial ischemia, ST depression appears at different intensities according to its degree [36], while in the case of sub-epicardial, also called transmural ischemia, ST elevation and Q wave changes occurs [37, 16]. In some patients, however, precordial ST depression might be the equivalent of ST elevation [33], indicating an acute myocardium infarction of the posterior wall, caused by the complete occlusion of the left circumflex coronary artery.

Despite the frequent use of ST deviation in clinical practise, several studies have shown the limitations of using it as the only diagnostic tool due to its low specificity [33]. In addition to ischemic ST episodes (IE), there are other ST events such as heart rate related episodes (HRE), body position changes ($BPCE$) or conduction changes (CCE) which also result in ST segment modifications being considered artefactual events when ischemia is the target. The dynamics of the different ST events is different in each case. HRE as well as IE are considered transient ST segment episodes (TE) and characterized by a length and an extremum deviation. In contrast, $BPCE$ and CCE, characterized with a sudden shift in the ST level function, are denoted as sudden step events (SSE) and are characterized by the time instance they occur.

1.4. Objectives and implications of the thesis

This thesis can be divided into two main parts. The first part (chapters 2 to 4) is focused on ischemia detection in Holter recordings and how to cancel out other ST episodes which also produce changes in the ST segment and are misidentified as ischemic events. The second part aims at searching for arrhythmia risk markers by evaluating rate adaptation of the T wave peak to T wave end (T_{pe}) interval (chapter 6) and by quantifying dispersion in the action potential duration (APD) restitution(APDR), measured at cellular level, from the surface ECG (chapter 7).

In the first part we have evaluated and improved an ischemia detector [38] based on changes in the ST segment, on the "Long-Term ST database" (LTSTDB) [39]. This database contains 24 hour duration records with a large number of human annotated ischemic and non-ischemic ST-segment events, such as heart rate related events, body position changes or conduction changes; giving a much more extensive tool to evaluate

and develop ischemia detectors than the early "European Society of Cardiology ST-T" (ESCDB) [40]. A new module has been included in the ischemia detector to cancel out body position change (BPC) events misclassified as ischemic events. A BPC detection technique [41] which has been applied to the RMS series of the QRS complex and ST segment is used.

Additionally, it is shown that noise distribution of the KLT of both QRS and STT complexes is more 'heavy-tailed' than Gaussian noise due to outliers (e.g. artifacts, impulsive noise, baseline wandering or ectopic beats). Then, a new BPC detector based on the Generalized Likelihood Ratio Test (GLRT) for Laplacian noise distribution has been derived and evaluated on different databases.

In the detection part, it has been shown that in addition to ischemic ST episodes (IE), there are other ST events such as heart rate related episodes (HRE), body position changes ($BPCE$) or conduction changes (CCE) which also result in ST segment modifications being considered artefactual events when ischemia is the target. Then after dealing with the detection problem, several indices based on repolarization and depolarization intervals have been used to classify and discriminate between different ST events in Holter recordings. This will help us to understand better which ECG-based indices are involved when ischemia is present and which ones change when non ischemic events with ST segment deviation are misclassified.

The second part of this thesis aims at searching for risk markers. Dependence of action potential duration (APD) to heart rate changes has been shown to provide relevant information for arrhythmic risk stratification. APD restitution (APDR) curve characterizes the relationship between action potential duration (APD) and the RR interval under stationary conditions. Heterogeneities in ventricular myocardium make the APDR curve present spatial variations that leads to APDR dispersion, which has been proposed to act as a potent arrhythmogenic substrate. In particular, enhanced ADR dispersion has been associated to ventricular tachycardia. In this thesis, it is shown a complete methodology to quantify this index non-invasively from the surface ECG.

1.5. Organization of the thesis

- **Chapter 2:** A modified ischemia detector based on the root mean square (RMS) of the ST segment is presented. This ischemia detector is evaluated on the LTST database including a module to cancel body position change events using the RMS series of the ST segment and QRS complex. The content of this chapter has been published in the proceedings of an international conference:

  - Mincholé A., B. Skarp, P. Laguna. Evaluation of a Root Mean Square Based Ischemia Detector on the LTST Database. XXXII Ann. Conf. *Computers in Cardiology*. Lyon. IEEE Press. pp. 853-856. 2005

- **Chapter 3:** This chapter presents a method for detecting body position changes (BPC) on the ECG based on the Generalized Likelihood Ratio Test (GLRT) for

Laplacian noise distribution. This detector is evaluated in two databases: one with controlled BPCs which assesses the detector performance and the other with ECG recordings of patients undergoing a percutaneous coronary intervention, where ECG changes are abrupt but there are not BPCs, which assess the rate of false alarms. A comparison between the performance of this GLRT-based detector that assumes laplacian noise distribution and a previous one assuming gaussian noise has been made.

- **Chapter 4:** In this chapter, different types of episodes related to changes in the ST segment: ischemic, heart rate related events and sudden step ST changes (body position changes and conduction changes) have been analyzed and characterized. The very similar signatures of ST modifications have led us to look for other ECG indices such as heart rate-based indices, correlation between the absolute ST segment deviation and heart rate series, the interval between the Tapex and the Tend, T wave amplitude, the signal-to-noise ratio and changes in the upward/downward slopes of the QRS complex, to distinguish between them. Classification between the different types of episodes has been performed showing the most significant indices involved. This study has been published in:

  - A. Mincholé, F. Jager, P. Laguna. Discrimination Between Ischemic and Artifactual ST Segment Events in Holter Recordings. *Biomedical signal processing and control*, Vol. 5 pp. 21-31, 2010.
  - A. Mincholé, F. Jager and P. Laguna (2007). Discrimination between Demand and Supply Ischemia Episodes in Holter Recordings . *29th Annual International Conference of the IEEE Engineering in Medicine and Biology Society* (EMBC07), Lyon, pp. 2579-2582

- **Chapter 5:** This chapter introduces the Valsalva maneuver and characterizes the changes in different repolarization indices during the strain. RR, QT, T_{pe} and T_w (T wave width) intervals are analyzed under the hypothesis that during the strain of the Valsalva maneuver an increase in the myocardium requirements is produced, leading to a transient demand ischemia. This work has been published in:

  - A. Mincholé, J. P. Martínez Cortes, P. Arini, M. Risk, P. Laguna Lasaosa. T Wave Width Alterations during Valsalva Maneuvers in Diabetic Patients. *Computers in Cardiology* 2006. September. 2006. pp. 709-712

  A database referred to as ANS-UZ DB, has been acquired to characterize changes in the repolarization intervals generated by the tilt test and the Valsalva maneuver. This database includes 15 control subjects of about 28 years old, and the signals recorded were the 12-lead ECG, the blood pressure, photoplethysmographic signal, the respiratory signal and the expiration pressure. A complete description of the ANS-UZ DB and a study of changes in some repolarization indices is shown.

- **Chapter 6:** In this chapter, the T peak to T end interval (T_{pe}) adaptation to sudden changes in heart rate is modelled, characterized and compared with the QT rate adaptation, using the tilt test database described in chapter 5. Published in:

  - A. Mincholé, E. Pueyo, P. Laguna. Transmural Differences in Rate Adaptation of Repolarization Duration Quantified from ECG Repolarization Interval Dynamics. *XXXVI Ann. Conf. Computers in Cardiology*, Park City, pp. 597-600. Septiembre. 2009

- **Chapter 7:** This chapter aims at quantifying an arrhythmia risk marker, APD restitution (APDR) dispersion, measured at cellular level, by making only use of the surface ECG. The proposed estimate accounts for rate normalized differences in the steady state T wave peak to T wave end interval (T_{pe}). A methodology was developed for its computation, which includes compensation for the T_{pe} memory lag after heart rate (HR) changes. The capability of the proposed estimate to reflect APDR dispersion was assessed using a combination of ECG signal processing and computational modeling and simulation. This study has been published in:

  - A. Mincholé, E. Pueyo, J. F. Rodríguez, E. Zacur, M. Doblaré, P. Laguna. Quantification of Restitution Dispersion from the Dynamic Changes of the T wave peak to end, measured at the Surface ECG. *IEEE Transactions on Biomedical Engineering, 2011, doi:10.1109/TBME.2010.2097597.*
  - A. Mincholé, E. Pueyo and P. Laguna. Dispersion of APD restitution quantified from the surface ECG. *Journal of Electrocardiology*, Volume 43, Issue 6, 2010, Pages 643-644
  - A. Mincholé, E. Pueyo, J. F. Rodríguez, E. Zacur, M. Doblaré, P. Laguna. Evaluation of a Method for Quantification of Restitution Dispersion from the surface ECG. *XXXVII Ann. Conf. Computing in Cardiology*, Belfast, 2010.

Chapter 2

Evaluation of a Root Mean Squared Based Ischemia Detector on the Long-Term ST Database

2.1. Introduction

Today 24-hour ECG monitoring is widely used to evaluate patients with suspected or known coronary artery disease. The long duration and huge amount of data of these recordings require some kind of automatization by signal processing techniques in order to effectively detect potential ischemic events on the ECG-signal.

The ST deviation is considered the most sensitive marker to diagnose ischemia in clinical practice, and therefore most ischemia detectors mainly relies on ST segment-based indices [42, 43, 44, 45, 38], as it is described in section §2.1.1. By analysing changes of the ST-segment (see Figure 2.1), silent ischaemia is often diagnosed with the help of Holter recordings. However, ST segment changes can also result from other causes such as heart rate related events, changes in the electrical axis of the heart due to body position changes (BPC) and conduction changes among others. Reliable ST detectors should distinguish between ischemic and non-ischemic ST changes, although this task remains being a challenge [46].

Most of ST segment based detectors [42, 43, 44, 47, 38] were developed and tuned using the European Society of cardiology ST-T database (ESCDB) [40]. ESCDB consists of 90 annotated ambulatory ECG recordings from 79 subjects. Each record is two hours in duration and contains two leads. ST segment and T-wave changes were identified in both leads (using predefined criteria which were applied uniformly in all cases), and those event onsets, extremum, and ends were annotated. However, the origin of each ST event was not determined. A more recent database, the Long Term ST Database (LTSTDB) [39], contains longer records (24 hour duration records) than the ESCDB with a large number of human annotated ischemic and non-ischemic ST-segment events such as heart rate related events, body position changes or conduction changes. Therefore, the LTSTDB becomes a much more interesting and extensive tool to evaluate and develop ischemia

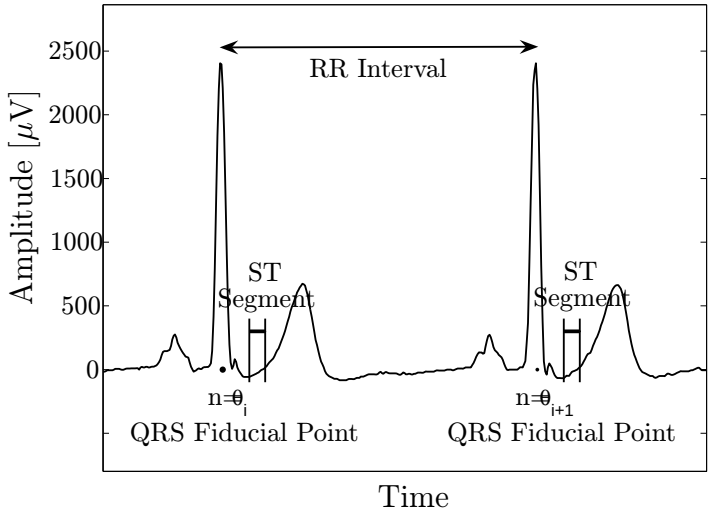

Figure 2.1: Example of two beats where the QRS fiducial points, the segmented ST length and the RR interval are represented.

detectors than the ESCDB.

In this work, the ischemia detector [38], based on the RMS of the ST segment and developed and tuned using the ESCDB, is re-evaluated on the LTSTDB. Here, we group together heart rate related (HRE) and ischemic events (IE), considered transient ST segment episodes (TE) and characterized by a length and an extremum deviation, as the target "group", such that performance in the LTSTDB can be compared to performance in the ESCDB. Therefore, BPC and conduction changes (CCE), also resulting in ST segment deviations, need to be cancelled to avoid false detections. These two types of events are characterized by sudden shifts of the ST segment which result in a step-like signature in different ECG representations such as Karhunen-Loève Transform (KLT) or the root mean square (RMS) of the QRS complex and the ST segment [46].

Besides revisiting and modifying the RMS-based ischemia detector [38] to improve its performance under the new LTSTDB perspective, a module to cancel out false ischemic alarms due to body position changes has been incorporated.

2.1.1. Automated Methods for Ischemia Detection in Holter Recordings

A large variety of techniques to detect myocardial ischemia in long-duration ECGs have been published. Most of them are based on the identification of ST segment deviations and changes in the T wave morphology. Among the detection techniques using the time-domain approach, there are some that set thresholds to the ST segment deviations [42, 43]. In the work [44], episode detection is based on the analysis of the 2-D path described by the two ST deviations derived from the two ECG leads. Root mean square series of

differences between each ST segment (or ST-T) and an averaged segment is used by [38].

Other studies are based on the analysis of the Karhunen-Loève transform (KLT) which provides a very useful tool to estimate morphological changes. KLT maximizes the variability of the signal and concentrates in a few coefficients most of the signal information [48]. KLT coefficient series of the ST segment and the QRS complex have been used in [47] to detect ischemia. Also, the KLT coefficient series of the ST-T complex was used to detect ischemic events [49].

Some of these detectors have been developed under the ESCDB database, obtaining a performance in terms of sensibility/positive predictivity of 81.5%/82.5% ([43]), 84%/81% ([44]), 84.7%/86.1% ([38]), and 87.1%/87.7% ([47]). When [47] is applied to the LTSTDB, performance lowers to 74.0%/61.4% as it is shown in [45].

The work in [45] presents a technique that combines ST level deviations and morphological KLT series of the ST segment and QRS complex that has been developed under the LTSTDB [39] reaching a performance of 78.9%/80.7% when detecting significant ST changes. Performance using the ESCDB improve up to 81.3%/89.2%.

Ischemic detectors described above are the ones with better performances in ESC and LTST databases.

Other studies have analyzed the ST segment in the frequency-domain, showing that ischemic beats contain lower frequencies than normal ones, [50]. In the time-frequency domain, heart rate variability has been investigated to identify ischemic segments, [51]. Different scales in the wavelet transform have been used to describe and identify heart beats. Their capability of discrimination between normal, ventricular premature and ischemic beats has been studied by a linear discriminant analysis [52].

Other methods apply artificial intelligence techniques to classify individual ischemic beats as a preliminary step for detection of ischemic episodes. Among these methods, methods based on a variety of neural network architectures have been also presented [53, 54, 55]. The work in [53] used information from the ST segment (ST deviation and slope) together with a noise cancellation strategy and classified each beat as ischemic or not getting a performance of 85%/88% using 47 out of 90 recordings of the ESC ST-T database. The work in [54] used a set of three rules (ST-segment elevation, ST depression, and T wave inversion or flattening) and was evaluated in the ESCDB (94%/79%).

Only a few of these methods explicitly address the real-time analysis case where less information (only past and present) is available to take a decision and computational restrictions could exist [43, 51]. A recent study providing a real-time execution combines signal processing methods (time-domain analysis) to detect possible ischemic episodes with artificial intelligence techniques to discriminate between ischemic and non-ischemic episodes [56]. It has evaluated on the 48 freely distributed recordings of the the ESCDB achieving 82.2%/79.48% and on the 43 freely distributed recordings of the LTSTDB, lowering the performance to 85.28%/48.44%.

2.2. Methods

2.2.1. Long Term ST Database

The LTST DB [39] contains 86 24-hour duration ambulatory ECG records of 80 patients sampled at $f_s = 250$ Hz. This database offers a very accurate representation of "clinical world" data with two- or three-lead records with a great variety of lead combinations. The leads used in the two-channel records included different pairs from: precordial leads V2, V3, V4 or V5, together with modified limb lead III (MLIII); or lead V5 and lead V2; or modified limb lead L2 (ML2) and modified lead V2 (MV2). The leads used in the three-channel records included: a combination from leads V3, V4, V5, V6, II and aVF, or Zymed's EASI lead system [57] with the leads E-S, A-S and A-I.

Complete expert annotations have been provided for the database following three different annotation protocols. Electrocardiogram waveform is not enough to diagnose myocardial ischemia, so the gold standard for annotating a transient ST segment (TE), IE or HRE, was based not only on ECG waveforms but also on detailed clinical information from the subjects including other clinical investigations, the clinical history and the opinion of expert annotators of the database [39]. Thus, a classification of a particular episode can be driven by a previous knowledge about the patient rather than physiological evidences. This is one limitation we should have in mind when analyzing the results.

Annotations include IE and other ST-segment events such as HRE, $BPCE$ and CCE, providing an extensive and tough tool to evaluate ischemia detectors.

One transient ST episode (TE) has to be significant to be annotated according to the following rules: a) an episode beginning when the magnitude of the ST deviation first exceeds 50 μV, b) the deviation must reach a magnitude of V_{min} or more throughout a continuous interval of at least T_{min} s and c) an episode ending when the deviation becomes smaller than 50 μV, provided that it does not exceed 50 μV in the following 30 s. A simplified figure of these parameters is shown in Fig. 2.2

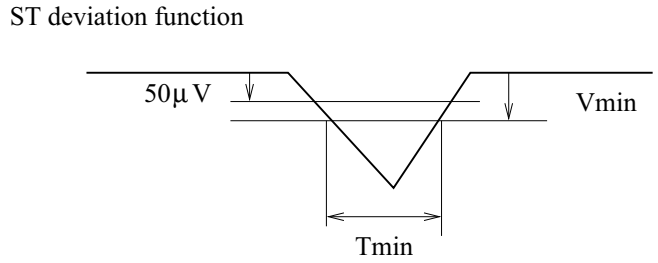

Figure 2.2: Simplified figure of the parameters V_{min} and T_{min}, used to annotate a significant transient ST episode under different protocols.

Three different protocols A, B and C are set depending on V_{min} and T_{min}.

- *Protocol A*: $V_{min} = 75$ μV and $T_{min} = 30$ s.

- *Protocol B*: $V_{min} = 100\ \mu V$ and $T_{min} = 30$ s.
- *Protocol C*: $V_{min} = 100\ \mu V$ and $T_{min} = 60$ s.

Any significant sudden step-change of the ST level function accompanied by a simultaneous sudden step-change in QRS complex morphology was annotated as significant $BPCE$ or significant CCE, according to its nature. These two types of episodes related to sudden step changes in the QRS complex and ST level are referred to as SSE.

2.2.2. Generation of global ST episode annotations from expert lead annotations

Annotations are made independently in each lead of each recording, so they are attached to the lead or leads where the episode is significant. However, since ischemia is a global phenomena and the RMS series are derived using information of all the leads, we have combined the lead by lead annotations. For transient ST episodes, IE and HRE, the time which is first annotated in either lead is set as the onset limit and the time which is last annotated in either lead, as the offset limit, as Fig. 2.3 shows. Also TE, including both IE and HRE annotations, are merged together. In the case of SSE which are annotated by single marks, these marks are combined by using a logical OR, as Fig. 2.3 shows.

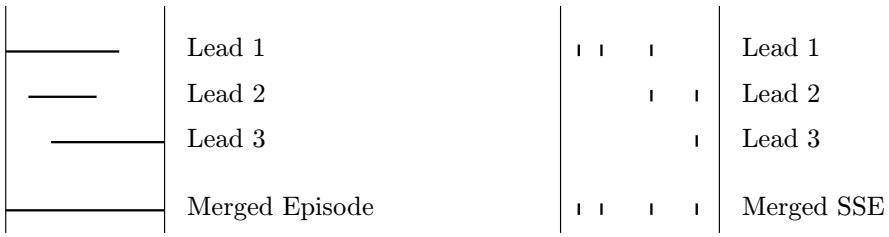

Figure 2.3: Merged episode for three lead annotations and merged SSE marks (BPC or CCE).

The number of different merged events for the different protocols are shown in Table 2.1. Ischemic and HR-related ST episodes which have and onset, extremum and end are referred to as transient ST episodes.

2.2.3. ST segment changes detector

The RMS-based detector operates finding ST segment changes in the series resulting from computing the root mean square (RMS) difference series between the ST segment of a reference beat and the running beat. Then a threshold-based adaptive detector is applied on the RMS series.

	Protocol A	Protocol B	Protocol C
Merged IE annotations	1158	747	580
Merged HRE annotations	378	173	100
Merged TE annotations	1487	903	660
Merged SSE	1563	1563	1563

Table 2.1: Number of different annotations (ischemic IE, HR-related HRE, both which are transient episodes TE and sudden step change events SSE) after merging individual annotations over the leads.

The structure of the detector is shown in Figure 2.4, and consists of a preprocessing stage, estimation of the RMS series, a postprocessing stage and eventually the detection algorithm.

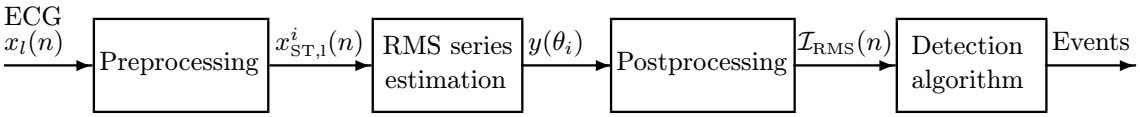

Figure 2.4: Block diagram of the ST change detector presented in this work.

Preprocessing stage

Preprocessing techniques are applied individually on each lead of the raw ECG signal, $x_l(n)$, where l is the corresponding lead and n is the sample index. This preprocessing step consists of first applying a QRS detector (ARISTOTLE arrhythmia detector [58]) in order to find the *QRS fiducial points* of each i^{th} beat (θ_i), defined as the center of gravity of the QRS complex, and removing the non normal labeled beats.

Then, *baseline wander attenuation* is performed using cubic splines [15]. Eventually, a rejection of noisy beats (those with differences in mean isoelectric level with respect to adjacent beats larger than 400 μV). In order to avoid the influence of electrical power line interference and high frequency noise in the RMS difference series, the ECG was *low-pass filtered* using a linear phase FIR filter with a cutoff frequency of 25 Hz. Note that the ST segment frequency band is far below 15 Hz.

The *ST segmentation* (see Figure 2.1) is done selecting a fixed length window of 50 ms, $x^i_{\mathrm{ST,l}}(n)$, starting from a heart rate related sample reference ($n^i_{\mathrm{ST}_0}$) [59], and defined as:

$$x^i_{\mathrm{ST,l}}(n) = x_l(n^i_{\mathrm{ST}_0} + n) \qquad n = 0, ..., N-1$$
$$\text{with} \qquad n^i_{\mathrm{ST}_0} = \theta_i + \frac{40}{1000} f_s + 1.3\sqrt{\frac{rr_i}{1000} f_s} \tag{2.1}$$

where $N = \frac{50}{1000} f_s$ is the window length corresponding to 50 ms, f_s is the sampling frequency (250 Hz in the LTST database) and $rr_i = \theta_i - \theta_{i-1}$ represents the RR interval at the i^{th} beat in sample units.

RMS difference series estimation

In order to calculate the RMS difference series, a reference ST segment, $\overline{x}_{\mathrm{ST,l}}(n)$, has to be defined. This step is very important because a wrong reference ST segment would make non ischemic events be detected as ischemic and ischemic be detected as non-ischemic. In the old version of the ST segment detector [38], the first 100 beats were averaged and the resultant ST segment used as the reference. However, when a recording begins with an ischemic episode, the ST segment selected as the non ischemic reference is indeed ischemic. We have derived a ST level series defined as the first sample of the ST segment of each beat, $x^i_{\mathrm{ST,l}}(1)$ with $i = 1, ..., M$ where M is the number of beats in each record. We choose the lead with highest standard deviation, where an interval of 30 minutes called "*basal interval*" is searched for when two restrictions apply: 1) having the shortest peak to peak amplitude in the series, and 2) the whole interval series being below 4/3 of the $x^i_{\mathrm{ST,l}}(1)$ absolute median value of the recording. Within this "*basal interval*", the middle 100 beats are averaged to calculate the reference beat in each lead $\overline{x}_{\mathrm{ST,l}}$.

Finally the RMS difference series, $y(\theta_i)$ is calculated using the following equation:

$$y(\theta_i) = \frac{1}{L} \sum_{l=1}^{L} \sqrt{\frac{1}{N} \sum_{n=0}^{N-1} \left(x^i_{\mathrm{ST,l}}(n) - \overline{x}_{\mathrm{ST,l}}(n) \right)^2} \tag{2.2}$$

where L is the number of leads of the recording. In this work we have included a normalization factor $\frac{1}{L}$ that accounts for different number of leads in the recording.

Post-processing stage

There are different factors such as motion artifacts that distort the RMS-series and therefore, a post-processing stage is needed. This is done by rejecting beats whose signal-to-noise ratio (SNR) differs more than 20 dB from the running exponentially averaged SNR series with forgetting factor equal to 0.02. Latter, as outlier rejection, a median filter of 5 beats length is subsequently used on the RMS series. This series is evenly resampled to 1 Hz and an exponential running average (with forgetting factor equal to 0.05) is applied to smooth the series resulting in a RMS- series suitable for analysis and denoted hereinafter by $\mathcal{I}_{\mathrm{RMS}}(n)$.

An example of this post-processing over the RMS series of heart rate related episodes is shown in Fig. 2.5.

A second example of potentially ischemic episodes that exhibit the same variations pattern, and may be due to coronary vasospasms (Prinzmetals angina) [16], is shown in Fig. 2.6.

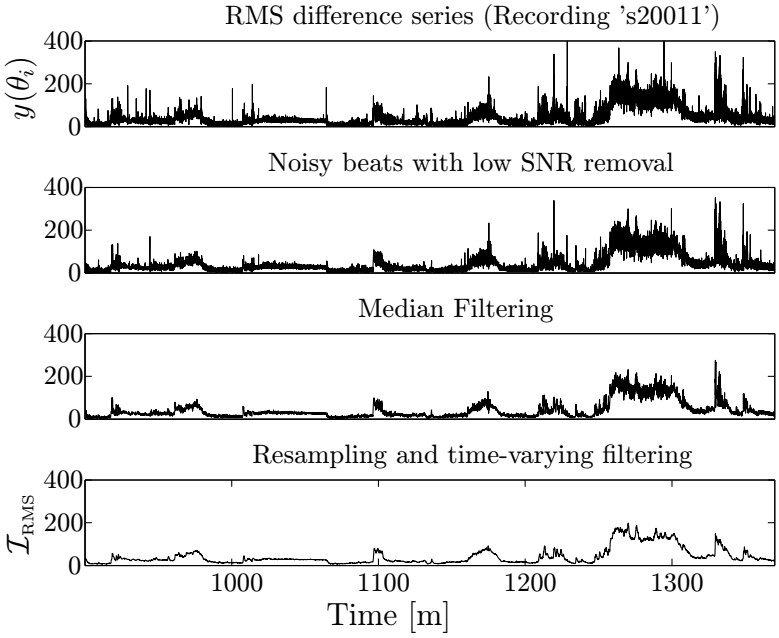

Figure 2.5: Example of the postprocessing stage for the RMS series $y(\theta_i)$.

Detection algorithm

The final stage of the detector incorporates an adaptive threshold that looks for the amplitude of the $\mathcal{I}_{\text{RMS}}(n)$ series and accounts for the slow drift changes of the series. When $\mathcal{I}_{\text{RMS}}(n)$ overcomes that threshold, the detection starts and the threshold is no longer adaptive until the $\mathcal{I}_{\text{RMS}}(n)$ amplitude gets back under the threshold (see 2.7). The threshold adapts itself by adding a fixed amount "η" (first parameter) to the baseline $\xi(n)$ of the $\mathcal{I}_{\text{RMS}}(n)$ series, that is estimated as an exponential average applied on the RMS series:

$$\xi(n) = \xi(n-1) + \beta\left(\mathcal{I}_{\text{RMS}}(n) - \xi(n-1)\right) \tag{2.3}$$

where β is a second parameter that adjusts the speed in the adaptation of the baseline to the $\mathcal{I}_{\text{RMS}}(n)$ series. An episode is detected when:

$$\mathcal{I}_{\text{RMS}}(n) > \xi(n) + \eta \tag{2.4}$$

for a period of more than 45 s, as Fig. 2.7 shows. Some extra rules are also included:

- Baseline is not updated for those beats considered as ischemic.
- Initial value of the baseline $\xi(n)$, is estimated using the average value of the first two hours of the recording. This rule is used to avoid artifacts at the very beginning of the recording or missing ST episodes which have already started before the recording.

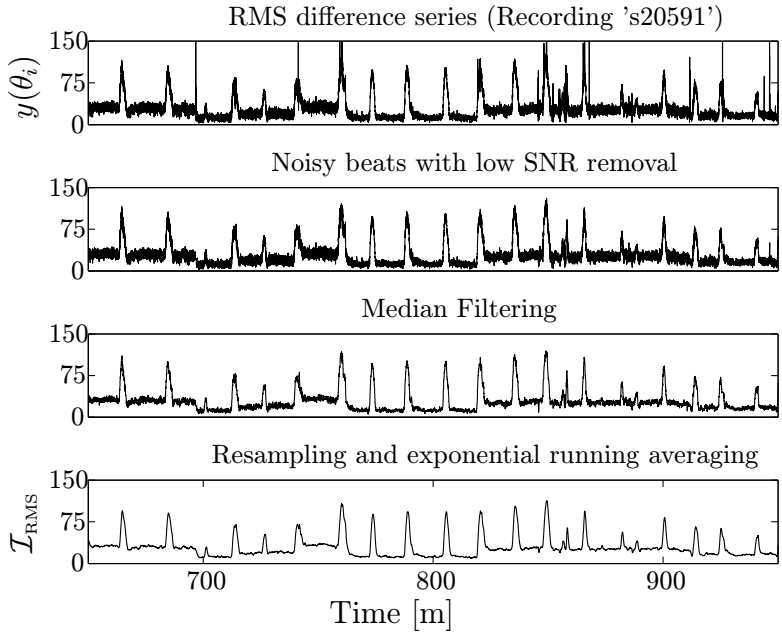

Figure 2.6: Postprocessing stage for the RMS series $y(\theta_i)$ of annotated periodic ischemic events.

- Episodes shorter than 45 s are removed.
- If a new episode began shortly after the previous one, less than 5 min, it was considered to be the same episode.

Both parameters, β and η, are selected experimentally.

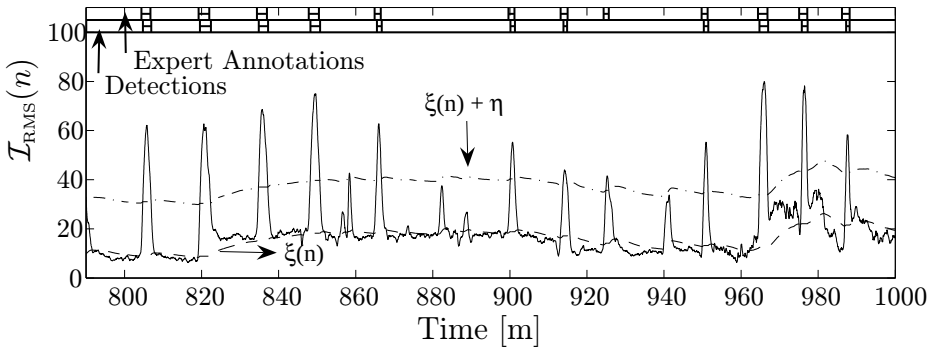

Figure 2.7: Example of ST changes detection on the record *"s20591"* showing, in the highest bar, the annotated ischemic events (protocol B) and in the lowest one the detections. The baseline estimation, $\xi(n)$, (dashed line) and the threshold (dotted-dashed line) are plotted over the $\mathcal{I}_{\mathrm{RMS}}(n)$ series.

2.2.4. BPC cancellation

Body position changes are often manifested as shifts in the electrical axis and may be misclassified as ischemic changes during ambulatory monitoring. Previous studies use the Karhunen-Loève transform (KLT), which tracks morphological changes, to detect body position changes [46, 41]. During these non ischemic events the QRS an STT signatures change rapidly generating step-like function features in their KLT coefficient series.

In this work we have slightly modified a BPC detection technique [41] that was applied to the KLT coefficient series of the QRS and ST-T complexes. This detection technique consists of looking for peaks in the squared output of the matched filter of the QRS and ST-T KLT coefficient series with a step-like function. During a BPC the morphological changes observed in the QRS and STT complexes have a step-like change as shows Fig. 2.8(a). When convoluting these series with a step like function as the one shown in Fig. 2.8(b), we obtain a peak just in each BPC episode (Fig. 2.8(c)).

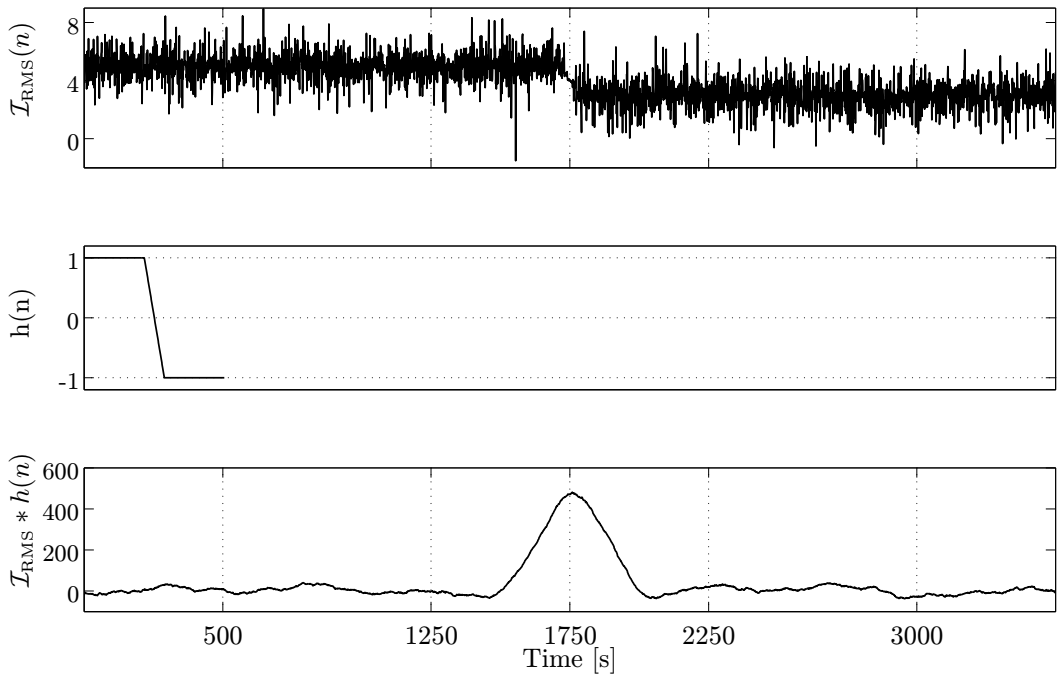

Figure 2.8: Example of the detection strategy. (a): Simulated RMS series with a BPC occurring at the time instant 1750 s. (b): step like function **h**. (c): Resulting detection output after convoluting the KLT or RMS series with the step like function.

In this study, we modified the step-like function to improve performance, lengthening it up to 504 s, 216 s in the two flat intervals with a linear transition of 72 s (see Fig. 2.9).

Instead of using the KLT coefficient series of the QRS and ST-T complexes, we have used the RMS of the QRS complex and the ST segment. The KLT coefficient series and the RMS track morphological changes in a similar way, so the same strategy may be applied. A fixed threshold is applied to the squared matched filter output to detect

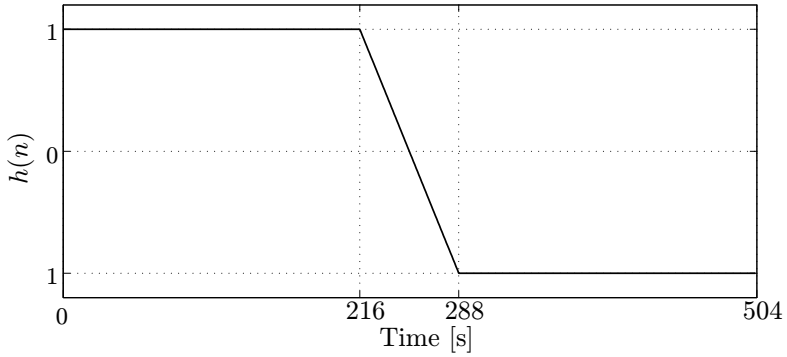

Figure 2.9: Step function used in the BPC detector.

onsets and offsets of each BPC. The energy of each detected episode have to overcome a minimum fixed by another threshold. These thresholds are described in [41, 60].

Additionally, we perform a *flatness test* which consists of forcing a flat interval before and after each corroborated BPC detection. Finally a logic combination of detected events in both series, QRS and ST-T, is done resulting the final BPC detections.

In the next chapter we will further describe the current BPC detection technique and a more suitable detection technique will be proposed.

2.2.5. Performance Evaluation

Detector performance is assessed in terms of sensitivity (SE) and positive predictivity value ($+PV$). Sensitivity is defined as the percentage of actual positives which are correctly identified or detected, and positive predictivity as the percentage of detected episodes which correspond to actual positives:

$$\begin{aligned} SE &= \frac{TP}{TP+FN} \times 100 \\ +PV &= \frac{TP}{TP+FP} \times 100 \end{aligned} \tag{2.5}$$

where TP represents the true positives, FN the false negatives and FP the false positives.

The performance of the detector is computed by two types of statistics: the gross (g) and the average (av) statistics [61]. In the gross statistics each episode has the same weight while in the average statistics the same weight is given to each record.

2.3. Results

Since the detector looks for changes in the ST-segment, ischemic and heart rate related events are combined in the sense of logical OR fuction in the performance analysis. The annotation protocol B from the LTSTDB is used by default since it follows the same

criteria as the ESCDB annotations in which the performance figures reached in terms of sensitivity / positive predictivity ($SE/+PV$) were 85%/86% [38].

In order to choose the optimum β and η values, η has been evaluated from 4 to 18 and β from 0.1 to 0.0001. Then, the minimum distance of $\sqrt{(100-(SE))^2+(100-(+PV))^2}$, where SE and $+PV$ represent the percentages of sensitivity and positive predictivity respectively, has been chosen to set β and η (see Fig. 2.10). Receiving operating characteristics (ROC) curves that characterize the performance SE versus $+PV$ corresponding to the transient episode detection and obtained for different values of β and η, are shown in Fig. 2.11. Selected values for SE and $+PV$ are also shown.

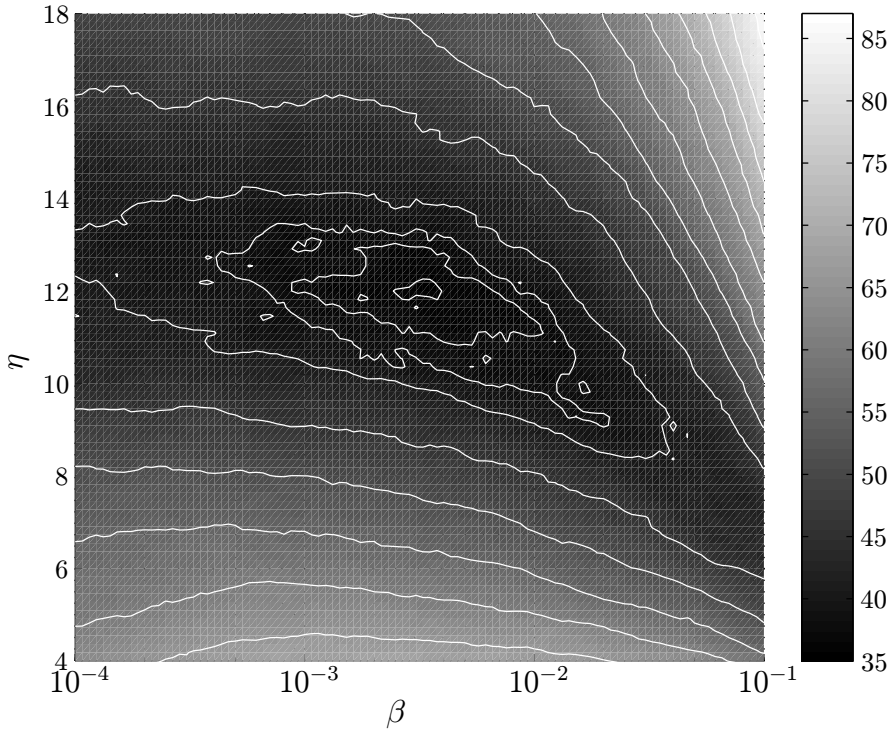

Figure 2.10: Optimization of β and η values such that $\sqrt{(100-(SE))^2+(100-(+PV))^2}$ is minimum. Isocontours with the same $\sqrt{(100-(SE))^2+(100-(+PV))^2}$ distance are represented by white lines.

An example of detection of transient events in a complete recording is shown in Fig. 2.12. The annotated SSE, HRE and IE are indicated together with the detections. Note that at time instants 930 m and 1005 m, two BPCs are found, so baseline is updated.

First, we should note that just a straight forward adaptation of the original RMS-based detector [38], tuned in the ESCDB with the parameter values, $\eta = 18.1$ and $\beta = 0.0083$, reduces its performance figures in the LTSTDB in terms of $SE/+PV$ to 70.5%/68.2%. See Table 2.2, "*Original RMS*".

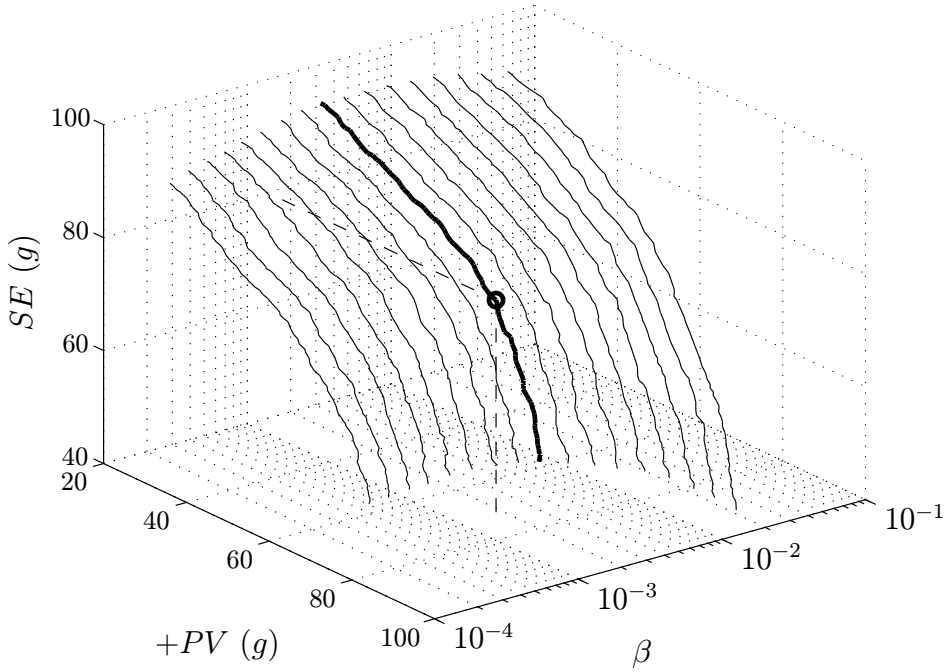

Figure 2.11: ROC curves (SE versus $+PV$ representations) have been calculated varying β and η values.

After including in the preprocessing step the search for the"*basal interval*" to define a reference ST segment $\overline{x}_{ST}(n)$, and modifying the detector as described in the Methods section, the performance has improved up to $SE/+PV$: 78.0%/71.7% (using $\eta = 11.8$ and $\beta = 0.0017$). This is shown in Table 2.2, "*No BPC det.*".

In order to evaluate the need of including a BPC detection technique, we have used the information of the annotated BPC events and with this ideal BPC detector, the positive predictivity has improved about a 6%. See Table 2.2, "*Ideal BPC det.*"

With the BPC detector described in [41, 60] applied to both RMS series from the QRS complex and the ST segment, and modified as explained in section §2.2.4 using the pair of RMS series from the QRS complex and the ST segment, the performance has not improved remarkably (See Table 2.2, "*Current BPC det.*").

If we are restricted to detect ischemia episodes and we just consider the heart rate (HR) related ones as false positives, the detector performance increases in SE (see Table 2.2 "*No HR events*") but decreases in $+PV$. Then showing the detector as suitable for ischemic events but claiming for appropriate discrimination rules to increase $+PV$.

The performance analysis of the detector without the BPC cancellation technique, for the three different protocols, is shown in Table 2.3 with fixed parameters values $\eta = 11.8$ and $\beta = 0.0017$.

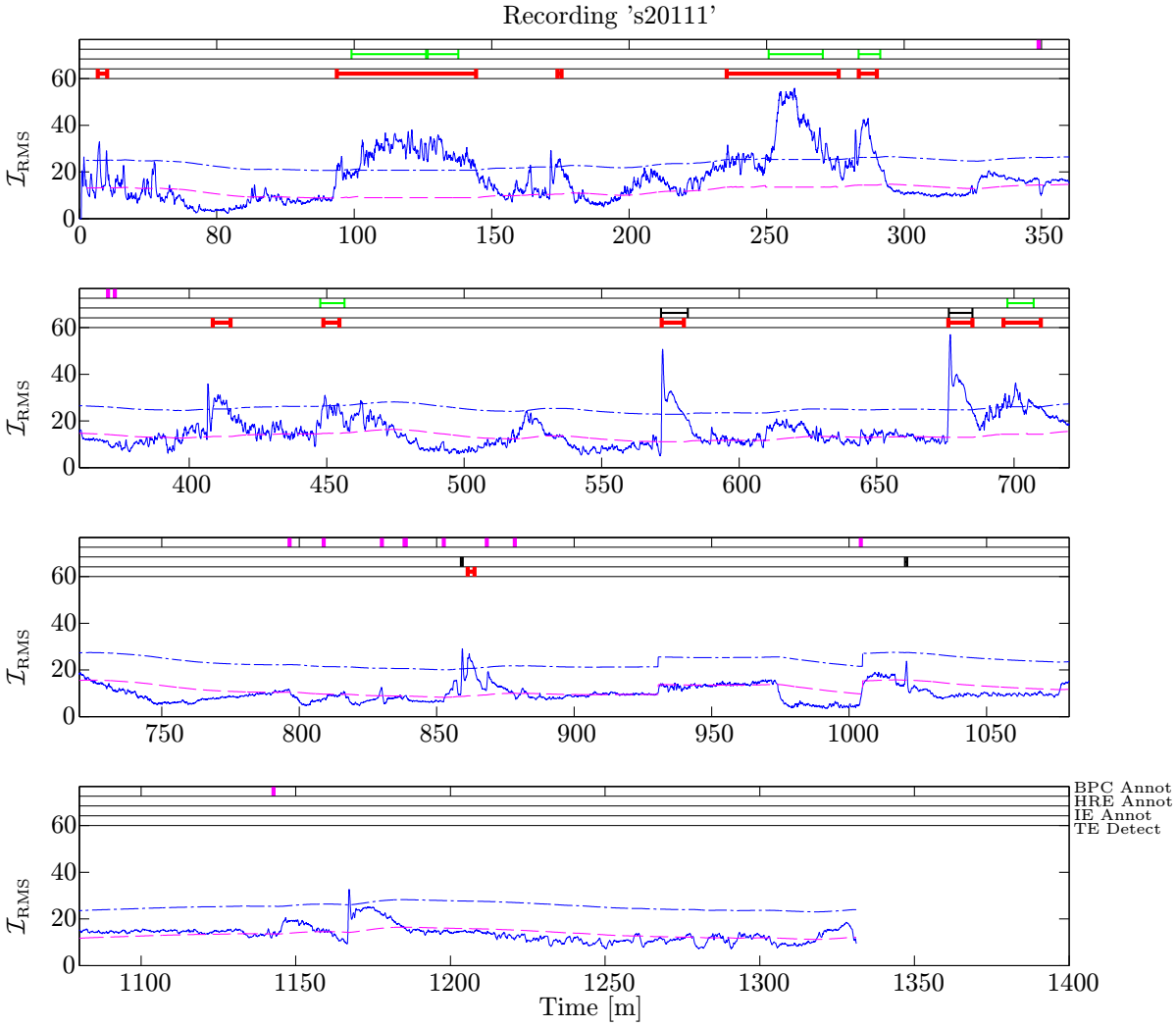

Figure 2.12: Example of RMS series of a recording with the baseline in dashed line and the threshold in dotted-dashed line. In the rows above the RMS series, BPC (1^{st} row), HR-related (2^{nd} row) and ischemic (3^{rd} row) episode annotations ar indicated. In the last row, the detections of transient episodes are also indicated.

2.4. Discussion

The RMS-based detector [62] showed a significant drop in performance on the LTSTDB compared to the results on the ESCDB ($SE/+PV$: 84.7%/86.1%). The main reason is due to the fact that the LTSTDB is much more diverse in the sense that it includes several recordings where only body position changes are present, and most of the recordings combine different types of ST episodes: ischemic and non ischemic. LTSTDB was developed to contain a wide variety of real-world data and therefore it contains a much greater number of non-ischemic events compared to the ESCDB. Besides, several

	SE(g)	*+PV(g)*	*SE(av)*	*+PV(av)*
Original RMS				
Original RMS	70.5%	68.2%	70.1%	62.0%
Modified RMS with Basal Interval Search				
No BPC det.	78.0%	71.7%	79.5%	66.4%
Ideal BPC det.	78.0%	77.8%	79.5%	72.3%
Current BPC det.	77.0%	73.5%	77.9%	67.8%
No HR events	80.5%	60.5%	81.4%	52.9%

Table 2.2: Performance of the original ($\eta = 18.1$, $\beta = 0.0083$) and modified ($\eta = 11.8$, $\beta = 0.0017$) RMS-based detectors on the LTSTDB. In the modified RMS detector, first performance is shown without BPC detection, then using an ideal BPC detector, with the current BPC detector and finally we are restricted to detect only ischemic events and not HR events.

	SE(g)	*+PV(g)*	*SE(av)*	*+PV(av)*
Protocol A	57.1%	81.1%	60.0%	77.2%
Protocol B	78.0%	71.7%	79.5%	66.4%
Protocol C	86.7%	62.1%	87.4%	56.5%

Table 2.3: Performance of the RMS-based detector on the LTSTDB without BPC detection in the three protocols.

combinations of leads are present as it happens in the clinical praxis. This fact affects negatively the detector performance, since ischemia is reflected differently in different leads. Therefore, not only this RMS-based detector has decreased its performance when applying to the LTSTDB, but also the rest of detectors that have published their results in both databases. The detector published in [47] lowers its performance from 87.1%/87.7% in the ESCDB to 74.0%/61.4% when applying to the LTSTDB, as it is shown in [45]. Also, the detector presented in [45] lowers its performance from 81.3%/89.2% to 78.9%/80.7%, and the realtime detector presented on [56] and evaluated on the 48 freely distributed recordings of the the ESCDB achieves 82.2%/79.48% and on the 43 freely distributed recordings of the LTSTDB, lowers the performance to 85.28%/48.44%.

The modifications included and the basal interval search provide remarkably improvements in the performance analysis (Table 2.2, "*No BPC det.*"), while the BPC detector hardly improves the results (Table 2.2, "*Current BPC det.*"). Nevertheless, the improvement reached is not the maximum which is shown in Table 2.2, "*Ideal BPC det.*". This evidence the difficulties in developing a robust BPC detector in ambulatory recordings.

When comparing our results (78.0%/71.7%), obtained over the LTSTDB, to the ones obtained by other detectors, we find the work in [45], whose performance reaches 78.9%/80.7% when detecting significant ST changes in the B protocol. This technique has been devel-

oped under the LTSTDB, and combines three sources of information, ST level deviations and morphological KLT series of the ST segment and QRS complex. Another detector which provides a real-time execution and combines signal processing methods (time-domain analysis) to detect possible ischemic episodes with artificial intelligence techniques [56], has been evaluated on the 43 freely distributed recordings of the LTSTDB, reaching a performance of 85.28%/48.44%, which is lower than the one presented in this work and [45].

If we try to just detect ischemic events avoiding heart rate related changes the sensitivity increases up to 81% (see Table 2.2, "*No HR events*"). This result suggests the need for searching different ECG indices which help us to distinguish between different types of ST events.

When observing Table 2.3, the protocol C is the most restrictive, having then less annotated ischemic and heart rate related events what makes the detector improve the sensitivity. On the other hand, the protocol A is the less restrictive having many annotated episodes and making the sensitivity drop and the specificity improve.

In brief, the previous RMS detector has been modified and has improved the performance on the LTSTDB. The modified detector is more general in the sense that it accepts recordings with different number of leads without setting new parameters, and it does not assume non ischemic reference beats in the beginning of the recordings.

However, the RMS-based ischemia detector, tuned in the LTSTDB, has decreased the performance obtained in the ESCDB and claims for much more robust false alarm cancellation rules, accounting for the very different nature of ST episodes. This opens new working lines which will be developed in the next chapters. Improving the strategy to detect and cancel out body position changes will be developed in chapter 3, and the search for new indices from the repolatization or depolarization phases, which better discriminate between ischemic and non ischemic ST episodes will be developed in chapter 4.

Chapter 3

GLRT-based Detection of Body Position Changes from the ECG

3.1. Introduction

As we introduced briefly in the previous chapter, electrocardiogram variations due to body position changes (BPC) are problematic in ambulatory recordings. Rotation of the heart in relation to surface electrocardiographic (ECG) electrodes when a patient turns to one side has been reported to cause ST-segment shifts, triggering false ischemic alarms with continuous ST-segment monitoring [63]. In this work, we implemented a BPC detector with the aim to be used in ST monitoring to cancel out this type of false positives in ischemia detection. BPC detectors can also be used in other clinical applications such as polysomnographic studies where these events can also be misinterpreted as false apnea detections.

Changes in body position alter the relative angle between ECG electrodes and the mean axis of the heart, leading to changes on the ECG projections. Therefore, BPC produce significant changes in the ECG signal, specially in the QRS and ST-T complexes [64, 65]. Fig. 3.1 shows an example of the morphologic changes of the ECG during a BPC from supine to right lateral position at the time instant: 60 s. In Fig. 3.1(a) it is observed how just at the BPC, the signal to noise ratio of the ECG seems to decrease, and the amplitude of the QRS increases after the BPC. Fig. 3.1(b) shows the ECG in the two positions. The complexes QRS and STT are the ones which higher morphologic changes.

First studies explored the use of the Karhunen-Loève transform (KLT) in the detection of BPC. In [66, 47], the series of feature vectors in the KLT space for both ST segment and QRS complex were extracted to detect transient ST segment episodes and cancel out the false positives due to shifts of the electrical axis of the heart. The underlying architecture of the axis-shift detection procedure is a band-pass differentiation of the ST segment and the QRS complex distance functions, since during an axis shift, those series change rapidly, and during transient ST episodes, they hardly change (in the case of the QRS complex morphology), or do it slowly (in the case of the ST segment morphology).

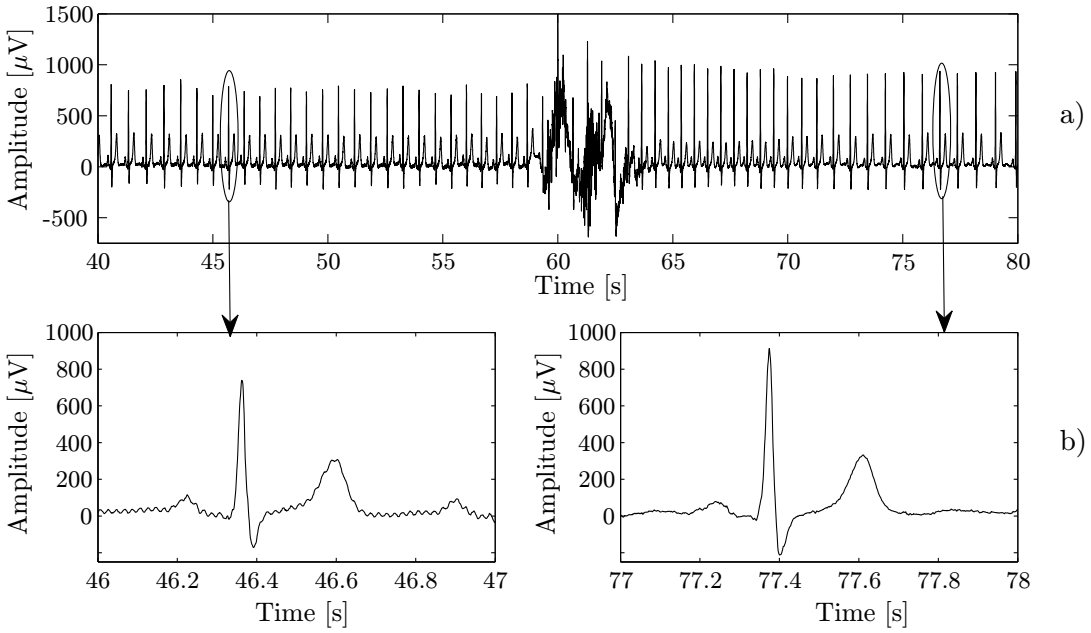

Figure 3.1: Example of a BPC from supine to right lateral position in the time instant 60 s. (a) shows the ECG and (b) shows a closer view of a beat in the two positions.

Later studies used the KLT feature vectors of the QRS and ST-T complexes. They constructed a combined KL-based distance function that reflected morphologic changes in ST-T and mostly in QRS complex. A BPC detector was developed to search for step-like patterns in gaussian noise [41] This BPC detector using a Bayesian approach and assuming gaussian noise was also applied to the series of the vectorcardiogram (VCG) angle series [60].

Measurements of R-wave duration defined as the time between two inflection points adjacent to every R-wave peak, were used to identify changes in body position [67]. Intervals from the left inflection point to the peak of the R wave and from the R-wave peak to the right inflection point were used to classify the BPC into four different positions.

In this study, the KLT of QRS and ST-T complexes are used to develop a generalized likelihood ratio test (GLRT) based BPC detector.

3.1.1. Karhunen-Loève Transform

The Karhunen-Loève transform (KLT) is the optimum orthogonal transform for signal representation in terms of minimizing the energy of a data set [68]. The corresponding KLT basis are a set of orthogonal directions, computed as the eigenvectors of the correlation matrix of the data set, and each KLT coefficient series represent the projection of the data onto each direction. This transformation statistically maximizes the energy of the first KLT coefficient, and each next coefficient in turn contains the highest remaining energy.

It is optimal in the sense that most of the signal information, in terms of energy, is concentrated in a few coefficients. For example, it was shown that using a universal data set of 100000 beats, the first four coefficients were sufficient to represent 90% of the ST-T segment energy [49].

KLT is similar to principal components analysis (PCA) [69]. However, KLT maximizes the energy, deriving its basis from the correlation matrix, while PCA maximizes the variance, deriving instead its basis from the covariance matrix [70].

Therefore, KLT, applied to different ECG complexes, such as QRS and ST-T complexes, is a useful tool to estimate or track the morphologic changes present in a postural change.

3.2. Methods

3.2.1. Reference Material

The evaluation of the GLRT-based BPC detector is performed regarding two aspects: first, the ability of the system to detect BPCs, and second, the false alarm rate of BPCs in ischemic episodes. The first aspect is assessed using a database with healthy subjects doing BPCs and referred to as "BPC database". The second aspect is evaluated over the "STAFF3 database" with subjects undergoing a percutaneous coronary intervention (PCI). In both databases the standard 12-lead ECG was recorded with a sampling rate of 1 kHz and an amplitude resolution of 0.6 μV.

Healthy Subjects: BPC database

The performance of the BPC detector is studied on an ECG database consisting of twenty subjects (11 males/9 females, 32$\pm$9 years old). The BPC database was recorded following the next protocol: supine-to-right side, supine-to-left side and so on. The complete sequence was repeated five times with a duration of 1 min per BPC in order to give more reliable statistical results. The interval between the changes (1 min) was chosen in order to allow muscular activity and other artifacts to decay before the next BPC was initiated. Further description of this database can be found in [41].

Subjects undergoing PCI: STAFF III database

The second database contains severe induced ischemic events. The study group consisted of 83 patients undergoing a percutaneous coronary intervention (PCI), commonly known as coronary angioplasty or simply angioplasty. In this intervention, used to treat the stenotic (narrowed) coronary arteries, a balloon is inflated, blocking the artery in one of the major coronary arteries. The recordings were done at the Charleston Area Medical Center in West Virginia, USA. The locations of the dilations were the left anterior descending artery (LAD), right coronary artery (RCA) or the left circumflex artery (LCX). A control ECG, recorded in the patient room or catheterization laboratory prior to the

procedure, and the angioplasty ECG were considered for each patient. In this study, the control and angioplasty recordings are denoted with (c) and (a), respectively. A more extensive description of the STAFF III database is found in [71, 72]. It is assumed in this study that no BPCs occurred during the recording of this data. Although no one kept track of body position changes during PTCA, it is highly unlikely that any of the patients moved during surgery.

3.2.2. GLRT-based Detector

In the continuous, a random variable X has a probability density $p(X, \theta)$ which depends on a parametric model θ. The **likelihood** of a set of observed data $X = \{x_1, x_2, ..., x_N\}$, all assumed to be independent and selected from the same population or model θ, is defined by:

$$L(\theta; X) = \prod_{i=1}^{N} p(x_i; \theta) \tag{3.1}$$

Therefore, the likelihood is the joint probability density function of the observed sample set given a parametric model. In other words, the likelihood represents the probability density of the sample set to come from the model θ [73]. Note that likelihood depends on the number of samples of the data set, N.

Detection Theory: Generalized Likelihood Ratio Test (GLRT)

The detector that maximizes the probability of detection for a given probability of false alarm is the likelihood ratio test as specified by the Neyman-Pearson theorem [74].

The Neyman-Pearson theorem states that when performing a hypothesis test between two point hypotheses $\mathcal{H}_0$ and $\mathcal{H}_1$ on a data set $\boldsymbol{\varphi}$, then the **likelihood ratio test (LRT)** which rejects $\mathcal{H}_0$ in favour of $\mathcal{H}_1$ [74]:

$$\Lambda(\boldsymbol{\varphi}) = \frac{p(\boldsymbol{\varphi}; \mathcal{H}_1)}{p(\boldsymbol{\varphi}; \mathcal{H}_0)} > \gamma \tag{3.2}$$

maximizes the probability of detection ($\mathcal{H}_1$) for a given probability of false alarm (P_{FA}) α from which the threshold γ is obtained:

$$P_{FA} = \sum_{\boldsymbol{\varphi}:\Lambda(\boldsymbol{\varphi})>\gamma} p(\boldsymbol{\varphi}; \mathcal{H}_0) d\varphi = \alpha \tag{3.3}$$

$\Lambda(\boldsymbol{\varphi})$ is termed the likelihood ratio since it indicates for each value of $\boldsymbol{\varphi}$, the likelihood of $\mathcal{H}_1$ versus the likelihood of $\mathcal{H}_0$.

Formulation of the problem as a Hypothesis Testing Problem

Step-like changes in the distance function have been observed when postural changes occur. This observation is translated to a detection problem where a step-like pattern is searched for in the observation window, and then a sliding window approach will be used in the whole recording.

The distance function $\varphi_l[n]$ computed on lead l, is considered to determine whether a BPC has occurred (hypothesis $\mathcal{H}_1$) or only noise is present (hypothesis $\mathcal{H}_0$). The onset of the observation interval occurs at the sliding time instant $n = n_0$. A BPC is characterized by the scaled unitary step-like signature $s[n]$ which is disturbed by an additive random Laplacian signal (noise) $\mathbf{w}_l[n]$ with central value m_l, referred to the l^{th} lead. This m_l can be interpreted as the DC level of $\varphi_l[n]$ within the observation window. This model is summarized as follows:

$$\begin{aligned} \mathcal{H}_0: \quad & \varphi_l[n] = w_l[n] && n = n_0, n_0+1, ..., n_0+D-1 \\ \mathcal{H}_1: \quad & \varphi_l[n] = a_l \cdot s[n-n_0] + w_l[n] && n = n_0, n_0+1, ..., n_0+D-1 \end{aligned} \tag{3.4}$$

where $l = [1, ..., L]$ represents the lead where $\varphi_l[n]$ is computed, a_l is the scaling factor of the unitary step-like function $s[n]$ and D represents the length of the observation window. $\boldsymbol{\varphi} = [\boldsymbol{\varphi}_1\ \boldsymbol{\varphi}_2\ ...\ \boldsymbol{\varphi}_L]^T$ and $\mathbf{w} = [\mathbf{w}_1\ \mathbf{w}_2\ ...\ \mathbf{w}_L]^T$ are $L \times D$ matrices and $\mathbf{a} = [a_1\ a_2\ ...\ a_L]^T$ is a $L \times 1$ vector, all representing information related to each of the orthogonal leads.

In this study, we modeled $s[n]$ as a step like change:

$$s[n] = \begin{cases} 1 & \text{if } n = 0, ..., \frac{D}{2} - 1 \\ -1 & \text{if } n = \frac{D}{2}, ..., D-1 \end{cases} \tag{3.5}$$

where the length of $s[n]$ is an even valued integer D. A BPC is manifested in $\varphi_l[n]$ by either a lower to upper level, or an upper to lower one, with equal probability. Therefore, the scaling factor of the transition, a_l, is positive for upper to lower level and negative for lower to upper. The absolute value of a_l represents half of the shift due to the BPC as it is shown in Fig. 3.2.

The additive noise w_l is supposed to be Laplacian with mean m_l and variance σ^2. All variables are supposed to be mutually independent and uncorrelated to the observation signal $\varphi_l[n]$.

The Neyman-Pearson theorem is used to develop the BPC detector. The probabilistic model for the observed data $\boldsymbol{\varphi}$ under the hypothesis $\mathcal{H}_0$ and $\mathcal{H}_1$ are:

$$\begin{aligned} p(\boldsymbol{\varphi}; \mathcal{H}_1) &= \prod_{l=1}^{L} \prod_{n=n_0}^{n_0+D-1} \frac{1}{(2\sigma^2)^{\frac{D}{2}}} \exp\left[-\sqrt{\frac{2}{\sigma^2}} |\varphi_l[n] - m_l - a_l s[n-n_0]|\right] \\ p(\boldsymbol{\varphi}; \mathcal{H}_0) &= \prod_{l=1}^{L} \prod_{n=n_0}^{n_0+D-1} \frac{1}{(2\sigma^2)^{\frac{D}{2}}} \exp\left[-\sqrt{\frac{2}{\sigma^2}} |\varphi_l[n] - m_l|\right] \end{aligned} \tag{3.6}$$

respectively. Then, the **maximum likelihood ratio test (LRT)** which rejects $\mathcal{H}_0$ in favour of $\mathcal{H}_1$ is:

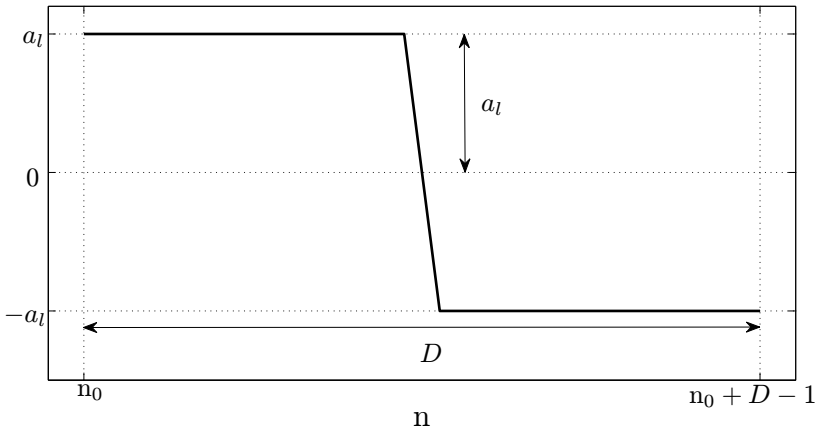

Figure 3.2: Representation of $a_l \cdot s[n - n_0]$.

$$\Lambda(\boldsymbol{\varphi}) = \frac{p(\boldsymbol{\varphi}; \mathcal{H}_1)}{p(\boldsymbol{\varphi}; \mathcal{H}_0)} = \frac{\exp\left[-\sqrt{\frac{2}{\sigma^2}} \sum_{l=1}^{L} \sum_{n=n_0}^{n_0+D-1} |\varphi_l[n] - m_l - a_l s[n - n_0]|\right]}{\exp\left[-\sqrt{\frac{2}{\sigma^2}} \sum_{l=1}^{L} \sum_{n=n_0}^{n_0+D-1} |\varphi_l[n] - m_l|\right]} > \gamma \quad (3.7)$$

This optimum detector LRT cannot be implemented because the PDF under $\mathcal{H}_0$ and $\mathcal{H}_1$ in (3.6) contain the unknown parameters m_l and a_l. The **generalized likelihood ratio test (GLRT)** deals with unknown parameters as deterministic constants. Specifically, it consists of substituting unknown parameters with their maximum likelihood estimators (MLE). Utilizing the joint probability density function $p(\cdot)$ of $\boldsymbol{\varphi}$ conditioned on the two hypotheses, the GLRT results in:

$$\Lambda_G(\boldsymbol{\varphi}) = \frac{p(\boldsymbol{\varphi}; \widehat{a}_{l,\mathcal{H}_1}, \widehat{m}_{l,\mathcal{H}_1}, \mathcal{H}_1)}{p(\boldsymbol{\varphi}; \widehat{m}_{l,\mathcal{H}_0}, \mathcal{H}_0)} \underset{\mathcal{H}_0}{\overset{\mathcal{H}_1}{\gtrless}} \gamma \quad (3.8)$$

where $\widehat{a}_{l,\mathcal{H}_i}$ and $\widehat{m}_{l,\mathcal{H}_i}$ denote their MLE under the hypothesis $\mathcal{H}_i$. The unknown $\widehat{m}_{l,\mathcal{H}_i}$ is regarded as nuisance parameter.

Then, analogous to 3.7, the GLRT rejects $\mathcal{H}_0$ if:

$$\Lambda_G(\boldsymbol{\varphi}) = \frac{\exp\left[-\sqrt{\frac{2}{\sigma^2}} \sum_{l=1}^{L} \sum_{n=n_0}^{n_0+D-1} |\varphi_l[n] - \widehat{m}_{l,\mathcal{H}_1} - \widehat{a}_{l,\mathcal{H}_1} s[n - n_0]|\right]}{\exp\left[-\sqrt{\frac{2}{\sigma^2}} \sum_{l=1}^{L} \sum_{n=n_0}^{n_0+D-1} |\varphi_l[n] - \widehat{m}_{l,\mathcal{H}_0}|\right]} > \gamma \quad (3.9)$$

Calculation of the maximum likelihood estimation of $m_{l,\mathcal{H}_0}$

In order to search for the maximum likelihood estimator of $m_{l,\mathcal{H}_0}$ under the null hypothesis, the PDF of $\boldsymbol{\varphi}_l$ needs to be maximized over $m_{l,\mathcal{H}_0}$.

$$p(\boldsymbol{\varphi}_l) = \frac{1}{(2\sigma^2)^{\frac{D}{2}}} \exp\left[-\sqrt{\frac{2}{\sigma^2}} \sum_{n=n_0}^{n_0+D-1} |\varphi_l[n] - m_{l,\mathcal{H}_0}|\right] \quad (3.10)$$

Maximizing (3.10) corresponds to minimize the following cost function:

$$J(m_{l,\mathcal{H}_0}) = \sum_{n=n_0}^{n_0+D-1} |\varphi_l[n] - m_{l,\mathcal{H}_0}| \tag{3.11}$$

$$\frac{\partial J}{\partial m_{l,\mathcal{H}_0}} = -\sum_{n=n_0}^{n_0+D-1} sgn(\varphi_l[n] - m_{l,\mathcal{H}_0}) \tag{3.12}$$

where $sgn(\cdot)$ is the sign function. Recalling that $sgn(\varphi_l[n] - m_{l,\mathcal{H}_0}) = 1$ if $m_{l,\mathcal{H}_0} < \varphi_l[n]$ and $sgn(\varphi_l[n] - m_{l,\mathcal{H}_0}) = -1$ if $m_{l,\mathcal{H}_0} > \varphi_l[n]$, $\partial J/\partial m_{l,\mathcal{H}_0} = 0$ can be reached when $m_{l,\mathcal{H}_0}$ is equal to the median of the data samples $[\varphi_l(n_0), ..., \varphi_l(n_0 + D - 1)]$. Then, the maximum likelihood estimator of $m_{l,\mathcal{H}_0}$ is:

$$\widehat{m}_{l,\mathcal{H}_0} = med(\varphi_l[n_0], ..., \varphi_l[n_0 + D - 1]) \tag{3.13}$$

Calculation of the maximum likelihood estimation of $m_{l,\mathcal{H}_1}$ and $a_{l,\mathcal{H}_1}$

Analogously to $m_{l,\mathcal{H}_0}$, the MLE of $m_{l,\mathcal{H}_1}$ and $a_{l,\mathcal{H}_1}$ under $\mathcal{H}_1$ are obtained by maximizing:

$$p(\boldsymbol{\varphi}_l) = \frac{1}{(2\sigma^2)^{\frac{N}{2}}} \exp\left[-\sqrt{\frac{2}{\sigma^2}} \sum_{n=n_0}^{n_0+D-1} |\varphi_l[n] - m_{l,\mathcal{H}_1} - a_{l,\mathcal{H}_1} \cdot s[n - n_0]|\right] \tag{3.14}$$

or, by minimizing the cost function $J(m_{l,\mathcal{H}_1}, a_{l,\mathcal{H}_1})$:

$$J(m_{l,\mathcal{H}_1}, a_{l,\mathcal{H}_1}) = \sum_{n=n_0}^{n_0+D-1} |\varphi_l[n] - m_{l,\mathcal{H}_1} - a_{l,\mathcal{H}_1} \cdot s[n - n_0]| \tag{3.15}$$

To do so, both $\frac{\partial J}{\partial m_{l,\mathcal{H}_1}}$ and $\frac{\partial J}{\partial a_{l,\mathcal{H}_1}}$ should be set to zero:

- For $m_{l,\mathcal{H}_1}$

$$\frac{\partial J}{\partial m_{l,\mathcal{H}_1}} = -\sum_{n=n_0}^{n_0+D-1} sgn(\varphi_l[n] - m_{l,\mathcal{H}_1} - a_{l,\mathcal{H}_1} \cdot s[n - n_0]) \tag{3.16}$$

  and this is set to zero when:

$$\widehat{m}_{l,\mathcal{H}_1} = med(\varphi_l[n] - a_{l,\mathcal{H}_1} \cdot s[n - n_0]) \quad \text{for } n = n_0, ..., n_0 + D - 1 \tag{3.17}$$

  The signal $\varphi_l[n] - a_{l,\mathcal{H}_1} \cdot s[n - n_0]$ represents under $\mathcal{H}_1$ the laplacian random signal $w_l[n]$, which is centered at m_l (see PDF in Fig. 3.3(a)).

  $\varphi_l[n]$ can be interpreted under $\mathcal{H}_1$ as the first half of w_l shifted $+a_l$ and the second half shifted $-a_l$. Then, we can see the PDF of $\varphi_l[n] - a_{l,\mathcal{H}_1} \cdot s[n - n_0]$ as the PDF of the signal $\varphi_l[n]$ shifted $+a_{l,\mathcal{H}_1}$ and $-a_{l,\mathcal{H}_1}$, as shown in Fig. 3.3. Therefore, the

median value of $\varphi_l[n] - a_{l,\mathcal{H}_1} \cdot s[n - n_0]$ could be replaced by the median value of $\varphi_l[n]$, which would not require any knowledge of a_l. This replacement suffers from the fact that at m_l estimated as in Fig. 3.3(b), the signal $\varphi_l[n]$ has few data which will cause a big uncertainty in the estimation of $med(\varphi_l[n] - a_{l,\mathcal{H}_1} \cdot s[n - n_0])$. $\widehat{m}_{l,\mathcal{H}_1} = med(\varphi_l[n])$ will be used as an initial estimate, and then iterate (see below).

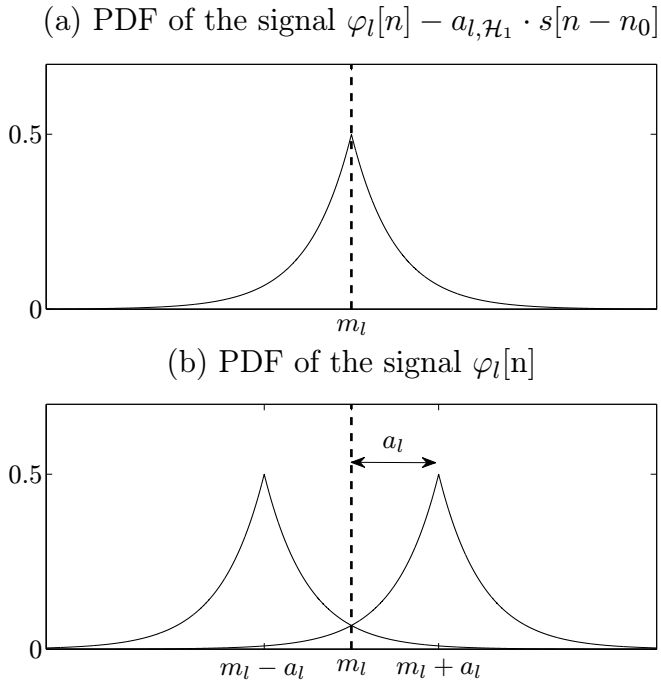

Figure 3.3: (a) PDF of $\varphi_l[n] - a_{l,\mathcal{H}_1} \cdot s[n - n_0]$. (b) PDF of the signal $\varphi_l[n]$.

- For $a_{l,\mathcal{H}_1}$

$$\begin{aligned}\frac{\partial J}{\partial a_{l,\mathcal{H}_1}} &= -\sum_{n=n_0}^{n_0+D-1} s[n-n_0] \cdot sgn(\varphi_l[n] - m_{l,\mathcal{H}_1} - a_{l,\mathcal{H}_1} \cdot s[n-n_0]) = \\ &\underset{using(3.5)}{=} -\sum_{n=n_0}^{n_0+D/2-1} 1 \cdot sgn(\varphi_l[n] - m_{l,\mathcal{H}_1} - a_{l,\mathcal{H}_1}) - \\ &\quad -\sum_{n=n_0+D/2}^{n_0+D-1} -1 \cdot sgn(\varphi_l[n] - m_{l,\mathcal{H}_1} + a_{l,\mathcal{H}_1}) \end{aligned} \tag{3.18}$$

if we replace $\widetilde{\varphi}_l[n-n_0] = \varphi_l[n] - m_{l,\mathcal{H}_1}$:

$$\begin{aligned}\frac{\partial J}{\partial a_{l,\mathcal{H}_1}} &= -\sum_{n=n_0}^{n_0+D/2-1} sgn(\widetilde{\varphi}_l[n] - a_{l,\mathcal{H}_1}) - \sum_{n=n_0+D/2}^{n_0+D-1} -sgn(\widetilde{\varphi}_l[n] + a_{l,\mathcal{H}_1}) \\ &= -\sum_{n=n_0}^{n_0+D/2-1} sgn(\widetilde{\varphi}_l[n] - a_{l,\mathcal{H}_1}) - \sum_{n=n_0+D/2}^{n_0+D-1} sgn(-\widetilde{\varphi}_l[n] - a_{l,\mathcal{H}_1}) \\ &= -\sum_{n=n_0}^{n_0+D-1} sgn(\widetilde{\varphi}_l[n] \cdot s[n-n_0] - a_{l,\mathcal{H}_1}) \end{aligned} \tag{3.19}$$

Thus, the MLE of $a_{l,\mathcal{H}_1}$ is:

$$\begin{aligned}\widehat{a}_{l,\mathcal{H}_1} &= \text{med}(\widetilde{\varphi}_l[n] \cdot s[n-n_0]) \\ &= \text{med}((\varphi_l[n] - m_{l,\mathcal{H}_1}) \cdot s[n-n_0]) \quad \text{for } n = n_0, ..., n_0+D-1 \end{aligned} \tag{3.20}$$

Note that both $\widehat{m}_{l,\mathcal{H}_1}$ and $\widehat{a}_{l,\mathcal{H}_1}$ have to be estimated together, being alternatively optimized. A proper initial estimate for $m_{l,\mathcal{H}_1}$ has been shown in Fig. 3.3 to be the median of $\varphi_l[n]$. This is then included in equation 3.20 to estimate $\widehat{a}_{l,\mathcal{H}_1}$, which is including in equation 3.17 and so on until convergence.

GLRT detector T($\boldsymbol{\varphi_l}$)

Once $\widehat{m}_{l,\mathcal{H}_0}$, $\widehat{m}_{l,\mathcal{H}_1}$ and $\widehat{a}_{l,\mathcal{H}_1}$ have been obtained, logarithms of both sides in the equation (3.9) are taken, resulting in:

$$\begin{aligned}\ln \Lambda_G(\varphi_l) &= -\sqrt{\frac{2}{\sigma^2}} \sum_{n=n_0}^{n_0+D-1} (|\varphi_l[n] - \widehat{m}_{l,\mathcal{H}_1} - \widehat{a}_{l,\mathcal{H}_1} s[n-n_0]| - |\varphi_l[n] - \widehat{m}_{l,\mathcal{H}_0}|) \\ &= \sqrt{\frac{2}{\sigma^2}} \sum_{n=n_0}^{n_0+D-1} (|\varphi_l[n] - \widehat{m}_{l,\mathcal{H}_0}| - |\varphi_l[n] - \widehat{m}_{l,\mathcal{H}_1} - \widehat{a}_{l,\mathcal{H}_1} s[n-n_0]|) \end{aligned} \tag{3.21}$$

Thus,

$$\text{T}(\boldsymbol{\varphi_l}) = \sum_{n=n_0}^{n_0+D-1} (|\varphi_l[n] - \widehat{m}_{l,\mathcal{H}_0}| - |\varphi_l[n] - \widehat{m}_{l,\mathcal{H}_1} - \widehat{a}_{l,\mathcal{H}_1} s[n-n_0]|) \underset{\mathcal{H}_0}{\overset{\mathcal{H}_1}{\gtrless}} \sqrt{\frac{\sigma^2}{2}} \ln(\gamma) \tag{3.22}$$

As σ is assumed to be constant, $\sqrt{\frac{\sigma^2}{2}}\ln\gamma$ is comprised in a new threshold γ'.

This GLRT detector T($\boldsymbol{\varphi_l}$) includes two main terms:

- First term: $|\varphi_l[n] - \widehat{m}_{l,\mathcal{H}_0}| = |\varphi_l[n] - med(\varphi_l[n])|$ represents the absolute value of the observation window centered at zero.

- Second term: $|\varphi_l[n] - \widehat{m}_{l,\mathcal{H}_1} - \widehat{a}_{l,\mathcal{H}_1} s[n - n_0]|$ represents the absolute value of the Laplacian noise w_l centered at zero.

Fig. 3.4 shows an example to understand how this GLRT detector works. In this example there is a step-like change ($a = 10$) centered at a window length $D = 200$ with an additive Laplacian noise with mean $m = 5$ and standard deviation $\sigma = 1$. The detection output is the sum of $|\varphi_l[\mathrm{n}]\text{-}\widehat{m}_{l,\mathcal{H}_0}| - |\varphi_l[n] - \widehat{m}_{l,\mathcal{H}_1} - \widehat{a}_{l,\mathcal{H}_1} s[n - n_0]|$ for $n = n_0, ..., n_0 + D - 1$. The detection output accounts for the estimation of the amplitude a minus the amplitude

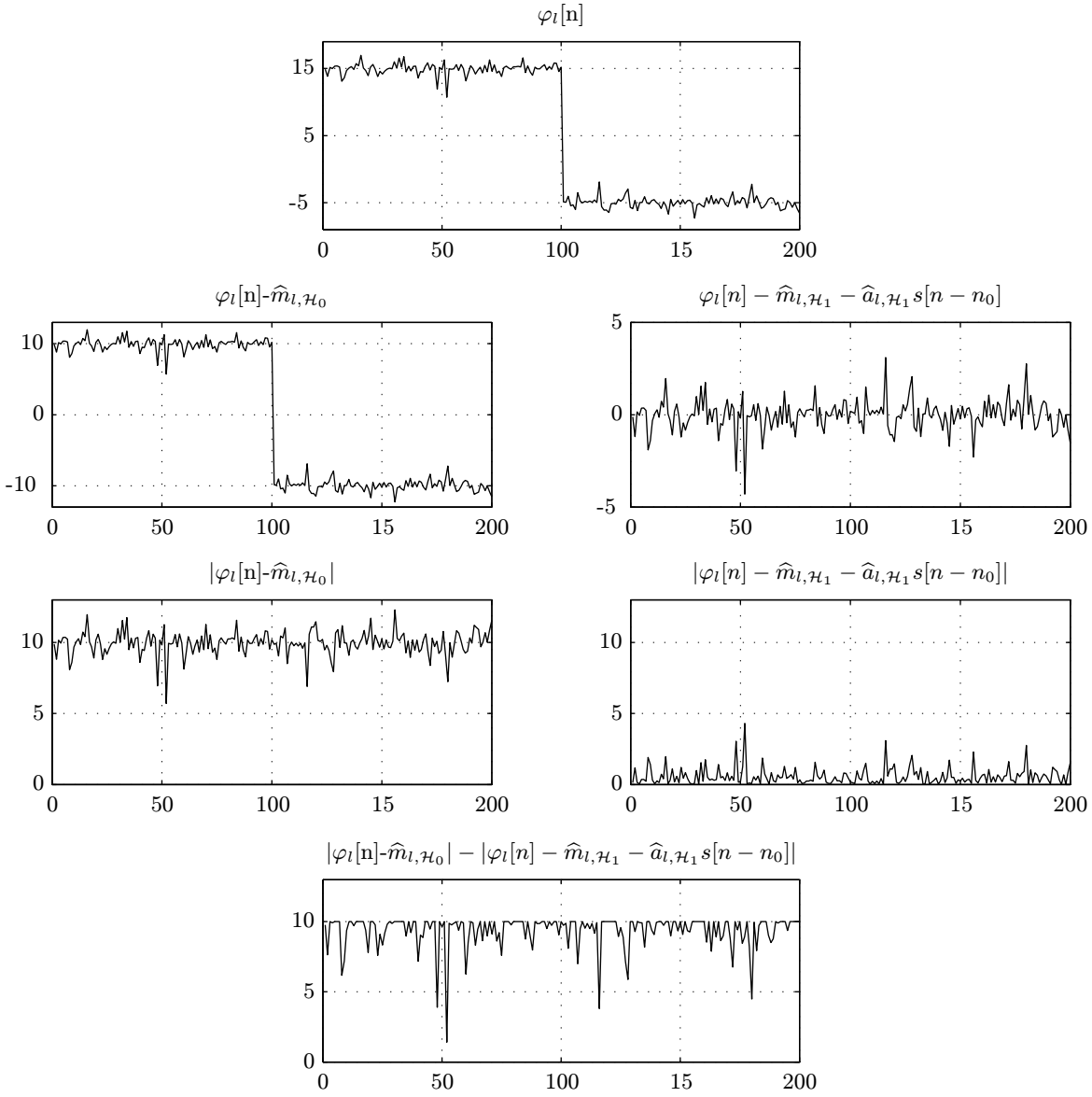

Figure 3.4: Example of the BPC detection output using as an input signal $\varphi[n]$, a BPC change with $a = 10$ with a Laplacian noise of mean $m = 5$ and standard deviation $\sigma = 1$.

In case of having several leads, the GLRT output is the sum of the GLRT outputs of each lead l, as it is shown in equation 3.9 and it is referred to as $\mathrm{T}(\boldsymbol{\varphi})$ in the following equation:

$$\mathrm{T}(\boldsymbol{\varphi}) = \sum_{l=1}^{L} \mathrm{T}(\boldsymbol{\varphi}_l) \tag{3.23}$$

In order to accomplish the detection of several BPCs, the detector $\mathrm{T}(\boldsymbol{\varphi})$ repeats the GLRT in successive, overlapping intervals of length D, i.e a sliding window, until the entire signal has been processed.

3.2.3. BPC detection

In this work we measured the induced changes during the a BPC reflected on the KLT-derived indexes estimated for the QRS and the STT complexes. The first four order coefficients for each interval (with the largest representation strength) were considered. The beat-to-beat dynamic evolution of the signal can be characterized by the study of the coefficients time series evolution. The KLT was applied to different segments of the ECG (QRS and the entire STT complexes) including ventricular depolarization and repolarization.

The BPC detector follows the scheme shown in Fig. 3.5.

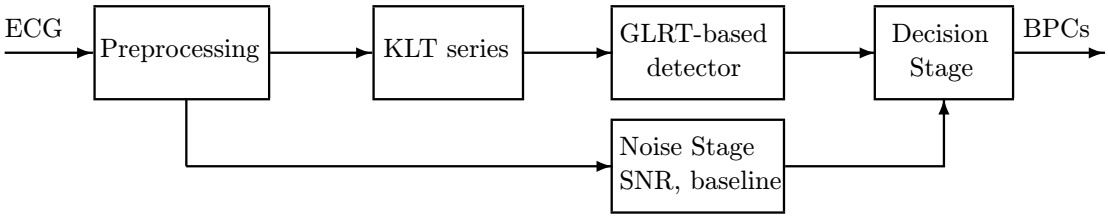

Figure 3.5: Block diagram of the BPC GLRT based detector presented in this work.

Preprocessing

The preprocessing of the ECG recordings consists of the following stages:

- Baseline wander attenuation using cubic splines [75].
- Synthesis of vectocardiographic (VCG) leads obtained from the 12-lead ECG, by making use of the inverse Dower matrix [18].
- QRS fiducial point detection using the ARISTOTLE detector [58].
- Rejection of beats with low signal to noise ratio (SNR), estimated as the peak-to-peak QRS amplitude over the RMS value of the high-frequency noise (above 25 Hz),

differs more than 20 dB from the running exponentially averaged SNR series. The forgetting factor of the exponential averaging is set to 0.02.

- Rejection of beats with differences in mean isoelectric level with respect to adjacent beats larger than 400 μV.

- QRS and ST-T complex segmentations are done by selecting fixed length windows of 130 and 600 ms, respectively as have their KLT basis. The QRS complex time window is centered on the QRS fiducial points for all beats of the recording. The ST-T complex time window starts from a heart rate related sample reference defined in 2.1. Short ST-T complexes are lengthened up to 600 ms by appending zeros.

KLT coefficient series

In this section, the KLT coefficient series of the QRS and the ST-T complexes are derived.

We have used a set of KLT basis (for QRS and STT complexes) derived using more than 200000 preprocessed and selected waveforms as it is described in [76, 49]. The first four KL basis functions derived for the QRS and STT complexes are shown in Fig. 3.6.

The first four order coefficient series for each interval (with the largest representation strength) were derived by projecting each segmented QRS/ST-T complex over the the first four KLT QRS/ST-T basis. They are referred to as α_k^l, where l is the lead and k is the KLT order.

Distance functions, f_{QRS} and f_{STT}, are derived for each lead l. These functions are basically the distance series between each KLT coefficient series (in which only the first four components are considered) and a mean reference value (r) estimated using the first 20 samples of the series.

$$f^l(t_i) = \left(\sum_{k=1}^{4} \left(\alpha_k^l(t_i) - \alpha_k^l(r) \right)^2 \right)^{1/2}, \quad l \in \{X, Y, Z\} \tag{3.24}$$

where $\alpha_k^l(t_i)$ if the kth order coefficient at t_i estimated from the lth lead beat.

Two examples, one with high signal to noise ratio (SNR) and the other with low SNR, of the first order coefficient series of the QRS and ST-T complexes normalized by the mean complex energy is shown in 3.7.

These $f^l(t_i)$ distance functions are resampled to 1 Hz.

GLRT-based Detector Stage

In order to use the GLRT-based detector, the step-like signature $s[n]$ should be defined, setting also the sliding window, which correspond to the length of $s[n]$, D. $s[n]$ is defined in Fig. 3.8 and then D is set to 44 samples which correspond to 44 s because all the distance functions are resampled to 1 Hz.

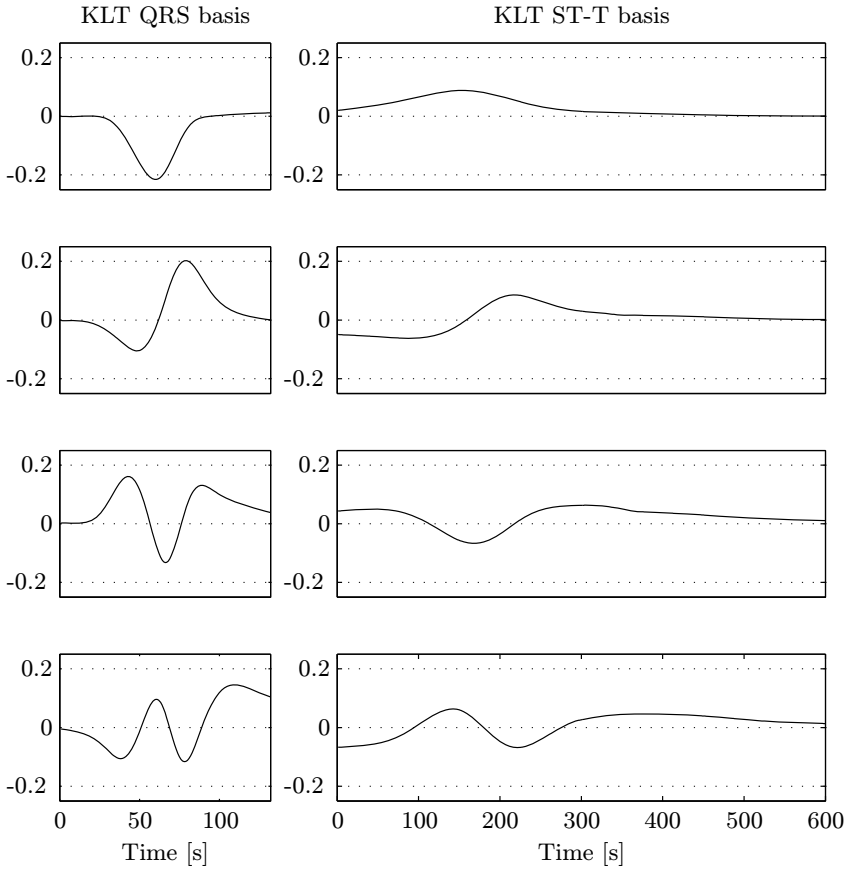

Figure 3.6: KLT basis functions for the QRS and ST-T complexes.

The GLRT-based detector T(.), is applied to each of the six distance functions $f^l_{\mathrm{QRS}}(t_i)$ and $f^l_{\mathrm{STT}}(t_i)$, where l=[X, Y, Z], normalized by the square root of the mean energy of the complex in each lead, obtained from the first fifty beats of the recording. The obtained detection outputs (see Fig. 3.9), $\mathrm{T}(f^l_{\mathrm{QRS}}(t_i))$ and $\mathrm{T}(f^l_{\mathrm{STT}}(t_i))$ are combined as described in the following equation:

$$\mathrm{T}(t_i) = \sum_{l=1}^{3}(\lambda_{\mathrm{QRS}} \cdot \mathrm{T}(f^l_{\mathrm{QRS}}(t_i)) + \lambda_{\mathrm{STT}} \cdot \mathrm{T}(f^l_{\mathrm{STT}}(t_i)) \tag{3.25}$$

where λ_{QRS} and λ_{STT} represent the weights of the QRS and STT detection outputs.

Although the largest changes during BPCs are usually related to the QRS complex it is also desirable to keep the information of possible changes on the ST-T complex; and therefore, values of $\lambda_{\mathrm{QRS}} = 0.8$ and $\lambda_{\mathrm{STT}} = 0.2$ were selected as weights as in [41].

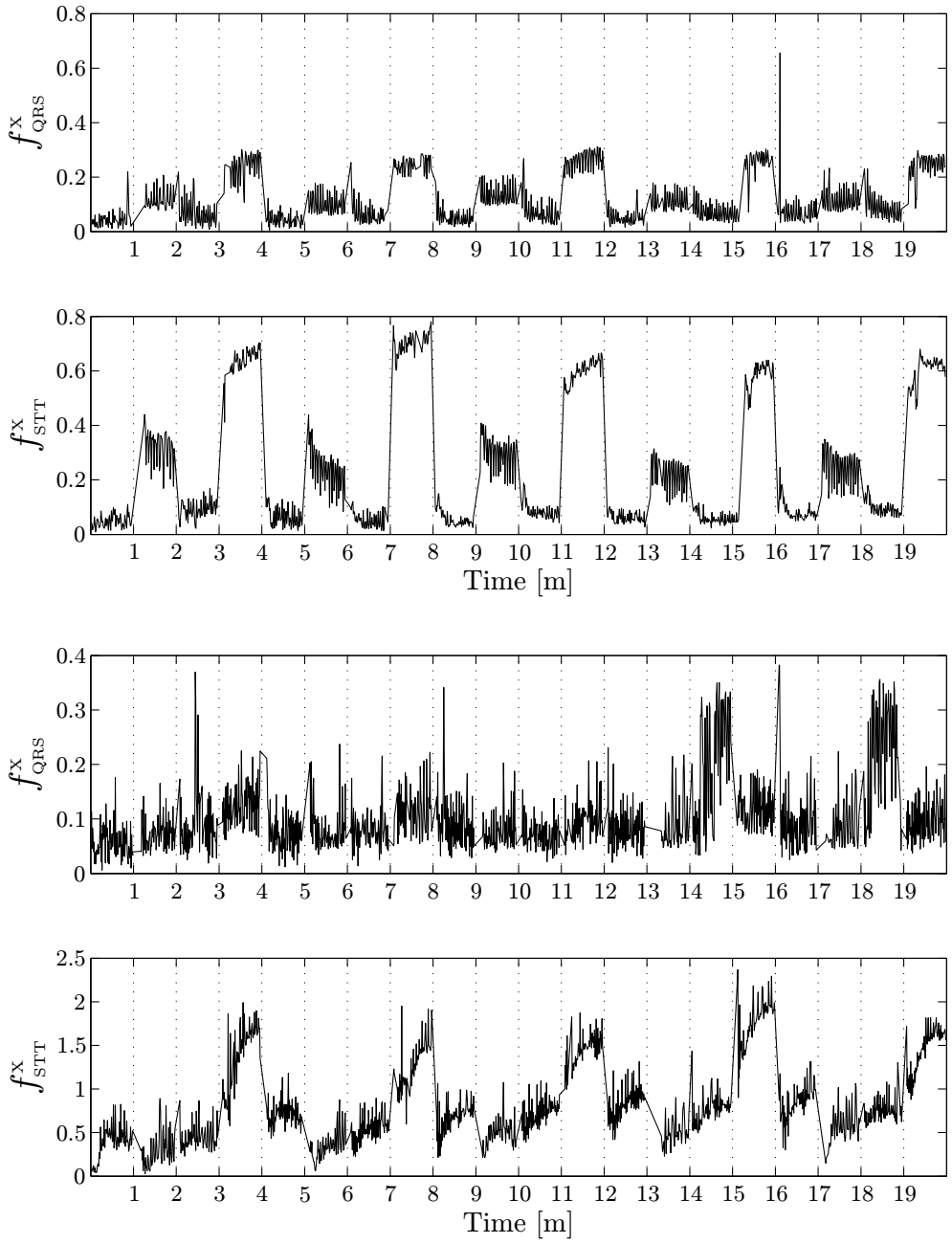

Figure 3.7: Two examples, one with high SNR and the other with low SNR, of the first order coefficient series of the QRS and ST-T complexes in the lead X, normalized by the mean complex energy.

Decision Stage

We apply a fixed threshold η set to 0.55, to the combined output $\Lambda'(t_i)$, and thus, both the beginning and the end of a single BPC may be detected as two separate events.

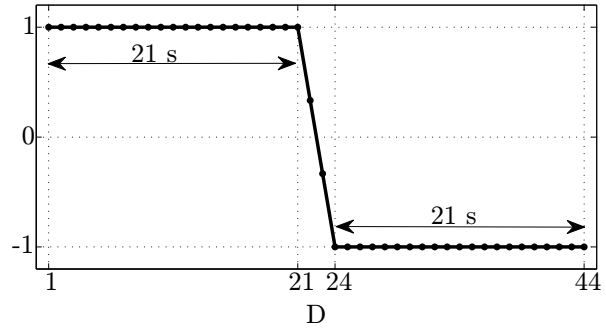

Figure 3.8: Step function $s[n]$ used in the GLRT-based detector with D=44 s.

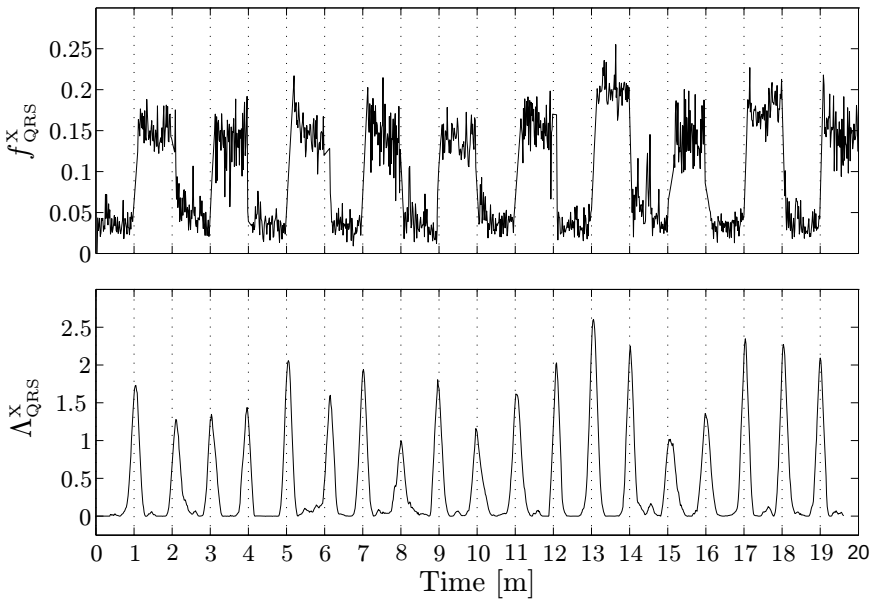

Figure 3.9: Example of the output of the detector.

In case that between the beginning and the end, there are more than one peak, we choose the first one in the interval which is the maximum within a window of 40 seconds.

Besides, a BPC is characterized by a sudden change, which produce a peak in the GLRT-based detector applied to the KLT coefficient series and flat intervals before and after the BPC, which produce flat intervals near to zero because the GLRT detector in those intervals estimate $a = 0$ under $\mathcal{H}_1$, and then the output is zero. In order to force those flat intervals, BPCs with widths that exceed 55 s and widths at one quarter of the maximum height between 19 and 39 seconds are excluded.

Some rules are included in the decision algorithm such as a refractory period which dis-

qualifies detections made within a small time interval following the most recent detection. The time interval is chosen as typically 10 s.

Noise Stage

Performance in the BPC database results to be very good (see section §3.3.1), while the proposed detector does not work well in the STAFF III database, due to the large number of false positives. Therefore, an extra stage is considered after analysing the results, to be added to the detection scheme (Fig. 3.5). The idea consists of making use of the information contained in the noisy beats which are rejected from the study and the SNR estimated in the preprocessing stage, due to the fact that all recordings of the BPC database present a very low SNR just during each BPC as shows Fig. 3.10.

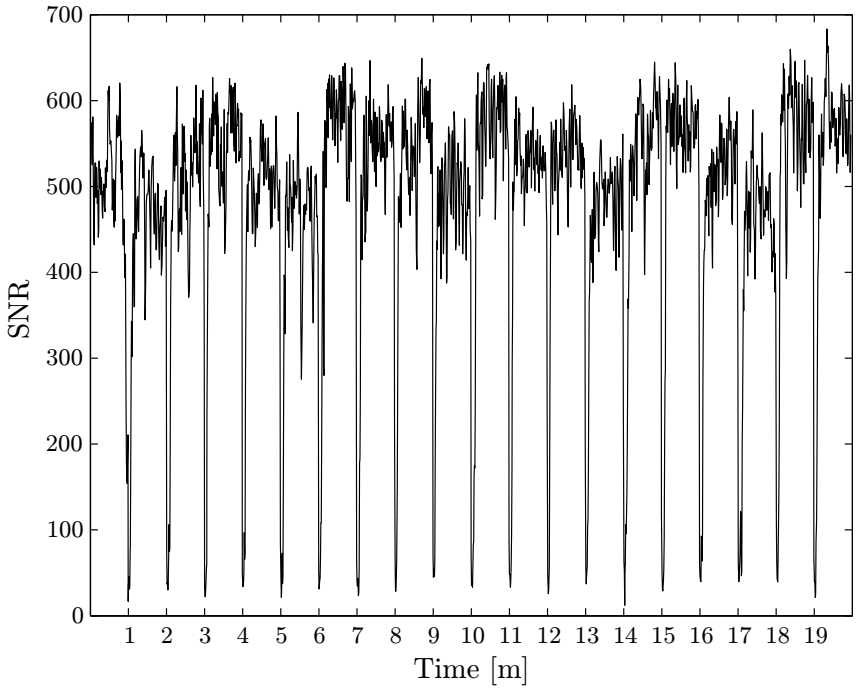

Figure 3.10: Example of the SNRs calculated in the $f^{\mathrm{X}}_{\mathrm{QRS}}$.

As it was shown and used in [41, 60], a BPC episode implies a few noisy beats around its position (a noisy beat is a low SNR beat or a beat with high baseline wandering as defined in the preprocessing). Noisy beats information does not improve detection, but do help in rejecting false BPC detections, and then decreasing the false alarm rate, defined as the number of false BPCs per hour. The noisy stage includes two rules for each BPC detection: four noisy beats should be present in the surrounding 20 beats interval and a minimum average SNR value between 20 and 80 should be reached, to be considered as a BPC event.

3.3. Results

Characterization of the KLT noise

First, the zero median noise of the KLT coefficient series of the QRS and STT complexes is characterized. Fig. 3.11 show an example representing a normalized histogram of the random signal w_l with the median subtracted, together with the Laplacian and gaussian probability density functions that maximize the likelihoods.

For each recording of the BPC database, stationary segments of the KLT coefficient series have been selected, and their mean subtracted. These segments are concatenated resulting in the zero mean KLT noise for each segment and for the STT/QRS complexes. The maximum log-likelihood of the KLT noise assuming a gaussian PDF versus the maximum log-likelihood assuming a laplacian PDF, has been plotted in Fig. 3.12, for each recording, and for STT/QRS complexes. Fig. 3.12 shows that for all BPC recordings and for both STT and QRS complexes, the noise of their distance functions is more likely to come from a laplacian PDF than from gaussian PDF. Since each recording has different number of samples in the KLT noise, the likelihood values cannot be compared among recordings.

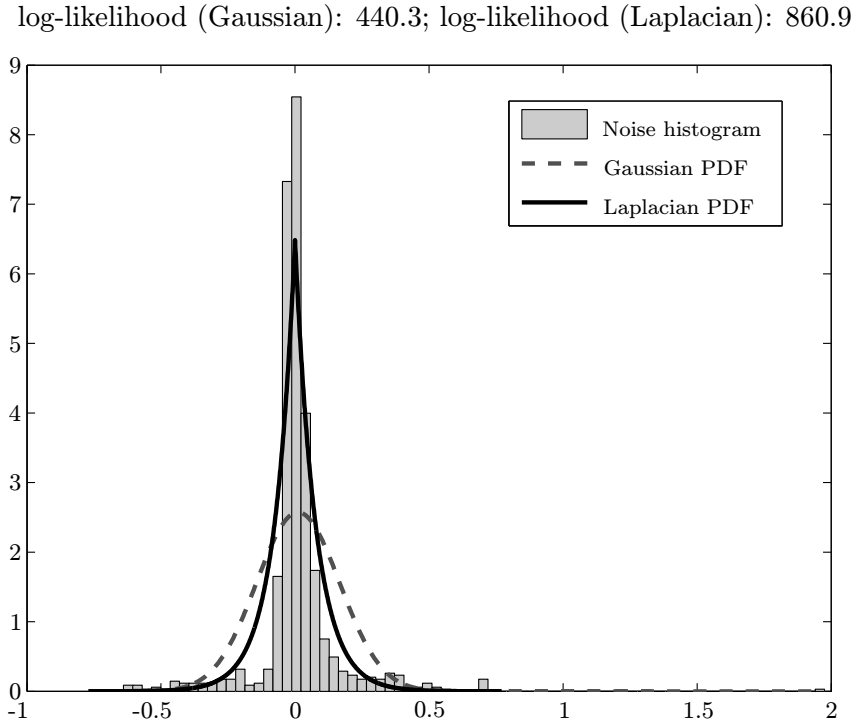

Figure 3.11: Example of a normalized histogram of the random signal w_l with the median subtracted. The Laplacian and Gaussian probability density functions that maximize the likelihoods, are represented.

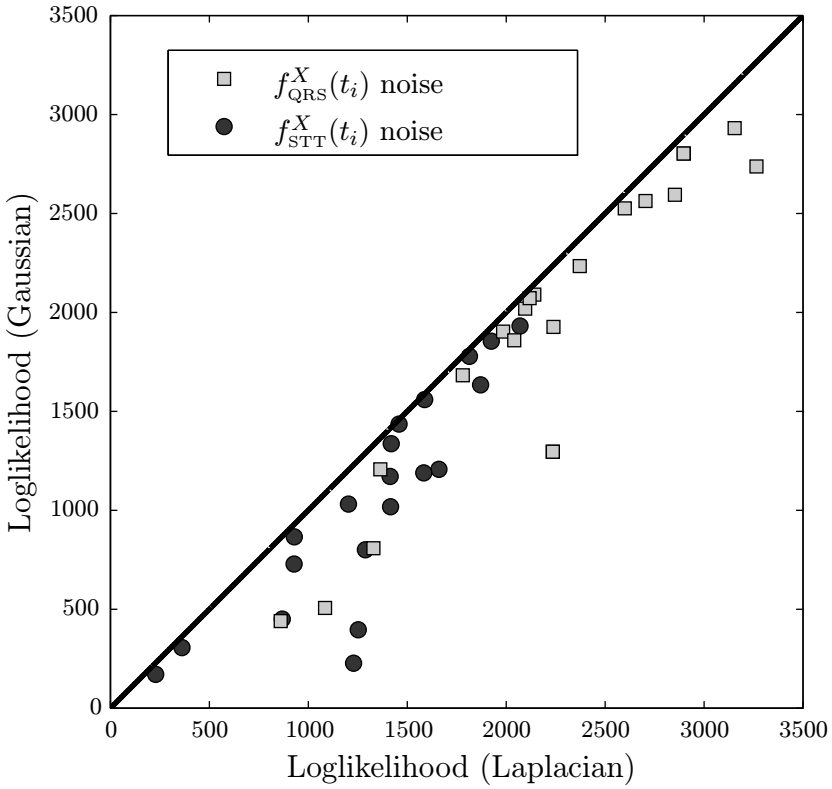

Figure 3.12: The maximum log-likelihood of the noise of the QRS and ST-T distance functions assuming a gaussian distribution versus the maximum log-likelihood assuming a laplacian distribution model.

3.3.1. GLRT-based performance

The performance of the proposed GLRT-based detector is assessed in terms of sensitivity (SE) and positive predictivity value ($+PV$) with average statistics (av), that assigns the same weight to each recording, for the BPC database. For the STAFF-III database, where it is assumed that there are not any BPC, performance is assessed in terms of the false alarm rate defined as the number of false BPCs per hour. Performance of the GLRT-based detector assuming laplacian noise is compared to the performance of LRT detector assuming gaussian noise [41, 60]. In these works, the median absolute deviation (MAD) [77] was used for outlier rejection. Results of these three strategies (laplacian, gaussian and gaussian with MAD), with and without the noise rejection stage, are presented in Table 3.1.

The GLRT detector with the constraints related to the width of the detector output, described in section §3.2.3, presents a satisfactory performance in the BPC database ($SE/+PV$: 94.2%/97.3%). However, when the detector is applied to the STAFF III database where no BPCs are supposed, it lowers its previous performance (about $R_{FA}(a)$=14 false alarms per hour). Some angioplasty recordings contain sudden step changes in the KLT cefficient series as the example shown in Fig. 3.13. This recordings need the noise

	BPC database		STAFF III database	
	SE(av)	*+PV(av)*	$R_{FA}(c)$	$R_{FA}(a)$
Without Noise Stage				
Laplacian	94.2%	97.3%	13.2 ± 16.0	14.1 ± 9.2
Gaussian	83.4%	95.2%	14.2± 14.1	11.9 ± 11.1
Gaussian (with MAD)	88.9%	96.7%	13.9± 14.3	12.1 ± 10.0
With Noise Stage				
Laplacian	92.6%	99.3%	2.5 ± 7.2	1.7 ± 4.0
Gaussian	82.1%	99.7%	1.9 ± 5.8	1.4 ± 4.0
Gaussian (with MAD)	85.3%	99.4%	2.2 ± 5.7	0.9 ± 2.8

Table 3.1: Performance statistics for the BPC detectors on the BPC and STAFF III databases. The false alarm rates $R_{FA}(a)$, and $R_{FA}(c)$ are expressed in terms of mean and standard deviation.

stage in order to remove the false BPC detections.

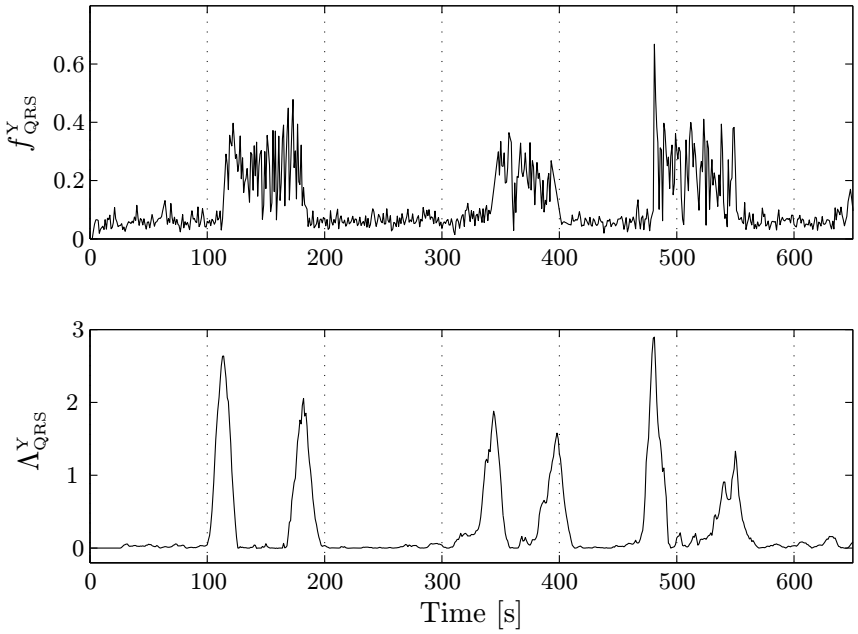

Figure 3.13: Example of false BPC detections in an angioplasty recording of STAFF III database.

Performance assuming a gaussian noise and using the detector published in [41, 60] with suitable width constraints, is lower as expected due to the PDF of the noise.

As expected, when including the noise stage after the detection algorithm, SE decreases to 92.6% and $+PV$ increase in the BPC database to 99.3%. In the case of the

STAFF III database, the number of false BPCs decrease considerable to $R_{FA}(c)$=2.5 and $R_{FA}(a)$=1.7 episodes per hour.

Using the gaussian LRT detector with the noise stage, performance on the BPC database is much lower (85.3%/99.4%), but performance on the STAFF III database is a little bit better than with the GLRT detector.

3.4. Discussion

The aim of this study is to develop a BPC detector to eventually be used to cancel false ischemic detections due to BPC in Holter or ambulatory monitoring . We have used the KLT coefficient series to propose a model consisting of a hypothesis test. First, the PDF of the 'noise' $w_l[n]$ has been characterized under the hypothesis $\mathcal{H}_0$. The resulting KLT noise in all recordings of the BPC database has been proven to have a higher likelihood to come from a laplacian distribution than from a gaussian one, as shows Fig. 3.11 and Fig. 3.12. Therefore, when using the GLRT- based detector for laplacian noise, performance should improve with respect to the LRT-based detector for gaussian distribution with the MAD filter presented in [41, 60], and it does.

In the case of angioplasty recordings, where there is a complete cessation of blood flow through a coronary artery, sudden changes in the ECG are produced, and those result in step like changes in the KLT of the QRS and STT complexes. However, those events are not likely to come from a BPC.

The false alarm rate significantly decreased when the noise stage was included in the detection (from 14 to 2 detections per hour). However, although the false alarm rate in the control recordings (same subjects who underwent the percutaneous coronary intervention) is higher than during the PCI recordings. This could be explained because during the control recording, subjects were awaken and some postural changes could have taken place.

In the angioplasty recordings, the occlusion is complete and very fast, while most of the ischemic events have a softer transient signature in the KLT coefficient series of the QRS and STT complexes. Then, the false alarm rate would be lower in ambulatory recordings or in ST monitoring, which are the targets, where ischemic events are less severe.

However, this detector when applied to the Holter recordings of the LTSTDB gets similar results to the gaussian one presented in Table 2.2. This may be due to the lower SNR of the ECG, baseline wandering or abrupt changes related to heart rate variations.

Chapter 4

Discrimination Between Ischemic and Artifactual ST Segment Events in Holter Recordings

4.1. Introduction

In chapter 1 and 2, we introduced how most of the techniques that automate ischemia detection, rely on ST changes [38, 45]. However, in addition to ischemic ST episodes (IE), there are other ST events such as heart rate related episodes (HRE), body position changes ($BPCE$) or conduction changes (CCE) which also result in ST segment modifications being considered artefactual events when ischemia is the target. Then, reliable ST detectors should distinguish between ischemic and non-ischemic ST changes, although this task remains being a challenge [46].

Ischemia could originate as supply or demand ischemia. "Supply ischemia" results from a partial occlusion of a coronary artery, reducing the amount of oxygenated blood to the myocardium, and "demand ischemia" refers to a condition where an increased oxygen demand caused by exercise, tachycardia or emotion, leads to a transitory imbalance [23, 24]. In the database we are using, the Long Term ST Database (LTST DB) [39], ischemia is not classified as demand or supply. An ST event is annotated as IE when it is associated with a patient with a clinical history showing evidences of cardiac pathology. On the other hand, if there is an episode associated with an increase or alteration of heart rate in the ECG and other clinical investigations do not suggest ischemia, these episodes are annotated as HRE. Typically, the ST level is measured at the point J+80ms, or at the point J+60ms if the heart rate exceeds 120 bpm [39]. This adaptation of the ST level measurement point to heart rate is still a crude adaptation so it may produce ST segment episodes with a similar signature to ischemic episodes generated by the T wave incursion into the point where the ST level is measured. These ST events, that are not associated to ischemia mechanisms, are denoted as HRE.

The dynamics of the different ST events is different in each case. HRE as well as IE are considered transient ST segment episodes (TE) and characterized by a length and an

extremum deviation. In contrast, $BPCE$ and CCE, characterized with a sudden shift in the ST level function, are denoted as sudden step events (SSE) and are characterized by the time instance they occur.

The novelty of the present work lies in the use of several indices based on repolarization and depolarization intervals to distinguish in Holter recordings between different events scenarios called tasks:

Task 1 - Distinguishing between the three independent and different origin types of ST events: the target IE, the artefactual HRE and the also artefactual SSE.

Task 2 - Distinguishing between the different ST level signatures: transient (TE) and sudden step ST change (SSE).

Task 3 - Distinguishing between IE and HRE, both with a very similar ST level pattern, so being the more problematic to differentiate by automatic ischemia detectors.

Task 4 - Distinguishing between IE and non ischemic events (NIE) in order to isolate the ischemic problem.

The availability of the annotated LTST DB has provided the possibility of quantifying the results of classifiers such as those presented in this work, always under the framework in which the annotations were developed.

Previous studies have covered some of the proposals outlined in this article. Task 3, distinguishing between IE and HRE, has not been the subject of much analysis due to the fact that no other database provides annotations of HRE. There are two studies which also use the LTST DB. In the work in [78], the selected features for classification were changes of heart rate, changes of time domain morphologic parameters of the ST segment and changes of the Legendre orthonormal polynomial coefficients of the ST segment, all obtained at 20-second intervals at the beginning and at the extrema of each ST episode, and achieving a sensitivity when classifying ischemia and heart rate related episodes of 77.9 % and a specificity of 73.9%. In a posterior work of Faganeli [79], they obtained the best performance when combining the heart-rate features, the Mahalanobis distance and the Legendre orthonormal polynomial coefficient features. They reached an average sensitivity of 98.1% and average specificity of 85.2%.

Similarly to Task 4, the 2003 Physionet/Computers in Cardiology Challenge [80] consisted of classifying ST changes as ischemic (IE) or non-ischemic (HRE, $BPCE$ or CCE) using a set of 43 freely available annotated records of the LTST DB as a training set and the remaining 43 as a test set. Note that not all annotated ST change events from the database were used, but only the selected subset. The top scoring entry of this challenge [81] achieved a performance in terms of sensitivity/positive predictivity of 98%/83% considering only the change in ST level relative to the baseline ST level, provided by the database and manually corrected by experts, and based on level thresholding within specified time windows.

To separate detection from classification problems, we assume the episodes are correctly detected so we take the manual annotations (onset, extremum and offset) provided

with the database as the detection output and just focus on the classification problem. Automatic detection rules in addition to the ones presented in chapter 2 and [62], can be found in works by García [38] and Smrdel [45].

4.1.1. Multivariate discriminant analysis

Discriminant analysis is a statistical technique, widely used to study the differences between two or more groups with respect to several variables simultaneously [82]. The method generates a discriminant function (or a set of uncorrelated discriminant functions to classify more than two groups), based on linear combinations of the variables, which allows the best inter group classification. These functions are generated from a training set and can be applied to the test set.

Differences between groups

Analysis of variance (ANOVA) provides a statistical test of whether or not the means of several groups (classes) are all equal, and therefore generalizes t-test to more than two groups [83]. In order to consider valid the results provided by ANOVA, the studied variables should be normally distributed and with the same variances in the groups. In case, this is not true, results from ANOVA should by taken into account with caution.

Multivariate analysis of variance (MANOVA) is a generalization form of ANOVA. It is used in cases where there are two or more dependent variables. As well as identifying whether changes in the independent variable(s) have significant effects on the dependent variables, MANOVA is also used to identify interactions among the dependent variables and among the independent variables.

Linear and Quadratic discriminant analysis

Linear discriminant analysis (LDA) is an statistical method to find a linear combination of features which better characterize or separate two or more classes (groups) [83]. The resulting combination is used as a linear classifier.

LDA approaches the problem by assuming that the probability density functions (PDF) of the feature vectors in each class are gaussian distributed with different means and a common covariance matrix (i.e., homoscedastic distributions). The Gaussian parameters for each class can be estimated from training set with, for example, the maximum likelihood (ML) estimation. Under these assumptions, LDA minimizes the Bayes error in each 1-dimensional subspace determined by each feature vector, and is called the Bayes optimal classifier.

The quadratic classifier is a more general version of the linear classifier. Quadratic discriminant analysis (QDA) assumes that the features which define the classes, are normally distributed. Unlike LDA however, in QDA there is no assumption that the covariance of each of the classes is identical.

Fisher's linear discriminant (FDA) maximizes the variance between the classes and minimizes the variance within the classes by maximizing the ratio of both variances [84],

and does not make any assumption. When the assumptions of LDA are satisfied, the maximum separation between classes obtained by FDA is equivalent to LDA.

Feature or variable selection

Feature extraction involves simplifying the number of variables included in the model, selecting the most significant ones and removing the ones with redundant information. Besides, a large number of variables with respect to the size of the data set can lead to a biased estimation of the discriminant functions that reduces the capability of the classifier to generalize and discriminate in a new data set. A rule of thumb says that the number of variables used should be lower than the square root of the number of cases of the smallest group of the data set.

The most common approach to the variable selection is the forward-backward stepwise approach, in which in each step a new variable is added (*forward*), or a previously included variable is removed (*backward*), obtaining the variables with the highest discriminant power according a specific selection criteria. In this study, the selection criteria is based on the Wilks' lambda and the F-statistic test.

Wilks' lambda is a test statistic used in multivariate analysis of variance (MANOVA), which calculates the ratio of within-groups sums of squares to the total sums of squares. This represents the proportion of the total variance in the discriminant scores not explained by differences among groups. A lambda of 1.00 occurs when observed group means are equal (all the variance is explained by factors other than difference between those means), while a small lambda occurs when within-groups variability is small compared to the total variability. A small lambda indicates that group means appear to differ.

The test statistic in a F-test is the ratio of the between-group mean square value to the within-group mean square value as defined in [85]. F-statistics is statistically significant when F is greater than 3.68 for inclusion.

In each step, the variable with the less value of the Wilks' lambda which fulfill the criteria of a statistically significant F-statistics (F>3.68 for inclusion), is included in the model. In each step, the model is evaluated, the variable with the less F-statistics value is identified and rejected if this is less than 2.71 (F <2.71 for rejection). When none of the variable fulfill the inclusion or the rejection criteria, then the variable selection process is finished.

4.2. Materials and Methods

4.2.1. The Data: Long-Term ST Database

In this study, the Long-Term ST Database (LTSTDB) [39], described in 2.2.1 is used to derive the ECG indices proposed. Expert annotations include IE and other ST-segment events such as HRE, $BPCE$ and CCE, providing an extensive tool to evaluate classifiers aimed at distinguishing among ST episodes of different origin.

Hereinafter we will denote the "ischemia group" as IG, the "heart rate related group" as HRG and the "sudden step group", comprising $BPCE$ and CCE, as SSG. TG will stand for the transient group composed of IG and HRG, and NIG will stand for the non-ischemic group that comprises HRE, $BPCE$ and CCE. A comprehensive scheme is shown in Table 4.1.

	ST events		
Non-Ischemic group (NIG)	*Ischemic group*	(IG)	Transient group (TG)
	Heart rate related group	(HRG)	
	Axis Shifts		Sudden step group (SSG)
	Conduction changes		

Table 4.1: Summary of ST events grouping and their acronyms.

The classification evaluation of this work has been done for the three different sets relative to the annotation protocols. The number of episodes of each type used for the classification analysis in protocols A, B and C is shown in Table 4.2. The number of analysed events is slightly lower than in the original database [39] (in square brackets in Table 4.2) due to the fact that some episodes at the beginning of the record have not got any onset annotations since their onsets start before the beginning of the records and were excluded from the analysis.

	Protocol A			*Protocol B*			*Protocol C*		
IG	[1795]	1788	(*1163*)	[1130]	1126	(*623*)	[857]	855	(*505*)
HRG	[516]	513	(*358*)	[234]	232	(*112*)	[116]	115	(*54*)
SSG		2388			2388			2388	
Total		4689	(*1521*)		3746	(*735*)		3358	(*559*)

Table 4.2: Number of IE, HRE and SSE used in discrimination for each annotation protocol. These numbers are a bit lower than in the original database (see text) that are displayed in square brackets. The numbers in parentheses refer to episodes that additionally allow reliable T wave delineation when these parameters are to be used.

When classifying IG and HRG, we have added T wave related variables which have caused us to additionally remove manually those episodes with unreliable annotations in the T wave delineation process, resulting in the number of episodes for protocols A, B and C as presented in parentheses in Table 4.2.

Any significant sudden step-change of the ST level function accompanied by a simultaneous sudden step-change in QRS complex morphology was annotated as significant $BPCE$ or significant CCE, according to its nature (see Fig. 4.1).

Annotations are attached to the lead or leads where the episode is significant, so all the study has been done considering the lead to which the annotated episodes are linked. An example of ST traces in the four different cases can be found in Fig. 4.1.

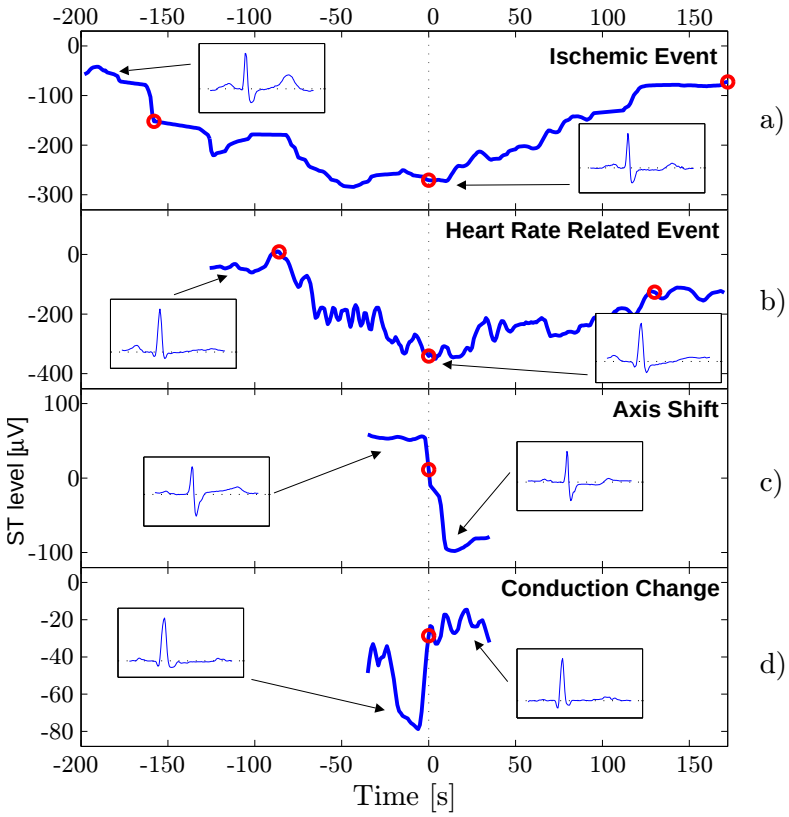

Figure 4.1: Example of the ST segment deviation caused by the four different annotated episodes: (a) ischemic, (b) heart rate related, (c) axis shifts and (d) conduction change events. The circles indicate the annotated onset, extremum and offset in transient episodes and the occurrence time in the sudden step changes. Time "0" is referred to the extremum in TE, or occurrence time in SSE.

4.2.2. ECG Preprocessing and Beat Identification

Before deriving index series from the ECG, typical preprocessing techniques are applied on the raw ECG signal, $x_l(n)$, where l is the corresponding lead and n is the sample index. This preprocessing stage consists of first applying a QRS detector [58] in order to find QRS fiducial points of each i^{th} beat (θ_i) and selecting only normal beats classified according to [58], then baseline wander attenuation using cubic splines is performed [75] and finally those beats with differences in mean isoelectric level with respect to adjacent beats larger than 400 μV are rejected. There are different factors such as motion artifacts that distort the ECG signal so an extra beat rejection rule is applied for those whose signal-to-noise ratio (SNR), estimated as the peak-to-peak QRS amplitude over the RMS value of the high-frequency noise (above 25 Hz), differs more than 20 dB from the running exponentially averaged SNR series. The forgetting factor of the exponential averaging is set to 0.02 as in [62].

4.2.3. T wave delineation

An ECG delineation system based on the wavelet transform (WT) has been used for T wave location and delineation. This delineator has been previously described and evaluated in standard databases [86].

The WT provides a description of the signal in the time-scale domain, allowing the representation of the temporal features of a signal at different resolutions; therefore it is a very suitable tool to analyze the different patterns which have different frequency content (QRS complex, P and T wave) occurring in the ECG. The multiscale approach allows to attenuate noise at rough scales, and then to refine the precision of the positions with the help of finer scales.

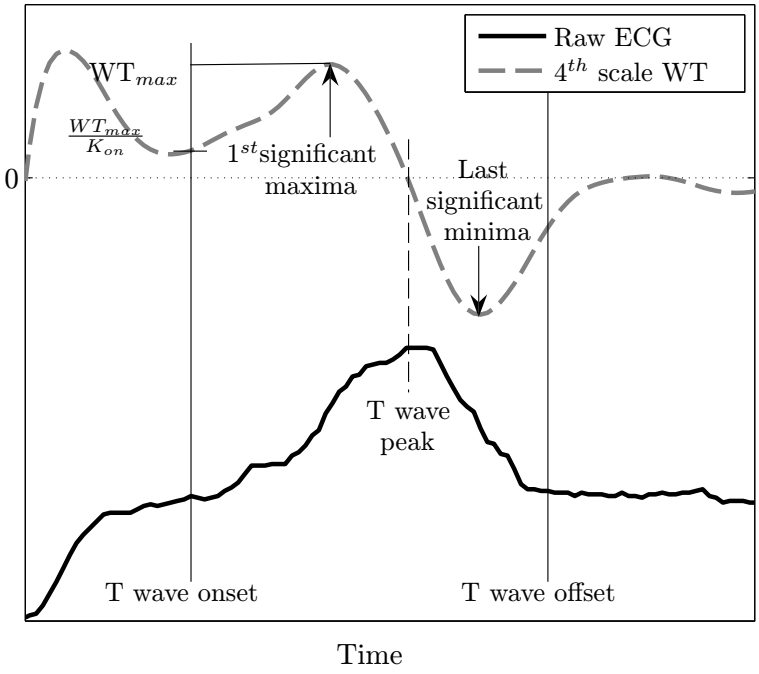

Figure 4.2: Example of T wave onset and end delineation.

The process for multiscale T wave detection and delineation consists of first defining a T wave search region window for each beat, relative to the QRS position and function of the recursively computed RR interval. Within this window, at least two local maxima in the 4^{th} scale, exceeding a threshold, need to be found in order to asses the presence of a T wave. The zero crossing between them are considered as T wave peaks. Depending on the number and the polarity of the found maxima there are six different possible T waves: positive (+), negative (-), biphasic (+/- or -/+), only upwards and only downwards . If the T wave is not found in the 4^{th} scale the process is repeated over the 5^{th} scale. The onset (offset) of the T wave is identified by finding the crossing point of the WT signal with a threshold defined by a fraction K_{on} (K_{off}) of the first (last) significant maximum

(WT_{max}) of the WT modulus (see figure 4.2). If a local minimum is found before the threshold is crossed, the local minimum is considered as the onset (offset).

4.2.4. Indices for the discriminant analysis

In this work, different ECG features ($\mathcal{I}$) and their transient variations ($\Delta\mathcal{I}$), measured from repolarization, depolarization and heart rate indices have been used in the discriminant analysis.

In order to distinguish between both transient episodes, IG and HRG, these features have been computed over three different intervals (I_1, I_2 and I_3) of 20 s duration each (the duration was selected empirically), located as described in Fig. 4.3a. I_1 is defined as 20 s interval ending at the sample where the episode begins, I_2 as 20 s interval starting at the sample of the episode onset and I_3 as 20 s interval centered at the extremum episode sample. The changes of the mean feature value in interval I_k with respect to I_j ($\Delta\mathcal{I}_{jk}$) have been computed and proposed as indices for the classification analysis (see eq. 4.1).

$$\Delta\mathcal{I}_{jk} = \frac{\sum_{i\in I_k}\mathcal{I}(i)}{N_{I_k}} - \frac{\sum_{i\in I_j}\mathcal{I}(i)}{N_{I_j}} \qquad j,k = 1,2,3 \quad \text{and} \quad j \neq k \tag{4.1}$$

where i is an integer denoting the i^{th} beat order in interval I and N_{I_k} and N_{I_j} are the number of beats contained in interval I_k and I_j respectively.

Alternatively, when discriminating between the three types of events including IG, HRG and SSG, only two intervals are considered since SSG is characterized by a unique mark. For SSG two intervals of 20 s each is defined; I_1, just before the event and I_2, just after, which is going to be paired to the I_3 interval of the TG group (IG plus HRG) when the two ST signatures are to be discriminated (see Fig. 4.3b).

All the indices are computed over the ECG after the preprocessing stage. Some of them are shown in Fig. 1.5.

Repolarization indices

- As has been previously described, the ST level is a common marker of ischemia and has therefore been included in the classification analysis. The underlying mechanism responsible of the shift in the ST level is the injury current produced between normal and ischemic myocardial zones [16]. The ST level series is estimated at each i^{th} beat and lead by averaging 8 ms (to make the measurement more stable) of the preprocessed ECG signal starting from a heart rate related sample reference ($n^i_{\mathrm{ST}_0}$) [59] and defined in equation 2.1.

  Changes in the deviation of the ST level are denoted as $\Delta\mathcal{I}_{\mathrm{ST}_{12}}$, $\Delta\mathcal{I}_{\mathrm{ST}_{13}}$ and $\Delta\mathcal{I}_{\mathrm{ST}_{23}}$. The absolute values of these changes in the ST level series are also considered for the classification analysis and denoted as $|\Delta\mathcal{I}_{\mathrm{ST}_{12}}|$, $|\Delta\mathcal{I}_{\mathrm{ST}_{13}}|$ and $|\Delta\mathcal{I}_{\mathrm{ST}_{23}}|$.

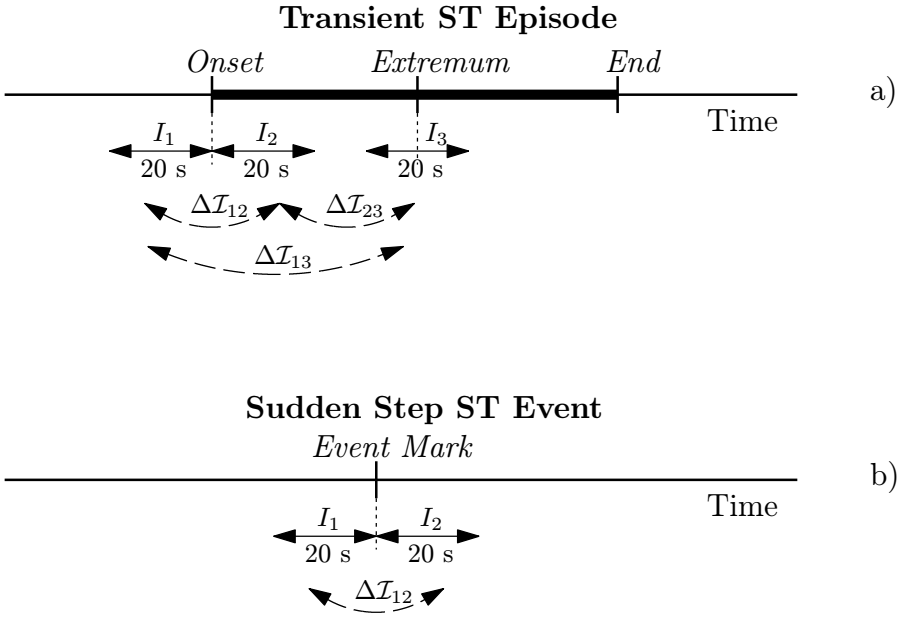

Figure 4.3: a) For discriminating between transient events, the three different intervals I_1, I_2 and I_3 used to compute $\Delta\mathcal{I}_{12}$, $\Delta\mathcal{I}_{13}$ and $\Delta\mathcal{I}_{23}$ are shown. b) For sudden step events, only two intervals I_1 and I_2, are defined.

- The root mean square (RMS) of the difference of the ST segment with respect to the ST of a reference beat ($\mathcal{I}_{\text{RMS}}$) is analysed. The hypothesis here is that differences in the area under the ST segment is a more robust measurement than the ST level itself, since it includes information about changes in energy of this segment [38].

  In order to avoid the influence of high frequency noise in the calculation of the RMS difference series, the preprocessed ECG signal is further low-pass filtered using a linear phase FIR filter with a cutoff frequency of 25 Hz at the ST segment.

  The ST segmentation and the reference beats in each lead are performed as in section §2.2.3. Finally a first RMS difference series, $y_l(\theta_i)$ is calculated using the following equation:

$$y_l(\theta_i) = \sqrt{\frac{1}{N}\sum_{n=0}^{N-1}\left(x^i_{\text{ST,l}}(n) - \overline{x}_{\text{ST,l}}(n)\right)^2} \tag{4.2}$$

  where l is the corresponding lead.

  As an outlier rejection, a median filter of 5 beats length is subsequently used on the $y_l(\theta_i)$ series. This series is evenly resampled to 1 Hz and an exponential running average (with a forgetting factor set to 0.05) is applied to smooth the series resulting in a RMS- series suitable for analysis and denoted hereinafter by $\mathcal{I}_{\text{RMS}}$.

- The Karhunen-Loéve transform (KLT signature) of the ST-T and QRS complexes are also analysed. Body position changes are often manifested as shifts in the electrical axis and may be misclassified as ischemic changes during ambulatory monitoring. These shifts in the electrical axis and therefore in the ECG, are manifested as abrupt changes on the QRS and STT complexes, property which can be used to discriminate ischemia from other events.

  Previous studies have used the Karhunen-Loéve transform (KLT) to detect non-ischemic episodes such as body position changes or conduction changes [41]. During these non-ischemic events the QRS signatures also change rapidly (generally over a period of half a minute) generating step function features in KLT coefficient series which are useful for discriminating "from just" episodes restricted to repolarization changes. Besides, the KLT of the QRS and ST segment has already been used in differentiating between true ischemic ST segment changes and non-ischemic ST deviations caused by axis shifts [66]. The distance functions used for each complex (QRS and ST-T) at time (θ_i) are simply the distance series between each normalized KLT coefficients vector (in which only the first four components are considered) and a mean reference value ($\tilde{\alpha}_j^l$):

$$\mathcal{I}^e_{\mathrm{KL,l}}(\theta_i) = \sqrt{\sum_{j=1}^{4} \left(\alpha_j^l(\theta_i) - \tilde{\alpha}_j^l\right)^2} \tag{4.3}$$

  with $\alpha_j^l(\theta_i)$ being the j-th order KLT coefficient at beat i estimated for the l-th lead. The $\alpha_j^l(\theta_i)$ coefficient series is estimated using adaptive filtering to remove noise uncorrelated to the signal, thus improving the KLT estimation [49]. A compromise between noise reduction and convergence time is reached using a step-size parameter for the LMS algorithm of $\mu = 0.10$, that yields a SNR improvement in the series of 10 dB, with a convergence time of one beat [49]. An extra reduction of noise was achieved by applying a median filtering and a smoothing to the KLT trends resulting in the KLT series denoted as: $\mathcal{I}^e_{\mathrm{KL_{QRS}}}$ and $\mathcal{I}^e_{\mathrm{KL_{ST\text{-}T}}}$. As an alternative, we used the first order Mahalanobis distance functions in order to calculate the KLT series as follows:

$$\mathcal{I}^m_{\mathrm{KL,l}}(\theta_i) = \sqrt{\sum_{j=1}^{4} \left(\frac{\alpha_j^l(\theta_i)}{\sigma(\alpha_j^l(\theta_i))}\right)} \tag{4.4}$$

  where $\sigma(\alpha_j^l(\theta_i))$ is the standard deviation of the KLT coefficient series over the beat series.

  We applied the same post processing procedure as previously explained and obtained the KLT coefficient feature vectors denoted as $\mathcal{I}^m_{\mathrm{KL_{QRS}}}$ and $\mathcal{I}^m_{\mathrm{KL_{ST\text{-}T}}}$.

- The width of the T wave was measured as a potential feature related to repolarization dispersion and eventually related also to ischemia [87], in each lead of the

ECG. Delineation was done using a wavelet-based ECG delineator [86]. Changes of the T wave width across the three intervals are denoted as $\Delta\mathcal{I}_{\mathrm{T}_w}$.

- Alternatively, changes in the interval from the peak (T_{apex}) to the end (T_{end}) of the T wave (T_{pe}) are measured in each lead. T_{pe} has been proposed as a marker related to transmural dispersion [88] and also as a more robust measurement than T width since it avoids uncertainties in the detection of T onset when ST elevation occurs. These changes measured in each ST episode are denoted as $\Delta\mathcal{I}_{\mathrm{T}_{pe}}$.

- The amplitude of the T wave has been taken into account as T wave morphology has been shown as a useful marker of acute transmural ischemic change. It is also a measure of the repolarization dispersion generated by ischemia [89]. Changes in the T wave amplitude ($\Delta\mathcal{I}_{\mathrm{T}_A}$), measured referring to the voltage level at the T_{end} fiducial point, have been computed using the delineation marks defined previously.

- QT interval provides information of repolarization dispersion and also is strongly and inversely related to heart rate. The adaptation of the QT interval to the HR has led us to include these changes of QT as a variable for the discrimination between events. Differences in the QT interval have also been measured ($\Delta\mathcal{I}_{\mathrm{QT}}$).

- The correlation between the heart rate series ($\mathcal{I}_{\mathrm{HR}}$) and the $\mathcal{I}_{\mathrm{RMS}}$ of the ST level calculated previously within an interval (I_ρ) of 60 s centered at the onset of the annotated ST episode has also been evaluated as a potential discriminator of HRG episodes and referred to as ρ. This has been calculated after resampling the series to an even sampling frequency of 1 Hz in the following way:

$$\rho = \sum_{k \in I_\rho} \frac{(\mathcal{I}_{\mathrm{RMS}}(k) - \mu_{\mathrm{RMS}})(\mathcal{I}_{\mathrm{HR}}(k) - \mu_{\mathrm{HR}})}{N\sigma_{\mathrm{RMS}}\sigma_{\mathrm{HR}}} \tag{4.5}$$

where μ_{RMS} and μ_{HR} are the mean, and σ_{RMS} and σ_{HR} are the standard deviation of the $\mathcal{I}_{\mathrm{RMS}}$ and $\mathcal{I}_{\mathrm{HR}}$ series respectively in I_ρ, and N the number of samples at the I_ρ interval.

Depolarization indices

Alterations in the late steepest slope of the QRS complex has been proposed as an index to quantify ECG changes in supply ischemia [29]. The conduction velocity reduction generated by ischemia has a strong effect on the downward stroke of the QRS complex, which reduces its amplitude and its slope considerably. Therefore changes in the steepest slopes of the QRS complex referred to as the early (Se) and late (Sl) slopes are considered in the classification analysis. Se and Sl can be sequenced either upward/downward or downward/upward depending on the QRS morphology. The QRS slope series are computed from the processing during the QRS delineation [86], using the second scale-wavelet transform maximum (minimum) that corresponds to the maximum (minimum) derivative

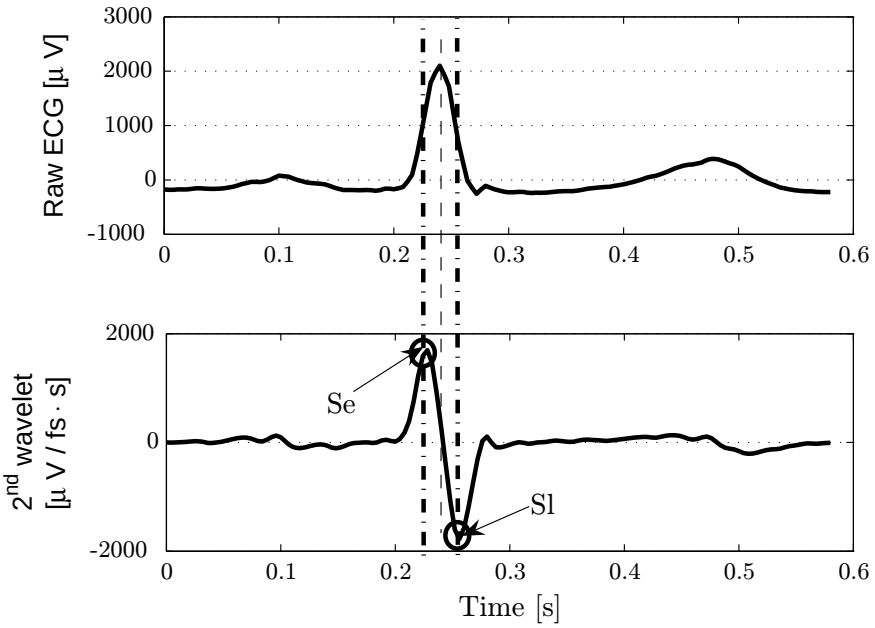

Figure 4.4: In the upper figure, the QRS complex of the raw ECG signal and, in the lower figure, its second scale wavelet transform are shown. The maximum and minimum of the wavelet transform correspond to the two steepest slopes. Note that zero crossing of the wavelet transform corresponds with the peak of the QRS complex.

of the QRS complex (see Fig. 4.4). At the latter stage, the slope series is recomputed by normalizing the QRS amplitude to give the unit mean value at the I_1 interval, so the unit dimension of the slope will be Hz instead of $\mu V/s$. Changes in the absolute values of these series (early and late QRS slopes) across the three intervals are taken into account and denoted as $\Delta\mathcal{I}_{\mathrm{Se}}$ and $\Delta\mathcal{I}_{\mathrm{Sl}}$.

Heart rate indices

Changes in the heart rate corresponding to the three intervals are also measured ($\Delta\mathcal{I}_{\mathrm{HR}}$). The absolute value of these changes are also analysed and referred to as $|\Delta\mathcal{I}_{\mathrm{HR}}|$. The mean heart rate values at intervals I_1 and I_3 were computed and denoted as $\mathcal{I}_{\mathrm{HR}_1}$ and $\mathcal{I}_{\mathrm{HR}_3}$ respectively.

Signal to noise ratio (SNR) index

With the aim of accounting for the higher noise in SSG or HRG in comparison with IG, the SNR index ($\mathcal{I}_{\mathrm{SNR}}$) has been considered as introduced in section 4.2.2.

4.2.5. Performance Evaluation: Statistical Analysis

First monovariate ANOVA discriminant analysis is performed for each variable so as to establish the individual significance for classification performance. Multivariate discriminant analysis has been used to pick out the ECG indices that best classify different types of episodes. The stepwise approach is then applied, using the Wilk's Lambda minimization as the criteria for inclusion and removal of variables (F =3.84 for inclusion and F=2.71 for rejection)[82]. The classification results are calculated using the cross-validated estimation (leave-one-out). A rule of thumb says that the number of variables used should be lower than the square root of the number of cases of the smallest group of the data set.

Five variables were calculated to asses the classification performance: sensitivity (SE), specificity (SP), positive predictivity value (+PV), negative predictivity value (-PV) and exactness (EX). SE, +PV, SP and -PV when clustering between two groups, are defined as follows:

$$SE = \frac{TP}{TP + FN} \qquad +PV = \frac{TP/N_1}{TP/N_1 + FP/N_2}$$

$$SP = \frac{TN}{TN + FP} \qquad -PV = \frac{TN/N_2}{TN/N_2 + FN/N_1}$$

while EX, also called accuracy, is defined as:

$$EX = \frac{TP + TN}{N_1 + N_2}$$

where TP represents the true positives, FN the false negatives, FP the false positives, TN the true negatives and N_1 and N_2 are the number of elements belonging to the group "1" and "2" respectively. The normalization factors (N_1 and N_2) when estimating the $+PV$ are due to the imbalance of the number of elements in each group involved in the discriminant analysis (see table 4.2).

When clustering among more than two groups (three groups in this study), SE and SP have no meaning. Then, performance is assessed by the confusion matrix and the EX, now defined as:

$$EX = \frac{TP_1 + TP_2 + TP_3}{N_1 + N_2 + N_3}$$

where TP_1, TP_2 and TP_3 are the true positives of each of the three groups and N_1, N_2 and N_3 correspond to the number of elements in each group.

4.3. Results

4.3.1. Classification between IG, HRG and SSG

For the ANOVA classification, variables related to the T wave delineation such as $\Delta\mathcal{I}_{\mathrm{QT}}$, $\Delta\mathcal{I}_{\mathrm{T}_A}$, $\Delta\mathcal{I}_{\mathrm{T}_w}$ and $\Delta\mathcal{I}_{\mathrm{T}_{pe}}$, have not been included because body position changes

VARIABLES	IG	HRG	SSG	p-value
$\Delta\mathcal{I}_{\mathrm{RMS_{ST}}}$ $[\mu\mathrm{V}]$	38.7 ± 33.7	24.9 ± 21.3	$-0.2\pm$ 20.1	0
$\Delta\mathcal{I}_{\mathrm{ST}}$ $[\mu\mathrm{V}]$	-65.0 ± 181.5	$-58.8\pm$ 107.9	$-0.4\pm$ 73.9	$5.1\ E-53$
$\lvert\Delta\mathcal{I}_{\mathrm{ST}}\rvert$ $[\mu\mathrm{V}]$	152.3 ± 119.0	106.9± 60.2	47.7± 56.4	$9.8\ E-247$
$\Delta\mathcal{I}_{\mathrm{HR}}$ $[bpm]$	7.2 ± 15.5	18.9± 18.2	1.8± 8.6	$2.4\ E-107$
$\lvert\Delta\mathcal{I}_{\mathrm{HR}}\rvert$ $[bpm]$	12.1 ±12.0	22.1 ± 14.1	6.5 ± 5.9	$1.4\ E-164$
$\mathcal{I}_{\mathrm{HR_3}}$ $[bpm]$	90.5 ± 24.1	110.2 ±21.3	82.6 ± 17.5	$1.4\ E-95$
$\mathcal{I}_{\mathrm{HR_1}}$ $[bpm]$	83.3 ± 17.9	91.3 ±15.6	80.8 ± 18.0	$8.1\ E-18$
$\lvert\Delta\mathcal{I}^{e}_{\mathrm{KL_{ST\text{-}T}}}\rvert$	0.5± 0.6	0.3 ±0.3	0.1± 0.1	$9.7\ E-227$
$\lvert\Delta\mathcal{I}^{m}_{\mathrm{KL_{ST\text{-}T}}}\rvert$	1.4 ± 1.4	1.0± 0.9	0.2± 0.2	$3.7\ E-281$
$\lvert\Delta\mathcal{I}^{e}_{\mathrm{KL_{QRS}}}\rvert$	0.1 ± 0.2	0.1 ± 0.1	0.1 ± 0.1	$2.7\ E-15$
$\lvert\Delta\mathcal{I}^{m}_{\mathrm{KL_{QRS}}}\rvert$	0.5 ± 0.5	0.6 ± 0.6	0.3 ± 0.2	$5.9\ E-85$
$\Delta\mathcal{I}_{\mathrm{SNR}}$	-7.0 ±69.3	-36.3 ± 79.7	-15.0 ± 31.6	$8.2\ E-16$
$\mathcal{I}_{\rho}$	0.2 ± 0.5	0.4 ± 0.5	-0.08 ± 0.5	$7.9\ E-69$
$\Delta\mathcal{I}_{\mathrm{Se}}$ $[Hz]$	0.11 ± 6.8	0.71 ± 5.11	-0.2 ± 7.1	0.09
$\Delta\mathcal{I}_{\mathrm{Sl}}$ $[Hz]$	1.29 ± 8.0	1.9± 6.3	$-8E-5$ ± 7.5	$2.0\ E-7$

Table 4.3: Summary of the means and standard deviations (mean ± std) of different indices variations used in classification analysis at the annotated ischemic (IG), heart rate related (HRG) and sudden step ST change- (SSG) groups applying protocol B, between intervals I_1 and I_3 (in SSG, I_3 is replaced by I_2). The p-value of each feature is also shown.

linked to high noisy beats make T wave delineation problematic. In Table 4.3, means and standard deviations of each index for each type of episode are shown for protocol B.

Multivariate linear discriminant analysis results for classifying the three groups (IG, HRG and SSG) are presented in terms of the confusion matrix in Table 4.4 for the three protocols A, B and C. The selected set of features $\mathcal{V}$ ordered by significance of the classification for each annotation protocol is also included below the confusion matrix.

The group dispersion diagram obtained with the two discriminant functions, $\mathcal{F}_1(\mathcal{V})$ and $\mathcal{F}_2(\mathcal{V})$, for protocols A, B and C, are shown in Fig. 4.5.

For protocol B, when using the quadratic discriminant analysis, the accuracy is 82.4%, and the probabilities to classify correctly the IG, HRG and the SSG are 55.7%, 76.3% and 95.6%, respectively. Results are similar to the ones obtained with the linear discriminant analysis.

4.3.2. Classification between different ST level patterns: TG and SSG

As regards distinguishing between different ST signatures, the TG and the SSG, results are shown in Table 4.5 in terms of SE, SP and EX. The most significant variables selected by the classification analysis for each protocol are also shown.

	Type	PREDICTION								
		Prot A (EX=72.0%)			Prot B (EX=82.3%)			Prot C (EX=85.4%)		
		IG	*HRG*	*SSG*	*IG*	*HRG*	*SSG*	*IG*	*HRG*	*SSG*
PERCENTAGE OF EVENTS (%)	*IG*	50.8	25.6	23.6	59.7	21.3	19.0	62.8	18.5	18.7
	HRG	12.3	67.4	20.3	15.9	66.4	17.7	14.8	64.3	20.9
	SSG	4.2	7.1	88.7	2.0	3.5	94.6	3.5	1.9	94.6
Included Set of Variables $\mathcal{V}$		$\{\Delta\mathcal{I}_{\mathrm{RMS}_{\mathrm{ST}}}$, $\mathcal{I}_{\mathrm{HR}_3}$, $\lvert\Delta\mathcal{I}^{e}_{\mathrm{KL}_{\mathrm{ST\text{-}T}}}\rvert$, $\lvert\Delta\mathcal{I}_{\mathrm{HR}}\rvert$, $\mathcal{I}_{\rho}$, $\lvert\Delta\mathcal{I}^{m}_{\mathrm{KL}_{\mathrm{ST\text{-}T}}}\rvert$, $\Delta\mathcal{I}_{\mathrm{SNR}}$, $\Delta\mathcal{I}_{\mathrm{ST}}$, $\lvert\Delta\mathcal{I}^{m}_{\mathrm{KL}_{\mathrm{QRS}}}\rvert$, $\lvert\Delta\mathcal{I}^{e}_{\mathrm{KL}_{\mathrm{QRS}}}\rvert$, $\lvert\mathcal{I}_{\mathrm{ST}}\rvert$ and $\lvert\Delta\mathcal{I}_{\mathrm{RMS}_{\mathrm{ST}}}\rvert\}$			$\{\Delta\mathcal{I}_{\mathrm{RMS}_{\mathrm{ST}}}$, $\lvert\Delta\mathcal{I}_{\mathrm{HR}}\rvert$, $\lvert\Delta\mathcal{I}^{e}_{\mathrm{KL}_{\mathrm{ST\text{-}T}}}\rvert$, $\mathcal{I}_{\rho}$, $\lvert\Delta\mathcal{I}^{m}_{\mathrm{KL}_{\mathrm{ST\text{-}T}}}\rvert$, $\mathcal{I}_{\mathrm{HR}_3}$, $\Delta\mathcal{I}_{\mathrm{SNR}}$, $\Delta\mathcal{I}_{\mathrm{ST}}$, $\mathcal{I}_{\mathrm{Se}}$ and $\mathcal{I}_{\mathrm{Sl}}\}$			$\{\Delta\mathcal{I}_{\mathrm{RMS}_{\mathrm{ST}}}$, $\lvert\Delta\mathcal{I}^{e}_{\mathrm{KL}_{\mathrm{ST\text{-}T}}}\rvert$, $\lvert\Delta\mathcal{I}_{\mathrm{HR}}\rvert$, $\lvert\Delta\mathcal{I}^{m}_{\mathrm{KL}_{\mathrm{QRS}}}\rvert$, $\mathcal{I}_{\mathrm{HR}_3}$, $\Delta\mathcal{I}_{\mathrm{SNR}}$, $\mathcal{I}_{\rho}$ and $\Delta\mathcal{I}_{\mathrm{ST}}\}$		

Table 4.4: Summary of the linear classification performance in terms of the confusion matrix for the annotation protocols A, B and C. The selected sets of variables for the prediction, $\mathcal{V}$, are displayed beneath the confusion matrix.

	Prot A (EX=82.7%)		Prot B (EX=90.5%)		Prot C (EX=93.0%)	
Events	SE(%)	SP(%)	SE(%)	SP(%)	SE(%)	SP(%)
TG vs *SSG*	71.6	93.3	76.8	98.3	78.3	99.0
Included Set of Variables $\mathcal{V}$	$\{\Delta\mathcal{I}_{\mathrm{RMS}_{\mathrm{ST}}}$, $\lvert\Delta\mathcal{I}^{e}_{\mathrm{KL}_{\mathrm{ST\text{-}T}}}\rvert$, $\lvert\Delta\mathcal{I}_{\mathrm{HR}}\rvert$, $\mathcal{I}_{\rho}$, $\lvert\Delta\mathcal{I}^{m}_{\mathrm{KL}_{\mathrm{ST\text{-}T}}}\rvert$, $\mathcal{I}_{\mathrm{HR}_3}$, $\Delta\mathcal{I}_{\mathrm{SNR}}$, $\Delta\mathcal{I}_{\mathrm{Sl}}$ and $\Delta\mathcal{I}_{\mathrm{Se}}\}$		$\{\Delta\mathcal{I}_{\mathrm{RMS}_{\mathrm{ST}}}$, $\lvert\Delta\mathcal{I}^{e}_{\mathrm{KL}_{\mathrm{ST\text{-}T}}}\rvert$, $\lvert\Delta\mathcal{I}_{\mathrm{HR}}\rvert$, $\mathcal{I}_{\rho}$, $\lvert\Delta\mathcal{I}^{m}_{\mathrm{KL}_{\mathrm{ST\text{-}T}}}\rvert$, $\mathcal{I}_{\mathrm{HR}_3}$, $\Delta\mathcal{I}_{\mathrm{SNR}}$, $\Delta\mathcal{I}_{\mathrm{Sl}}$ and $\Delta\mathcal{I}_{\mathrm{Se}}\}$		$\{\Delta\mathcal{I}_{\mathrm{RMS}_{\mathrm{ST}}}$, $\lvert\Delta\mathcal{I}^{e}_{\mathrm{KL}_{\mathrm{ST\text{-}T}}}\rvert$, $\lvert\Delta\mathcal{I}_{\mathrm{HR}}\rvert$, $\mathcal{I}_{\rho}$, $\lvert\Delta\mathcal{I}^{m}_{\mathrm{KL}_{\mathrm{ST\text{-}T}}}\rvert$, $\mathcal{I}_{\mathrm{HR}_3}$, $\Delta\mathcal{I}_{\mathrm{SNR}}$, $\Delta\mathcal{I}_{\mathrm{Sl}}$ and $\Delta\mathcal{I}_{\mathrm{Se}}\}$	

Table 4.5: Summary of the linear classification performance in terms of sensitivity (SE), specificity (SP) and exactness (EX) between transient events TG (ischemic plus heart rate related episodes) and sudden ST shifts (SSG) for the annotation protocols A, B and C. The variables included for the classification for each protocol are also shown.

In order to represent the linear discriminant punctuation classifying the TG and SSG for the three protocols, box plots have been used (see Fig. 4.6). Each box plot represents the 25-75th percentile and the line within the box denotes the mean.

Using the same variables, the quadratic discriminant analysis has been used to classify the events. Results are slightly better than the ones reported for the LDA. For protocol B, the accuracy has improved up to 92.1%, being the sensitivity to detect transient events 84.3% and the specificity 96.5%.

4.3.3. Discrimination between the ischemic group (IG) and the heart rate related group (HRG)

For classifying IG and HRG events, we have first used all the variables except the T wave related indices, reaching an accuracy of 77.2% for protocol B. The selected set of

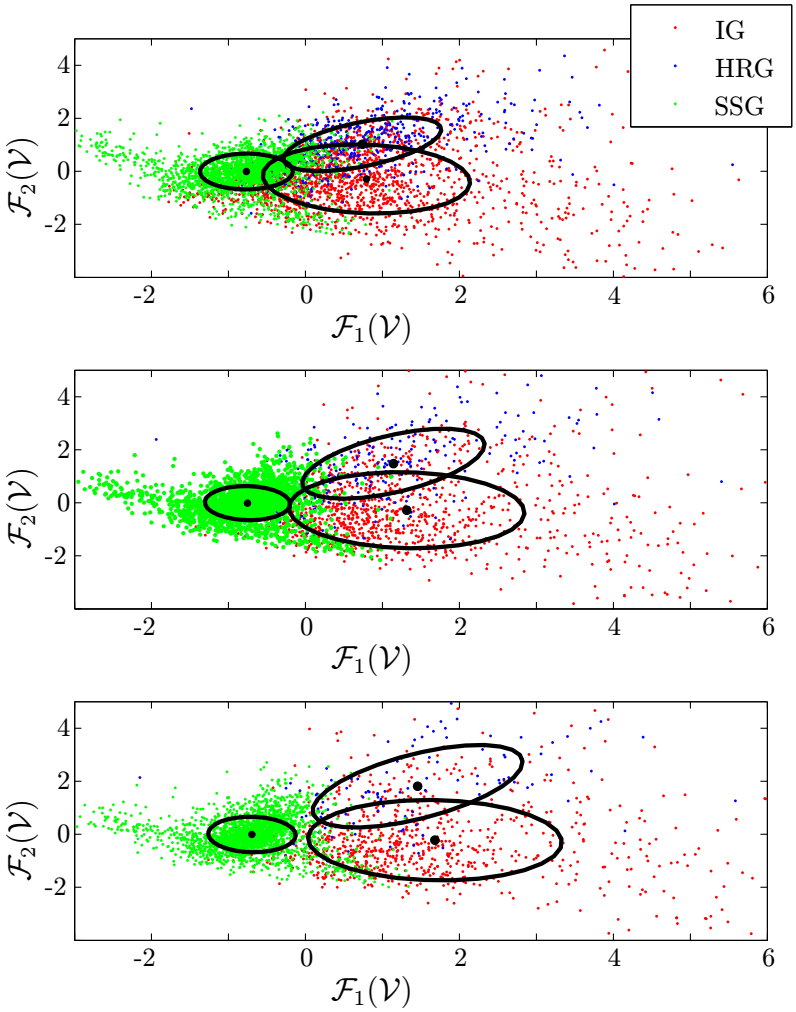

Figure 4.5: Group dispersion diagrams for the discriminant functions $\mathcal{F}_1(\mathcal{V})$ and $\mathcal{F}_2(\mathcal{V})$, obtained using the set of features, $\mathcal{V}$, giving the best performance for protocols A, B and C. The standard deviation and the mean value of each group distribution are also shown.

variables for protocol B used in the linear classification analysis is: $\mathcal{V}$ =$\{\mathcal{I}_{\mathrm{HR}_3}$, $|\Delta\mathcal{I}^e_{\mathrm{KL_{ST\text{-}T}}}|$, $\Delta\mathcal{I}_{\mathrm{ST}}$, $|\Delta\mathcal{I}_{\mathrm{HR}}|$, $\Delta\mathcal{I}_{\mathrm{RMS}}$, $\mathcal{I}_\rho$, $|\Delta\mathcal{I}^m_{\mathrm{KL_{QRS}}}|$, $|\Delta\mathcal{I}^e_{\mathrm{KL_{QRS}}}|$ and $\Delta\mathcal{I}_{\mathrm{SNR}}\}$.

In order to improve the discrimination performance, we have added the T wave related variables and included changes between the three different intervals I_1, I_2 and I_3.

The mean and the standard deviation of several variables evaluated in the discriminant analysis for the two different groups (IG and HRG) are presented in Table 4.6. The performance analysis and the p-value of the discrimination between the groups have also been evaluated for each variable individually.

Table 4.7 shows the classification performance for protocol B, in terms of SE, SP, +PV and -PV, obtained when adding new T wave related variables in the stepwise approach and also a summary of the performance and the selected set of variables for protocols A and C.

VARIABLES	IG	HRG	p-value
$\Delta\mathcal{I}_{\mathrm{RMS}_{ST13}}$ $[\mu\mathrm{V}]$	37.4 ± 24.8	22.8 ± 16.2	$4\ E-09$
$\Delta\mathcal{I}_{\mathrm{ST}_{13}}$ $[\mu\mathrm{V}]$	-69.87 ± 148.2	-26.54 ± 107.6	0.003
$\lvert\Delta\mathcal{I}_{\mathrm{ST}_{13}}\rvert$ $[\mu\mathrm{V}]$	140.28 ± 84.53	98.8 ± 49.5	$6\ E-07$
$\lvert\Delta\mathcal{I}_{\mathrm{HR}_{12}}\rvert$ $[bpm]$	3.8 ± 4	8.4 ± 7.1	$2\ E-21$
$\lvert\Delta\mathcal{I}_{\mathrm{HR}_{13}}\rvert$ $[bpm]$	10.07 ± 9.4	19.16 ± 11.14	$6\ E-19$
$\mathcal{I}_{\mathrm{HR}_3}$ $[bpm]$	85.6 ± 19.9	103.6 ± 20.7	$2\ E-17$
$\Delta\mathcal{I}_{\mathrm{QT}_{13}}$ $[ms]$	-5.2 ± 28.2	-30.6 ± 34	$1.2\ E-16$
$\Delta\mathcal{I}_{\mathrm{QT}_{23}}$ $[ms]$	-3.8 ± 24.9	2.5 ± 30	$8\ E-16$
$\Delta\mathcal{I}_{\mathrm{T}_{w13}}$ $[ms]$	-18.1 ± 27.1	-32.9 ± 40.3	$1\ E-06$
$\Delta\mathcal{I}_{\mathrm{T}_{pe13}}$ $[ms]$	-5.8 ± 14.2	-12.9 ± 22.2	$1\ E-05$
$\lvert\Delta\mathcal{I}^{e}_{\mathrm{KL}_{\mathrm{QRS}_{12}}}\rvert$	0.03 ± 0.03	0.02 ± 0.02	0.008
$\lvert\Delta\mathcal{I}^{e}_{\mathrm{KL}_{\mathrm{ST\text{-}T}_{13}}}\rvert$	0.03 ± 0.03	0.02 ± 0.02	$6\ E-08$
$\lvert\Delta\mathcal{I}^{m}_{\mathrm{KL}_{\mathrm{ST\text{-}T}_{12}}}\rvert$	0.04 ± 0.3	-0.06 ± 0.3	0.046
$\Delta\mathcal{I}_{\mathrm{Sl}_{23}}$ $[Hz]$	0.35 ± 5.87	1.75 ± 5.19	0.02
$\Delta\mathcal{I}_{\mathrm{Se}_{23}}$ $[Hz]$	-0.41 ± 5.06	0.87 ± 4.12	0.01
$\mathcal{I}_{\rho}$	-0.16 ± 0.5	0.36 ± 0.5	$1\ E-04$
$\Delta\mathcal{I}_{\mathrm{SNR}_{13}}$	-4.2 ± 70.4	-39.7 ± 84.4	$2.3\ E-06$
$\Delta\mathcal{I}_{\mathrm{T}_A 13}$ $[\mu\mathrm{V}]$	-37.2 ± 271.2	-116.8 ± 201.9	0.003

Table 4.6: Summary of the mean and the standard deviation (mean ± std) of different indices variations used for the classification analysis of the annotated ischemic (IG) and heart rate related episodes (HRG). The p-value of those indices is also shown.

	Set of Variables $\mathcal{V}$ (ordered by relevance)	**SE**	**SP**	**+PV**	**-PV**	**EX**
P	$\lvert\Delta\mathcal{I}_{\mathrm{HR}_{12}}\rvert$	78.7	54.5	63.4	71.9	75.0
R	$\{\lvert\Delta\mathcal{I}_{\mathrm{HR}_{12}}\rvert, \Delta\mathcal{I}_{\mathrm{QT}_{23}}\}$	80.5	67.0	70.9	77.4	78.4
O	$\{\lvert\Delta\mathcal{I}_{\mathrm{HR}_{12}}\rvert, \Delta\mathcal{I}_{\mathrm{QT}_{23}}, \lvert\Delta\mathcal{I}_{\mathrm{ST}_{13}}\rvert\}$	81.0	68.8	72.2	78.3	79.1
T	$\{\lvert\Delta\mathcal{I}_{\mathrm{HR}_{12}}\rvert, \Delta\mathcal{I}_{\mathrm{QT}_{23}}, \lvert\Delta\mathcal{I}_{\mathrm{ST}_{13}}\rvert, \Delta\mathcal{I}_{\mathrm{ST}_{13}}\}$	80.3	79.5	79.6	80.2	80.2
O	$\{\lvert\Delta\mathcal{I}_{\mathrm{HR}_{12}}\rvert, \Delta\mathcal{I}_{\mathrm{QT}_{23}}, \lvert\Delta\mathcal{I}_{\mathrm{ST}_{13}}\rvert, \Delta\mathcal{I}_{\mathrm{ST}_{13}}, \mathcal{I}_{\mathrm{HR}_3}\}$	83.5	76.8	78.2	82.3	82.5
C	$\{\lvert\Delta\mathcal{I}_{\mathrm{HR}_{12}}\rvert, \Delta\mathcal{I}_{\mathrm{QT}_{23}}, \lvert\Delta\mathcal{I}_{\mathrm{ST}_{13}}\rvert, \Delta\mathcal{I}_{\mathrm{ST}_{13}}, \mathcal{I}_{\mathrm{HR}_3}, \lvert\Delta\mathcal{I}^e_{\mathrm{KL}_{\text{ST-T}_{13}}}\rvert\}$	82.7	82.1	82.2	82.6	82.6
O	$\{\lvert\Delta\mathcal{I}_{\mathrm{HR}_{12}}\rvert, \Delta\mathcal{I}_{\mathrm{QT}_{23}}, \lvert\Delta\mathcal{I}_{\mathrm{ST}_{13}}\rvert, \Delta\mathcal{I}_{\mathrm{ST}_{13}}, \mathcal{I}_{\mathrm{HR}_3}, \lvert\Delta\mathcal{I}^e_{\mathrm{KL}_{\text{ST-T}_{13}}}\rvert, \lvert\Delta\mathcal{I}_{\mathrm{HR}_{13}}\rvert\}$	83.8	81.3	81.7	83.4	83.4
L	$\{\lvert\Delta\mathcal{I}_{\mathrm{HR}_{12}}\rvert, \Delta\mathcal{I}_{\mathrm{QT}_{23}}, \lvert\Delta\mathcal{I}_{\mathrm{ST}_{13}}\rvert, \Delta\mathcal{I}_{\mathrm{ST}_{13}}, \mathcal{I}_{\mathrm{HR}_3}, \lvert\Delta\mathcal{I}^e_{\mathrm{KL}_{\text{ST-T}_{13}}}\rvert, \lvert\Delta\mathcal{I}_{\mathrm{HR}_{13}}\rvert, \lvert\Delta\mathcal{I}^e_{\mathrm{KL}_{\mathrm{QRS}_{12}}}\rvert\}$	84.0	85.7	85.5	84.3	84.3
B	$\{\lvert\Delta\mathcal{I}_{\mathrm{HR}_{12}}\rvert, \Delta\mathcal{I}_{\mathrm{QT}_{23}}, \lvert\Delta\mathcal{I}_{\mathrm{ST}_{13}}\rvert, \Delta\mathcal{I}_{\mathrm{ST}_{13}}, \mathcal{I}_{\mathrm{HR}_3}, \lvert\Delta\mathcal{I}^e_{\mathrm{KL}_{\text{ST-T}_{13}}}\rvert, \lvert\Delta\mathcal{I}_{\mathrm{HR}_{13}}\rvert, \lvert\Delta\mathcal{I}^e_{\mathrm{KL}_{\mathrm{QRS}_{12}}}\rvert, \Delta\mathcal{I}^m_{\mathrm{KL}_{\mathrm{QRS}_{23}}}\}$	84.5	86.6	86.3	84.8	84.8
A	$\{\mathcal{I}_{\mathrm{HR}_3}, \Delta\mathcal{I}_{\mathrm{ST}_{13}}, \lvert\Delta\mathcal{I}^e_{\mathrm{KL}_{\text{ST-T}_{13}}}\rvert, \lvert\Delta\mathcal{I}_{\mathrm{HR}_{13}}\rvert, \Delta\mathcal{I}_{\mathrm{RMS}_{ST23}}, \Delta\mathcal{I}_{\mathrm{T}_{pe12}}, \lvert\Delta\mathcal{I}^e_{\mathrm{KL}_{\mathrm{QRS}_{12}}}\rvert, \lvert\Delta\mathcal{I}^m_{\mathrm{KL}_{\mathrm{QRS}_{13}}}\rvert, \Delta\mathcal{I}_{\mathrm{SNR}_{12}}, \lvert\Delta\mathcal{I}_{\mathrm{HR}_{12}}\rvert, \lvert\Delta\mathcal{I}^e_{\mathrm{KL}_{\text{ST-T}_{12}}}\rvert, \lvert\Delta\mathcal{I}^m_{\mathrm{KL}_{\text{ST-T}_{12}}}\rvert\}$	76.0	76.5	76.4	76.1	76.1
C	$\{\lvert\Delta\mathcal{I}_{\mathrm{HR}_{12}}\rvert, \Delta\mathcal{I}_{\mathrm{HR}_{13}}, \Delta\mathcal{I}_{\mathrm{ST}_{13}}, \Delta\mathcal{I}_{\mathrm{RMS}_{ST23}}, \Delta\mathcal{I}_{\mathrm{Sl}_{23}}, \mathcal{I}_{\mathrm{HR}_3}, \Delta\mathcal{I}_{\mathrm{SNR}_{12}}\}$	86.5	81.5	82.4	85.8	86.0

Table 4.7: The improvement in linear classification performance between *IG* and *HRG* episodes in terms of SE, SP, +PV, -PV and EX, in each step of the method for protocol B, is shown. A summary of the performance together with the selected set of variables for protocols A and C is also shown.

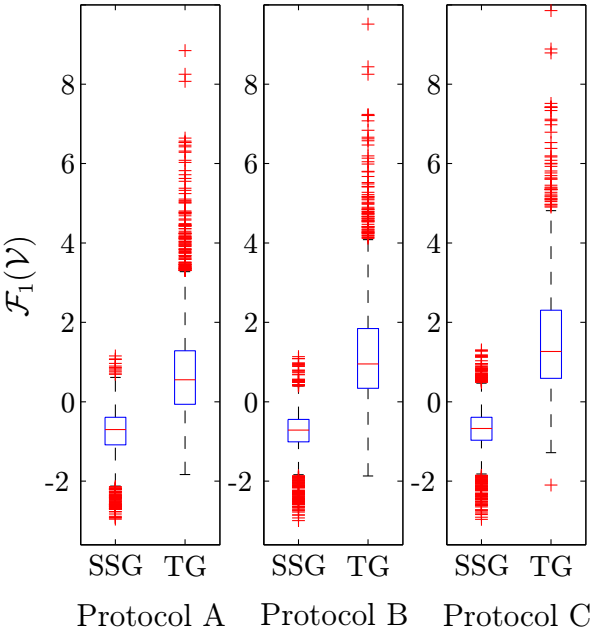

Figure 4.6: Linear discriminant punctuation for classifying between the transient group (TG) and the sudden step group (SSG) for the three protocols.

The discriminant punctuation between IG and HRG calculated analogously to the the discrimination between TG and SSG is shown in Fig. 4.7.

4.3.4. Classification between IG and NIG

The performance analysis when distinguishing between IG and NIG (HRE, $BPCE$ and CCE) reaches an exactness of 87.5% for protocol B. A summary of the classification performance is shown in Table 4.8.

Applying QDA to the same sets of variables, results are similar to LDA. For protocol B, the sensitivity in the classification between ischemic and non ischemic events is 71.9%, the specificity 93.6% and the accuracy 87.1%.

Classification of episodes on each recording (patient) has been calculated using leave one out over recordings. The percentages of patients whose sensitivity, specificity and exactness are within the ranges: less than 50%, from 50% to 60%, from 60% to 70% and so on until more than 90% are shown in figure 4.8.

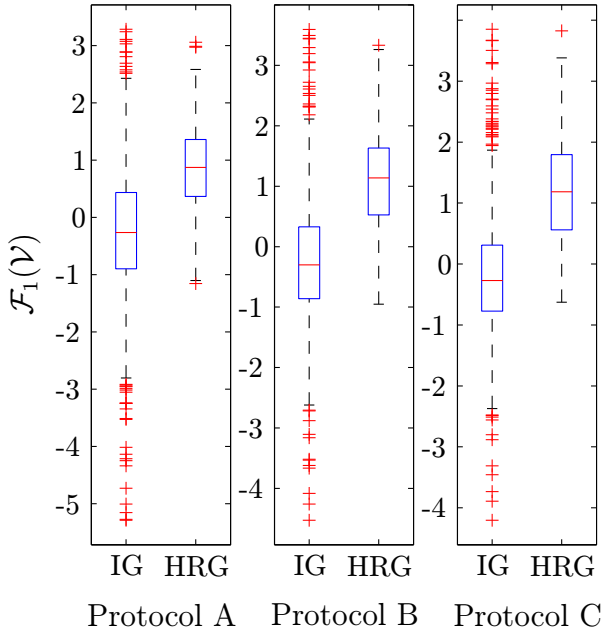

Figure 4.7: Discriminant punctuation for classifying between the ischemic (IG) and the heart rate related (HRG) group for the three protocols.

	Prot A (EX=79.0%)		Prot B (EX=87.5%)		Prot C (EX=91.0%)	
Events	SE(%)	SP(%)	SE(%)	SP(%)	SE(%)	SP(%)
IG vs *NIG*	65.0	87.7	74.2	93.2	77.7	95.6
Included Set of Variables $\mathcal{V}$	$\{\Delta\mathcal{I}_{\mathrm{RMS_{ST}}}, \lvert\Delta\mathcal{I}^{e}_{\mathrm{KL_{ST\text{-}T}}}\rvert, \Delta\mathcal{I}_{\mathrm{SNR}}, \mathcal{I}_{\rho}, \Delta\mathcal{I}_{\mathrm{ST}}, \lvert\Delta\mathcal{I}^{m}_{\mathrm{KL_{ST\text{-}T}}}\rvert, \Delta\mathcal{I}_{\mathrm{Se}}$ and $\Delta\mathcal{I}_{\mathrm{Sl}}\}$		$\{\Delta\mathcal{I}_{\mathrm{RMS_{ST}}}, \lvert\Delta\mathcal{I}^{e}_{\mathrm{KL_{ST\text{-}T}}}\rvert, \lvert\Delta\mathcal{I}^{m}_{\mathrm{KL_{ST\text{-}T}}}\rvert, \Delta\mathcal{I}_{\mathrm{SNR}}, \mathcal{I}_{\rho}, \Delta\mathcal{I}_{\mathrm{Sl}}, \Delta\mathcal{I}_{\mathrm{Se}}$ and $\lvert\Delta\mathcal{I}_{\mathrm{HR}}\rvert\}$		$\{\Delta\mathcal{I}_{\mathrm{RMS_{ST}}}, \lvert\Delta\mathcal{I}^{e}_{\mathrm{KL_{ST\text{-}T}}}\rvert, \lvert\Delta\mathcal{I}^{m}_{\mathrm{KL_{ST\text{-}T}}}\rvert, \Delta\mathcal{I}_{\mathrm{SNR}}, \mathcal{I}_{\rho}, \Delta\mathcal{I}_{\mathrm{Sl}}, \Delta\mathcal{I}_{\mathrm{Se}}$ and $\lvert\Delta\mathcal{I}_{\mathrm{HR}}\rvert\}$	

Table 4.8: Summary of the classification performance in terms of sensitivity (SE) and specificity (SP) between the ischemic group IG and the non ischemic group NIG for the annotation protocols A, B and C. The set of variables, $\mathcal{V}$, included for each protocol are also shown.

4.4. Discussion

4.4.1. Classification between IG, HRG and SSG

In the first part of this work we have approached the task of classifying the three different types of ST events, IE, HRE and SSE, obtaining an accuracy of 82.3% and using a set of 11 indices for protocol B (see Table 4.4). The ordered index set proposed as significant by the step wise approach is shown for each protocol. Note that the two

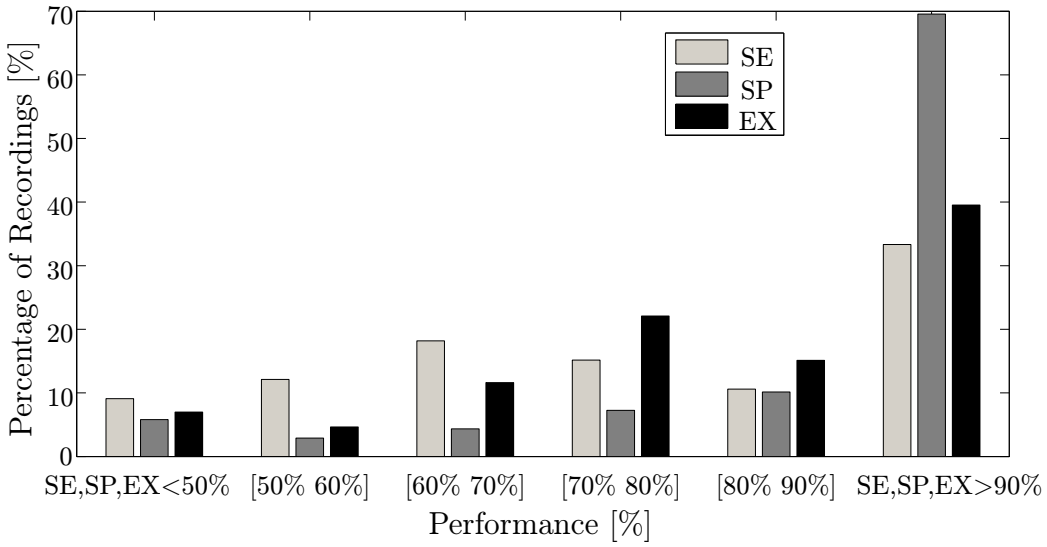

Figure 4.8: Percentages of recordings whose sensitivity, specificity or exactness when detecting ischemia, are within different ranges.

most significant indices are $\Delta\mathcal{I}_{\mathrm{RMS_{ST}}}$ followed by $|\Delta\mathcal{I}_{\mathrm{HR}}|$. The first shows a first attempt to classify the two different patterns of the ST level, the transient TG and the sudden step group SSG, while the second shows greater differences within the TG, between IE and HRE.

If we analyze each index individually (see Table 4.3), $\Delta\mathcal{I}_{\mathrm{RMS_{ST}}}$ associated to changes in energy of the ST segment, is higher in the IG (38.7 μV) than in the HRG (24.9 μV) and hardly changes in the SSG (-0.2 μV). These results agree with indices $\Delta\mathcal{I}_{\mathrm{ST}}$ and $|\Delta\mathcal{I}_{\mathrm{ST}}|$, which show greater values in the TG (more in the IG than in the HRG) than in the SSG group, where the ST level change is abrupt and with low amplitude. However, $\Delta\mathcal{I}_{\mathrm{ST}}$ does not appear among the first selected classification variables (see Table 4.4) because $\Delta\mathcal{I}_{\mathrm{RMS_{ST}}}$ contains similar information and it is a more robust measurement to noise present in the ECG.

Heart rate related indices show higher increments during HRE ($|\Delta\mathcal{I}_{\mathrm{HR}}| \backsimeq 22.1$ bpm) in comparison with IE ($\backsimeq 12.1$ bpm) and SSE ($\backsimeq 6.5$ bpm). The heart rate value at the extremum is also higher in mean during HRE ($\backsimeq 110.2$ bpm) than during IE ($\backsimeq 90.5$ bpm) and much more than in SSE ($\backsimeq 82.6$ bpm).

The KL- based indices, associated to changes in the QRS and ST-T complexes and mostly used to detect body position changes in the ECG [41], show higher differences between the TG and the SSG than within the TG (IG and HRG).

The early and the late QRS slopes show differences between the transient ($\Delta\mathcal{I}_{\mathrm{Sl}} \backsimeq 1.56$ Hz) and the sudden step group ($\Delta\mathcal{I}_{\mathrm{Sl}} \backsimeq 0.06$ Hz).

Index $\mathcal{I}_{\rho}$, associated to the correlation between the heart rate and the RMS of the ST segment is higher in mean in HRG events ($\backsimeq 0.4$) than in IG events ($\backsimeq 0.2$), showing that an increase of heart rate in IE could be secondary to the oxygen demand-supply imbalance while in HRE, the ST segment change is directly the result of T wave incursion

into the ST segment because of the high heart rate. SSG events hardly show correlation in mean ($\backsimeq -0.08$).

In terms of protocols, protocol C, with the least number of transient events and the most restrictive, achieves the highest accuracy when classifying, followed by protocols B and A, the least restrictive. This is in accordance with the fact that protocol C retains only the very evident episodes.

4.4.2. Classification between different ST level patterns: TG and SSG

The very different origins and patterns of the ST level in the TG and the SSG result in the accuracy of distinguishing between these two groups increasing up to 90.5% for protocol B (see Table 4.5). The sensitivity when classifying the TG is 77% and 98% for the SSG.

Most variables included in the classification analysis rely on changes in the ST segment, $\Delta\mathcal{I}_{\mathrm{RMS_{ST}}}$, associated to changes in the area defined by the ST segment, being the most significant index, followed by $|\Delta\mathcal{I}^{e}_{\mathrm{KL_{ST\text{-}T}}}|$. This agrees with the fact that they have different ST level patterns.

KL-based indices of the ST-T and QRS are suggested in the literature as markers for the detection of body position changes [41] that are associated to sudden step ST changes, agreeing with our results that propose $|\Delta\mathcal{I}^{e}_{\mathrm{KL_{ST\text{-}T}}}|$ as a significant parameter in the discrimination. This index accounts for the complete repolarization feature, adding which could be missed by just looking at the ST segment exclusively.

ST level is also a crucial parameter for classification. Calculation of the deviation of the ST in mean for TG ($\backsimeq 130\mu V$) is higher than in the SSG ($\backsimeq 48\mu V$).

Information about heart rate is also included in the discriminant function. $|\Delta\mathcal{I}_{\mathrm{HR}}|$ shows greater changes in mean of heart rate during TG ($\backsimeq$ 12 bpm) in comparison to SSG ($\backsimeq$ 2 bpm).

4.4.3. Discrimination between the ischemic group (IG) and the heart rate related group (HRG)

A first attempt in distinguishing between IE and HRE without using T wave related indices achieved an accuracy of 77.2% for protocol B. However, the accuracy increases up to 84.8% when we add those indices related to the repolarization dispersion as described in section 4.2.4 (see Table 4.7).

Note that the variables with lower p-values are those related to heart rate and QT interval and thus the first ones included in the step wise approach are $|\Delta\mathcal{I}_{\mathrm{HR_{12}}}|$ and $\Delta\mathcal{I}_{\mathrm{QT_{23}}}$ (see Table 4.6).

HRE are mostly associated to more remarkable changes in heart rate than IE and in order to group these episodes the first variable included in the classification analysis is $|\Delta\mathcal{I}_{\mathrm{HR_{12}}}|$ ($\backsimeq$ 3.8 bpm in mean for IG and $\backsimeq$ 8.4 bpm for HRG). However, heart rate acceleration is also a key factor to induce ischemia in patients with coronary occlusion

and therefore other indices in addition to the heart rate change related to changes in the ST segment are needed to avoid overlapping with the HRG. Regarding the IG, in [90] it is claimed that much larger number of the records of the LTST DB contain demand ischemic episodes, related to heart rate. However, episodes in the database are not clinically classified as demand or supply episodes. Besides, care should be taken in the sense that not all episodes in HRG are associated with an increase in heart rate. In about 10% of the episodes, heart rate is oscillating or even decreasing.

QT interval changes are typically adapted to changes in the RR interval, therefore the QT interval is hardly shortened in IE ($\backsimeq$ 4 ms) while in HRE it is reduced by about 28 ms.

Alterations in the late steepest slope has been proposed as an index to quantify ECG changes in supply ischemia, with the result that QRS slopes were considerably less steep during prolonged ($\backsimeq$ 4 minutes) artery occlusion [29]. However, in short term ($\backsimeq$ 1 minute) angioplasty episodes, discrepant slope variations were found [91]. Our results show no systematic changes and agrees mostly with [91].

A greater shortening in the T width, in mean, is observed in HRE ($\backsimeq$ -32 ms) while in IE it is lower ($\backsimeq$ -18 ms). A similar behaviour is observed in $\Delta\mathcal{I}_{\mathrm{T}_{pe}}$ where the shortening is greater in HRE. Both indices are closely related to heart rate with the difference that T_w interval adapts slower to heart rate changes than T_{pe} interval [92].

In general, transmural or epicardial ischemia is reflected in ST elevation while sub-endocardial ischemia shows ST depression [16]. Our results (Table 4.6) show depression in the ST level function during IE ($\backsim -70\mu V$ in mean) and agrees with [16] due to the fact that most of ischemic events in Holter recordings are sub-endocardial. The absolute deviation of the ST level is higher in IE ($\backsim 144\mu V$ in mean) than in HRE ($\backsim 93\mu V$) as expected.

The amplitude of the T wave is reduced during both types of episodes, being lower during HRE in comparison to IE. The depression of the T wave agrees with [93], which states that epicardial ischemia increases the peak T amplitude while endocardial ischemia produces a size-dependent reduction in T amplitude. As we commented above most of the IE in Holter recordings are subendocardial.

Finally, note that in [78] it is also presented a discrimination between IG and HRG, reaching a sensitivity of 77.9% and a specificity of 73.9%. Without including T wave related variables, we obtained similar results. In this work, we added T wave related indices and achieved an increase up to 84.5% in sensitivity and up 86.6% in the specificity.

4.4.4. Classification between IG and NIG

When the classification target is ischemia, we observe that the two first variables that best distinguish between IG and NIG are those related to the ST segment: $\Delta\mathcal{I}_{\mathrm{RMS_{ST}}}$ and $|\mathcal{I}^{e}_{\mathrm{KL_{ST\text{-}T}}}|$. Note that these indices are also the most significant when distinguishing between different ST segment patterns (TG and SSG). The reason is that the IG has a much higher change in the RMS of the ST segment and also in the ST-T complex than HRG and SSG (see Table 4.3).

In relation with the Physionet/Computers in Cardiology Challenge, our results are comparable with [81] (EX=90.7% in [81] and EX=87.5% with our method), being the ST level change a very substantial parameter for distinguishing between IG and NIG. However, [81] uses indices such as changes in the ST level manually corrected by experts while our method is fully automated.

Performance on recordings rather than on episodes, is shown in figure 4.8. This figure shows the percentages of recordings which sensitivity, specificity or accuracy are below 50%, between 50% an 60% and so on. An important implication of Fig. 4.8 is that more than 70% of the recordings have the specificity above 90% and more than 60% of the patients have well classified more than 70% of the ischemic episodes. About 80% of the patients have an exactness of more than 70%.

4.4.5. General Remarks

An important limitation of this study is that although the expert annotations are used as gold standard, classification of a particular episode can be driven by a previous knowledge about the patient rather than physiological evidences. Also, the usage of different lead configurations in this database adds difficulties when classifying.

In addition to use the magnitude of the feature change to account for the dynamic effects of ST episodes, we have also considered to use the percentage change. However, this strategy was not as significant as the one related to the magnitude of the change when inserted in the discriminant analysis

Due to the fact that some indices have leptokurtic distributions, a logarithmic transformation has also been tested. However, it has been discarded as no improvement was reached. This is in concordance with some studies that show that linear discriminant analysis is relatively robust even when there are modest violations of the assumptions of homogeneity of variances and normal distributions of indices [82].

In linear discriminant analysis, the covariance matrix of each of the classes is assumed to be identical. Quadratic discriminant analysis is a more general classifier where a different covariance matrix is estimated for each class. The usage of quadratic discriminant analysis has not improved the performance (about $\pm$ 0.5% in exactness). Besides, the obtained performance in test set is similar to the one obtained in the training set. These results suggest that no improvement could be reached in linear classification and non linear statistical techniques such as artificial neural networks and support vector machines could be explored as alternative classifiers. Non-linear indices to differentiate normal states from ischemic ones such as shifts in the Shannon's entropy could also be studied [94].

Chapter 5

Repolarization changes induced by Autonomic Nervous system testing. The ANS-UZ Database

5.1. Introduction

As we studied in the previous chapter, many repolarization features change during ischemia. However, other factors than ischemia also generate changes in the repolarization such as modifications of the autonomic nervous system. The autonomic nervous system is an important modulator of ventricular repolarization and arrhythmia vulnerability. Cardiac repolarization is known to play an important role in arrhythmogenesis, and autonomic activity is known to alter repolarization. In order to study those repolarization changes and their potential use, we have used two tests: Valsalva maneuver (VM) and tilt test trial.

In subsection §5.2, repolarization intervals are studied during VM in a database of diabetic patients. In particular, the T wave width evolution is studied to assess whether the VM is accompanied with early signs of ischemia and if those are measurable by T wave shortening. The hypothesis for this T wave shortening is that endocardial action potentials could reduce their duration as a consequence of an initial demand ischemia generated by the VM while epicardial action potentials duration remains unchanged so reducing the overall T width.

Based on the experience gained from this study in diabetic patients, we have acquired a database consisting of volunteers without any previous cardiovascular disease undergoing a tilt test trial, and three different Valsalva maneuvers. A complete description of the database, referred to as ANS-UZ DB, is done in section §5.3. Repolarization changes during those tests are also reported.

5.2. Repolarization changes during Valsalva maneuver in diabetic patients

The Valsalva maneuver is used as a test to evaluate the performance of the autonomic nervous system (ANS), which provides automatic, involuntary regulation of several body functions including the cardiac muscle activation. This regulation is controlled by the activation of the sympathetic and the parasympathetic autonomous branches [95].

The maneuver is performed by having the subject conduct a maximal, forced expiration against a pressure of 40 mmHg, and holding this for about 15 seconds. Before, during and after this maneuver, the expiratory pressure and the electrocardiogram (ECG) are monitored and registered. The Valsalva maneuver leads to hemodynamic changes in heart rate (HR), blood pressure and cerebral blood flow and may be divided into four phases. See figure 5.1.

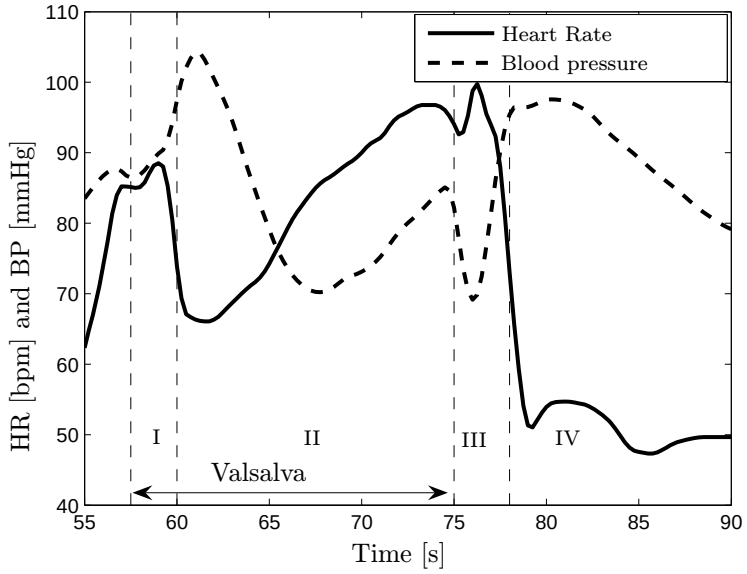

Figure 5.1: Response of the arterial pressure and the heart rate during the Valsalva maneuver describing the four phases.

When the strain starts, contraction of the thoracic cage compresses the lungs and causes a large rise in intrathoracic pressure (the pressure measured in the space between the lungs and thoracic wall). This rise in intrathoracic pressure compresses the vessels within the chest. Aortic compression results in a transient rise in aortic pressure (Phase I), which causes a reflex bradycardia due to baroreceptor activation. Because the thoracic vena cava also becomes compressed, venous return to the heart is compromised, resulting in a large fall in cardiac output. This leads to a secondary fall in aortic pressure (Phase II), and as aortic pressure falls, the baroreceptor reflex increases HR. After several seconds, arterial pressure (both mean and pulse pressure) is reduced, and HR is elevated. When

the subject starts breathing again, the sudden loss of compression on the aorta can cause a small, transient dip in arterial pressure and further reflex increase in HR (Phase III). When compression of the vena cava is removed, venous return suddenly increases causing a rapid rise in cardiac output several seconds later which leads to a transient increase in arterial pressure (Phase IV). Arterial pressure overshoots during Phase IV because the systemic vascular resistance is increased due to sympathetic activation that occurred during Phase II. HR reflexively decreases during Phase IV in response to the transient elevation in arterial pressure [96].

This maneuver generates a diminution in the blood flow that could lead to an initiation of myocardial ischemia. In the first phase, the ischemia is subendocardial since subendocardium is the first affected region by the myocardial blood flow. The transmembrane action potential duration of ischemic cells gets shorter in the first minutes of a coronary occlusion at the endocardium, then reducing the dispersion in duration between endo and epicardium, and so generating a narrowing of the T wave [16, 30, 31].

Ischemia modifies action potentials in amplitude and duration what may alter ventricular repolarization dispersion (VRD). VRD is related to the variance among recovery times throughout ventricular myocardium as a result of differences in both activation times and action potential duration and morphology. An increased VRD implies a modification of the T wave morphology. New experimental studies seem to point out T wave duration as a good quantifier of VRD [97].

In this work, we study the evolution of the T wave duration during the different phases of Valsalva maneuver, in order to evaluate the extent of flow reduction and their manifestation on the T wave width as a marker of early ischemia at the endocardium cells. The T wave duration is measured by an automatic delineator of the T onset and T end and their values at different time instants of the maneuver are compared.

5.2.1. Methods

Population

The database consists of single-lead ECG and expiratory pressure records before, during and after the VM in 27 diabetic patients: 12 women (2 with diabetes type I and 10 with diabetes type II) and 15 are men (4 with diabetes type I and 11 with type II). The age of the patients range from 28 to 76 with a mean of 48 years and the duration of the diabetes range from 1 to 45 years with a mean of 13 years [98].

Diabetes may alter the autonomic nervous system and it has been demonstrated that autonomic conditions directly affect the ventricular myocardium causing differences in QT interval that are independent of the HR [99].

Repolarization series

An ECG delineation system based on the wavelet transform (WT) has been used for QRS and T wave location and delineation [86] and it has been previously described in chapter 4. T width series (T_w), T wave peak to end (T_{pe}), and QT intervals have been

computed. The root mean square series (RMS) of the the ST level has been derived with the same technique we used in [62] and chapter 2.

Then, we have distinguished five different stages where the median of each repolarization series is calculated: 5 seconds before the start of the VM (bef), during the 5 seconds immediately after the beginning of the VM (VM_1), from 5 s to 10 s within the VM (VM_2), between the 10^{th} second and the end of the VM (VM_3) and finally during 5 seconds immediately after the end of the VM (aft).

Student's t test

Student's t test is one of the most commonly used techniques for statistically testing a hypothesis on the basis of a difference between sample means; that is, the t test determines a probability that two populations are the same with respect to the variable tested. It is analogous to one-way Analysis of Variance (ANOVA), and therefore, Student's t test considers the same two hypothesis: (1) gaussian distribution of the groups and (2) equal variances in both groups. However, it is generally believed that the t test is conservative for a sample from a long-tailed symmetric distribution [100]. Also, if variances of both groups are clearly different, then there are modifications of the t test that overcome this problem [101].

In this study we use the paired t test, consisting of a sample of matched pairs since subjects are tested prior, during and after the VM.

5.2.2. Results

We have compared the median value of each repolarization series in the interval before the VM interval with the ones during and after the VM. To do so, the paired Student's t test is used in order to assess whether the means of T_w in each two periods are statistically different from each other. Results in terms of p-value and 95% confidence interval (C.I.) are shown in Table 5.1

Delineation of the T wave onset using the WT method, in contrast with the rest of significant points, had not been validated before, due to the absence of databases with manual T wave onset annotations. Therefore we studied the behavior of the delineator by varying the threshold K_{on} trying to find the K_{on} value at which the shortening of the T wave is better observed.

We tested evenly distributed K_{on} values from 1.5 to 7, performed the delineation process and calculated the differences in T width between before VM (bef) and during either VM_1, VM_2 or VM_3. The p-values obtained from the Student's t test are shown in figure 5.2. A minimum in the p-value is not reached because determination of T wave onset is bounded by the local minimum protection rule, which does not move further the onset even if the K_{on} is extremely reduced. Figure 5.2 seems to point out 4 to 4.5 as optimal values for the K_{on} fraction. In our results we have used $K_{on} = 4$, as proposed in [86].

	p-value	C.I.
$HR_{VM_1} - HR_{bef}$ *[bpm]*	0.08	[-7.3, 0.5]
$HR_{VM_2} - HR_{bef}$	0.002	[2.4, 9.6]
$HR_{VM_3} - HR_{bef}$	$4 \cdot 10^{-8}$	[10.6, 18.3]
$HR_{aft} - HR_{bef}$	$2 \cdot 10^{-12}$	[15.0, 21.0]
$T_{w,VM_1} - T_{w,bef}$ *[ms]*	$2 \cdot 10^{-5}$	[-26.6, -11.7]
$T_{w,VM_2} - T_{w,bef}$	$9 \cdot 10^{-6}$	[-36.6, -16.7]
$T_{w,VM_3} - T_{w,bef}$	$5 \cdot 10^{-6}$	[-35.7, -16.8]
$T_{w,aft} - T_{w,bef}$	0.12	[-14.7, 1.8]
$T_{pe,VM_1} - T_{pe,bef}$ *[ms]*	0.47	[-2.5, 5.3]
$T_{pe,VM_2} - T_{pe,bef}$	0.78	[-6.0, 4.6]
$T_{pe,VM_3} - T_{pe,bef}$	0.05	[-7.8, -0.1]
$T_{pe,aft} - T_{pe,bef}$	0.17	[-9.3, 1.7]
$ST_{VM_1} - ST_{bef}$ *[μV]*	0.76	[-1.0, 1.4]
$ST_{VM_2} - ST_{bef}$	0.94	[-1.9, 1.8]
$ST_{VM_3} - ST_{bef}$	0.61	[-2.1, 3.5]
$ST_{aft} - ST_{bef}$	0.9	[-2.0, 2.2]
$QT_{VM_1} - QT_{bef}$ *[ms]*	0.005	[2.1, 11.2]
$QT_{VM_2} - QT_{bef}$	0.04	[0.1, 7.7]
$QT_{VM_3} - QT_{bef}$	0.07	[-0.4, 10.4]
$QT_{aft} - QT_{bef}$	0.38	[-7.0, 2.8]

Table 5.1: Differences in heart rate (HR), T wave width (TW), interval from T apex to T end (T_{pe}), QT interval (QT), and RMS value of ST segment (ST) between the different segments during and after the VM ($VM1$, $VM2$, $VM3$, aft) with respect to the 5 second segment previous to the maneuver (bef).

5.2.3. Discussion and conclusions

Table 5.1 shows a statistically significant shortening in T_w during the VM strain ($p = 2 \cdot 10^{-5}$), which enlarges again after the release, attaining a width similar to the one before the maneuver ($p = 0.12$). The increased HR does not seem to be the responsible since after the VM, the HR is even higher than during VM whilst T wave has recovered its original width (see figure 5.3). This observation might evidence the viability of the T width to mark very early signs of ischemia and its potential use for ischemia monitoring like in coronary care unit, etc.

T width shortening seems to result from a width reduction from the onset to the T peak rather than from the peak to the T wave end T_{pe}. This may be related to the spatial distribution of action potential modifications which will require some deeper clinical investigations. T wave is also very sensitive to cardiac axis shifts and either a change of body posture or the compression of thoracic cage during the strain, may result in it.

The differences in HR between before the VM and during the first 5 seconds of it are

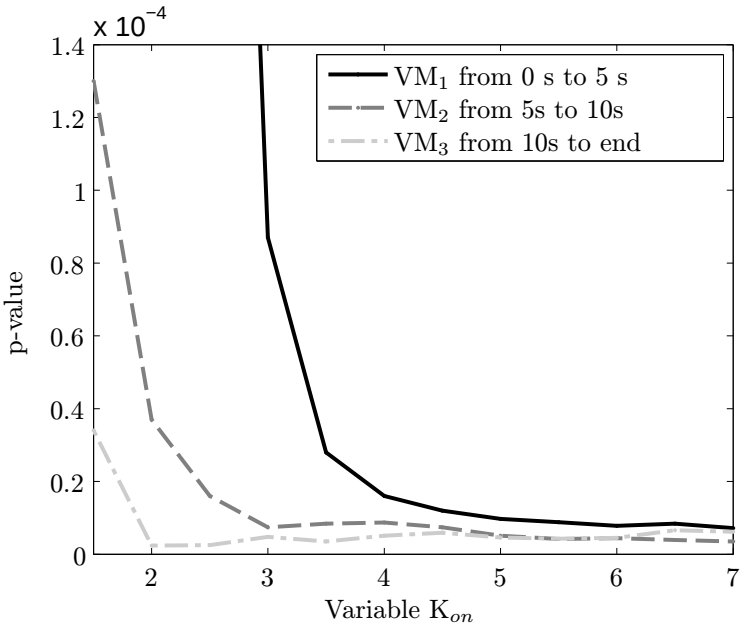

Figure 5.2: Significance (p-value) of the Student's t test for the differences between T wave width before VM and in the the 5s segments (initial, medium and final) of the VM, as a function of the K_{on} values used in the T wave onset delineation process.

not yet statistically different ($p = 0.08$). However the HR after the first 5 seconds of the maneuver is increasing during and even after VM and the divergences are statistically significant.

ST segment changes are not statistically significant between before and during and after VM. This supports the fact that compression of the arteries and flow reduction due to the effort during VM does not cause a severe ischemia, rather just the initial blood flow reduction which is perceived by the T width shortening as a result of a shortening in duration of the action potential at the endocardium, the first affected part when flow reduction occurs [30, 31].

QT shows an adaptation to the increment of HR in the beginning of the VM but after the second 10, QT interval is not following the shortening which occurs with RR interval. As diabetes may alter the autonomic nervous system and autonomic conditions directly affect the ventricular myocardium, the QT adaptation to RR may be impaired and this may be the explanation of the observed behaviour.

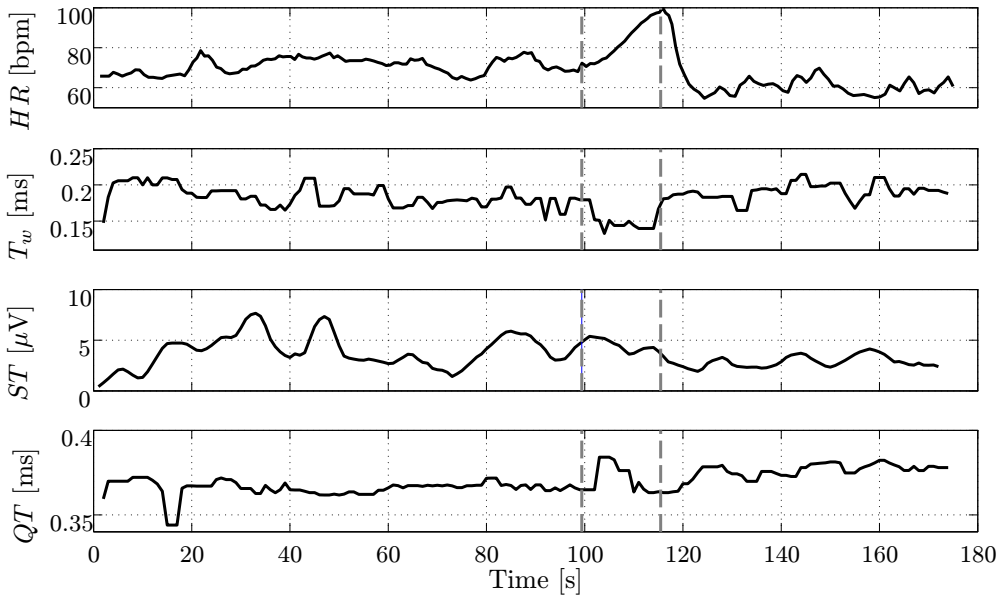

Figure 5.3: The figure shows in dashed lines the duration of the VM strain. The repolarization series: HR (dotted-solid line), T wave width T_w, the RMS of the ST segment and the QT interval, are also shown.

5.3. Acquisition of a Tilt Test and Valsalva Maneuver Database

After analyzing the results in diabetic patients in the previous section, a database of healthy volunteers undergoing different autonomic nervous system tests is acquired. The purpose is to explore the extrapolation of previous results to healthy patients and to evaluate repolarization changes in the tilt test where the ANS modifications are more controlled. This database records several biomedical signals with different sampling frequencies, making use of the generic acquisition system Biopac MP150. This database consists of 17 recordings undergoing a tilt test trial and three Valsalva maneuvers. These trials are established tests for cardiovascular autoregulatory function by provoking blood pressure changes which result in heart rate (HR) fluctuations. These fluctuations in HR result in changes of the different repolarization indices which are described below.

5.3.1. Biopac MP150

In order to record and acquire several biomedical signals, we have used the Biopac MP150 data acquisition and analysis system which consists of the following units:

- MP150 acquisition system: It connects up to sixteen analog input channels plus two analog output channels, sixteen digital leads and a synchronization input. It

consists of a dual analog-digital converter (ADC) of 16 bits and maximum sampling frequency of 400 kHz for each channel.

- Universal Interface module UIM100C: It is used to connect 100-series amplifier modules and signal cables to the acquisition module MP150. The UIM100C also provides a direct link to the analog and digital I/O lines of the MP device when collecting or sending data to external equipment.

- Amplifiers: The amplifiers can be of general purpose as the DA100C to amplify different type of signals or specific for an specific type of signal. In our case we have use the specific amplifiers ECG100C (ECG signals), RSP100C (respiratory signal) and PPG100C (photoplethysmographic (PPG) signal). Also, we have used the transducer TSD160A to monitor differential pressure that is connected to the amplifier DA100C.

- Sensors and transducers: we have used different sensors or transducers that monitor biomedical signals, such as disposable Ag-AgCl to measure potential over the body surface, TSD201 transducer to measure abdominal or thoracic expansion and contraction while breathing, TSD160A to monitor differential pressure, and photoelectric pulse transducer TSD200 to measure changes in infrared reflectance resulting from varying blood flow.

Biopac MP150 allows us to acquire standard 12-lead ECG using the Biopacs ECG100C amplifier and disposable Ag-AgCl electrodes with a hardware amplification of 1000. Besides, allows to synchronize external analog signals such as the blood pressure signal acquired from the Finometer device.

Finometer

This device measures the blood pressure in a continuous way and non invasively by the volume-clamp method, first introduced by Czech physiologist Peñaz in 1967. With this method, finger arterial pressure is measured using a finger cuff and an inflatable bladder in combination with an infrared plethysmograph, which consists of an infrared light source and detector. The infrared light is absorbed by the blood, and the pulsation of arterial diameter during a heart beat causes a pulsation in the light detector signal.

The first step in this method is determining the proper unloaded diameter of the finger arteries, the point at which finger cuff pressure and intra-arterial pressure are equal and at which the transmural pressure across the finger arterial walls is zero. Then the arteries are clamped (kept at this unloaded diameter) by varying the pressure of the finger cuff inflatable bladder using the fast cuff pressure control system.

A servo-controller system usually defines a target value or setpoint and a measured value that is compared with this setpoint. In the servo-controller the setpoint is the signal of the plethysmograph (unloaded diameter of the arteries) that must be clamped. The measured value comes from the light detector. The amplified difference between the setpoint and measured value, "the error signal," is used to control a fast pneumatic

proportional valve in the frontend unit. This proportional valve modulates the air pressure generated by the air compressor, thus causing changes in the finger cuff pressure in parallel with intra-arterial pressure in the finger so as to dynamically unload the arterial walls in the finger. The cuff pressure thus provides an indirect measure of intra-arterial pressure. The device has also a height sensor to account for the difference in pressure between the heart and the finger due to the different altitudes. From these measurements, the device is able to reconstruct the arterial blood pressure. The device is connected to a PC by a parallel port, or by four analog inputs and four analog outputs to record the different signals in a synchronized way.

Finometer works with a sampling frequency of 200 Hz, quantification of 12 bits and resolution of 0.25 mmHg/LSB. Digitalized signal is converted into an analog in the device and gets into an analog input to the interface UIM100C to be resampled and digitalized by the MP150 (with a sampling frequency of 250 Hz and 16 bits of quantification). As a consequence, this blood pressure signal is delayed 5 seconds (introduced by the DAC of the Finometer) with respect of the other signals acquired directly in the Biopac MP150.

Photoplethysmographic signal (PPG)

Pulse photoplethysmography (PPG), introduced by Hertzman (1938), is a simple and useful method for measuring the relative blood volume changes in the microvascular bed of peripheral tissues and evaluating peripheral circulation.

The PPG signal is recorded from the index finger using the Biopacs PPG100C amplifier with the TSD200 transducer with a sampling frequency of 250 Hz.

Software

The MP 150 (BIOPAC Systems) records the data with the software AcqKnowledge®3.9. The format 'acq' was converted into the MIT format with WFDB header file format.

5.3.2. Description of the Database

The database was acquired at the Centro Politécnico Superior in the University of Zaragoza and consists of 12 lead ECG, blood pressure, respiratory, PPG and expiratory pressure (EP) signals recorded from seventeen healthy volunteers (11 males and 4 females). These volunteers are aged from 25 to 33 years old, without any previous history of cardiovascular disease, and have undergone a head-up tilt test trial and three Valsalva maneuvers according to the following protocol:

- Head-up Tilt Test trial
  - 4 minutes in the supine position as shown in Fig. 5.4 (left).
  - 5 minutes in the orthostatic position at an angle of 70° as shown in Fig. 5.4 (right).
  - 4 minutes back in the supine position

Figure 5.4: Pictures of the supine and the orthostatic position at an angle of 70° degrees, which are held during the tilt test trial.

- The three Valsalva maneuvers are done in standing position as it is shown in Fig. 5.5 (left).
  - 2 minutes in the standing position
  - At the end of an expiration, straining during 15 seconds (Expiratory VM). Strain pressure of more than 40 mmHg
  - Resting in standing position 2.5 minutes
  - After a deep inspiration, straining by VM during 15 seconds (Inspiratory VM). Strain pressure of more than 40 mmHg
  - Resting in standing position 3 minutes
  - After a deep inspiration, straining by VM during 30 seconds (Long inspiratory VM). Strain pressure of more than 40 mmHg
  - Resting in standing position 2.5 minutes

The recorded signals and their sampling frequencies are:

- 12-lead ECG (1000 Hz)
- Blood pressure measured in the finger (250 Hz)
- Respiratory signal (125 Hz)
- Pulse photoplethysmography signal (250 Hz)
- Expiratory pressure (125 Hz)

Fig. 5.6 shows an example of two ECG leads, V2 and V4, the PPG signal, the respiration signal, the blood pressure signal and the expiratory signal during the recording of the inspiratory Valsalva maneuver. The beat to beat interval increases while the PPG and blood pressure signals decreases during the Valsalva strain. The respiratory signal is held, as expected, during the strain whose pressure is in this case, above 80 mmHg.

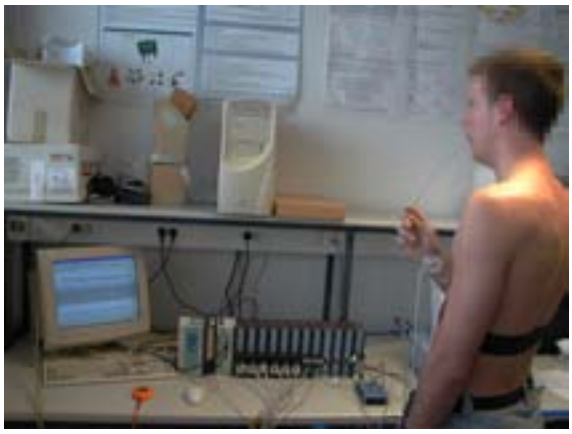

Figure 5.5: Picture of a volunteer performing the Valsalva maneuver.

5.3.3. Repolarization changes during autonomic nervous system testing

Tilt test and Valsalva maneuvers are commonly used to evaluate the autonomic nervous system (ANS) response to changes in the venous return. The autonomic system manages all internal functions such as blood pressure, blood flow, and sweating. Autonomic tests measure how the systems in the body that are controlled by the autonomic nerves respond to stimulation.

Repolarization intervals

ECG delineation is performed using a wavelet-based delineator [86]. In each subject, the lead with the highest signal to noise ratio (SNR), estimated as the maximum T wave amplitude over the RMS value of the high-frequency noise (above 25 Hz) of the interval between the ST segment to the end of the P wave, is selected. In our database, leads V2, V3 or V4 have always been the leads with highest SNR. RR, QT, T width T_w and T peak to T end T_{pe} interval series are computed from the ECG delineation marks in the selected lead, after visually examining and removing the erroneous delineation marks. The T wave amplitude T_A series computed as the difference between the ECG amplitude position at the T wave end and the one at the T wave peak, is also computed.

Head-up Tilt test

Tilt test trial is commonly used to diagnose orthostatic hypotension or syncope. When a normal person is tilted, blood pressure does not drop dramatically because the body compensates for this posture with an increase in heart rate (HR) and constriction of the blood vessels in the legs. Therefore, the common HR signature is an abrupt increment when the person is tilted.

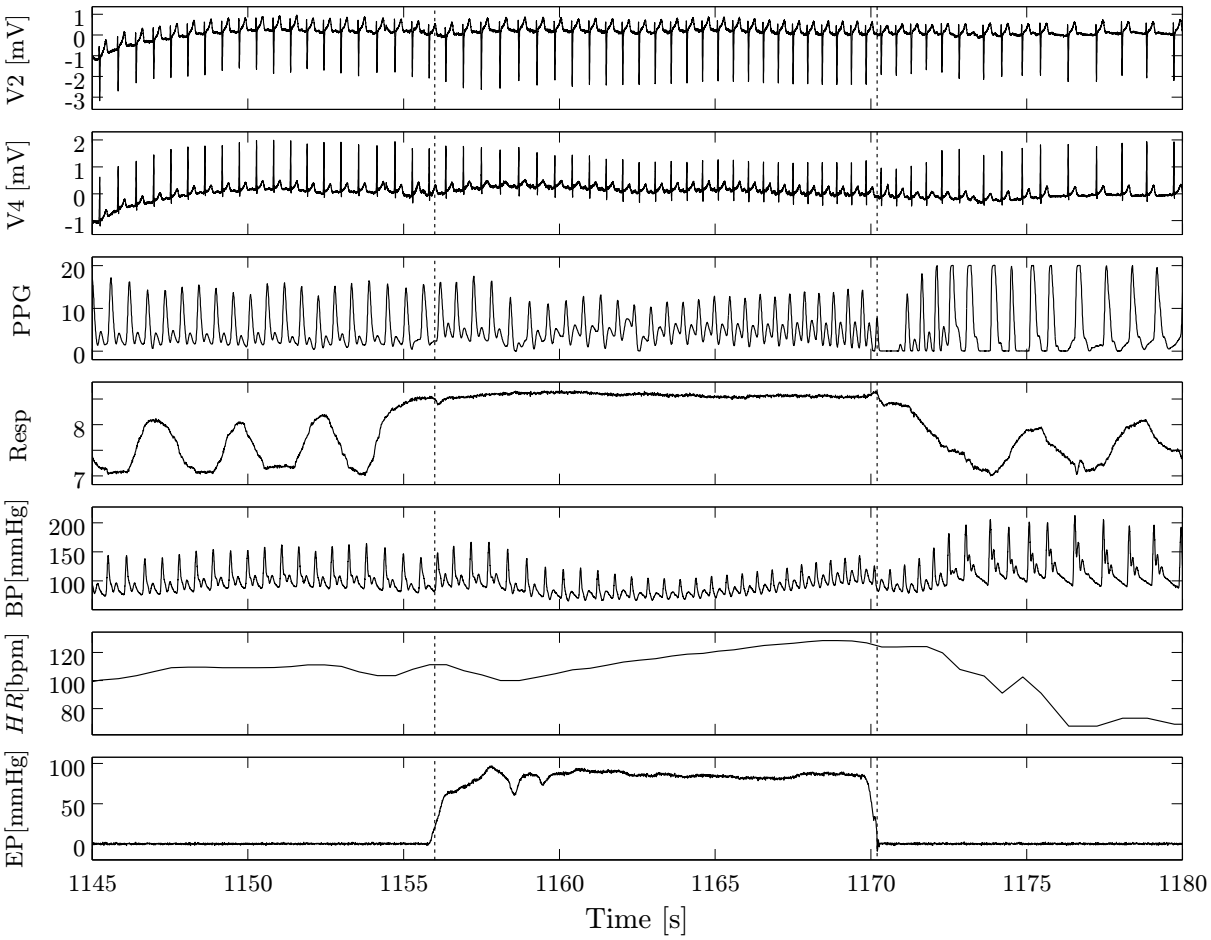

Figure 5.6: Example of some recorded signals: 2 ECG leads, V2 and V4, PPG, respiratory, blood pressure, heart rate and expiratory signals, during the inspiratory Valsalva maneuver.

An example of the repolarization interval series described before during the tilt test trial are shown in Fig. 5.7. The ECG signal changes when the person is tilted. As we described in chapter §3, body position changes produces changes in the main complexes QRS and ST-T. In the ECG signal in Fig. 5.7, it is just observed that the QRS amplitude changes. The T wave amplitude also decreases during the tilt, but this is due to the body position change which affects the whole STT complex. The HR increases during the orthostatic position at 70° as expected, to compensate for the blood pressure drop. The T wave width T_w decreases during the tilt and seems to have a similar memory effect to the QT interval. QT adapts slowly to changes in heart rate as many publications have reported [1]. However the T_{pe} interval seems to adapt faster than QT interval to the abrupt HR changes generated by this tilt test protocol. This systematic observation along the database has led us to study T_{pe} rate adaptation and compare it to QT rate adaptation in chapter 6.

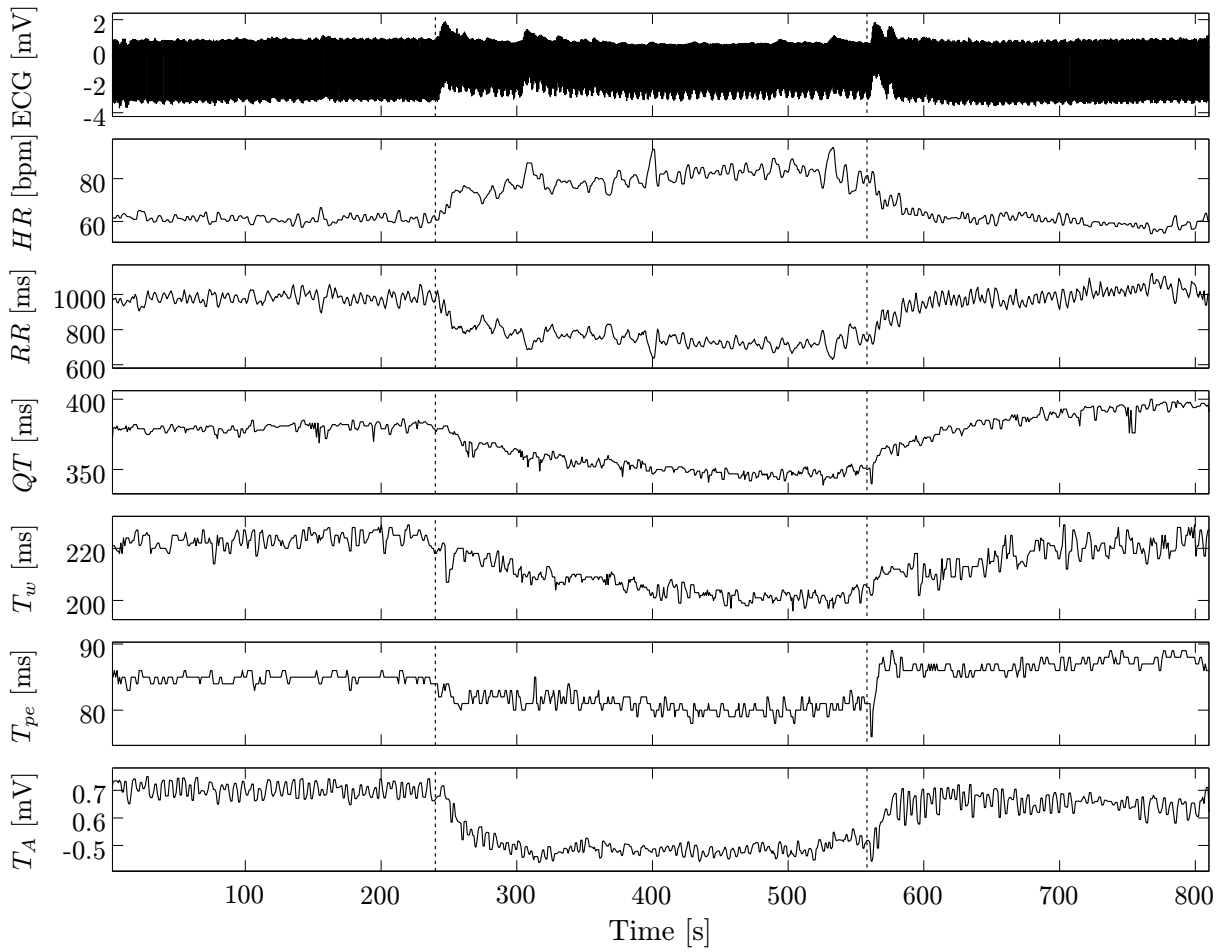

Figure 5.7: Example of different repolarization intervals and an ECG lead during the tilt test.

Valsalva maneuver

Valsalva maneuver activates both branches of the autonomic nervous system: sympathetic and parasympathetic. In healthy subject, the reflex response for the Valsalva maneuver includes tachycardia and peripheral vasoconstriction during strain, followed by an overshoot in blood pressure and bradycardia after release of strain. Therefore, this test generates also changes in the repolarization intervals which also play an important role in arrhythmogenesis.

An example of the expiratory Valsalva maneuver, where the strain starts at the end of an expiration, is shown in Fig. 5.8. The strain pressure is about 70 mmHg. HR slightly decreases 80 bpm after the strain (due to the increase in blood pressure) and then it increases during the rest of the strain and even after the strain up to more than 120 bpm to decrease abruptly afterwards to less than 60 bpm. The first HR decrease is hardly noticed in the repolarization indices. Just the T_{pe} interval changes which is in agreement with the observation of a fast response of the T_{pe} to HR changes.

The posterior increment in HR reaches more than 120 bpm due to a drop in blood pressure, make the ECG waves modify their morphology. Then, we can notice that repolarization intervals reduce their length but when HR is above 110 bpm, delineations of the T wave onset and end are affected.

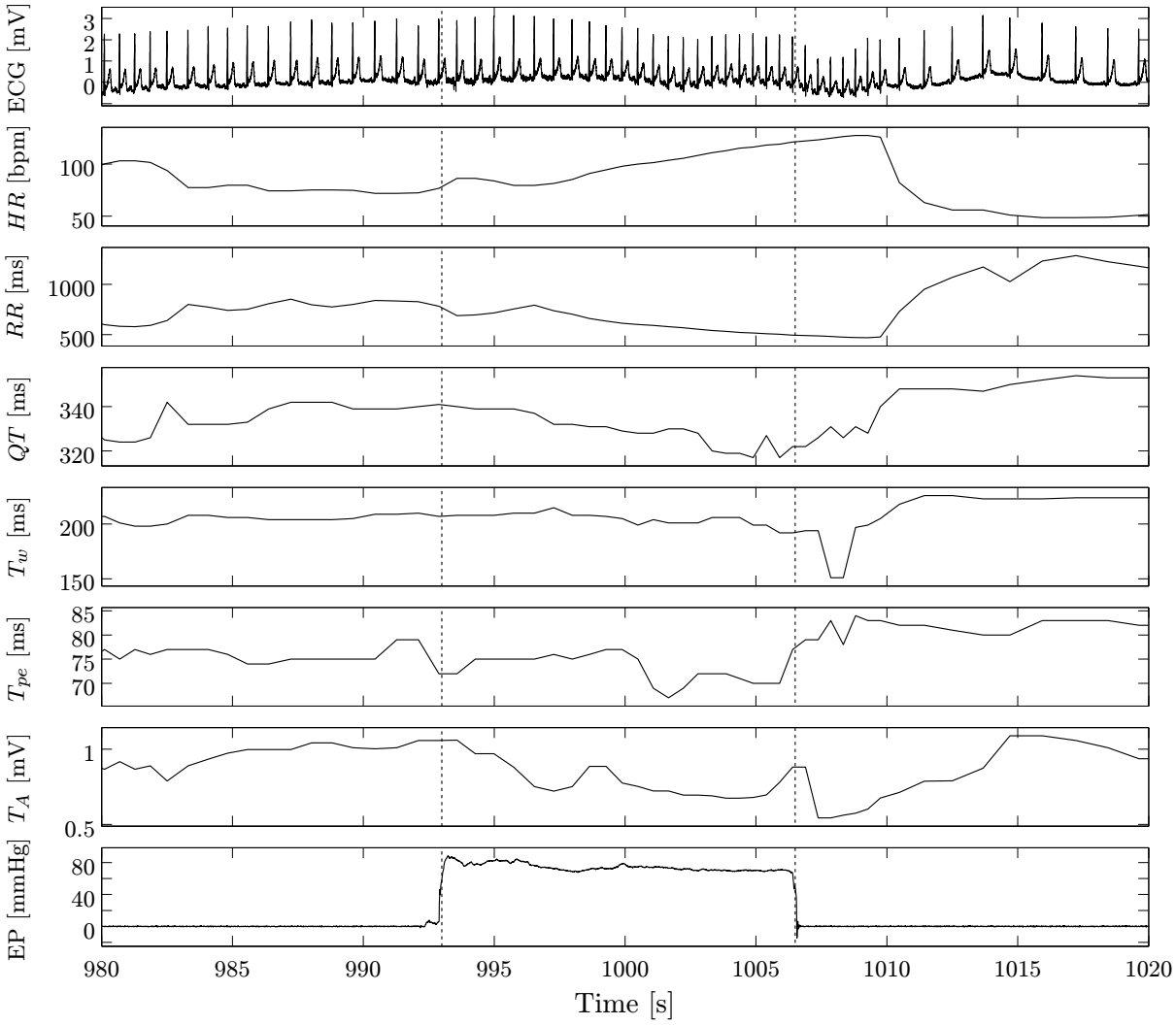

Figure 5.8: Example of different signals during the expiratory Valsalva maneuver. The ECG signal is expressed in mV, the HR in beats per minute (bpm), the RR, T_w, T_{pe} and QT intervals are expressed in ms and the expiratory pressure in mmHg.

Fig. 5.9 shows an example of the inspiratory Valsalva maneuver where the strain is done after a deep inspiration. The HR signature only differ from the expiratory Valsalva maneuver in the HR increment before the strain. In this example the expiratory pressure (EP) is about 80 mmHg, but the maximum HR reached is about 100 bpm what makes easier the delineation procedure. Then, all repolarization intervals follow the RR changes, being the T_{pe} faster in the rate adaptation than the QT interval. In this example it can be observed the respiratory sinus arrythmia, specially after the strain.

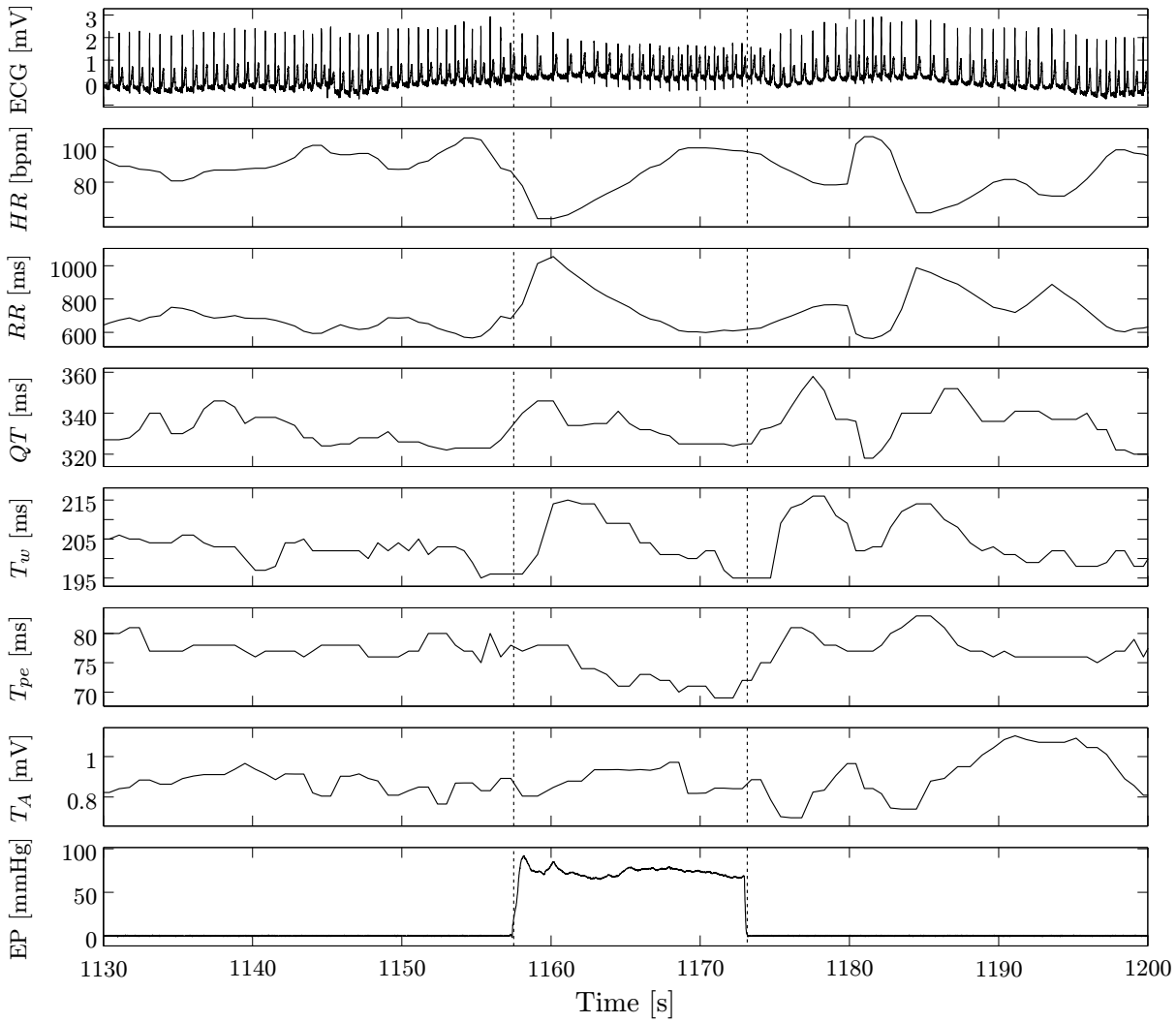

Figure 5.9: Example of different signals during the inspiratory Valsalva maneuver.

The last example in Fig. 5.10 corresponds to the long inspiratory Valsalva maneuver, where the strain is maintained during 30 seconds exerting a maximal expiration pressure. The signature is similar to the standard inspiratory maneuver but the HR decreases slightly before finishing the strain and increases again until the end. HR vary from 140 bpm to 60 bpm. Those variations make the T width series hardly follows RR changes at hight HR. In this example, a respiratory sinus arrhythmia is observed before and after the strain.

The short term changes of HR and blood pressure make the ECG waves change their morphology, so the ECG delineation is affected. We observe systematic behaviours in the repolarization intervals, but we are not able to draw definitive conclusions in Valsalva maneuver.

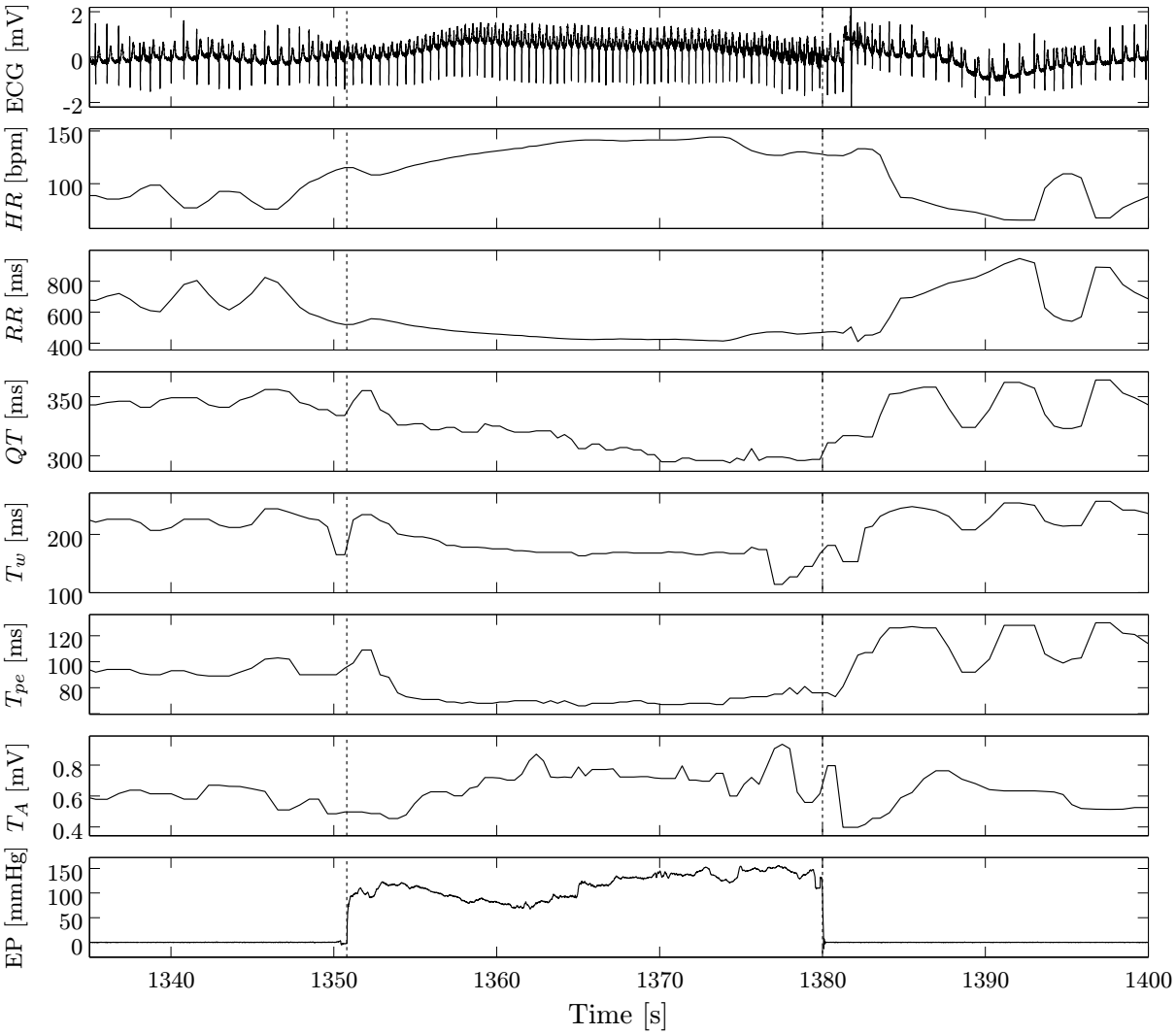

Figure 5.10: Example of an ECG signal and different repolarization intervals during the long inspiratory Valsalva maneuver.

Chapter 6

Characterization of T_{pe} rate adaptation

Clinical and experimental studies have suggested that abnormalities of ventricular repolarization, and therefore in the QT interval, play a role in the genesis of ventricular arrhythmias [102, 103]. In particular, QT interval prolongation correlates to an increased duration of cardiac action potential and has been considered as an indicator of arrhythmic risk [104]. However, there is growing evidence that an increase in action potential duration and QT interval prolongation by themselves cannot accurately predict the arrhythmic risk [105]. Besides, as QT interval is known to be influenced by changes in heart rate, the use of heart rate correction is crucial in the estimation of QT interval prolongation. QT/RR hysteresis and restitution have been investigated mostly in studies of QT interval adaptation to abrupt changes in pacing rate [106]. QT interval and action potential duration (APD) response to an abrupt change in HR are characterized by two phases: an initial fast adaptation and a subsequent slow adaptation as reported in [107, 106]. Studies of this QT response suggest that longer time lags in the QT rate adaptation have been associated to the propensity of suffering ventricular arrhythmias [108]. Other QT related indices, such as the temporal QT variability has been studied as markers of the clinical risk of drug-induced proarrhythmia in dogs [109].

Other ECG markers have been proposed in the last years; most of them related to the T wave, and specially in the last part of it, the interval between the T wave peak and the T wave end (T_{pe}) [110]. T_{pe} interval has been suggested to be a predictor of ventricular arrhythmias in an increasing number of studies involving animal and human data. Spatial heterogeneity in cardiac repolarization can mainly be assessed through changes in T wave morphology in particular in its descending limb [111]. In turn, these changes can result in electrical re-entry and the triggering of arrhythmic events such as Torsades de Pointes (TdP) [112].

As QT interval, prolonged T_{pe} interval has been found in patients with hypertrophic cardiomyopathy [113, 114], inducible ventricular tachycardias VT [111] and long QT syndrome (LQTS) [115] and also in arrhythmic events in patients with Brugada syndrome [116]. Furthermore, T_{pe} has been suggested to be a predictor of arrhythmias such as

Torsades de Pointes (TdP) [115].

Differences in the time course of repolarization of the different cells in the myocardium cell types have been shown to contribute to the inscription of the T wave of the electrocardiogram (ECG). T_{pe} interval is generally accepted to reflect differences in the time for completion of repolarization at different regions in the ventricle and it is used clinically as a measure of dispersion of repolarization [111, 115]. Some studies have proposed T_{pe} as an index of transmural dispersion of repolarization [117, 118], while others have claimed that T_{pe} does not correlate only with transmural dispersion of repolarization but it also includes other heterogeneities, such as apico-basal ones [119, 120]. Anyway, changes in this parameter are thought to be capable of reflecting changes in spatial dispersion of repolarization, and thus may be prognostic of arrhythmic risk under a variety of conditions [118].

The rate dependence of T_{pe} interval is still an issue. Previous studies characterizing T_{pe} rate dependence are controversial, with T_{pe} shown to be independent of HR by some authors [121] and markedly HR dependent by others [122]. In this study we characterize T_{pe} rate adaptation, and compare it with QT rate adaptation.

In brief, dispersion in repolarization has been associated with life-threatening arrhythmias [123] as well as restitution characteristics of the tissue which are very important in the occurrence of reentry [124]. Therefore, the study of the rate adaptation of the T peak to T end interval is well motivated.

6.1. Methods

6.1.1. Mathematical formulation

The model shown in Fig. 6.1, previously proposed to quantify QT rate adaptation [108], is used to characterize the T_{pe} dependence on RR. The input $x_{\mathrm{RR}}[n]$ and output $y_{T_{pe}}[n]$ denote the RR and the T_{pe} series of each recording after interpolation and resampling to a sampling frequency of $f_s = 1$ Hz.

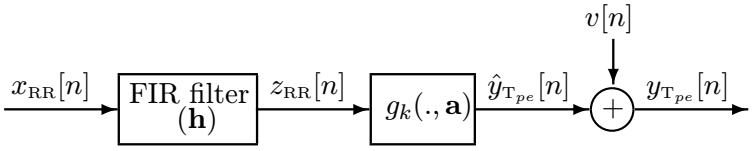

Figure 6.1: Block diagram describing the [RR, T_{pe}] relationship consisting of a time invariant FIR filter (impulse response $\mathbf{h}$) and a nonlinear function $g_k(., \mathbf{a})$ described by the parameter vector $\mathbf{a}$. $v[n]$ accounts for the modeling error.

The first block corresponds to a time invariant N-order FIR filter with impulse response:

$$\mathbf{h} = (h[1] \ ... \ h[N])^T \in \mathbb{R}^{\mathrm{N}} \tag{6.1}$$

and with an output denoted by $z_{\mathrm{RR}}[n]$. Impulse response $\mathbf{h}$ includes information about the memory of the system, that is, a characterization of the influence of a history of previous RR intervals on each T_{pe} measurement. Therefore, $z_{\mathrm{RR}}[n]$ represents a surrogate of $x_{\mathrm{RR}}[n]$ with the memory effect of T_{pe} compensated for.

The length N of vector $\mathbf{h}$ was set to 150 samples that correspond to 150 seconds, which widely exceeds the T_{pe} and the QT memory lag for the data population used in this study. N also agrees with [5] which claim that on average, RR intervals of the past 150 beats (approximately 2.5 min) are required to model the QT response accurately.

The second block is the function $g_k(., \mathbf{a})$ which is dependent on the biparameter vector:

$$\mathbf{a} = [a_0 \; a_1]^T \in \mathbb{R}^2 \tag{6.2}$$

$g_k(., \mathbf{a})$ represents the relationship between the RR interval and the T_{pe} interval once the memory effect has been compensated for (i.e. under stationary conditions), and it is particularized and optimized for each subject using one (k) of the ten regression models described below.

The output of the model $\hat{y}_{\mathrm{T}_{pe}}[n]$ is defined as:

$$\hat{y}_{\mathrm{T}_{pe}}[n] = g_k(z_{\mathrm{RR}}[n], \mathbf{a}) \tag{6.3}$$

In vector notation, $\mathbf{z}_{\mathrm{RR}}$, is the convolution between the input vector $\mathbf{x}_{\mathrm{RR}}$ and the impulse response $\mathbf{h}$, and can be expressed as:

$$\mathbf{z}_{\mathrm{RR}} = \mathbf{x}_{\mathrm{RR}} * \mathbf{h} = \mathbf{h} * \mathbf{x}_{\mathrm{RR}} = \mathbf{X}_{\mathrm{RR}}\mathbf{h} \tag{6.4}$$

where $\mathbf{X}_{\mathrm{RR}}$ is the convolution (Toeplitz) matrix of $\mathbf{x}_{\mathrm{RR}}$:

$$\mathbf{X}_{\mathrm{RR}} = \begin{bmatrix} x_{\mathrm{RR}}[N] & x_{\mathrm{RR}}[N-1] & \dots & x_{\mathrm{RR}}[2] & x_{\mathrm{RR}}[1] \\ x_{\mathrm{RR}}[N+1] & x_{\mathrm{RR}}[N] & \ddots & & x_{\mathrm{RR}}[2] \\ \vdots & \ddots & \ddots & & \\ x_{\mathrm{RR}}[D-1] & & & & \vdots \\ x_{\mathrm{RR}}[D] & x_{\mathrm{RR}}[D-1] & \dots & x_{\mathrm{RR}}[D-N+2] & x_{\mathrm{RR}}[D-N+1] \end{bmatrix} \tag{6.5}$$

Note that $\mathbf{X}_{\mathrm{RR}}$ is a $(D-N)$xN matrix, where N is the length of the filter $\mathbf{h}$ and D is the length of the signal $x_{\mathrm{RR}}[n]$.

Ten different biparametric regression models that span from a linear to a hyperbolic relationship, as described in [108], are considered for $g_k(., \mathbf{a})$, and the one that best fits the data of each subject is identified.

$$\text{Linear: } y_{\mathrm{T}_{pe}}[n] = g_1(z_{\mathrm{RR}}[n], \mathbf{a}) = a_0 + a_1 z_{\mathrm{RR}}[n] \tag{6.6}$$

$$\text{Hyperbolic: } y_{\mathrm{T}_{pe}}[n] = g_2(z_{\mathrm{RR}}[n], \mathbf{a}) = a_0 + \frac{a_1}{z_{\mathrm{RR}}[n]} \tag{6.7}$$

$$\text{Parabolic: } y_{\mathrm{T}_{pe}}[n] = g_3(z_{\mathrm{RR}}[n], \mathbf{a}) = a_0\, z_{\mathrm{RR}}[n]^{a_1} \tag{6.8}$$

$$\text{Logarithmic: } y_{\mathrm{T}_{pe}}[n] = g_4(z_{\mathrm{RR}}[n], \mathbf{a}) = a_0 + a_1\, \log(z_{\mathrm{RR}}[n]) \tag{6.9}$$

$$\text{Shifted Logarithmic: } y_{\mathrm{T}_{pe}}[n] = g_5(z_{\mathrm{RR}}[n], \mathbf{a}) = \log(a_0 + a_1\, z_{\mathrm{RR}}[n]) \tag{6.10}$$

$$\text{Exponential: } y_{\mathrm{T}_{pe}}[n] = g_6(z_{\mathrm{RR}}[n], \mathbf{a}) = a_0 + a_1\, \exp(-z_{\mathrm{RR}}[n]) \tag{6.11}$$

$$\text{Arc tangent: } y_{\mathrm{T}_{pe}}[n] = g_7(z_{\mathrm{RR}}[n], \mathbf{a}) = a_0 + a_1\, \arctan(z_{\mathrm{RR}}[n]) \tag{6.12}$$

$$\text{Tangent Hyperbolic: } y_{\mathrm{T}_{pe}}[n] = g_8(z_{\mathrm{RR}}[n], \mathbf{a}) = a_0 + a_1\, \tanh(z_{\mathrm{RR}}[n]) \tag{6.13}$$

$$\text{Arc sin hyperbolic: } y_{\mathrm{T}_{pe}}[n] = g_9(z_{\mathrm{RR}}[n], \mathbf{a}) = a_0 + a_1\, \mathrm{arcsinh}(z_{\mathrm{RR}}[n]) \tag{6.14}$$

$$\text{Arc cosine hyperbolic: } y_{\mathrm{T}_{pe}}[n] = g_{10}(z_{\mathrm{RR}}[n], \mathbf{a}) = a_0 + a_1\, \mathrm{arccosh}(1 + z_{\mathrm{RR}}[n]) \tag{6.15}$$

The optimum values of the FIR filter response $\mathbf{h}$, vector $\mathbf{a}$, and function g_k are searched for, by minimizing the difference between the estimated output $\hat{y}_{\mathrm{T}_{pe}}[n]$ (see (6.3)) and the T_{pe} interval series $y_{\mathrm{T}_{pe}}[n]$, for each subject independently using the whole recording.

In order to identify the system parameters, $\mathbf{h}$ and $\mathbf{a}$, the least square estimator between $\mathbf{y}_{T_{pe}}$ and $\hat{\mathbf{y}}_{T_{pe}}$, both in vector notation, is computed. To do so, the following cost function could have been minimized:

$$J(\mathbf{h}, \mathbf{a}) = \left\| \mathbf{y}_{T_{pe}} - \hat{\mathbf{y}}_{T_{pe}} \right\|^2 \tag{6.16}$$

However, as described in [108], this optimization problem is an 'ill-posed' problem which can have multiple solutions. When dealing with 'ill-posed' problems, a regularization term including a priori information of the solution, can be added. This study uses the Tikhonov regularization [125].

In previous studies, rate dependence of QT and action potential duration (APD) of myocardial cells have been modelled as exponential decays. As T_{pe} accounts for differences in the repolarization times, we propose to regularize, penalizing the deviations of $\mathbf{h}$ from having an exponential decay.

To measure this deviation, we propose to use the same Tikhonov matrix used for regularizing the QT rate adaptation [126]:

$$\mathbf{D} = \begin{bmatrix} \tau & -1 & 0 & \dots & \dots & 0 \\ 0 & \tau & -1 & 0 & \dots & 0 \\ \vdots & 0 & \tau & -1 & & \\ \vdots & \vdots & & \ddots & \ddots & \\ 0 & 0 & 0 & & \tau & -1 \end{bmatrix} \tag{6.17}$$

Note that in case of $\mathbf{h}$ having an exponential decay expressed as $h[n] = e^{-\lambda n} = \tau^n$, then $\|\mathbf{Dh}\| = 0$.

In order to calculate τ, $\mathbf{h}$ is initialized as an exponential function $h[n] = \tau^n$, where the parameter τ is swept from 0 to 1. For each of these $\mathbf{h}$ vectors, a_0 and a_1 are estimated using the linear regression model g_1. The τ value which generates the minimum mean square error between $\mathbf{y}_{T_{pe}}$ and $\hat{\mathbf{y}}_{T_{pe}}$ is selected to define the regularization matrix $\mathbf{D}$. To reduce the number of steps in the optimization stage, $\mathbf{h}$, a_0 and a_1 are initialized using τ.

Then, the estimator used for the optimization is a regularized least square estimator:

$$\begin{aligned}\{\mathbf{h}^*, \mathbf{a}^*, k^*\} &= \arg\min_{\{\mathbf{h},\mathbf{a},k\}} \left(\left\| \mathbf{y}_{T_{pe}} - \hat{\mathbf{y}}_{T_{pe}} \right\|^2 + \beta^2 \left\| \mathbf{D}\mathbf{h} \right\|^2 \right) \\ &= \arg\min_{\{\mathbf{h},\mathbf{a},k\}} \left(\left\| \mathbf{y}_{T_{pe}} - g_k(\mathbf{z}_{\mathrm{RR}}, \mathbf{a}) \right\|^2 + \beta^2 \left\| \mathbf{D}\mathbf{h} \right\|^2 \right) \end{aligned} \tag{6.18}$$

where β is the regularization parameter which control how much weight is given to the energy of $\|\mathbf{D}\mathbf{h}\|$ relative to the energy of the residual $\left\|\mathbf{y}_{T_{pe}} - \hat{\mathbf{y}}_{T_{pe}}\right\|$, and whose value is obtained by using the "L-curve" criterion [127]. L-curve plots the relation between the regularization term ($\|\mathbf{D}\mathbf{h}\|$) and the residual term ($\left\|\mathbf{y}_{T_{pe}} - \hat{\mathbf{y}}_{T_{pe}}\right\|$) for a range of β. This plot has a characteristic L-shaped corner that correspond to a tradeoff between both and that value for β is selected (see Fig. 6.2).

Regarding k^* in (6.18), in order to account for the inter-subject variability in the $[RR, T_{pe}]$ relationship, the regression function $g_k(., \mathbf{a})$ is determined as the one that minimizes the mean square error for each subject independently. Then, the cost function to be minimized for each regression function is:

$$J(\mathbf{h}, \mathbf{a}) = \left\| \mathbf{y}_{T_{pe}} - \hat{\mathbf{y}}_{T_{pe}} \right\|^2 + \beta^2 \left\| \mathbf{D}\mathbf{h} \right\|^2 \tag{6.19}$$

where the first term corresponds to the residual energy of the model and the second one corresponds to the regularization energy. Note that $\hat{\mathbf{y}}_{T_{pe}}(\mathbf{h}, \mathbf{a}) = g_k(\mathbf{z}_{\mathrm{RR}}, \mathbf{a})$, with k corresponding to the k^{th} regression model.

Restrictions: The estimation of $\mathbf{h}$ is subject to two constraints: the sum of the $\mathbf{h}$ components is 1 ($\sum_{i=1}^{N} h[i] = 1$), to ensure normalized filter gain, and all the components of $\mathbf{h}$ are non-negative ($h[i] \geq 0$), to give a physiological plausible interpretation.

In [108], the way of minimizing the cost function 6.19 was using a global optimization technique DiRect [128], and then projecting to obtain $h[i] \geq 0$. In this work we have reformulated $\mathbf{h}$, in order to incorporate both constraints into the cost function, and we have used a "Quasi-Newton" optimization method to minimize the new cost function. This is shown in section §6.1.2.

6.1.2. Optimization including restrictions

As described in the previous subsection, for each recording and each regression model, the optimum $\mathbf{h}^*$ and $\mathbf{a}^*$ are estimated by minimizing the cost function in equation 6.19.

The estimation of $\mathbf{h}$ is subject to two constraints: the sum of the $\mathbf{h}$ components is 1 ($\sum_{i=1}^{N} h[i] = 1$) and all the components of $\mathbf{h}$ are non-negative ($h[i] \geq 0$). The inclusion

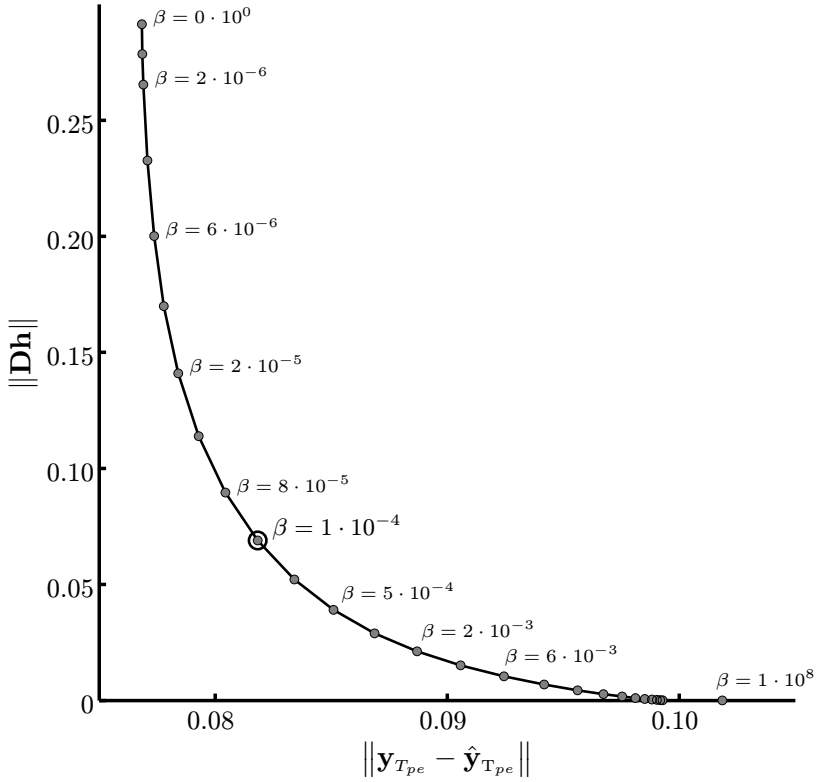

Figure 6.2: Example of a L-curve which represents the relation between the regularization term $\|\mathbf{Dh}\|$ and the residual term $\left\|\mathbf{y}_{T_{pe}} - \hat{\mathbf{y}}_{\mathrm{T}_{pe}}\right\|$. The selected β is also shown.

of both constraints in the estimation of $\mathbf{h}$ is done in this study by defining $h[i] = \frac{\tilde{h}[i]^2}{\sum \tilde{h}[i]^2}$, and optimizing over $\tilde{\mathbf{h}}$ without any constraints. Note that for notation simplicity, we use $\sum \tilde{h}[i]^2 \equiv \sum_{i=1}^{N} \tilde{h}[i]^2$

Then, we use a function:

$$\tilde{J}(\tilde{\mathbf{h}}, \mathbf{a}) = J\left(\frac{\tilde{\mathbf{h}}^2}{\sum \tilde{h}[i]^2}, \mathbf{a}\right) \quad \text{with } h[i] = \frac{\tilde{h}[i]^2}{\sum \tilde{h}[i]^2} \tag{6.20}$$

defined in the whole domain, and over which, unconstrained optimization techniques can be used. Note that $\tilde{\mathbf{h}}^2$ is defined as $\tilde{\mathbf{h}}^2 = \left[\tilde{h}[1]^2, \tilde{h}[2]^2, \ldots, \tilde{h}[N]^2\right]$.

The new cost function ($\tilde{J}$) is optimized over $\tilde{\mathbf{h}}$ and over $\mathbf{a}$. The estimated $\hat{\mathbf{y}}_{T_{pe}}$ depends on the regression function g_k ($\hat{\mathbf{y}}_{T_{pe}} = g_k(\mathbf{z}_{\mathrm{RR}}, \mathbf{a})$), which depends on $\mathbf{h}$ by the relationship $\mathbf{z}_{\mathrm{RR}} = \mathbf{x}_{\mathrm{RR}} * \mathbf{h}$. Then, in order to differentiate the cost function $\tilde{J}$ with respect to the first

variable vector $\tilde{\mathbf{h}}$, the chain rule is applied:

$$\frac{\partial \tilde{J}}{\partial \tilde{\mathbf{h}}} = \frac{\partial \tilde{J}}{\partial g_k(., \mathbf{a})} \cdot \frac{\partial g_k(., \mathbf{a})}{\partial \mathbf{h}} \cdot \frac{\partial \mathbf{h}}{\partial \tilde{\mathbf{h}}} + \beta^2 \frac{\partial \left\|\mathbf{Dh}\right\|^2}{\partial \mathbf{h}} \cdot \frac{\partial \mathbf{h}}{\partial \tilde{\mathbf{h}}} \tag{6.21}$$

where the first part is applied to estimation error and the second part is applied to the regularization term (regularization term does not depend on g_k).

- The derivative $\frac{\partial \mathbf{h}}{\partial \tilde{\mathbf{h}}}$, also called Jacobian matrix, is defined as the matrix of the derivatives of a vector-valued function with respect to another vector. After a perturbation, $d\tilde{\mathbf{h}}$ of the vector $\tilde{\mathbf{h}}$, which is the effect on $\mathbf{h}$?

$$\begin{pmatrix} dh[1] \\ dh[2] \\ \vdots \\ dh[N] \end{pmatrix} = \begin{bmatrix} \frac{dh[1]}{d\tilde{h}[1]} & \frac{dh[1]}{d\tilde{h}[2]} & \cdots & \frac{dh[1]}{d\tilde{h}[N]} \\ \frac{dh[2]}{d\tilde{h}[1]} & \frac{dh[2]}{d\tilde{h}[2]} & \cdots & \frac{dh[2]}{d\tilde{h}[N]} \\ \vdots & \vdots & \ddots & \vdots \\ \frac{dh[N]}{d\tilde{h}[1]} & \frac{dh[N]}{d\tilde{h}[2]} & \cdots & \frac{dh[N]}{d\tilde{h}[N]} \end{bmatrix} \begin{pmatrix} d\tilde{h}[1] \\ d\tilde{h}[2] \\ \vdots \\ d\tilde{h}[N] \end{pmatrix}$$

  Therefore, the derivative:

$$\frac{\partial \mathbf{h}}{\partial \tilde{\mathbf{h}}} = \begin{bmatrix} \frac{dh[1]}{d\tilde{h}[1]} & \cdots & \frac{dh[1]}{d\tilde{h}[N]} \\ \vdots & \ddots & \vdots \\ \frac{dh[N]}{d\tilde{h}[1]} & \cdots & \frac{dh[N]}{d\tilde{h}[N]} \end{bmatrix} = \begin{bmatrix} \frac{2\tilde{h}[1]\sum \tilde{h}[i]^2 - 2\tilde{h}[1]^3}{(\sum \tilde{h}[i]^2)^2} & \cdots & \frac{-2\tilde{h}[N]\tilde{h}[1]^2}{(\sum \tilde{h}[i]^2)^2} \\ \vdots & \ddots & \vdots \\ \frac{-2\tilde{h}[1]\tilde{h}[N]^2}{(\sum \tilde{h}[i]^2)^2} & \cdots & \frac{2\tilde{h}[N]\sum \tilde{h}[i]^2 - 2\tilde{h}[N]^3}{(\sum \tilde{h}[i]^2)^2} \end{bmatrix} \tag{6.22}$$

- Calculation of $\frac{\partial \tilde{J}}{\partial g_k(.,\mathbf{a})}$:

$$\begin{aligned} \tilde{J} &= \left\|\mathbf{y}_{T_{pe}} - \hat{\mathbf{y}}_{T_{pe}}(\mathbf{h}, a_0, a_1)\right\|^2 + \beta^2 \left\|\mathbf{Dh}\right\|^2 = \\ &= \left\|\mathbf{y}_{T_{pe}} - g_k(\mathbf{z}_{\mathrm{RR}}, \mathbf{a})\right\|^2 + \beta^2 \left\|\mathbf{Dh}\right\|^2 = \\ &= (\mathbf{y}_{T_{pe}} - g_k(\mathbf{z}_{\mathrm{RR}}, \mathbf{a}))^T (\mathbf{y}_{T_{pe}} - g_k(\mathbf{z}_{\mathrm{RR}}, \mathbf{a})) + \beta^2 (\mathbf{Dh})^T (\mathbf{Dh}) \end{aligned}$$

  Therefore [1],

$$\frac{\partial \tilde{J}}{\partial g_k(., \mathbf{a})} = -2 \cdot (\mathbf{y}_{T_{pe}} - g_k(\mathbf{z}_{\mathrm{RR}}, \mathbf{a}))^T \tag{6.23}$$

- Calculation of $\frac{\partial g_k(.,\mathbf{a})}{\partial \mathbf{h}}$:

  Taking into account that g_k depends on $\mathbf{z}_{\mathrm{RR}}$, and $\mathbf{z}_{\mathrm{RR}} = \mathbf{x}_{\mathrm{RR}} * \mathbf{h} = \mathbf{h} * \mathbf{x}_{\mathrm{RR}}$ on $\mathbf{h}$ (this convolution can be written as a product using the convolution (Toeplitz) matrix of $\mathbf{x}_{\mathrm{RR}}$ ($\mathbf{X}_{\mathrm{RR}}$), resulting that $\mathbf{z}_{\mathrm{RR}} = \mathbf{X}_{\mathrm{RR}}\mathbf{h}$):

$$\frac{\partial g_k(\mathbf{z}_{\mathrm{RR}}, \mathbf{a})}{\partial \mathbf{h}} = \frac{\partial g_k(\mathbf{z}_{\mathrm{RR}}, \mathbf{a})}{\partial \mathbf{z}_{\mathrm{RR}}} \cdot \frac{\partial \mathbf{z}_{\mathrm{RR}}}{\partial \mathbf{h}} = \frac{\partial g_k(\mathbf{z}_{\mathrm{RR}}, \mathbf{a})}{\partial \mathbf{z}_{\mathrm{RR}}} \cdot \mathbf{X}_{\mathrm{RR}} \tag{6.24}$$

[1] $d(Ax+b)^T(Ax+b) = 2(Ax+b)^T A\, dx$, where A is a matrix and x and b are vectors.

$\frac{\partial g_k(\mathbf{z}_{\mathrm{RR}},\mathbf{a})}{\partial \mathbf{z}_{\mathrm{RR}}}$ is a matrix since $\partial g_k(\mathbf{z}_{\mathrm{RR}},\mathbf{a})$ and $\partial \mathbf{z}_{\mathrm{RR}}$ are vectors. Besides, a perturbation of the i^{th} element of the vector $\mathbf{z}_{\mathrm{RR}}$, produces an effect only on the i^{th} element of the vector $g_k(\mathbf{z}_{\mathrm{RR}},\mathbf{a})$, and then $\frac{\partial g_k(\mathbf{z}_{\mathrm{RR}},\mathbf{a})}{\partial \mathbf{z}_{\mathrm{RR}}}$ is a diagonal matrix. Then, the diagonal of $\frac{\partial g_k(\mathbf{z}_{\mathrm{RR}},\mathbf{a})}{\partial \mathbf{z}_{\mathrm{RR}}}$ is calculated for the ten regression models as shown in Table 6.1.

MODEL (g_k)		$\mathrm{diag}\left(\frac{\partial g_k(.,\mathbf{a})}{\partial \mathbf{z}_{\mathrm{RR}}}\right)$	$\frac{\partial g_k(.,\mathbf{a})}{\partial a_0}$	$\frac{\partial g_k(.,\mathbf{a})}{\partial a_1}$
Linear	$a_0 + a_1\,\mathbf{z}_{\mathrm{RR}}$	$a_1\,\mathbf{1}$	$\mathbf{1}$	$\mathbf{z}_{\mathrm{RR}}$
Hyperbolic	$a_0 + \frac{a_1}{\mathbf{z}_{\mathrm{RR}}}$	$-\frac{a_1}{\mathbf{z}_{\mathrm{RR}}^2}$	$\mathbf{1}$	$\frac{1}{\mathbf{z}_{\mathrm{RR}}}$
Parabolic	$a_0\,\mathbf{z}_{\mathrm{RR}}^{a_1}$	$a_0\,a_1\,\mathbf{z}_{\mathrm{RR}}^{(a_1-1)}$	$\mathbf{z}_{\mathrm{RR}}^{a_1}$	$a_0\log(\mathbf{z}_{\mathrm{RR}})\,\mathbf{z}_{\mathrm{RR}}^{a_1}$
Logarithmic	$a_0 + a_1\,\log(\mathbf{z}_{\mathrm{RR}})$	$\frac{a_1}{\mathbf{z}_{\mathrm{RR}}}$	$\mathbf{1}$	$\log(\mathbf{z}_{\mathrm{RR}})$
Shifted log	$\log(a_0 + a_1\,\mathbf{z}_{\mathrm{RR}})$	$\frac{a_1}{(a_0+a_1\cdot\mathbf{z}_{\mathrm{RR}})}$	$\frac{1}{a_0+a_1\,\mathbf{z}_{\mathrm{RR}}}$	$\frac{\mathbf{z}_{\mathrm{RR}}}{a_0+a_1\,\mathbf{z}_{\mathrm{RR}}}$
Exponential	$a_0 + a_1\,\exp(-\mathbf{z}_{\mathrm{RR}})$	$-a_1\,\exp(-\mathbf{z}_{\mathrm{RR}})$	$\mathbf{1}$	$\exp(-\mathbf{z}_{\mathrm{RR}})$
Arc tangent	$a_0 + a_1\,\arctan(\mathbf{z}_{\mathrm{RR}})$	$\frac{a_1}{1+\mathbf{z}_{\mathrm{RR}}^2}$	$\mathbf{1}$	$\arctan(\mathbf{z}_{\mathrm{RR}})$
Tan. hyp.	$a_0 + a_1\,\tanh(\mathbf{z}_{\mathrm{RR}})$	$\frac{a_1}{\cosh(\mathbf{z}_{\mathrm{RR}})^2}$	$\mathbf{1}$	$\tanh(\mathbf{z}_{\mathrm{RR}})$
Arcsin hyp	$a_0 + a_1\,\mathrm{arcsinh}(\mathbf{z}_{\mathrm{RR}})$	$\frac{a_1}{\sqrt{(1+\mathbf{z}_{\mathrm{RR}}^2)}}$	$\mathbf{1}$	$\mathrm{arcsinh}(\mathbf{z}_{\mathrm{RR}})$
Arccos hyp	$a_0 + a_1\,\mathrm{arccosh}(1+\mathbf{z}_{\mathrm{RR}})$	$\frac{a_1}{\sqrt{(\mathbf{z}_{\mathrm{RR}})}\sqrt{(2+\mathbf{z}_{\mathrm{RR}})}}$	$\mathbf{1}$	$\mathrm{arccosh}(1+\mathbf{z}_{\mathrm{RR}})$

Table 6.1: Summary of the derivatives of the different functions $g_k(\mathbf{z}_{\mathrm{RR}},\mathbf{a})$ of the ten regression models with respect to $\mathbf{z}_{\mathrm{RR}}$ and $\mathbf{a}$. $\mathrm{diag}\left(\frac{\partial g_k(.,\mathbf{a})}{\partial \mathbf{z}_{\mathrm{RR}}}\right)$ is the diagonal of the matrix $\frac{\partial g_k(.,\mathbf{a})}{\partial \mathbf{z}_{\mathrm{RR}}}$. $\mathbf{1}$ represents a N-length vector of ones. All mathematical expressions are element-wise.

- The derivative $\frac{\partial \|\mathbf{Dh}\|^2}{\partial \mathbf{h}}$:

$$\frac{\partial \left\|\mathbf{Dh}\right\|^2}{\partial \mathbf{h}} = 2(\mathbf{Dh})^T\mathbf{D} \tag{6.25}$$

Eventually, $\frac{\partial \tilde{J}}{\partial \tilde{\mathbf{h}}}$ can be computed by introducing equations 6.22, 6.23, 6.24 and 6.25 into 6.21.

In order to differentiate the cost function $\tilde{J}$ with respect to the second variable vector $\mathbf{a} = [a_0, a_1]^T$, the chain rule is also applied:

$$\frac{\partial \tilde{J}}{\partial \mathbf{a}} = \frac{\partial \tilde{J}}{\partial g_k(.,\mathbf{a})} \cdot \frac{\partial g_k(.,\mathbf{a})}{\partial \mathbf{a}} \tag{6.26}$$

The first term is already calculated in equation 6.23, while the second term is a Nx2 matrix where the first column corresponds to $\frac{\partial g_k(.,\mathbf{a})}{\partial a_0}$ and the second column to $\frac{\partial g(.,\mathbf{a})}{\partial a_1}$, both computed in Table 6.1.

The optimum values, $\mathbf{h}^*$ and $\mathbf{a}^*$ in (6.18), are determined by using a "Quasi-Newton" optimization technique described in [129] which use the gradients $\frac{\partial \tilde{J}}{\partial \tilde{\mathbf{h}}}$ and $\frac{\partial \tilde{J}}{\partial \mathbf{a}}$.

Optimization technique

In this work, a *Quasi-Newton* optimization method, the BFGS (Broyden-Fletcher-Goldfarb-Shanno), is used to minimize the cost function $\tilde{J}(\tilde{\mathbf{h}}, \mathbf{a})$ [129].

Quasi-Newton methods are from the family of the descent methods with the advantage of an improved convergence rate with respect to the widely known steepest or gradient descent. They are based on Newton methods but instead of computing the Hessian matrix (matrix of second partial derivatives) of the function to be minimized, this is estimated by analysing successive gradient vectors. Other advantages of this method with respect to Newton methods include that the hessian matrix is not required to be derived and implemented, to be inverted, and to check whether it is a positive definite matrix.

Then, the BFGS *Quasi-Newton* method estimate the Hessian (or the inverse Hessian) matrix preserving symmetry and positive definiteness. In each step, the estimation of the Hessian matrix is updated using the gradient information [129].

The BFGS method has super-linear convergence, i.e. faster than linear but slower than quadratic.

In order to compute the step size along the descent direction, obtained by the Quasi-Newton method, a *parabolic* and a *golden ratio* line searches were used [101].

6.1.3. Population

From the ANS-UZ database described in chapter 5, fifteen ECG recordings of the head-up tilt test trial (§5.3.3, are used to characterize T_{pe} rate adaptation. The protocol generates two step-like RR changes with stabilized RR intervals after each of them. 12-lead ECGs are recorded during the whole test at a sampling frequency of 1000 Hz.

ECG delineation is performed using a wavelet-based delineator [86]. In each subject, the lead with the highest signal to noise ratio (SNR), estimated as the maximum T wave amplitude over the RMS value of the high-frequency noise (above 25 Hz) of the interval between the ST segment to the end of the P wave, is selected. In the ANS-UZ database, leads V2, V3 or V4 have always been the leads with highest SNR. RR, QT and T_{pe} intervals are computed from the ECG delineation marks in the selected lead, after visually examining and removing the erroneous delineation marks.

6.1.4. Quantification of the results

T_{pe} rate dependence is characterized using the model of Fig. 6.1. The time required for T_{pe} to complete 90% of its rate adaptation, denoted by t_{90}, is computed by setting a threshold of 0.1 to the cumulative sum of the filter impulse response, $c[n]$:

$$c[n] = \sum_{i=n}^{N} h[i], \quad \text{leading to}$$

$$t_{90} = \frac{1}{f_s} \arg\max_n (c[n] > 0.1) \tag{6.27}$$

An analogous procedure is used to calculate t_{70}, t_{50} and t_{25} by replacing the threshold 0.1 in (6.27), with 0.3, 0.5 and 0.75, respectively. Note that the cumulative sum $c[n]$, represents the response of a step function to the FIR filter $h[n]$.

Additionally, the adaptation rate is quantified as $r[n] = (1-c[n])\cdot 100$, which represents the percentage of the total T_{pe} adaptation reached at time instant n.

6.2. Results

T_{pe} interval is found to have a very fast adaptation to HR changes as compared to the QT interval. Fig. 6.3 shows an example of a tilt test recording with two sudden RR changes, to which the T_{pe} interval adapts in a shorter time than the QT interval.

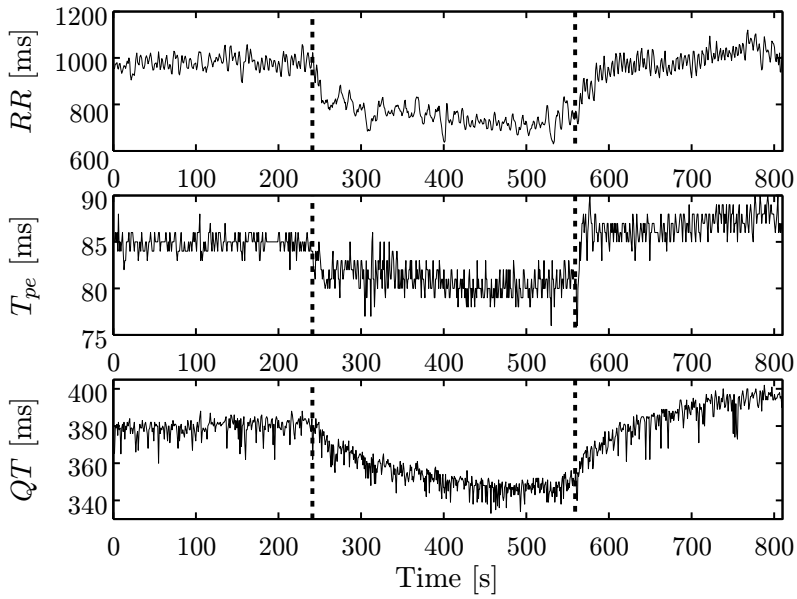

Figure 6.3: Rate adaptation of the T_{pe} and QT interval in a tilt test recording showing two abrupt RR changes.

An example of the reconstruction of the $y_{\mathrm{T}_{pe}}[n]$ and $y_{\mathrm{QT}}[n]$ series, after estimating $h[n]$, the regression model k and the coefficient vector $\mathbf{a}$ are shown in Fig. 6.4. The reconstructions $\hat{y}_{\mathrm{T}_{pe}}[n]$ and $\hat{y}_{\mathrm{QT}}[n]$, shown in black solid lines, begin after 150 seconds corresponding to the length of the filter $h[n]$. The estimated regression models in this example are different for the QT (linear model) and for the T_{pe} series (parabolic model).

The optimal regression functions $g_k(.,\mathbf{a})$ that characterize the $[z_{\mathrm{RR}}, T_{pe}]$ relationship are found to be linear, $g_k(z_{\mathrm{RR}}[n],\mathbf{a})=a_0 + a_1 \cdot z_{\mathrm{RR}}[n]$, in 33% of the recordings , hyperbolic, $g_k(z_{\mathrm{RR}}[n],\mathbf{a})=a_0 + \frac{a_1}{z_{\mathrm{RR}}[n]}$, in 20%, and hyperbolic tangent, $g_k(z_{\mathrm{RR}}[n],\mathbf{a})=a_0 + a_1 \cdot tanh(z_{\mathrm{RR}}[n])$, in 20%.

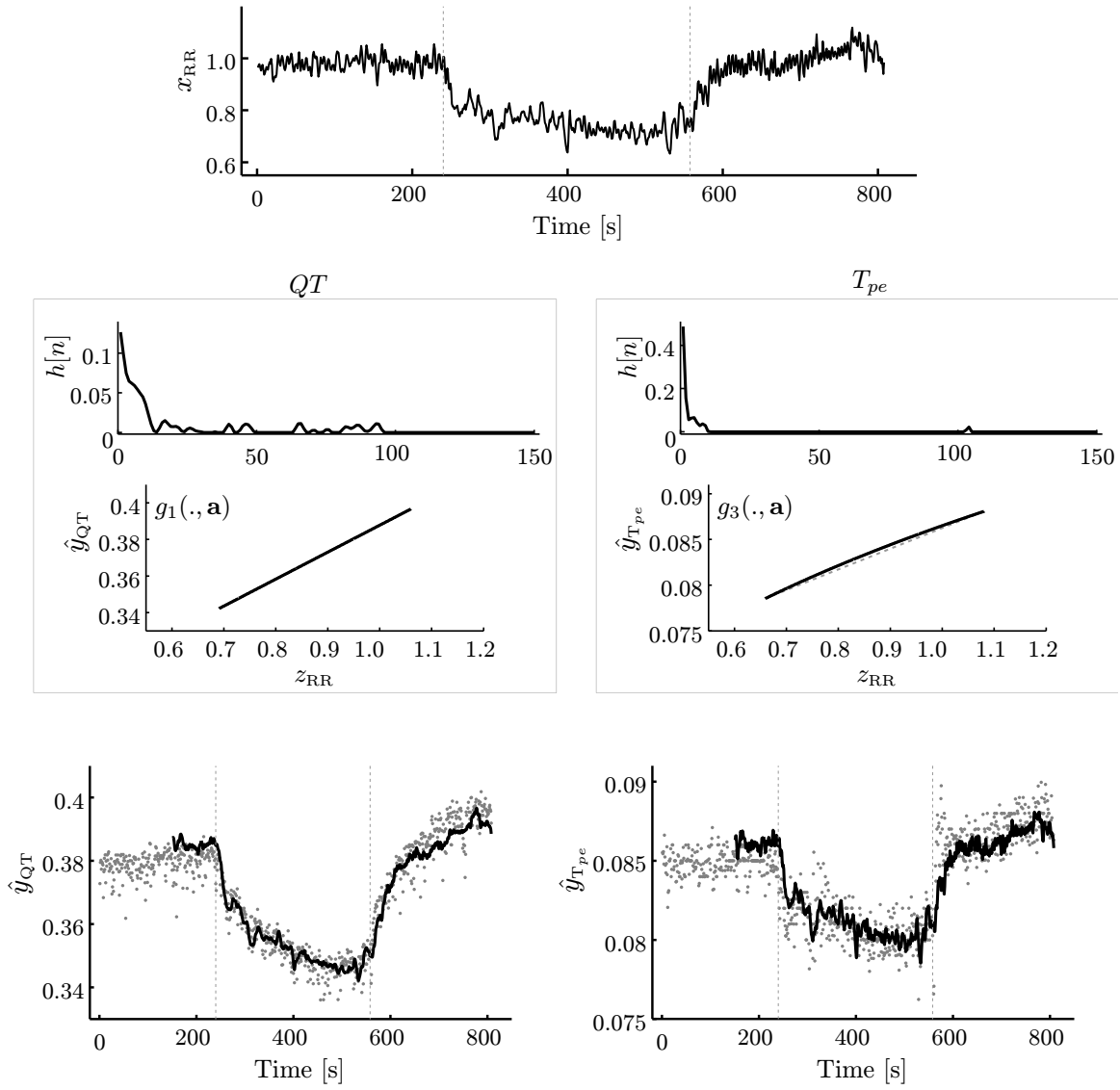

Figure 6.4: On the left, an example of how the reconstruction $\hat{y}_{\mathrm{QT}}$ (in black solid line) of the QT interval series y_{QT} (in gray dots), is obtained by x_{RR} through the estimations of $h[n]$ and $g_k(.,\mathbf{a})$. In this example, the optimum regression model for the QT interval is the linear one (k=1). In the right part, analogously for the T_{pe}, the reconstruction $\hat{y}_{\mathrm{T}_{pe}}$ (in black solid line) is shown. The optimum model regression in this case is the parabolic function (k=3). In dashed gray line, the linear function is also depicted for comparison purpose.

The adaptation profiles $h[n]$ for QT and T_{pe}, representing the memory of the system, are different as it is shown in Fig. 6.5. The initial estimations for $h[n] = \tau^n$, where τ is defined for the regularization matrix, are shown in dashed gray lines. The cumulative sums $c[n]$, which represent the filter response to a step function, are also shown in Fig.

6.5, indicating a more transient signature in the QT response with respect to the T_{pe} one. Besides, the memory lag t_{90} is longer for QT than for T_{pe} interval.

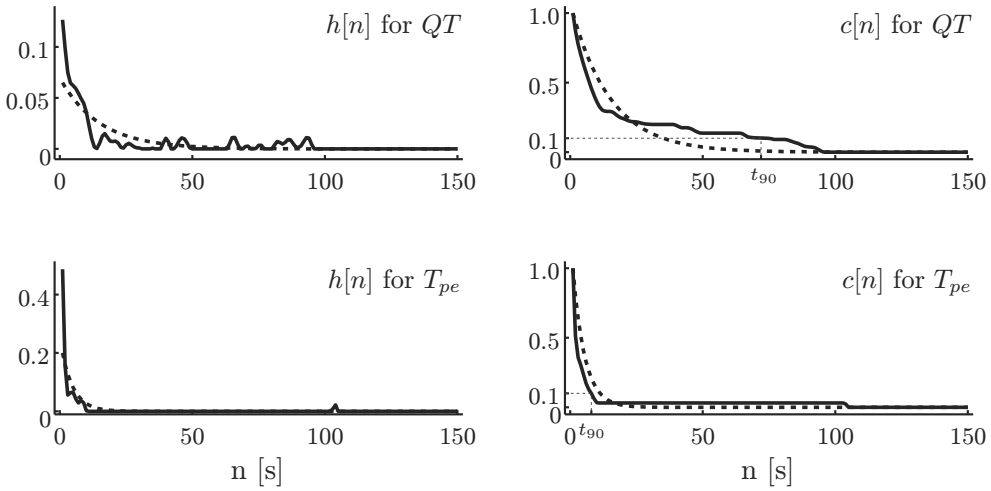

Figure 6.5: An example of the adaptation profile, $h[n]$, and its cumulative sum, $c[n]$, for the T_{pe} and QT intervals of a subject undergoing a tilt test protocol. In dashed lines, the corresponding exponential functions $h[n] = \tau^n$ used in the initialization of $h[n]$ with the τ value used in the regularization matrix. When showing $c[n]$, which represents the response of $h[n]$ to a step function, the memory lags t_{90} are also shown for both intervals.

Table 6.2 shows the mean across subjects of the time for 90% (t_{90}), 70% (t_{70}), 50% (t_{50}) and 25% (t_{25}) of the whole T_{pe} rate adaptation. Results are compared to those corresponding to the QT interval.

	QT	T_{pe}
t_{90} [s]	74.1 ± 25.4	23.5 ± 29.7
t_{70} [s]	40.8 ± 15.9	11.4 ± 16.6
t_{50} [s]	19.3 ± 8.9	5.6 ± 7.8
t_{25} [s]	4.2 ± 2.9	1.5 ± 1.9

Table 6.2: Mean ± std across subjects of the time for 90% (t_{90}), 70% (t_{70}), 50% (t_{50}) and 25% (t_{25}) of the complete rate adaptation.

In Fig. 6.6, the median, first and third quartile of the T_{pe} adaptation rate, $r[n]$ (see section §7.2.3), across the 15 recordings are shown and compared to those of the QT interval.

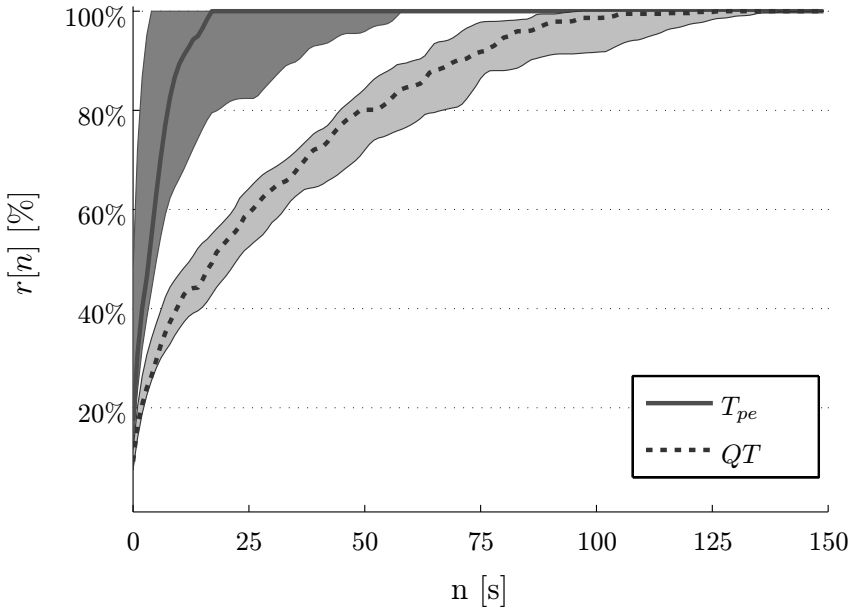

Figure 6.6: Median, first and third quartile of the adaptation rates, $r[n]$, of T_{pe} and QT intervals.

6.3. Discussion

There are clinical studies which suggest T_{pe} to be practically independent of HR [121], while other studies claim that it is markedly rate dependent [122]. An argument in favor of T_{pe} to be rate dependent is that T_{pe} interval accounts for differences of APDs in different cell regions and APDs are known to be rate related [106]. In this study, T_{pe} rate adaptation has been characterized, showing that it is rate related and it has a short memory lag.

T_{pe} takes about 25 s in mean to complete 90% of its rate adaptation and only 11 s to complete 70% of the whole adaptation. This is in contrast to QT rate adaptation, which has a pronounced memory effect, with about 74 s to complete 90% of its rate adaptation. However, this t_{90} value of 74 s in mean for the QT adaptation is lower than the t_{90} reported in [108], which is around 120 s. This may be due, among other reasons, to the younger age of the control subjects of the tilt test database used in this study. While T_{pe} dependence on a previous history of RR intervals presents a fast decay in one phase, in the case of the QT interval, the decay is performed in two phases, a fast one and a slow one, in concordance with observations from previous studies [106].

APD in ventricular myocytes (epi, mid and endocardial cells) are known to have a slow adaptation [106], which is performed in two phases: a fast initial one and a subsequent slow adaptation. In [5], APD has been shown to require around 2 min. in midmyocardial cells, and 3 min. in epicardial cells, to reach a new steady state after a step HR change. However, while the fast phases of APD rate adaptation are different in both cell types, with midmyocardial cells presenting faster decay than epicardial cells, they do have similar slow

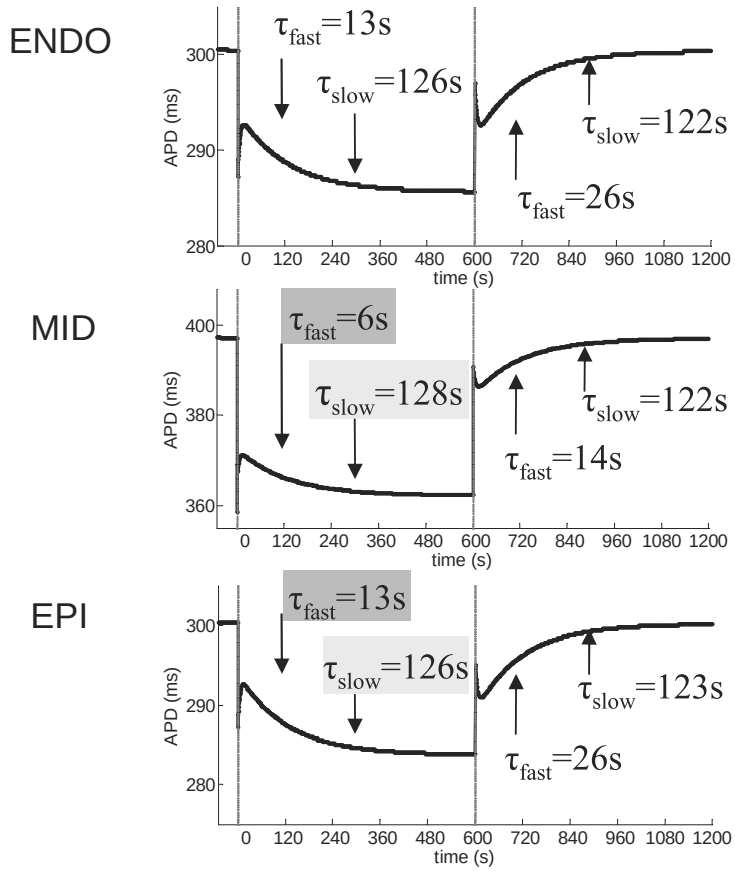

Figure 6.7: Simulated action potential (AP) duration (APD) rate adaptation in humans for CL of 1000 to 600 to 1000 ms for endocardial (Endo; top), midmyocardial (Mid; middle), and epicardial (Epi; bottom) cardiomyocytes. Data information extracted from [5].

phases (see fig. 6.7). Therefore, measures such as T_{pe}, which accounts for contributions of different cell types, would not have slow phase (it has been compensated) and the fast phase would include the maximum difference among the fast phases of the different cells in the tissue.

We should note that when characterizing T_{pe} rate adaptation, differences in heart rate accelerations and decelerations have not been accounted for. In the case of the QT interval or the APD, rate adaptation has been shown to be longer after HR decelerations than after HR accelerations [106, 5].

Chapter 7

Quantification of Restitution Dispersion measured at the surface ECG

7.1. Introduction

The underlying mechanisms of lethal arrhythmias which contribute to the primary cause of death in the industrialized world, i.e. cardiovascular disease, are poorly understood [8]. The generation of arrhythmias has been widely studied by dynamically pacing cardiac myocytes, cardiac tissue or whole hearts [130]. These experimental results have revealed that heart rate (HR) dependence of action potential duration (APD), also called restitution kinetics, is thought to be critical in activation instability and, therefore, provides relevant information for ventricular arrhythmic risk stratification [131, 132]. The dynamic APD restitution (APDR) curve, measured using the so-called dynamic restitution protocol, quantifies the relationship between the APD and the RR interval (inverse of HR) at steady-state when pacing at different RR values [133, 134].

Individual APDR curves have been reported to play an important role in the development of ventricular arrhythmias and APDR curves containing steep slopes are thought to induce alternans of APD and block propagation leading eventually to arrhythmia [135]. On the contrary, for shallow slopes, APD disturbances are smaller and eventually return to a stable activation [134]. This relationship between steeply sloped APDR curves and propensity of ventricular arrhythmia has been characterized under the condition of constant rapid pacing. However, it is unlikely that the conditions used to demonstrate this phenomenon experimentally apply to the clinical situation, where the induction of ventricular tachyarrhythmias is typically associated with the interruption of normal cardiac rhythm by only a few premature beats. Besides, several studies have reported that APD restitution is markedly heterogeneous, both on endocardium using non-contact mapping [136] and on epicardium [137] in humans, and in a guinea pig heart model [138]. Then, theories related to increased dynamic heterogeneity of repolarization have been reported [139].

Heterogeneities in the ventricle lead to non uniform restitution properties, which makes APDR curves present spatial variations [138]. Dispersion is a measure of that spatial variation. Recent studies have suggested that dispersion in the APDR curves may act as a potent arrhythmogenic substrate [137, 124]. A recent modelling study has provided further theoretical evidence that regional differences in APD restitution are an arrhythmogenic substrate that can be concealed at normal heart rates, independently of the steepness of the APD restitution curve [140]. Additionally, increments in that dispersion have been associated with greater propensity to suffer from ventricular tachycardia/fibrillation [141].

The main limitation on the usability of APDR dispersion as a risk index is that its quantification requires invasive procedures [136]. In this study we propose a method to indirectly estimate dispersion of restitution slopes by making only use of the surface electrocardiogram (ECG). We propose an ECG measure that quantifies dispersion in the dynamic APDR slopes by characterizing the relationship between the distance from T wave peak to T wave end (T_{pe}) and the RR interval under different stationary conditions.

T_{pe} interval is generally accepted to reflect differences in the time for completion of repolarization at different regions in the ventricle. Some studies have proposed that T_{pe} is an index of transmural dispersion of repolarization [117], while others have claimed that T_{pe} does not correlate only with transmural dispersion of repolarization but it also includes other heterogeneities, such as apico-basal ones [119, 120].

Each value of the APDR curve represents a stationary state corresponding to a specific HR value, and, therefore, the ECG measurement proposed to estimate restitution dispersion should in principle be computed using ECG segments of stable HR regimes. Since those type of segments are difficult to get in clinical practice, we propose to use the methodology described in chapter 6, that overcomes that restriction by modeling the dependence of the T_{pe} interval on a history of previous RR intervals and compensating for the T_{pe} memory lag.

Our proposed ECG-based estimate of APDR slope dispersion, is evaluated on a database of ECG recordings from healthy subjects undergoing a tilt test trial. In this trial, step-like heart rate changes are generated, which are used in this study to measure dynamic changes of the T_{pe}, and compute the proposed estimate.

The capability of the proposed ECG measurement to provide estimates of APDR slope dispersion at tissue level has been assessed by simulating electrical propagation in a 2D tissue representing a slice across the human left ventricular wall, and computing pseudo-ECGs. An electrophysiologically detailed human ventricular cell model, the ten Tusscher 2006 model [142], is used to generate action potentials. Pacings at different RR intervals are simulated to compute dynamic APDR curves, and eventually APDR slope dispersion.

A comparison of the proposed ECG estimate evaluated from the simulated pseudo-ECGs and from the tilt test ECG recordings shows that simulated data is in good agreement with clinical/experimental data. Additionally, using the 2D simulated data we confirm that the proposed ECG estimate is a measure of APDR slope dispersion at tissue level.

This chapter is outlined as follows: section §7.2 presents the method used to estimate APDR slope dispersion from the surface ECG and describes the 2D tissue modeling and

simulation; section §7.3 contains the results that show the capability of the proposed ECG measurement to provide estimates of the APDR slope dispersion and section §7.4 and §7.5 present the discussion and the main limitations of the study.

7.2. Materials and Methods

This section mainly includes the quantification of APDR dispersion from ECG-based estimates; and the introduction of a 2D modeling and simulation to assess the proposed estimates. Section §5.3.3 introduces the data and ECG signal processing delineation procedures. In section §7.2.2, the relationship between ventricular APDR slope dispersion, denoted by $\Delta\alpha$, and its surface ECG estimate, denoted by $\widehat{\Delta\alpha}^{\mathrm{ECG_s}}$, is presented for the case of stable RR segments (see Fig. 7.1 left). Hereinafter, "the hat" ($\widehat{\ }$) refers to estimates from the ECG. The difficulty of getting stable RR segments made us compensate for the T_{pe} memory lag after HR changes (section §7.2.3), and use it in the derivation of the ECG estimate for APDR slope dispersion for the case of unstable RR segments, denoted by $\widehat{\Delta\alpha}^{\mathrm{ECG_c}}$. In section §7.2.4, the 2D ventricular tissue model used to evaluate the extent to which ECG estimates reflect the underlying restitution dispersion is described. Simulated APDR dispersion from the 2D model, denoted by $\Delta\alpha^{\mathrm{SIM}}$, and its corresponding estimate measured from the pseudo-ECG, $\widehat{\Delta\alpha}^{\mathrm{pECG}}$, are computed (see Fig. 7.1 right).

7.2.1. Population and ECG delineation

The head-up tilt test trials of the 15 volunteers without any previous cardiovascular disease, from the ANS-UZ database described in chapter 5, have been used to compute the proposed estimations from the ECG. The protocol generates two step-like RR changes with stabilized RR intervals after each of them. 12-lead ECGs are recorded during the whole test at a sampling frequency of 1000 Hz.

ECG delineation is performed using a wavelet-based delineator [86]. In each subject, the lead with the highest signal to noise ratio (SNR), estimated as the maximum T wave amplitude over the RMS value of the high-frequency noise (above 25 Hz) of the interval between the ST segment to the end of the P wave, is selected. In the ANS-UZ database, leads V2, V3 or V4 have always been the leads with highest SNR. T_{pe} interval series is computed from the ECG delineation marks in the selected lead, after visually examining and removing the erroneous delineation marks.

7.2.2. Quantification of restitution dispersion using stable RR segments of the surface ECG

We propose a method to indirectly compute dispersion in dynamic APDR slopes within the ventricle, by making only use of the surface ECG (see Fig. 7.1, bottom-left).

T_{pe} interval reflects differences in the time for completion of repolarization by different cells spanning the ventricular wall. Therefore, and based on [124, 117], the T_{pe} interval

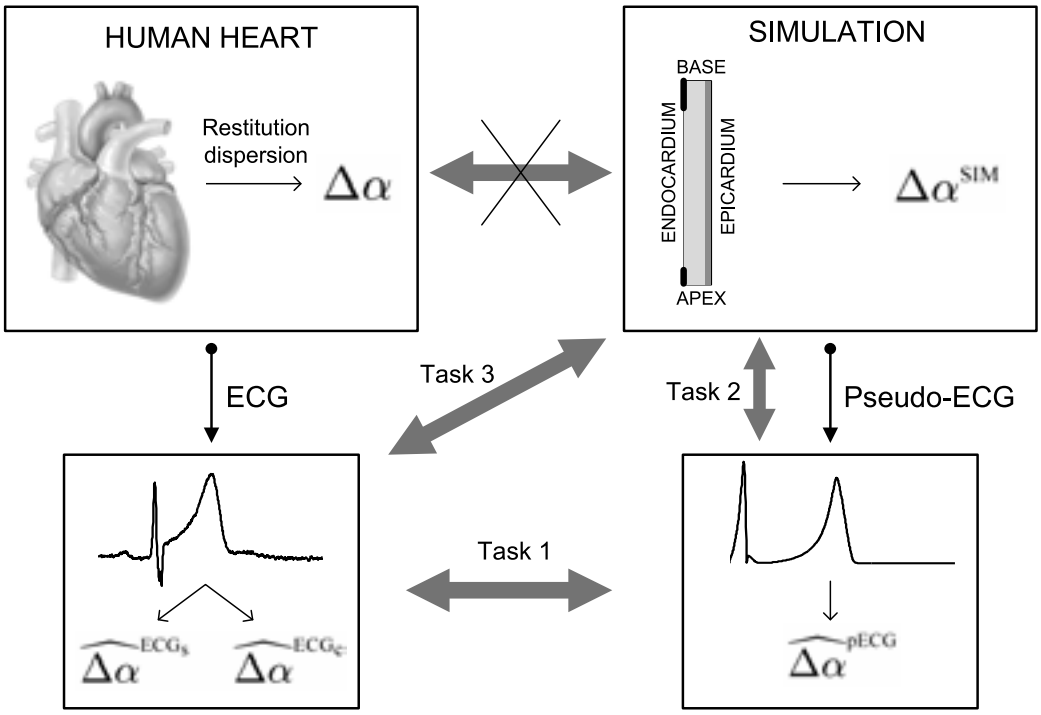

Figure 7.1: Outline of the methods used in this study. Crossed arrow shows a desirable but unaccessible connection. Tasks 1, 2 and 3 represent the different comparison tasks to be done in section §7.3. See subsections for details.

can be expressed in terms of APDs as follows:

$$T_{pe} = APD_{last} - APD_{min} - \Delta AT \tag{7.1}$$

where APD_{min} corresponds to the cell with the minimum APD among those which are currently repolarizing at the T wave peak instant (time instant when the maximum repolarization gradient sum occurs) and APD_{last} is the APD of the last cell to repolarize. ΔAT represents the activation time delay between both cells with APD_{min} and APD_{last}, as shown in Fig. 7.2. Note that in this work Δ is considered as a difference operator which is applied in this case to activation times at two spatial sites. This ΔAT delay hardly changes with RR for RR intervals above 600 ms [143, 142]. Therefore, changes in the T_{pe} under variations of the RR interval can be obtained as:

$$\frac{\partial T_{pe}}{\partial RR} = \frac{\partial APD_{last}}{\partial RR} - \frac{\partial APD_{min}}{\partial RR} \tag{7.2}$$

where $\partial\Delta AT/\partial RR$ has been neglected, under the premise that RR intervals above 600 ms are considered.

If we restrict (7.2) to the dynamic protocol, where each value of the APDR curve represents a steady-state APD value (Fig. 7.3), and the regions with APD_{min} and APD_{last}

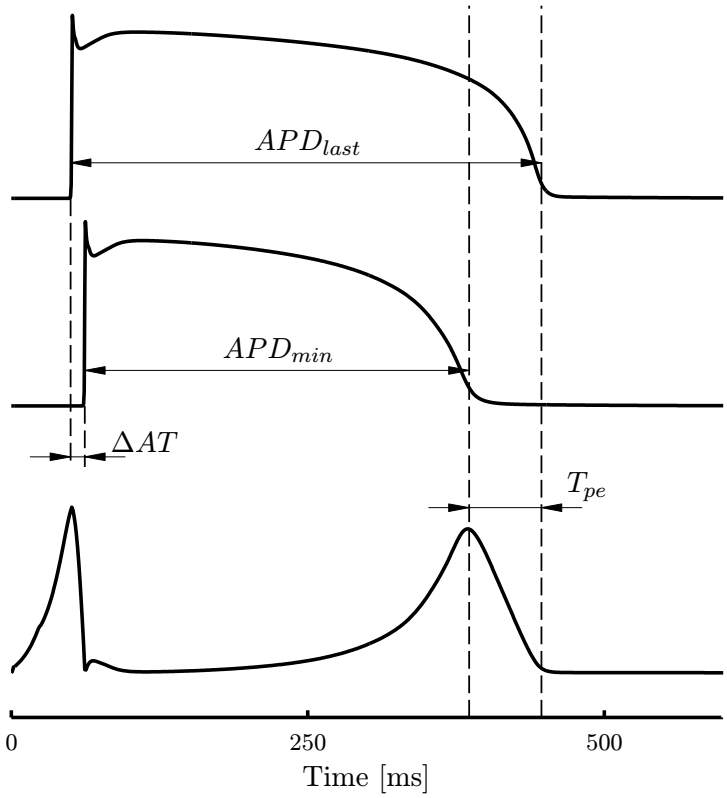

Figure 7.2: Representation of the T_{pe} interval in terms of APDs and delay of activation times (ΔAT).

remain fixed when varying RR, then:

$$\frac{\partial T_{pe}^{dyn}}{\partial RR} = \frac{\partial APD_{last}^{dyn}}{\partial RR} - \frac{\partial APD_{min}^{dyn}}{\partial RR} \tag{7.3}$$

where T_{pe}^{dyn} and APD^{dyn} refer to the steady values of T_{pe} and APD for each RR interval. Hereinafter, the superindex "*dyn*" refers to the dynamic protocol. In case of having only pairs of steady-state values, $[RR, T_{pe}^{dyn}]$, the derivatives in (7.3) may be approximated by increments Δ:

$$\frac{\partial T_{pe}^{dyn}}{\partial RR} \approx \frac{\Delta T_{pe}^{dyn}}{\Delta RR} \tag{7.4}$$

where ΔT_{pe}^{dyn} and ΔRR represent the variations in T_{pe} and RR, respectively, *between two stable ECG segments at different RR intervals.*

If we let α_{last} and α_{min} denote the slopes of the dynamic restitution curves at the regions corresponding to APD_{last} and APD_{min}, respectively:

$$\alpha_i = \frac{\partial APD_i^{dyn}}{\partial RR} \quad \text{where } i = \{last, min\}, \tag{7.5}$$

the spatial difference $\Delta\alpha = (\alpha_{last} - \alpha_{min})$ (see Fig. 7.3), which measures dispersion of restitution slopes, can be estimated from the ECG by introducing (7.5) into (7.3) and (7.4), resulting in:

$$\widehat{\Delta\alpha}^{\mathrm{ECG_s}} = \frac{\Delta T_{pe}^{dyn}}{\Delta RR} \tag{7.6}$$

where the superindex "ECG_s" indicates that quantification of restitution dispersion is done by using stable ECG segments, as required in the dynamic protocol, at two different RR intervals. Δ at left hand side of (7.6) refers to a difference of restitution slopes occurring at two regions, while both Δ at right hand side refer to beat interval differences associated with two RR levels.

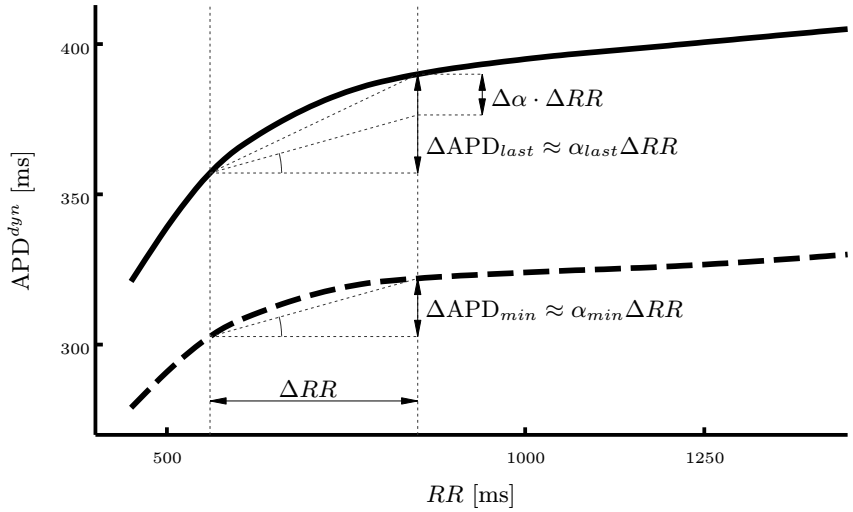

Figure 7.3: Dynamic restitution curves (APDR) in two regions corresponding to APD_{min} (dashed line) and APD_{last} (solid line). Slopes α_{min} and α_{last} are estimated for a change in the RR interval.

Note that in cases of e.g. ventricular wedges, where T_{pe} *includes mainly transmural heterogeneities*, APD_{last} and APD_{min} would correspond to APDs at the midmyocardium and epicardium, respectively, and therefore, $\widehat{\Delta\alpha}^{\mathrm{ECG_s}}$ would represent and estimation of transmural dispersion of restitution slopes.

7.2.3. Quantification of restitution dispersion using unstable RR segments of the surface ECG

Stable RR segments, needed to measure the rate related increment ΔT_{pe}^{dyn} in Eq. (7.6), are difficult to obtain in the clinical practice. In order to overcome this limitation, we use the methodology proposed in chapter 6 to compensate for the T_{pe} memory lag after RR changes. In the previous chapter we were interested in the rate adaptation of T_{pe} interval,

characterized by $\mathbf{h}$, while in this chapter we are interested in the steady-state relationship $[T_{pe}/RR]$, characterized by $g_k(z_{\mathrm{RR}}, \mathbf{a})$.

As we explained, $z_{\mathrm{RR}}(n)$ represents a surrogate of $x_{\mathrm{RR}}(n)$ with the memory effect of T_{pe} compensated for, and the function $g_k(., \mathbf{a})$, dependent on the parameter vector $\mathbf{a} = [a(0), a(1)]^T$, represents the relationship between the RR interval and the T_{pe} interval once the memory effect has been compensated for (i.e. under stationary conditions).

After $\mathbf{h}$ and $g_k(., \mathbf{a})$ have been optimized, we can make use of $z_{\mathrm{RR}}(n)$ as a surrogate of the running RR series that would generate a truly stationary period in the running repolarization interval T_{pe}. Then, the ith pair $[z_{\mathrm{RR}}(i), T_{pe}(i)]$ represents the surrogate for the RR interval and the T_{pe} interval measured in an stable ECG segment. Therefore, the estimate of restitution dispersion derived in (7.6) can be replaced with the following equation, obtained by differentiating (6.3) with respect to z_{RR}:

$$\widehat{\Delta\alpha}^{\mathrm{ECG_c}} = \left.\frac{\partial T_{pe}}{\partial z_{\mathrm{RR}}}\right|_{z_{\mathrm{RR}}=\bar{z}_{\mathrm{RR}}} = \left.\frac{\partial g_k(z_{\mathrm{RR}}, \mathbf{a})}{\partial z_{\mathrm{RR}}}\right|_{z_{\mathrm{RR}}=\bar{z}_{\mathrm{RR}}} \tag{7.7}$$

The above expression has the advantage of avoiding the need for stationary ECG segments. The superindex "ECG_c" indicates that the quantification of restitution dispersion from the ECG is done by compensating for the T_{pe} memory lag using the model described in Fig. 6.1. This estimate is a robust alternative to $\widehat{\Delta\alpha}^{\mathrm{ECG_s}}$ (see Fig. 7.1 bottom-left). In (7.7), the derivative is evaluated at the mean z_{RR} value, $\bar{z}_{\mathrm{RR}}$, of the complete recording.

7.2.4. Computational modeling and simulation

Computational modeling and simulation is used in this study to assess how the proposed estimates evaluated from the ECG, $\widehat{\Delta\alpha}^{\mathrm{ECG_s}}$ and $\widehat{\Delta\alpha}^{\mathrm{ECG_c}}$, represent dispersion of the APDR slopes at tissue level (see Fig. 7.1, right).

Propagation of the electrical activity in a left ventricular 2D tissue slice is simulated using the human ten Tusscher action potential model [142], with numerical integration performed as described in [144], with a 0.02 ms time step and 0.01 cm space step. The ten Tusscher model [142] describes the principal ionic currents through the cardiac cell membrane with high degree of electrophysiological detail for the three types of cells in the ventricular wall: endocardial, midmyocardial and epicardial cells. The 2D tissue slice used in this study is 7.5 cm long by 1 cm wide, representing the base to apex and the endocardial to epicardial distances, respectively, as shown in Fig. 7.4. Conductivity of the tissue along the fiber direction is set to σ_L= 0.0013 mS with a membrane capacitance of 1 μF/cm^2, obtaining a maximum conduction velocity of 71 cm/s. Perpendicular to the fiber direction, the conductivity is 60% lower, σ_T= 0.00052 mS, resulting in a conduction velocity of 42 cm/s, which is comparable to the average velocity of 44 cm/s recorded *in vivo* and across the arterially perfused transmural wedge preparation [145]. A transmural linear variation of the helix fiber angle from +60 degrees at the endocardium to -60 degrees at the epicardium is assumed based on [146].

As illustrated in Fig. 7.4, two areas in the subendocardium are stimulated simultaneously with a 2 ms square stimulus pulse of 1.5 times diastolic threshold: 1 cm at the

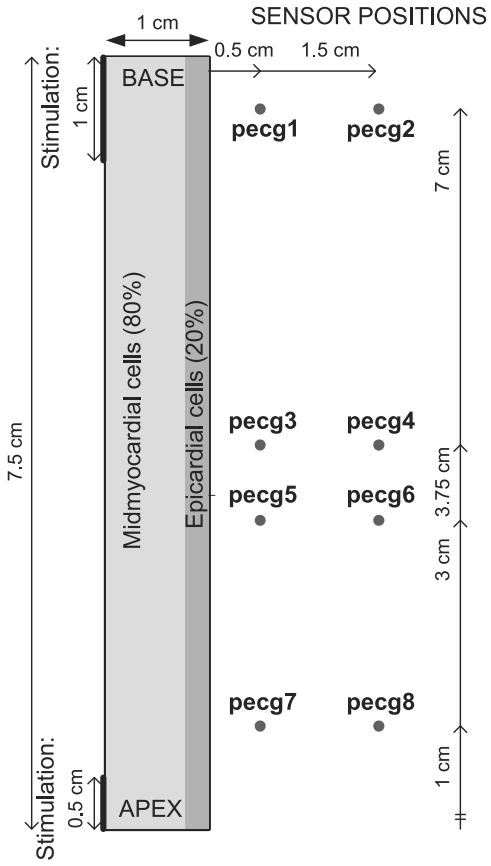

Figure 7.4: 2D tissue slice used in the simulation, with indication of the default cell type distribution across the ventricular wall, and sensor positions used for pseudo-ECG computation.

top of the base and 0.5 cm at the bottom of the apex, based on the activation sequence reported for an isolated human heart in [6]. Transmural heterogeneities are included in the 2D tissue preparation by using two cell types: midmyocardial and epicardial cells. In order to match the complete activation sequence of [6] and to account for the influence of Purkinje fibers, endocardial cells in the simulated preparation are replaced with midmyocardial cells, known to have longer APDs. This is justified by the fact that Purkinje cells have longer APDs than midmyocardial cells and much longer than endocardial cells. The coupling between Purkinje and endocardium makes endocardial cells enlarge their action potentials [145], leading to APDs values similar to those simulated in our preparation. The APD in the different regions across the 2D tissue slice are in agreement with the range reported in [147], where left ventricular wedge preparations from non-failing human hearts were optically mapped.

The distribution of cell types in the simulated tissue are 80% of midmyocardial cells and 20% of epicardial cells [148]. To represent possible heterogeneities in human hearts and measure a range of plausible restitution dispersion values, the effect of varying the

percentages of cell types within the ventricular wall is evaluated by considering additional distributions of 65/35% and 90/10% of midmyocardial/epicardial cells. For each cell type distribution, APDR curves are computed by pacing the 2D tissue preparation at different RR intervals, following the so-called dynamic restitution protocol [134]. Dispersion of APDR slopes at tissue level is denoted by $\Delta\alpha^{\text{SIM}}$ and is computed from the results of the 2D simulation as follows:

$$\Delta\alpha^{\text{SIM}} = \frac{\partial APD^{dyn}_{last}}{\partial RR} - \frac{\partial APD^{dyn}_{min}}{\partial RR} \tag{7.8}$$

where APD^{dyn}_{min} and APD^{dyn}_{last} are defined as described in section §7.2.2. Estimations of $\Delta\alpha^{\text{SIM}}$ are computed from pseudo-ECGs using (7.6). The pseudo-ECGs, each one measuring the extracellular potential at one of the sensor positions shown in Fig. 7.4 (Fig. 7.1, bottom-right), are computed as in [149]. The corresponding estimations are:

$$\widehat{\Delta\alpha}^{\text{pECG}} = \frac{\partial T^{dyn}_{pe}}{\partial RR} \tag{7.9}$$

where T^{dyn}_{pe} represents the T_{pe} interval measured from one of the pseudo-ECGs using the dynamic protocol.

Calculation of pseudo-ECG.

Considering the bi-domain model, myocardium is considered as a single cell along which, the action potential (AP) is propagated [150]. Then, the extracellular potential in a 2D tissue, can be computed as:

$$u(\overrightarrow{r}) = -\frac{\gamma}{4\pi}\frac{\sigma_i}{\sigma_e}\iint \overrightarrow{\nabla}' u_m(\overrightarrow{r}') \cdot \overrightarrow{\nabla}' \left[\frac{1}{|\overrightarrow{r}' - \overrightarrow{r}|}\right] da \tag{7.10}$$

where σ_i represents the intracellular conductivity (a weighted average between the longitudinal and transversal intracellular conductivities) and σ_e, the extracellular conductivity. $\overrightarrow{\nabla}' u_m(\overrightarrow{r}')$ is the gradient of membrane voltage in the differential of area da, and $|\overrightarrow{r}' - \overrightarrow{r}|$ represents the distance from the sensor position to da. γ is a scale factor that accounts for the intracellular and extracellular volume differences.

7.3. Results

This section presents the different comparison tasks shown in Fig. 7.1. In section §7.3.1, the 2D ventricular model is evaluated, with APDR estimates measured from pseudo-ECGs checked to be within the physiological range measured from ECG recordings (Task 1 in Fig. 7.1). In section §7.3.2, the capability of the proposed estimate measured from the pseudo-ECG ($\widehat{\Delta\alpha}^{\text{pECG}}$) to quantify APDR dispersion at tissue level is assessed (Task 2 in Fig. 7.1). In §7.3.3, ECG estimates evaluated in tilt test recordings and APDR dispersion $\Delta\alpha^{\text{SIM}}$ are compared (Task 3 in Fig. 7.1). Additionally, section §6.2 provides a characterization of T_{pe} rate adaptation.

7.3.1. Evaluation of the 2D simulations. Comparison between pseudo-ECGs and clinical ECGs

The human ventricular model used in this study has been shown to reproduce experimentally observed data on APD restitution in single cells from the endo, epi, and midmyocardial regions of the ventricle [151]. Also, conduction velocity restitution measured in a 1D cable of cells has been validated using experimental data [151].

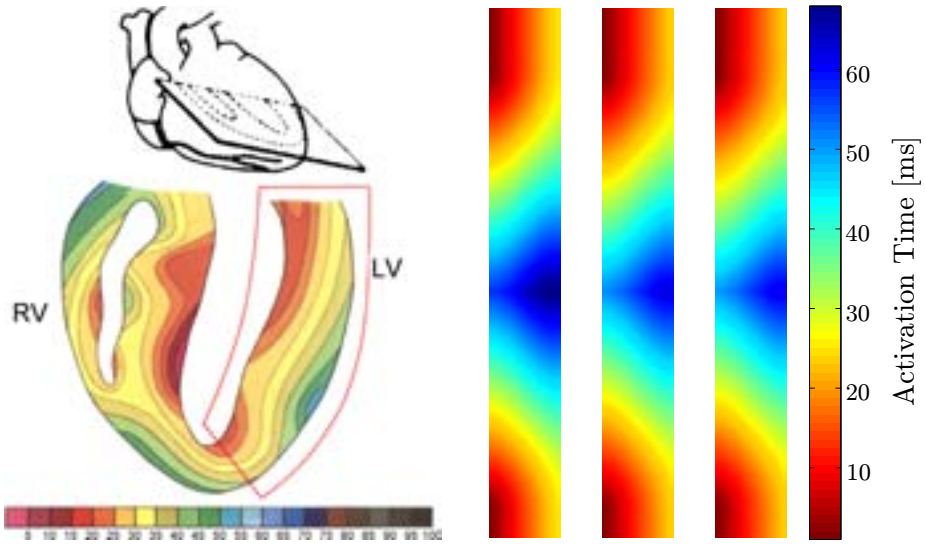

Figure 7.5: Isochronic representation (in milliseconds) of ventricular activation: (a) experiment results reproduced from [6]; (b) 2D tissue simulations when pacing at RR intervals of 450 ms, 1000 ms and 1450 ms.

The 2D tissue preparation built in this study yields an activation sequence that is in good agreement with the experimental results reported in [6], as illustrated in Fig. 7.5. Simulated activation sequences are shown for three different pacing RR intervals, 450 ms, 1000 ms and 1450 ms, leading to the observation that activation times have similar patterns in the three cases. Fig. 7.6 shows a simulated sequence of isochronic voltage representation during steady-state pacing at 1000 ms, with indication of the timing corresponding to the T wave peak and T wave end in the pseudo-ECG from **pecg3**, and of the regions where APD_{min} and APD_{last} are computed. Since our 2D preparation includes only transmural heterogeneities, the time instant corresponding to the peak of the T wave coincides with the time at which complete repolarization of the epicardium occurs, whereas T wave end coincides with the total repolarization of the tissue. The effect of varying the cell type distribution across the ventricular wall on the isochronic voltage representation at the T wave peak instant is shown in Fig. 7.7, for pacing RR intervals of 450 ms, 1000 ms and 1450 ms. In all isochronic voltage representations, for

different pacing rates and cell type distributions, the epicardium is completely repolarized at the T wave peak instant.

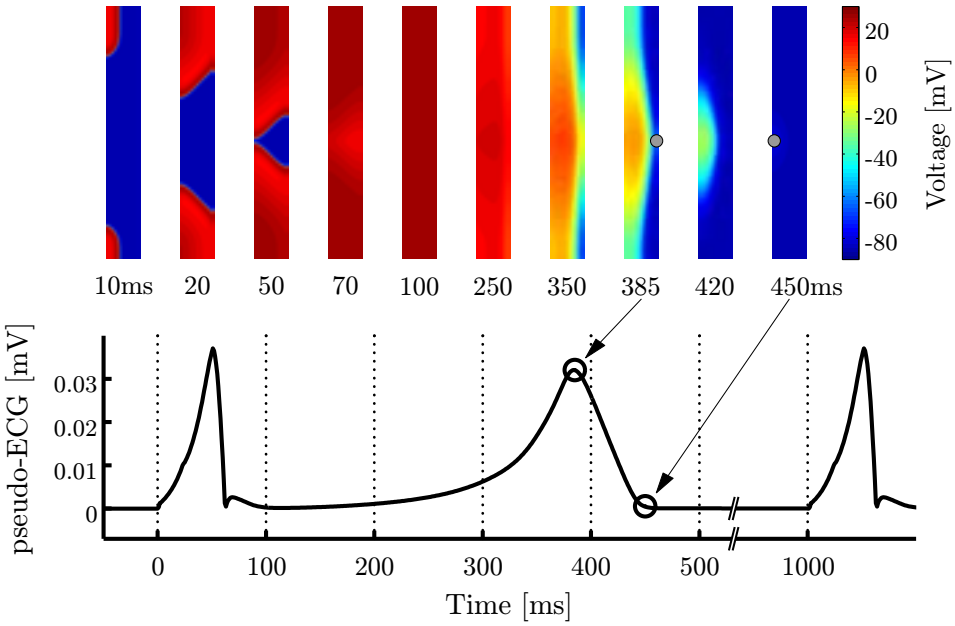

Figure 7.6: Top panel: simulated sequence of isochronic voltage representation during steady-state pacing at 1000 ms. The position of the two cells corresponding to APD_{min} for the peak of the T wave and APD_{last} for the end of the T wave, are shown with a gray point. Bottom panel: derived pseudo-ECG from **pecg3**.

Although we could have defined APD_{min} as the APD of any cell region chosen along the T peak wave front shown in Fig. 7.6, that region should remain fixed for the different RR levels to be able to apply equation (7.3). Note that in the simulations shown in Fig. 7.7, APD_{min} remains fixed at different RR levels as needed.

In Fig. 7.8, equation(7.1) is justified for the whole RR interval using the 80/20% cell type distribution. The difference $APD_{min}^{dyn} - APD_{last}^{dyn} - \Delta AT$ is compared with the steady state T_{pe}^{dyn} interval computed at different sensor position (**pecg3**).Note that ΔAT is constant during the whole RR range.

An indirect validation of the simulated restitution properties in the 2D tissue is performed by first comparing steady-state T_{pe}^{dyn} values computed at different RR intervals in tilt test ECGs and in simulated pseudo-ECGs. Fig. 7.9 shows three regions corresponding to simulations using cell type distributions of 65/35%, 80/20% and 90/10%. Each region represents the range of steady-state [RR, T_{pe}^{dyn}] curves computed for pseudo-ECGs at eight different sensor positions. The steady-state [z_{RR}, T_{pe}] curves obtained from the tilt test recordings are superimposed in the same graphic. Note that when the percentages of epi- and midmyocardial cells are more similar (65/35%), the difference between APD_{min} and APD_{last} is higher and, therefore, the T_{pe} interval is longer than the ones for 80/20%

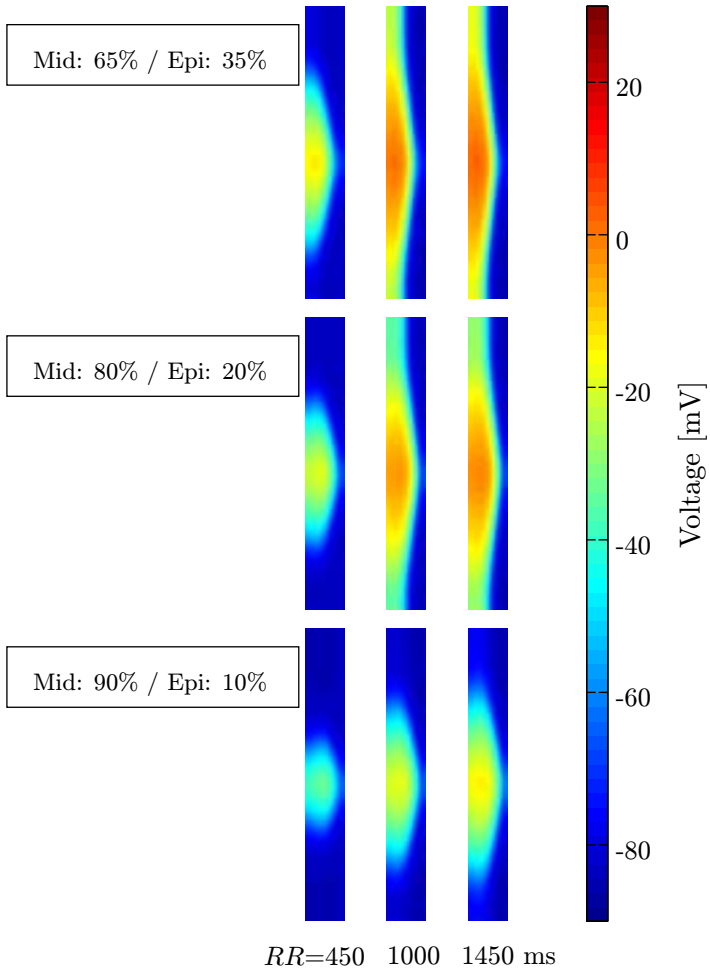

Figure 7.7: Isochronic voltage representation at T wave peak time instant using three different cell type distributions (mid/epi) and pacing RR intervals of 450 ms, 1000 ms and 1450 ms.

and 90/10% cell type distributions. Simulated values of T_{pe} at different RR intervals for 65/35% and 80/20% (default) cell type distributions are found to be within the range of values measured from the tilt test recordings. However, simulated T_{pe} values for the 90/10% percentage are outside the range of the tilt test recordings.

After confirming the good agreement in the repolarization $[RR,\ T_{pe}^{dyn}]$ values between pseudo-ECGs and clinical ECGs, the restitution dispersion estimates are also compared. Fig. 7.10 shows a comparison of pseudo-ECG-based estimates of APDR dispersion, $\widehat{\Delta\alpha}^{\mathrm{pECG}}$, in (7.9), at sensor positions **pecg3** and **pecg5**, and ECG-based estimates, $\widehat{\Delta\alpha}^{\mathrm{ECG_c}}$, in (7.7), obtained from the tilt test recordings. Both the average difference between $\widehat{\Delta\alpha}^{\mathrm{pECG}}$ (computed in **pecg3** and **pecg5**) and $\widehat{\Delta\alpha}^{\mathrm{ECG_c}}$, and the average percentage of the difference are shown in Table 7.1. Differences are below 20% in mean, which are

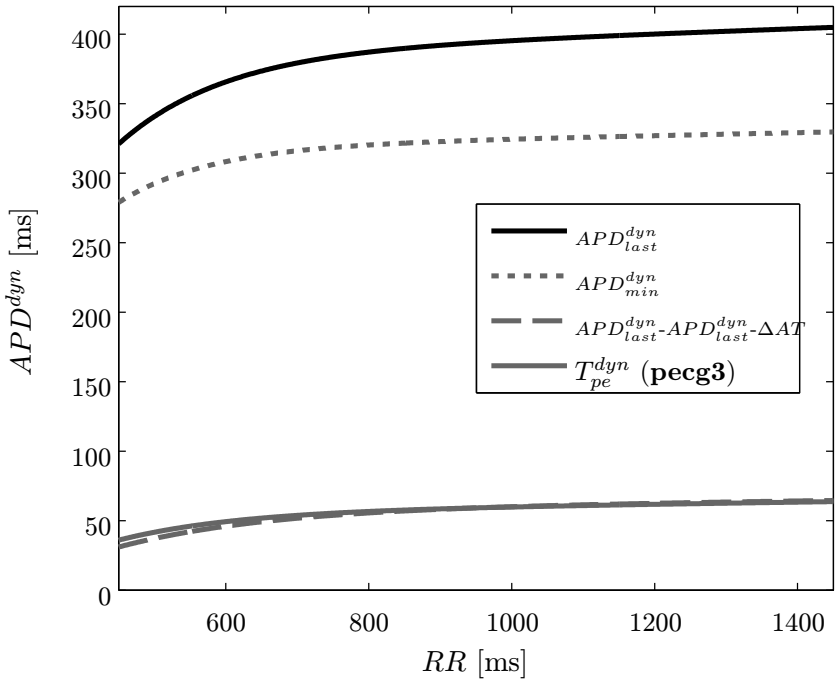

Figure 7.8: For 80/20% cell type distribution, APDR curves and their relation with steady-state T^{dyn}_{pe} interval derived from **pecg3**.

within physiological variability limits.

7.3.2. Assessment of APDR dispersion quantified from the pseudo-ECG

APDR slope dispersion at tissue level, denoted by $\Delta\alpha^{\text{SIM}}$, in (7.8), has been computed for each of the three cell type distributions. $\Delta\alpha^{\text{SIM}}$ is used to assess whether $\widehat{\Delta\alpha}^{\text{pECG}}$, computed from pseudo-ECGs, is a good estimate of APDR slope dispersion. Fig. 7.11 shows the comparison between $\Delta\alpha^{\text{SIM}}$ and $\widehat{\Delta\alpha}^{\text{pECG}}$ computed at sensor positions **pecg3**, **pecg4** and **pecg5** for the default cell type distribution 80/20%. The error between $\Delta\alpha^{\text{SIM}}$ and $\widehat{\Delta\alpha}^{\text{pECG}}$ from **pecg3** and **pecg5** relative to the slope range is found to be 4% in average, while from **pecg1** is 5% and from **pecg4**, is 6%.

7.3.3. Agreement between simulated APDR dispersion and estimates from clinical ECGs

Three stationary ECG segments during the tilt test protocol, corresponding to the end of each stage at supine, standing and back supine positions, are used to compute $\widehat{\Delta\alpha}^{\text{ECG}_s}$. Estimates computed at the mean of the corresponding RR range, are shown in

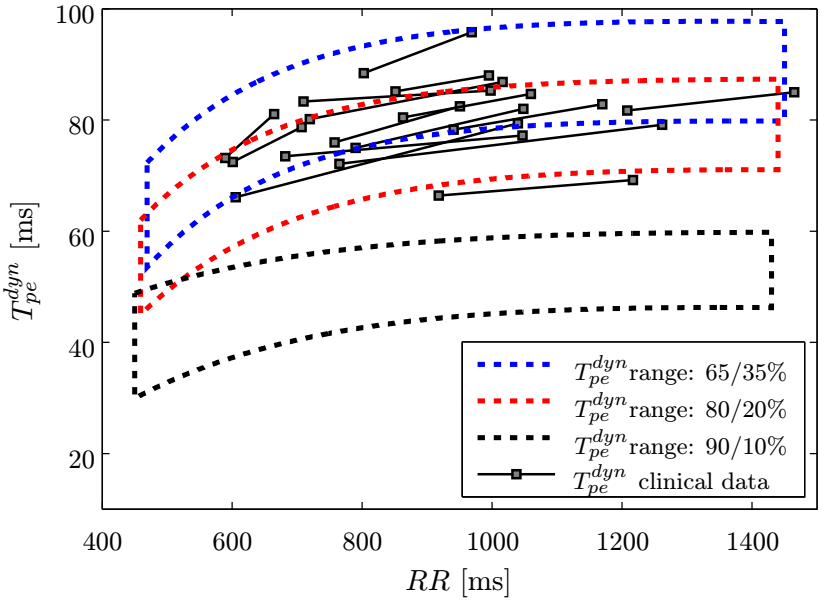

Figure 7.9: Steady-state T_{pe}^{dyn} as a function of RR from tilt test recordings (in squares) and from simulations. For the simulations, the regions correspond to cell type distributions of 65/35%, 80/20% and 90/10%, and each region represents the influence of computing steady-state $[RR, T_{pe}^{dyn}]$ curves for pseudo-ECGs at different sensor positions.

Fig. 7.12, where they are compared to values of $\Delta\alpha^{\mathrm{SIM}}$, representing simulated APDR slope dispersion at tissue level. Without assuming stationary ECG segments, $\widehat{\Delta\alpha}^{\mathrm{ECG_s}}$ is replaced with $\widehat{\Delta\alpha}^{\mathrm{ECG_c}}$, in which the T_{pe} memory lag is compensated for. A comparison between $\widehat{\Delta\alpha}^{\mathrm{ECG_c}}$ (in circles) and $\Delta\alpha^{\mathrm{SIM}}$ is shown in Fig. 7.13. The dashed lines depicted in Fig. 7.13 represent the derivatives of the optimal $g_k(., \mathbf{a})$ function in the z_{RR} range for each recording. These derivatives evaluated in the mean z_{RR} value are our estimates $\widehat{\Delta\alpha}^{\mathrm{ECG_c}}$. According to the results shown in Fig. 7.12 and Fig. 7.13, there is a good agreement between simulated APDR slope dispersion and the ECG estimates $\widehat{\Delta\alpha}^{\mathrm{ECG_s}}$ and $\widehat{\Delta\alpha}^{\mathrm{ECG_c}}$, particulary for $\widehat{\Delta\alpha}^{\mathrm{ECG_c}}$, in which the effects of T_{pe} rate adaptation are compensated for.

Quantification of the results shown in Fig. 7.12 and Fig. 7.13 is presented in Table 7.2, where average values of the individual differences between simulated $\Delta\alpha^{\mathrm{SIM}}$ and the two ECG estimates, $\widehat{\Delta\alpha}^{\mathrm{ECG_s}}$ and $\widehat{\Delta\alpha}^{\mathrm{ECG_c}}$, are computed. Expressions of those differences as percentages are also included, being 30% in average for $\widehat{\Delta\alpha}^{\mathrm{ECG_s}}$, and 20% for $\widehat{\Delta\alpha}^{\mathrm{ECG_c}}$.

As expected, results for the cell type distribution 90/10% show higher differences due to the fact that T_{pe} values from the pseudo-ECG are not within the range of our clinical data.

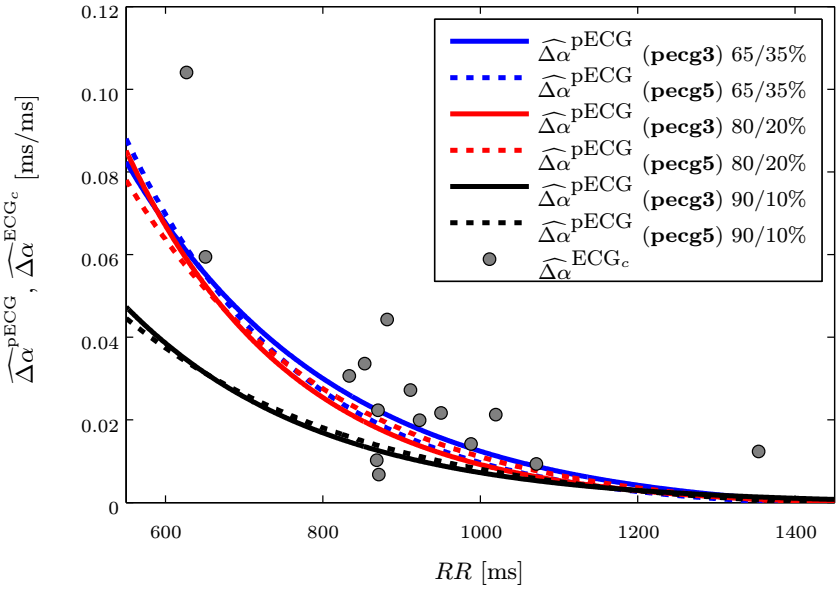

Figure 7.10: APDR slope dispersion estimates from the tilt test recordings ($\widehat{\Delta\alpha}^{\mathrm{ECG_c}}$) and from the pseudo-ECGs ($\widehat{\Delta\alpha}^{\mathrm{pECG}}$) derived from two sensor positions (**pecg3** and **pecg5**), and three cell type distributions (mid/epi: 65/35%, 80/20% and 90/10%).

7.4. Discussion

APDR dispersion is considered as an important risk marker in the development of ventricular arrhythmias [137, 124, 141] and is measured at tissue level. In this study, APDR dispersion, measured at tissue level, has been quantified from the surface ECG, using a novel methodology. To our best knowledge, this is the first time that APDR dispersion is quantified non-invasively by measuring changes in the steady-state T_{pe} with respect to changes in RR interval. First, a 2D tissue ventricular model has been built and indirectly validated, and the proposed estimate measured at pseudo-ECGs is shown to properly quantify APDR dispersion at tissue level. Then, estimates measured at the acquired ECG recordings are found to be in agreement with the simulated APDR dispersion. Additionally, results from the T_{pe} rate adaptation study show that T_{pe} adapts faster to changes in HR than the QT interval.

7.4.1. Evaluation of the 2D ventricular model

We have evaluated the 2D ventricular tissue model used in this study. First, the underlying model of the 2D simulation has been reported to reproduce experimentally observed data on APD restitution in single cells from epi, endo and midmyocardial regions correctly [151, 142]. Characteristics of the 2D tissue model built in this work, such as dimensions, conduction velocities in the fiber direction [142] and perpendicular to it

Simulated - Measured	*Cell Percentage*	Average (%) [ms / ms]
$\widehat{\Delta\alpha}^{\text{pECG}}$ (**pecg1**) - $\widehat{\Delta\alpha}^{\text{ECG}_\text{c}}$	(65/35%)	-0.0096 (-19%)
	(80/20%)	-0.0107 (-23%)
$\widehat{\Delta\alpha}^{\text{pECG}}$ (**pecg3**) - $\widehat{\Delta\alpha}^{\text{ECG}_\text{c}}$	(65/35%)	-0.0066 (-2%)
	(80/20%)	-0.0100 (-21%)
$\widehat{\Delta\alpha}^{\text{pECG}}$ (**pecg5**) - $\widehat{\Delta\alpha}^{\text{ECG}_\text{c}}$	(65/35%)	-0.0090 (-17%)
	(80/20%)	-0.0085 (-11%)

Table 7.1: Average value across subjects of the difference between the estimates measured from the simulated pseudo-ECGs in **pecg1**, **pecg3** and **pecg5** ($\widehat{\Delta\alpha}^{\text{pECG}}$), and from the tilt test recordings $\widehat{\Delta\alpha}^{\text{ECG}_\text{c}}$. Different percentages of cell types have been used to derive the pseudo-ECGs.

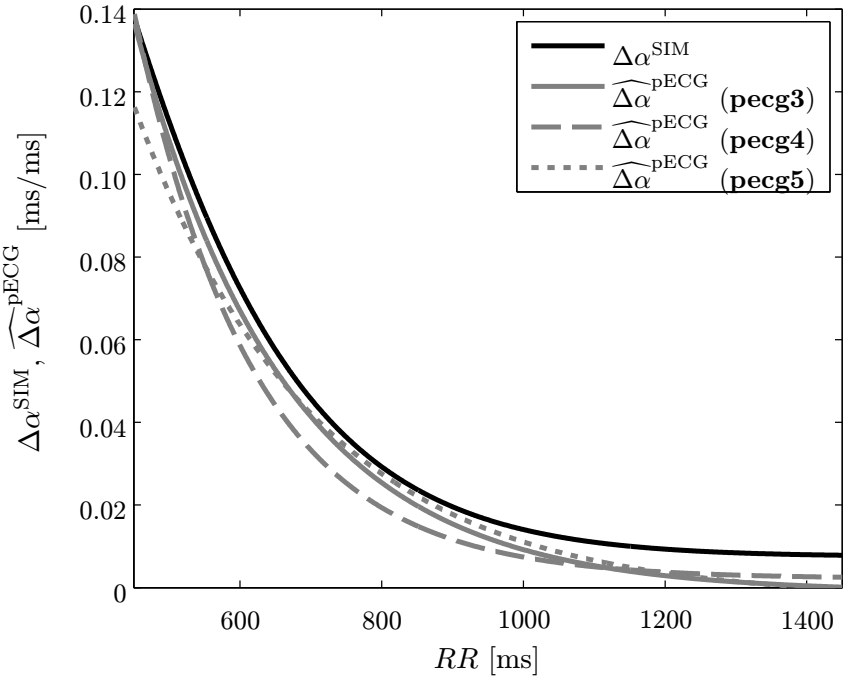

Figure 7.11: APDR slope dispersion, $\Delta\alpha^{\text{SIM}}$, for the cell type distribution 80/20%, and the proposed estimate measured from the pseudo-ECG in **pecg3**, **pecg4** and **pecg5**.

[145], transmural variation of the fiber angle [146], and heterogeneity of cell types across the ventricular wall [148], are in agreement with experimental studies. The simulated activation sequence is layered and agrees with the one of an isolated human heart section reported in [6].

Experimental studies in canine wedge preparation [88] show that in case of having transmural heterogeneities only, the time instant of the T wave peak corresponds to

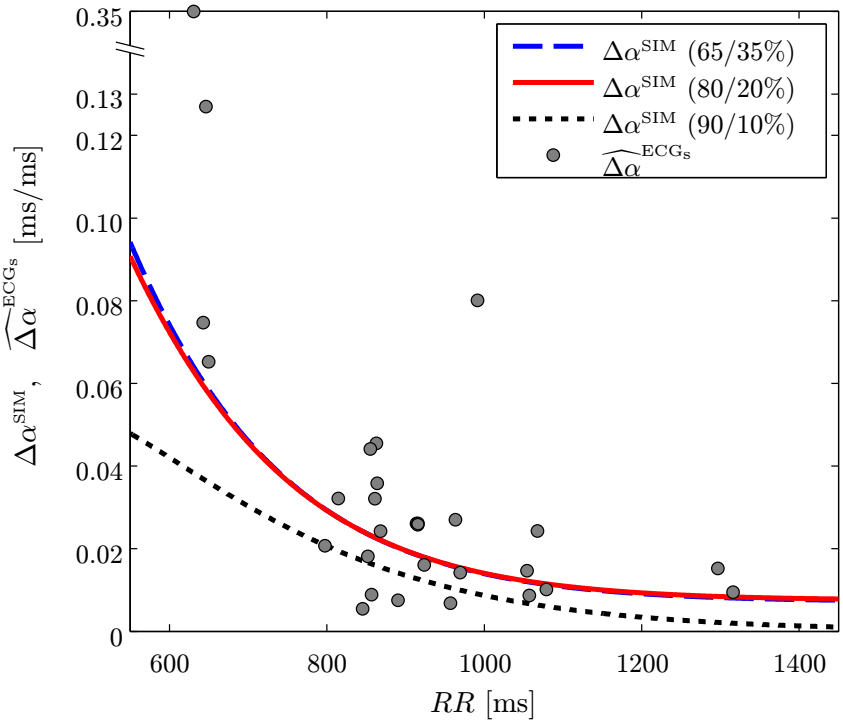

Figure 7.12: APDR slope dispersion, $\Delta\alpha^{\mathrm{SIM}}$, computed as a function of RR for three cell type distributions. For each tilt test recording, $\widehat{\Delta\alpha}^{\mathrm{ECG_s}}$ values are shown in circles at the mean of the corresponding RR interval range.

the complete repolarization of the epicardium. This agrees with the results of our 2D simulations, which include only transmural heterogeneities, where the peak of the T wave in pseudo-ECGs coincides with the total repolarization of the epicardium in the central part of the tissue (see the isochronic voltage representation in Fig. 7.6). This has been observed for pacing at different RR intervals and also for different cell type distributions (see Fig. 7.7).

Although we could have defined APD_{min} as the APD of any cell region chosen along the T peak wave front shown in Fig. 7.6, that region should remain fixed for the different RR levels to be able to apply equation (7.3). In Fig. 7.7, it is shown that in our simulations, the only region that remains in the T peak wave front for different RR levels is at the center of the epicardium (minimum APD at the T peak wave front).

The APD in the different cell regions of the 2D tissue slice are within the range of APDs of the sub-endocardium, midmyocardium and sub-epicardium reported in [147].

Steady-state T_{pe}^{dyn} at different RR levels obtained from simulated pseudo-ECGs are in agreement with those measured from ECG control recordings (see Fig. 7.9). Restitution properties have also been evaluated by comparing the simulated estimations of APDR slope dispersion $\widehat{\Delta\alpha}^{\mathrm{pECG}}$, derived from the pseudo-ECGs, with the values obtained from

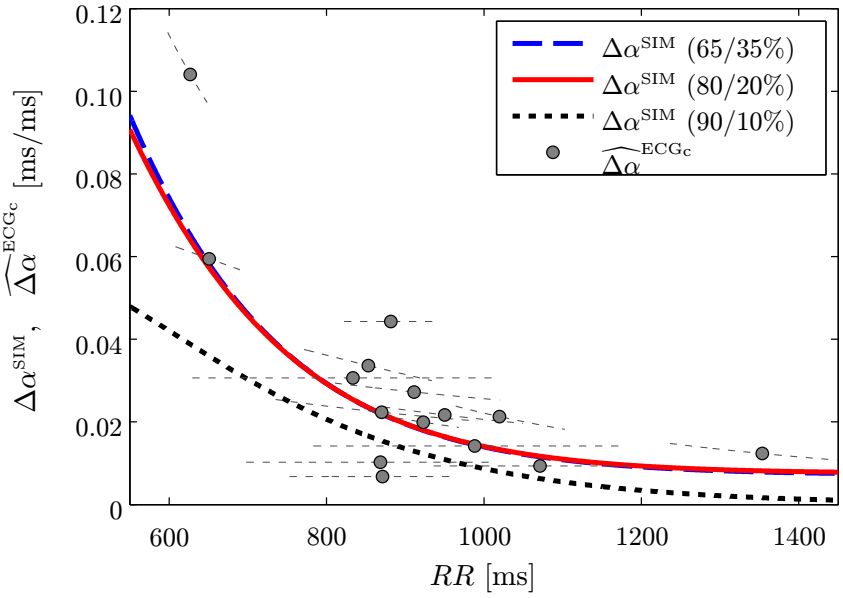

Figure 7.13: APDR dispersion, $\Delta\alpha^{\mathrm{SIM}}$, for different cell type distributions as a function of RR. For each tilt test recording, $\widehat{\Delta\alpha}^{\mathrm{ECG_c}}$ values are shown in circles at the mean of the surrogate RR interval range together with the derivative of the optimal $g_k(.,\mathbf{a})$ function over the corresponding RR range.

the tilt test recordings. Results in Table 7.1 and Fig. 7.10 show that simulated values in **pecg3** and **pecg5** are within the range measured in ECG recordings. Sensor positions **pecg3** and **pecg5**, located in the middle part of the tissue, are used to derive $\widehat{\Delta\alpha}^{\mathrm{pECG}}$ due to their similarity to the precordial leads V2, V3 and V4, used to compute the estimates in the tilt test recordings.

7.4.2. Assessment of APDR dispersion quantified from the pseudo-ECG

As Fig. 7.11 shows, $\widehat{\Delta\alpha}^{\mathrm{pECG}}$, measured from the pseudo-ECG provides a quantification of APDR slope dispersion $\Delta\alpha^{\mathrm{SIM}}$ at tissue level, being the mean error relative to the slope range below 6%. This result shows that APDR dispersion at tissue level is properly quantified using the proposed non-invasive estimates.

7.4.3. Agreement between simulated APDR dispersion and estimates from clinical ECG data

Two APDR slope dispersion estimates from the surface ECG were proposed: one computed from stationary ECG segments, $\widehat{\Delta\alpha}^{\mathrm{ECG_s}}$; and the other compensating for the

	Cell Percentage	Average [ms/ms]
$\Delta\alpha^{\mathrm{SIM}}$ - $\widehat{\Delta\alpha}^{\mathrm{ECG_s}}$	(65/35%)	-0.0117 (-29.5%)
$\left(\frac{\Delta\alpha^{\mathrm{SIM}}-\widehat{\Delta\alpha}^{\mathrm{ECG_s}}}{\Delta\alpha^{\mathrm{SIM}}}\cdot 100\right)$	(80/20%)	-0.0119 (-29.5%)
	(90/10%)	-0.0221 (-120.9%)
$\Delta\alpha^{\mathrm{SIM}}$ - $\widehat{\Delta\alpha}^{\mathrm{ECG_c}}$	(65/35%)	-0.0052 (-20.2%)
$\left(\frac{\Delta\alpha^{\mathrm{SIM}}-\widehat{\Delta\alpha}^{\mathrm{ECG_c}}}{\Delta\alpha^{\mathrm{SIM}}}\cdot 100\right)$	(80/20%)	-0.0053 (-19.8%)
	(90/10%)	-0.0137 (-116.8%)

Table 7.2: Average value across subjects of the differences between simulated dispersion of restitution slopes $\Delta\alpha^{\mathrm{SIM}}$ at tissue level and their ECG estimates $\widehat{\Delta\alpha}^{\mathrm{ECG_s}}$ and $\widehat{\Delta\alpha}^{\mathrm{ECG_c}}$.

T_{pe} hysteresis on RR, $\widehat{\Delta\alpha}^{\mathrm{ECG_c}}$.

In some cases, the estimates $\widehat{\Delta\alpha}^{\mathrm{ECG_s}}$ differ considerable from the $\Delta\alpha^{\mathrm{SIM}}$ values. Reviewing RR trends from those recordings, non stable RR periods are observed. Averaged differences between $\widehat{\Delta\alpha}^{\mathrm{ECG_s}}$ and $\Delta\alpha^{\mathrm{SIM}}$, are of 30% of the value in mean. If we do not assume stable ECG segments and compensate for the T_{pe} memory effect using $\widehat{\Delta\alpha}^{\mathrm{ECG_c}}$, results improve considerably. Averaged differences between $\widehat{\Delta\alpha}^{\mathrm{ECG_c}}$ and $\Delta\alpha^{\mathrm{SIM}}$, which also account for inter subject variability, are of about 20%. If we take into account the individual differences, the averaged difference between $\Delta\alpha^{\mathrm{SIM}}$ and $\widehat{\Delta\alpha}^{\mathrm{ECG_c}}$ is -0.0052, half of the one between $\Delta\alpha^{\mathrm{SIM}}$ and $\widehat{\Delta\alpha}^{\mathrm{ECG_s}}$ (-0.0117). Besides the good agreement between $\Delta\alpha^{\mathrm{SIM}}$ and the corresponding ECG estimates, a similar behaviour of the derivatives of the optimal $g_k(.,\mathbf{a})$ functions over each corresponding RR range is observed. Also, our results are in accordance with the slope values reported in [122] for healthy subjects.

The estimate $\widehat{\Delta\alpha}^{\mathrm{ECG_c}}$ shows promising results to extend this method to evaluate arrhythmic pathologies related to restitution dispersion.

7.5. Limitations of the Study

The 2D simulation does not incorporate a 3D geometry of a left ventricle wall to compute APDR dispersion. Also, heterogeneities other than transmural ones, e.g. apex to base, were not included, which could shed light on the understanding of the T_{pe}. Those considerations could have led to different sites associated with APD_{min} and APD_{last}, as described after equation (7.1). However, they would not imply any change in our methodology. Also, it is worth mentioning that the dispersion quantified in our study is that accounted for by the T_{pe} interval, which does not necessarily correspond to the maximum dispersion in the tissue.

Healthy subjects have been used to evaluate the proposed methodology to non-invasively quantify restitution dispersion. The next step will be to apply the methodology to estimate restitution dispersion in patients who experienced VT or VF and compare it with control subjects.

Tilt test recordings were obtained from subjects aged 25 to 33 years old with no previous history of cardiovascular disease. However, the data used for the development of the human ventricular action potential model used in this study are not always specific of young healthy hearts.

Chapter 8

Conclusions and Future extensions

In this section a summary of the most important contributions of this thesis and the potential future extensions are presented.

8.1. Conclusions

8.1.1. Ischemia detection in Holter recordings and body position change detection

A previous ischemia detector developed within the ESC DB framework and based on the root mean square of the ST segments with respect to a reference ST segment, has been modified and has improved its performance on a more extensive database, the Long-Term ST Database (LTST DB). In this database, ST episodes of different origin are present, making a much more challenging scenario for the detector. The modified detector is more general in the sense that it accepts recordings with different number of leads without setting new parameters, and the search for non ischemic reference beats.

As expected, the detector decreases the performance obtained in the ESC DB when it is applied in the LTST DB obtaining a sensitivity of 73% and a positive predictivity of 78% , claiming for much more robust false alarm cancellation rules, accounting for the very different nature of ST episodes. This opened new working lines as detecting and cancelling out body position changes.

We have developed a body position change detector based on the generalized likelihood ratio test (GLRT) for laplacian noise distribution, which is applied to the Karhunen-Loève transform coefficient series of the QRS and STT complexes. Its performance is shown to be higher than a previous detector developed for gaussian noise distribution. However an extra stage has been needed to decrease the false alarm rate in a database with patients undergoing a percutaneous coronary intervention, where not body position changes are present. Information of the noise in the ECG signal is used and it is shown that the occurrence of a BPC is associated with noisy beats. The performance about 92% in sensitivity and 99% in positive predictivity, makes the detector very useful in ST monitoring. However, in ambulatory monitoring with a lower SNR of the ECG, baseline

wandering and abrupt changes related to heart rate variations, the applicability should be further studied.

8.1.2. Classification of ST episodes

ST segment changes provide a sensitive marker in the diagnosis of myocardial ischemia in Holter recordings. However, not only the mechanisms of ischemia result in ST segment deviation, but also heart rate related episodes, body position changes or conduction changes among others, which are considered artifactual events when ischemia is the target. In order to distinguish between them, the very similar signatures of ST modifications has led us to look for other ECG indices such as heart rate-based indices, correlation between the absolute ST segment deviation and heart rate series, the interval between the Tapex and the Tend, T wave amplitude, the signal to noise ratio and changes in the upward/downward slopes of the QRS complex.

A linear discrimination analysis between the three types of events: ischemia, heart rate related episodes and sudden step ST changes (body position changes and conduction changes) has been performed on the LTST DB, reaching an accuracy of 82.3%. The differences in the number of episodes between groups, cause the step wise classification approach to focus first on classifying sudden step ST changes Then, changes in energy of the ST segment has been the first feature selected to classify transient and sudden step changes. The second input variable is related to heart rate and attempts to discriminate between the IG and HRG.

If we focus on distinguishing between different ST signatures, transient episodes (ischemic and heart rate related) and sudden step ST changes, it results in a sensitivity of 76.8% and a specificity of 98.3%. When classifying ischemia from heart rate related episodes, both with a very similar ST level pattern, a sensitivity of 84.5% and a specificity of 86.6% are reached. Finally, for separating ischemia from any other ST event, a sensitivity of 74.2% and a specificity of 93.2% are obtained.

The results notably improve when trying to distinguish between the two very different ST level patterns: transient and sudden step. As expected, the first included indices are $\Delta\mathcal{I}_{\mathrm{RMS_{ST}}}$ and $|\mathcal{I}^{e}_{\mathrm{KL_{ST\text{-}T}}}|$ related to changes in energy of the ST segment and the ST-T complex respectively.

For ischemia detectors based on changes in the ST segment, discrimination between IE and HRE, both very similar patterns in the ST level function, is a very useful tool for automatic screening of Holter episodes. The results show that further information such as heart rate indices, the QT interval or KL-based indices from both repolarization and depolarization, help in discriminating between them, allowing the sensitivity/specificity to increase to 84.5%/86.6%.

In order to diagnose pathological problems, we have attempted to discriminate between ischemic and non ischemic events. In this case, we achieved an accuracy of 87.5%, being changes in the ST energy the first selected feature.

8.1.3. Characterization of T_{pe} rate adaptation

We have used a time invariant model to describe the $[T_{pe}/RR]$ relationship, in which the RR interval series is considered as the input and the T_{pe} intervals series as the output. The first block represents a time invariant FIR filter and the second a biparametric function that accounts for intra-subject variability. The hypothesis of this work relies on the fact that current T_{pe} interval is influenced by a history of previous RR intervals. Therefore, the first system represent the memory of the T_{pe} with respect to the RR interval and the second one, the relationship between the T_{pe} and the RR intervals under steady-state conditions. Identification of each of the two blocks, where the input and output of the system are known, has been done by using the least mean square estimator. In order to optimize this ill posed problem, a regularization term to stabilize its solution has been used. Besides, to include the two restrictions described in section §6.1.2, in the cost function to be optimized, we have reformulated the problem and used the QuasiNewton optimization technique reducing the computational time with respect to the optimization solver used for the QT.

Results show that T_{pe} is practically synchronous with HR changes and much faster than QT interval adaptation. In the ANS-UZ database of control and young recordings (about 28 years old), the time to complete 90% of the HR adaptation is about 23 seconds for the T_{pe} interval while for the QT interval, it takes 75 seconds.

Besides, the fast T_{pe} rate adaptation correlates to a reported fast HR adaptation of a transmural 1D fiber [5].

The ANS-UZ database was acquired at the University of Zaragoza in the framework of this study and consists of 12 lead ECG, blood pressure, respiratory, pulse photoplethysmography and expiratory pressure signals recorded from seventeen healthy volunteers. These volunteers underwent a tilt test trial and three different Valsalva maneuvers as described in chapter 5.

8.1.4. Quantification of action potential duration restitution (APDR) dispersion from the surface ECG

Action potential duration restitution (APDR) curves present spatial variations due to the electrophysiological heterogeneities present in the heart. Enhanced spatial APDR dispersion in ventricle has been suggested as an arrhythmic risk marker. In this study we have proposed a method to non-invasively quantify dispersion of APDR slopes at tissue level by making only use of the surface electrocardiogram (ECG). The proposed estimate accounts for rate normalized differences in the steady state T wave peak to T wave end interval (T_{pe}). A methodology has been developed for its computation, which includes compensation for the T_{pe} memory lag after heart rate (HR) changes. The capability of the proposed estimate to reflect APDR dispersion has been assessed by using a combination of ECG signal processing and computational modeling and simulation. Specifically, ECG recordings of control subjects undergoing a tilt test trial are used to measure that estimate, while its capability to provide a quantification of APDR dispersion at tissue

level is assessed by using a 2D ventricular tissue simulation. From this simulation, APDR dispersion, denoted as $\Delta\alpha^{\text{SIM}}$, is calculated, and pseudo-ECGs are derived. Estimates of APDR dispersion measured from the pseudo-ECGs show to correlate with $\Delta\alpha^{\text{SIM}}$, being the mean relative error below 5%. A comparison of the ECG estimates obtained from tilt test recordings and the $\Delta\alpha^{\text{SIM}}$ values measured in silico simulations at tissue level show that differences between them are below 20%, which is within physiological variability limits. These results provide evidence that the proposed estimate is a non invasive measurement of APDR dispersion in ventricle.

8.2. Future extensions

8.2.1. Ischemia detection in Holter recordings and body position change detection

- Extrapolation of the body position change detector to Holter recordings in order to be used together with the ischemia detector. This would decrease the number of false positives due to BPC.

8.2.2. Classification of ST episodes

- In this work we have focused on the search for features which better discriminate between ischemic and non ischemic episodes, referred to as feature extraction. A future extension would be the use of more complex classifiers than the linear or the quadratic ones [94].

- Significant features extracted from the discriminant analysis between ischemic and non ischemic ST events could be included in the ischemia detector. This would improve performance by reducing the number of false positives.

8.2.3. Characterization of T_{pe} rate adaptation

- In order to characterize the T_{pe} rate adaptation, a time-invariant model has been used. However, differences in heart rate accelerations and decelerations have not been accounted for. In the case of the QT interval or the APD, rate adaptation has been shown to be longer after HR decelerations than after HR accelerations [106, 5]. A time-variant model can be formulated in order to account for HR accelerations and decelerations and also to normal changes occurring with time.

- Besides characterizing the T_{pe} rate adaptation in control recordings, it would be interesting to study it in pathological conditions to stratify the arrhythmic risk as done with the QT interval rate adaptation 6.1. Also, in the evaluation of drugs that leads to cardio toxicity, this T_{pe} rate adaptation time could be analysed as a potential biomarker to predict drug-induced arrhythmias. Indeed, some publications point

out different T wave features as alternative predictors (to QT or QTc) of malignant arrhythmias such as Torsades de Pointes [152, 153].

8.2.4. Action potential duration restitution (APDR) dispersion from the surface ECG

- With respect to the 2D model, a future extension would be to use a 3D geometry with a torso model to derive APDR dispersion at tissue level and compare it with results derived with the 2D model.
- To compute the ECG estimate, we have used the T_{pe} interval measured in the lead with higher SNR. The information of the T_{pe} interval measured in different leads could result in a more robust or complementary measurement.
- A natural future extension of this work is to test the proposed estimate in pathological conditions as patients which have already suffered an arrhythmic episode or which are prone to suffer it. We expect to measure enhanced values of APDR dispersion as some publications point out [141, 137, 124].
- Some drugs (mostly class III potassium channel blocker drugs for treatment of arrhythmias) lengthen the APD differently in different parts of the myocardium which may lead to develop malignant ventricular arrhythmias [153]. The proposed estimate can be used to identify those drugs.
- Pseudo-ECG represents the extracellular potential without considering a torso model. Then, a future work would be to evaluate the proposed estimate on unipolar electrograms (EGM).
- Ischemia results in physiological modifications (structural and/or functional abnormalities) in the myocardial ventricle, which are associated to arrhythmias [9, 10, 11]. Previous studies have shown that the main effects of ischemia on the electrical restitution curve are to lower action potential durations (APD) 1.7 and reduce its slope. This has lead to a controversy [154] taking into account that electrical alternans, precursor of ventricular fibrillation (VF) are known to be enhanced by a steep ERC slope and ischemic hearts with a shallower slope than normal hearts are related to arrhythmia [135]. We expect that the lower action potential durations in ischemic cells lead to an increase of restitution dispersion such that the proposed estimate can measure. This would explain the propensity of ventricular fibrillation in ischemic hearts.

List of Acronyms

RMS	Root mean square
LTST DB	Long-Term ST Database
ESC DB	European Society of Cardiology ST-T Database
ANS-UZ DB	Autonomic-nervous-system University of Zaragoza Database
IE	Ischemic Episodes
HRE	Heart Rate Episodes
$BPCE$	Body position Change Episodes
CCE	Conduction Change Episodes
TE	Transient Episodes
SSE	Sudden Step Episodes
NIE	Non Ischemic Events
IG	Ischemic Group
HRG	Heart Rate Group
TG	Transient Group
SSG	Sudden Step Group
NIG	Non ischemic Group
KLT	Karhunen-Loève Transform
BPC	Body position changes
GLRT	Generalized likelihood ratio test
LRT	Likelihood ratio test
RR	RR interval
QT	QT interval
T_w	T wave width
T_{pe}	T wave peak to T end interval
T_A	T wave amplitude
TT	Tilt test
VM	Valsalva maneuver
BP	Blood pressure
EP	Expiratory pressure
PPG	Photoplesthimographic signal
AP	Action potential
APD	Action potential duration
APDR	Action potential duration restitution

Publications derived from the thesis

Publications in Journal Articles

- A. Mincholé, E. Pueyo, J.F. Rodríguez, E. Zacur, M. Doblaré, P. Laguna. "Quantification of restitution dispersion from the dynamic changes of the T wave peak to end, measured at the surface ECG". *IEEE Trans Biomed Eng*, In press, 2010 doi:10.1109/TBME.2010.2097597.

- A. Mincholé, F. Jager, P. Laguna, "Discrimination Between Ischemic and Artifactual ST Segment Events in Holter Recordings". *Biomedical Signal Processing and Control*, vol. 5, issue 1, pp. 21-31, 2010

- A. Mincholé, L. Sörnmo, P. Laguna, "GLRT-based Detection of Body Position Changes from the ECG". *To be submitted, 2011*

Publications in Proceedings of international conferences

- A. Mincholé, B. Skarp, F. Jager, P. Laguna, "Evaluation of a Root Mean Squared Based Ischemia Detector on the LTST Database with body position changes cancellation", *Proc. Computers in Cardiology.* Vol. 31, pp. 89-92 Lyon (France), 2005.

- A. Mincholé, J. P. Martínez, P. Arini, M. Risk, P. Laguna. "T Wave Width Alterations during Valsalva Maneuvers in Diabetic Patients". *Proc. Computers in Cardiology*, vol. 32, pp. 709-712, Valencia (Spain), 2006.

- A. Mincholé, F. Jager y P. Laguna, "Discrimination between Demand and Supply Ischemia Episodes in Holter Recordings". 29th *Annual International Conference of the IEEE Engineering in Medicine and Biology Society (EMBC07)*, Lyon (France), 2007.

- A. Mincholé, E. Pueyo, P. Laguna, "Transmural Differences in Rate Adaptation of Repolarization Duration Quantified from ECG Repolarization Interval Dynamics", in *Proc. Computers in Cardiology*, vol. 35, pp. 597-600, IEEE Computer Society Press, Park City (USA), 2009.

- M. Orini, R. Bailón, L. Mainardi, A. Mincholé, P. Laguna, "Continuous Quantification of Spectral Coherence Using Quadratic Time-Frequency Distributions: Error

Analysis and Application", in *Proc. Computers in Cardiology*, vol. 35, pp. 681-684, IEEE Computer Society Press, Park City (USA), 2009.

- A. Mincholé, E. Pueyo, P. Laguna. "Dispersion of action potential restitution quantified from the surface electrocardiogram", *Journal of Electrocardiology*, Volume 43, Issue 6, November-December 2010, Pages 643-644.

- A. Mincholé, E. Pueyo, J.F. Rodríguez, E. Zacur, M. Doblaré, P. Laguna, "Evaluation of a method for quantification of restitution dispersion from the surface ECG", en *Proc. Computers in Cardiology*, vol. 36, IEEE Computer Society Press, Belfast (UK), 2010.

Bibliography

[1] E. Pueyo, J. P. Martínez, and P. Laguna, "Cardiac repolarization analysis using the surface electrocardiogram," *Phil. Trans. R. Soc. A*, vol. 367, pp. 213–233, 2009.

[2] J. G. Webster, *Encyclopedia of Medical Devices and Instrumentation.* John Wiley & Sons, New York, 1988.

[3] N. V. Thakor, J. G. Webster, and W. J. Tompkins, "Estimation of QRS complex power spectrum for design of a QRS filter," *IEEE Trans. Biomed. Eng.*, vol. 31, no. 11, pp. 702–706, 1984.

[4] B. Rodríguez, B. M. Tice, J. C. Eason, F. Aguel, J. M. Ferrero, and N. Trayanova, "Effect of acute global ischemia on the upper limit of vulnerability: a simulation study," *Am J Physiol Heart Circ Physiol*, vol. 286, pp. H2078–H2088, 2004.

[5] E. Pueyo, Z. Husti, T. Hornyik, I. Baczkó, P. Laguna, A. Varró, and B. Rodrguez, "Mechanisms of ventricular rate adaptation as a predictor of arrhythmic risk," *Am J Physiol Heart Circ Physiol*, vol. 298, pp. 1577–1587, 2010.

[6] D. Durrer, R. T. van Dam, G. E. Freud, M. J. Janse, F. L. Meijler, and R. C. Arzbaecher, "Total Excitation of the Isolated Human Heart," *Circulation.*, vol. 41, pp. 899–912, 1970.

[7] *World Health Statistics.* World Health Organization, Geneva, 2008.

[8] T. Thom, N. Haase, W. Rosamond, V. J. Howard, J. Rumsfeld, T. Manolio, Z. J. Zheng, K. Flegal, C. O'Donnell, S. Kittner, D. Lloyd-Jones, D. C. Goff, Y. Hong, R. Adams, G. Friday, K. Furie, P. Gorelick, B. Kissela, J. Marler, J. Meigs, V. Roger, S. Sidney, P. Sorlie, J. Steinberger, S. Wasserthiel-Smoller, M. Wilson, and P. Wolf, "Heart disease and stroke statistics–2006 update: a report from the American Heart Association Statistics Committee and Stroke Statistics Subcommittee," *Circulation*, vol. 113, pp. e85–151, 2006.

[9] E. Carmeliet, "Cardiac ionic currents and acute ischemia: from channels to arrhythmias," *Phys Rev*, vol. 79, pp. 917–1017, 1999.

[10] M. J. Janse and A. L. Wit, "Electrophysiological mechanisms of ventricular arrhythmias resulting from myocardial ischemia and infarction," *Phys Rev*, vol. 69, pp. 1049–1169, 1989.

[11] N. Luqman, R. J. Sung, C. L. Wang, and C. T. Kuo, "Myocardial ischemia and ventricular fibrillation: Pathophysiology and clinical implications," *Int J Cardiol.*, vol. 119, no. 3, pp. 283–290, 2007.

[12] T. W. Smith and M. E. Cain, "Sudden cardiac death: epidemiologic and financial worldwide perspective," *J. Interv. Card. Electrophysiol.*, vol. 17, p. 199203, 2006.

[13] R. Michael and P. Douglas, "Mechanisms of sudden cardiac death," *J. Clin. Invest.*, vol. 115, p. 2305, 2005.

[14] R. Myerburg and A. Castellanos, *Heart disease: a textbook of cardiovascular medicine*, ch. Cardiac arrest and sudden cardiac death, pp. 890–931. Philadelphia: WB Saunders, 2001.

[15] L. Sörnmo and P. Laguna, *Bioelectrical Signal Processing in Cardiac and Neurological Applications*. Academic Press, 2005.

[16] A. Bayés de Luna, *Clinical Electrocardiography: A Textbook*. Armonk, N.Y.: Futura Publishing Company, 1998.

[17] G. E. Dower, H. B. Machado, and J. A. Osborne, "On deriving the electrocardiogram from vectorcardiographic leads," *Clin Cardiol*, vol. 3, pp. 87–95, 1980.

[18] L. Edenbrandt and O. Pahlm, "Vectorcardiogram synthesized from a 12-lead ECG: Superiority of the inverse Dower matrix," *J. Electrocardiol.*, vol. 21, no. 4, pp. 361–367, 1988.

[19] J. DeMaso and C. Sellers, "Progress in Holter technology," *Cardiac Electrophysiology Review*, vol. 3, no. 4, pp. 239–242, 1999.

[20] S. Stern and D. Tzivoni, "The dynamic nature of the ST-T segment in ischemic heart disease," *Am Heart J*, vol. 91, pp. 820–822, 1976.

[21] L. Cromwell, F. J. Weibel, and E. A. Pfeiffer, *Biomedical Instrumentation And Measurements*. Prentice Hall, New Jersey, 1980.

[22] D. J. Hearse, "Myocardial ischaemia: can we agree on a definition for the 21st century?," *Cardiovascular Research*, vol. 28, pp. 1737–1744, 1994.

[23] J. Deanfield, M. S. M. Kensett, P. Horlock, R. Wilson, C. deLandsheere, and A. Selwyn, "Myocardial ischemia due to mental stress," *Lancet*, vol. 2, pp. 1001–1005, 1984.

[24] T. Andrews, T. Fenton, N. Toyosaki, S. Glasser, P. Young, G. MacCallum, R. Gibson, T. Shook, and P. Stone, "Subsets of ambulatory myocardial ischemia based on heart rate activity. circadian distribution and response to anti-ischemic medication," *Circulation*, vol. 88, pp. 92–100, 1993.

[25] B. M. Horáček and G. S. Wagner, "Spatial Patterns of ST Segment Shift During Myocardial Ischaemia," in *Dynamic Electrocardiography* (M. Malik and A. J. Camm, eds.), ch. 27, pp. 250–259, Futura, 2004.

[26] M. I. Noble, "Myocardial supply and demand," *Heart*, vol. 78, pp. 105–106, 1997.

[27] R. P. Holland and H. Brooks, "The qrs complex during myocardial ischemia: An experimental analysis in the porcine heart," *J. Clin. Invest.*, vol. 57, pp. 541–550, 1976.

[28] N. B. Wagner, D. C. Sevilla, M. W. Krucoff, K. L. Lee, K. S. Pieper, K. K. Kent, R. K. Bottner, R. H. Selvester, and W. G. S., "Transient alterations of the QRS complex and ST segment during percutaneous transluminal balloon angioplasty of the left anterior descending coronary artery," *Amer. J. Cardiol*, vol. 62, pp. 1038–1042, 1988.

[29] E. Pueyo, L. Sörnmo, and P. Laguna, "QRS Slopes for Detection and Characterization of Myocardial Ischemia," *IEEE Transaction on Biomedical Engineering*, vol. 55, no. 2, pp. 468–568, 2008.

[30] Y. W. Qian, W. T. Clusin, S. F. Lin, H. Jennifer, and R. J. Sung, "Spatial heterogeneity of calcium transient alternans during the early phase of myocardial ischemia in the blood-perfused rabbit heart," *Circulation*, vol. 104, no. 20, pp. 2082–2087, 2001.

[31] P. Sutton, P. Taggart, T. Opthof, R. Coronel, R. Trimlett, W. Pugsley, and P. Kallis, "Repolarisation and refractoriness during early ischaemia in humans," *Heart*, vol. 84, no. 4, pp. 365–369, 2000.

[32] R. P. Holland and H. Brooks, "TQ-ST segment mapping: Critical review and analysis of current concepts," *American Journal of Cardiology*, vol. 4, pp. 110–129, 1977.

[33] D. M. Mirvis, "Physiologic bases for anterior ST segment depression in patients with acute inferiorwall myocardial infarction," *Am Heart J*, vol. 116, pp. 1308–1322, 1988.

[34] E. Pueyo, J. García, G. Wagner, R. Bailón, L. Sörnmo, and P. Laguna, "Time course of ECG depolarization and repolarization changes during ischemia in PTCA recordings," *Methods Inf. Med*, vol. 43, pp. 43–46, 2004.

[35] T. J. Ryan, J. L. Anderson, E. M. Antman, B. A. Braniff, N. H. Brooks, R. M. Califf, L. D. Hillis, L. F. Hiratzka, E. Rapaport, B. Riegel, R. O. Russell, E. E. Smith, and W. D. Weaver, "ACC/AHA guidelines for the management of patients

with acute myocardial infarction: executive summary. a report of the American College of Cardiology/American Heart Association Task Force on Practice Guidelines (Committee on Management of Acute Myocardial Infarction).," *Circulation*, vol. 94, no. 9, pp. 2341–2350, 1996.

[36] I. B. Menown, J. Allen, J. M. Anderson, and A. A. Adgey, "ST depression only on the initial 12-lead ECG: early diagnosis of acute myocardial infarction," *Eur Heart J*, vol. 22, no. 3, pp. 218–227, 2001.

[37] D. Perera, S. J. Patel, and S. R. Redwood, "Dynamics of the ST Segment in Ischaemic Heart Disease," in *Dynamic Electrocardiography* (M. Malik and A. J. Camm, eds.), ch. 26, pp. 238–249, Futura, 2004.

[38] J. García, L. Sörnmo, S. Olmos, and P. Laguna, "Automatic Deteccion of ST-T Complex Changes on the ECG using Filtered RMS Difference Series: Application to Ambulatory Ischemia Monitoring," *IEEE Trans. on Biomedical Engineering*, vol. 47, no. 9, pp. 1195–1201, 2000.

[39] F. Jager, A. Taddei, G. Moody, M. Emdin, G. Antolič, R. Dorn, A. Smrdel, C. Marchesi, and R. Mark, "Long-Term ST database: a reference for the development and evaluation of automated ischaemia detectors and for the study of the dynamics of myocardial ischaemia," *Med Biol Eng Comput*, vol. 41, pp. 172–182, 2003.

[40] A. Taddei, G. Distante, M. Emdin, P. Pisani, G. Moody, C. Zeelenberg, and C. Marchesi, "The european st-t database: standard for evaluating systems for the analysis of st-t changes in ambulatory electrocardiography," *Eur Heart J.*, vol. 13, pp. 1164–1172, 1992.

[41] J. García, M. Åström, J. Mendive, P. Laguna, and L. Sörnmo, "Ecg-based detection of body position changes in ischemia monitoring," *IEEE Trans Biomed Eng*, vol. 25, no. 6, pp. 501–507, 2003.

[42] T. L. Shook, V. Valvo, M. Hubelbank, C. L. Feldman, and P. H. Stone, "Validation of a new algorithm for detection and quantification of ischemic ST segment changes during ambulatory electrocardiography," in *Computers in Cardiology*, vol. 87, pp. 57–62, 1988.

[43] R. W. Stadler, S. N. Lu, S. D. Nelson, and L. Stylos, "A real-time ST-segment monitoring algorithm for implantable devices," *J Electrocardiol*, vol. 34, pp. 119–126, 2001.

[44] A. Taddei, G. Constantino, M. Silipo, R. Emdin, and C. Marchesi, "A system for the detection of ischemic episodes in ambulatory ECG," in *Proc IEEE Comput Cardiol*, pp. 705–708, 1995.

[45] A. Smrdel and F. Jager, "Automated detection of transient st-segment episodes in 24 h electrocardiograms," *Med. Biol. Eng. Comput*, vol. 42, pp. 303–311, 2004.

[46] F. Jager, G. Moody, and R. Mark, "Characterization of transient ischemic and non-ischemic st segment changes," in *Comput. Cardiol.*, (Los Alamitos), pp. 721–724, IEEE Comput. Soc. Press, 1995.

[47] F. Jager, G. Moody, and R. Mark, "Detection of transient ST segment episodes during ambulatory EGG monitoring," *Comput. Biomed. Res.*, vol. 31, pp. 305–322, 1998.

[48] C. W. Therrien, *Discrete Random Signals and Statistical Signal Processing*. Englewood Cliffs NJ: Prentice-Hall, 1992.

[49] P. Laguna, G. Moody, J. García, A. Goldberger, and R. Mark, "Analysis of the ST-T complex of the electrocardiogram using the Karhunen-Loéve transform: Adaptive monitoring and alternans detection," *Med. Biol. Eng. Comput.*, vol. 37, pp. 175–189, 1999.

[50] F. Badilini, M. Merri, J. Benhorin, and A. J. Moss, "Beat-to-beat quantification and analysis of ST displacement from Holter ECGs: a new approach to ischemia detection," in *Proc IEEE Comput Cardiol*, pp. 179–182, 1992.

[51] J. Vila, F. Palacios, J. Presedo, M. Fernández-Delgado, P. Felix, and S. Barro, "Time-frequency analysis of heart-rate variability," *IEEE Eng Med Biol Mag*, vol. 16, no. 5, pp. 119–126, 1997.

[52] L. Senhadji, G. Carrault, J. J. Bellanger, and G. Passariello, "Comparing wavelet transforms for recognizing cardiac patterns," *IEEE Engineering in Medicine and Biology*, vol. 14, no. 2, pp. 167–173, 1995.

[53] R. Silipo, A. Taddei, and C. Marchesi, "Continuous monitoring and detection of ST-T changes in ischemic patients," in *IEEE Comput Cardiol*, pp. 225–228, 1994.

[54] C. Papaloukas, D. Fotiadis, A. Likas, and L. K. Michalis, "A knowledge-based technique for automated detection of ischemic episodes in long duration electrocardiograms," *Med Biol Eng Comput*, vol. 39, no. 1, pp. 105–112, 2001.

[55] C. Papaloukas, D. I. Fotiadis, A. Likas, and L. K. Michalis, "An ischemia detection method based on artificial neural networks," *Artificial Intelligence in Medicine*, vol. 24, no. 2, pp. 167–178, 2002.

[56] L. Dranca, A. Goi, and A. Illarramendi, "Real-time detection of transient cardiac ischemic episodes from ECG signals," *Physiol. Meas.*, vol. 30, pp. 983–998, 2009.

[57] J. P. Martínez, P. Laguna, S. Olmos, O. Pahlm, J. Pettersson, and L. Sörnmo, "Assessment of QT-measurement accuracy using the 12-lead electrocardiogram derived from EASI leads," *Journal of electrocardiology*, vol. 40(2), pp. 172–179, 2007.

[58] G. Moody and R. Mark, "Development and evaluation of a 2-lead ecg analysis program," in *Computers in Cardiology*, (Los Alamitos), pp. 39–44, IEEE Comput. Soc. Press, 1982.

[59] F. Badilini, W. Zareba, E. Titlebaum, and A. Moss, "Analysis of ST segment variability in Holter recordings," in *Noninvasive Electrocardiology: Clinical Aspects of Holter Monitoring. Frontiers in Cardiology*, pp. 357–372, London, U.K.: Saunders, 1996.

[60] M. Åström, J. García, P. Laguna, O. Pahlm, and L. Sörnmo, "Detection of body position changes using the surface electrocardiogram," *Med Biol Eng Comput*, vol. 41, no. 2, pp. 164–171, 2003.

[61] F. Jager, G. B. Moody, A. Taddei, and R. G. Mark, "Performance measures for algorithms to detect transient ischemic st segment changes," in *Computers in Cardiology 1991*, (Los Alamitos), pp. 369–372, IEEE Computer Society Press, 1991.

[62] A. Mincholé, B. Skarp, F. Jager, and P. Laguna, "Evaluation of a Root Mean Square Based Ischemia Detector on the LTST Database," in *XXXII Ann. Conf. Computers in Cardiology*, (Lyon), pp. 853–856, 2005.

[63] M. G. Adams and B. J. Drew, "Body position effects on the ECG: Implication for ischemia monitoring," *J Electrocardiol*, vol. 30, no. 4, pp. 285–291, 1997.

[64] B. L. Nørgaard, B. M. Rasmussen, M. Dellborg, and K. Thygesen, "Positional changes of spatial QRS- and ST-segment variables in normal subjects: implications for continuous vectorcardiography monitoring during myocardial ischemia," *J Electrocardiol.*, vol. 33, no. 1, pp. 23–30, 2000.

[65] S. P. Nelwan, S. H. Meij, T. B. van Dam, and P. Klootwijk, "Detection of body position changes and its effect on ST-changes in the continuous 12-lead electrocardiogram," in *Computers in Cardiology*, pp. 825–828, 2000.

[66] F. Jager, R. G. Mark, G. B. Moody, and S. Divjak, "Analysis of transient ST segment changes during ambulatory monitoring using the Karhunen-Loéve transform," in *Computers in Cardiology*, pp. 691–694, IEEE Comput. Soc. Press, 1992.

[67] Z. Shiner, A. Baharav, and S. Akselrod, "Detection of different recumbent body positions from the electrocardiogram," *Med Biol Eng Comput*, vol. 41, no. 2, pp. 206–210, 2003.

[68] N. Ahmed and K. R. Rao, *Orthogonal Transforms for Digital Signal Processing.* New York, NY, USA, 1975.

[69] I. T. Joliffe, *Principal Component Analysis.* New York, N.Y., USA, 2002.

[70] F. Castells, P. Laguna, L. S ornmo, A. Bollmann, and J. Millet, "Principal component analysis in ecg signal processing," *EURASIP Journal on Advances in Signal Processing*, 2007. Article ID 74580.

[71] J. García, P. Lander, L. Sörnmo, S. Olmos, G. Wagner, and P. Laguna, "Comparative study of local and Karhunen-Loeve based ST-T indexes in recordings from human subjects with induced myocardial ischemia," *Comput. Biomed. Res.*, vol. 31, pp. 271–292, 1998.

[72] J. Pettersson, E. Carro, L. Edenbrandt, O. Pahlm, M. Ringborn, L. Sörnmo, and G. W. S. Warren, "Changes in high frequency QRS components are more sensitive than ST segment deviations for detecting acute coronary artery occlusion," *J. Amer. College Cardiol*, vol. 36, pp. 1827–1834, 2000.

[73] E. S. Keeping, *Introduction to statistical inference*, ch. 6. Dover Books on Mathematics, 1995.

[74] S. M. Kay, *Fundamentals of Statistical Signal Processing: Detection Theory*. Prentice Hall, 1993.

[75] C. Meyer and H. Keiser, "Electrocardiogram baseline noise estimation and removal using cubic splines and state-space computation techniques," *Comput. Biomed. Res.*, vol. 10, pp. 459–470, 1977.

[76] J. García, P. Lander, L. Sörnmo, S. Olmos, G. Wagner, and P. Laguna, "Comparative study of local and Karhunen-Loève-based STT indexes in recordings from human subjects with induced myocardial ischemia," *Computers and Biomedical Research*, vol. 31, no. 4, pp. 271–292, 1998.

[77] F. Hampel, E. Ronchetti, P. Rousseeuw, and W. Stahel, *Robust Statistics*. Probability and Mathematical Statistics, New York: Wiley,, 1986.

[78] J. Faganeli and F. Jager, "Automatic Distinguishing Between Ischemia and Heart-Rate Related Transient ST Segment Episodes in Ambulatory ECG Records," in *Computers in Cardiology*, 2008.

[79] J. Faganeli and F. Jager, "Automatic classification of transient ischaemic and transient non-ischaemic heart-rate related ST segment deviation episodes in ambulatory ECG records," *Physiol. Meas.*, vol. 31, pp. 323–337, 2010.

[80] G. B. Moody and F. Jager, "Distinguishing Ischemic from Non-Ischemic ST changes: The Physionet/Computers in cardiology Challenge 2003," in *Computers in Cardiology*, pp. 235–237, IEEE Computer Society press, 2003.

[81] P. Langley, E. Bowers, J. Wild, M. Drinnan, J. Allen, A. S. A, and et al, "An algorithm to distinguish ischaemic and non ischaemic ST changes in the Holter ECG," in *Computers in Cardiology*, pp. 239–42, 2003.

[82] P. A. Lachenbruch, *Discriminant Analysis.* Hafner Press, 1975.

[83] G. J. McLachlan, *Discriminant Analysis and Statistical Pattern Recognition.* Wiley Interscience, 2004.

[84] R. A. Fisher, "The use of multiple measurements in taxonomic problems.," *Annals of Eugenics*, vol. 7, pp. 179–188, 1936.

[85] A. Pardo and M. A. Ruiz, *SPSS 11. Guía para el análisis de datos.* Mc Graw Hill, 2002.

[86] J. P. Martínez, R. Almeida, S. Olmos, A. P. Rocha, and P. Laguna, "A Wavelet-Based ECG Delineator: Evaluation on Standard Databases," *IEEE Transactions on Biomedical Engineering*, vol. 51, no. 4, pp. 570–581, 2004.

[87] P. Arini, G. C. Beltran, E. R. Valverde, and P. Laguna, "T-Wave Width as an Index for Quantification of Ventricular Repolarization Dispersion: Evaluation in an Isolated Rabbit Heart Model," *Biomedical Signal Processing and Control, Elsevier*, vol. 3, pp. 67–77, 2008.

[88] G. Yan and C. Antzelevitch, "Cellular basis for the normal t wave and the electrocardiographic manifestations of the long-qt syndrome," *Circulation*, vol. 98, pp. 1928–1936, 1998.

[89] E. Watanabe, I. Kodama, M. Ohono, and H. Hishida, "Electrocardiographic prediction of the development and site of acute myocardial infarction in patients with unstable angina," *International Journal of Cardiology*, vol. 89, pp. 231–237, 2003.

[90] A. Smrdel and F. Jager, "Diurnal Changes of Heart Rate and Sympathovagal Activity for Temporal Patterns of Transient Ischemic Episodes in 24-hour Electrocardiograms," *EURASIP Journal on Advances in Signal Processing*, vol. 2007, no. Article ID 32386, p. 10, 2007. 32386.

[91] G. Dory, A. Rosenthal, S. Fischman, Y. Denekamp, basil S. Lewis, and H. Bitterman, "Changes in the slope of the first major deflection of the ECG complex during acute coronary occlusion," *Computers in Biology and Medicine*, vol. 35, pp. 299–309, 2005.

[92] A. Mincholé, E. Pueyo, and P. Laguna, "Transmural Differences in Rate Adaptation of Repolarization Duration Quantified from ECG Repolarization interval dynamics," in *Computers in Cardiology*, 2009 (Accepted).

[93] H. Ritsema van Eck, J. Kors, and G. van Herpen, "Effect of ischemic action potentials on T and U Waves in the electrocardiogram," in *Journal of Electrocardiology*, vol. 40, p. S76, 2007.

[94] D. Lemire, C. Pharand, J.-C. Rajaonah, B. Dubé, and A.-R. LeBlanc, "Wavelet time entropy, T wave morphology and myocardial ischemia," *IEEE Trans. on Biomedical Engineering*, vol. 47, no. 7, pp. 967–970, 2000.

[95] R. Looga, "The Valsalva manoeuvrecardiovascular effects and performance technique: a critical review," *Respiratory Physiology & Neurobiology*, vol. 147, pp. 39–49, 2005.

[96] C. Porth, V. Bamrah, F. Tristani, and J. Smith, "The valsalva maneuver: mechanisms and clinical implications," *Heart Lung*, vol. 13, no. 5, pp. 507–518, 1984.

[97] P. Arini, E. Valverde, G. Beltran, and P. Laguna, "Geometrical and Temporal ECG Features for Quantification of Increased Ventricular Repolarization Dispersion in an Experimental Heart Rabbit Model," in *XXXII Ann. Conf. Computers in Cardiology*, pp. 89–92, IEEE Press, 2005.

[98] M. Risk, V. Bril, C. Broadbridge, and A. Cohen, "Heart rate variability measurement in diabetic neuropathy: review of methods.," *Diabetes Technol Ther*, vol. 3, no. 1, pp. 63–76, 2001.

[99] A. R. Magnano, S. Holleran, R. Ramakrishnan, J. A. Reiffel, and D. M. Bloomfield, "Autonomic nervous system influences on qt interval in normal subjects," *Journal of American College of Cardiology*, vol. 39, no. 11, pp. 1820–1826, 2002.

[100] Y. Benjamin, "Is the t Test really conservative when parent distribution is long-tailed?," *Journal of the American Statistical Association*, vol. 78, no. 383, pp. 645–654, 1983.

[101] W. H. Press, S. A. Teukolsky, W. T. Vetterling, and B. P. Flannery, *Numerical Recipes: The Art of Scientific Computing*. Cambridge University Press, 2007.

[102] P. Coumel, J. Fayn, P. Maison-Blanche, and P. Rubel, "Clinical relevance of assessing QT dynamicity in Holter recordings," *J. Electrocardiol.*, vol. 27, pp. 62–66, 1994.

[103] E. Homs, V. Marti, J. Guindo, P. Laguna, X. Violas, P. Caminal, R. Elosua, and A. B. de Luna, "Automatic measurement of corrected QT interval in Holter recordings: Comparison of its dynamic behavior in patients after myocardial infarction with and without live-threatening arrhythmias," *Amer. Heart J.*, vol. 134, pp. 181–187, 1997.

[104] A. S. Davis, "The pre-clinical assessment of QT interval prolongation: a comparison of in vitro and in vivo methods," *Hum Exp Toxicol.*, vol. 12, pp. 677–680, 1988.

[105] P. Hoffmann and B. Warner, "Are hERG channel inhibition and QT interval prolongation all there is in drug-induced torsadogenesis? A review of emerging trends.," *J Pharmacol Toxicol Methods*, vol. 53, no. 2, pp. 87–105, 2006.

[106] C. P. Lau, A. R. Freedman, S. Fleming, M. Malik, A. J. Camm, and D. E. Ward, "Hysteresis of the ventricular paced QT interval in response to abrupt changes in pacing rate," *Cardiovasc. Res.*, vol. 22, p. 6772, 1988.

[107] S. Ahnve and H. Vallin, "Influence of heart rate and inhibition of autonomic tone on the qt interval," *Circulation*, vol. 65, no. 3, pp. 435–439, 1982.

[108] E. Pueyo, P. Smetana, P. Caminal, Bayes, M. Malik, and P. Laguna, "Characterization of QT interval adaptation to RR interval changes and its use as a risk-stratifier of arrhythmic mortality in amiodarone-treated survivors of acute myocardial infarction," *IEEE Transactions on Biomedical Engineering*, vol. 51, no. 9, pp. 1511–1520, 2004.

[109] G. Hanton, A. Yvon, and A. Racaud, "Temporal variability of QT interval and changes in T wave morphology in dogs as markers of the clinical risk of drug-induced proarrhythmia," *Journal of Pharmacological and Toxicological Methods*, vol. 57, p. 194201, 2008.

[110] J.-P. Couderc, M. Zhou, N. Sarapa, and W. Zareba, "Investigating the effect of sotalol on the repolarization intervals in healthy young individuals," *J. Electrocardiol*, vol. 41, pp. 595–602, 2008.

[111] A. Lubinski, Z. Kornacewicz-Jach, A. M. Wnuk-Wojnar, J. Adamus, M. Kempa, T. Królak, E. Lewicka-Nowak, M. Radomski, and G. Swiatecka, "The terminal portion of the T wave: a new electrocardiographic marker of risk of ventricular arrhythmias," *Pacing Clin Electrophysiol.*, vol. 11, no. 2, pp. 1957–1959, 2000.

[112] W. Shimizu and C. Antzelevitch, "Cellular basis for long QT, transmural dispersion of repolarization and Torsade de Pointes in the long QT," *J. Electrocardiol*, vol. 32, pp. 177–184, 1998.

[113] Z. Zhao, Z. Yuan, Y. Ji, Y. Wu, and Y. Qi, "Left ventricular hypertrophy amplifies the QT, and Tp-e intervals and the Tp-e/QT ratio of left chest ECG," *Journal of Biomedical Research*, vol. 24, no. 1, pp. 69–72, 2010.

[114] I. Savelieva, Y. G. Yap, G. Yi, X. H. Guo, K. Hnatkova, A. J. Camm, and M. Malik, "Relation of ventricular repolarization to cardiac cycle length in normal subjects, hypertrophic cardiomyopathy, and patients with myocardial infarction," *Clin Cardiol*, vol. 22, pp. 649–654, 1999.

[115] M. Yamaguchi, M. Shimizu, H. Ino, H. Terai, K. Uchiyama, K. Oe, T. Mabuchi, T. Konno, T. Kaneda, and H. Mabuchi, "T wave peak-to-end interval and QT dispersion in acquired long QT syndrome: a new index for arrhythmogenicity," *Clinical Science*, vol. 105, pp. 671–676, 2003.

[116] J. Wang, Q. Shan, B. Yang, M. Chen, J. Zou, D. Xu, C. Chen, and K. Cao, "Tpeak-Tend interval as a new risk factor for arrhythmic event in patient with Brugada syndrome," *Journal of Nanjing Medical University*, vol. 21, no. 4, pp. 213–217, 2007.

[117] C. Antzelevitch, W. Shimizu, G. Yan, S. Sicouri, J. Weissenburger, V. Nesterenko, A. Burashnikov, J. Di Diego, J. Saffitz, and G. Thomas, "The M cell: its contribution to the ECG and to normal and abnormal electrical function of the heart," *J Cardiovasc Electrophysiol.*, vol. 10, pp. 1124–1152, 1999.

[118] C. Antzelevitch, S. Viskin, W. Shimizu, G.-X. Yan, P. Kowey, L. Zhang, S. Sicouri, J. M. D. Diego, and A. Burashnikov, "Does Tpeak-Tend provide an index of transmural dispersion of repolarization?," *Heart Rhythm*, vol. 4, no. 8, pp. 1114–1119, 2007.

[119] T. Opthof, R. Coronel, F. J. G. Wilms-Schopman, A. N. Plotnikov, I. N. Shlapakova, P. Danilo, M. R. Rosen, and M. J. Janse, "Dispersion of repolarization in canine ventricle and the electrocardiographic T wave: Tp-e interval does not reflect transmural dispersion," *Heart Rhythm*, vol. 4, no. 3, pp. 341–348, 2007.

[120] Y. Xia, Y. Liang, O. Kongstad, Q. Liao, M. Holm, B. Olsson, and S. Yuan, "In vivo validation of the coincidence of the peak and end of the t wave with full repolarization of the epicardium and endocardium in swine," *Heart Rhythm*, vol. 2, no. 2, pp. 162–169, 2005.

[121] M. P. Andersen, J. Q. Xue, C. Graff, J. K. Kanters, E. Toft, and J. J. Struijk, "New descriptors of T-wave morphology are independent of heart rate," *Journal of Electrocardiology*, vol. 41, no. 6, pp. 557–561, 2008.

[122] P. Smetana, V. Batchvarov, K. Hnatkova, A. J. Camm, and M. Malik, "Sex differences in the rate dependence of the t wave descending limb," *Cardiovasc Res*, vol. 58, no. 3, pp. 549–554, 2003.

[123] B. Surawicz, "Ventricular fibrillation and dispersion of repolarization," *J Cardiovasc Electrophysiol*, vol. 8, pp. 1009–1012, 1997.

[124] R. Coronel, F. J. G. Wilms-Schopman, T. Opthof, and M. J. Janse, "Dispersion of repolarization and arrhythmogenesis," *Heart Rhythm*, vol. 6, no. 4, pp. 537–543, 2009.

[125] P. C. Hansen, *Rank-deficient and Discrete ill-posed problems.* 1998.

[126] E. Pueyo, M. Malik, and P. Laguna, "A dynamic model to characterize beat-to-beat adaptation of repolarization to heart rate changes," *Biomedical Signal Processing and Control*, vol. 3, pp. 29–43, 2008.

[127] P. C. Hansen, "Analysis of discerte ill-posed problems by means of the L-curve," *SIAM Review*, vol. 34, no. 4, pp. 561–580, 1992.

[128] D. R. Jones, C. D. Perttunen, and B. E. Stuckman, "Lipschitzian optimization without the lipschitz constant," *J Optim Theory Applicat*, vol. 79, no. 1, pp. 157–181, 1993.

[129] J. Nocedal and S. J. Wright, *Numerical Optimization*, ch. 6, pp. 135–143. Springer, 2000.

[130] W. Bian and L. Tung, "Structure-related initiation of reentry by rapid pacing in monolayers of cardiac cells," *Circ Res*, vol. 98, pp. 29–38, 2006.

[131] D. S. Rosenbaum, L. E. Jackson, J. M. Smith, H. Garan, J. N. Ruskin, and C. R. J., "Electrical alternans and vulnerability to ventricular arrhythmias," *N Engl J Med.*, vol. 330, no. 4, pp. 235–241, 1994.

[132] M. L. Koller, M. L. Riccio, and R. F. Gilmour Jr, "Dynamic restitution of action potential duration during electrical alternans and ventricular fibrillation," *Am J Physiol Heart Circ Physiol*, vol. 275, pp. 1635–1642, 1998.

[133] M. R. Franz, C. D. Swerdlow, L. B. Liem, and J. Schaefer, "Cycle Length Dependence of Human Action Potential Duration In Vivo," *J. Clin. Invest.*, vol. 82, pp. 972–979, 1988.

[134] M. L. Riccio, M. L. Koller, and R. F. Gilmour Jr, "Electrical Restitution and Spatiotemporal Organization During Ventricular Fibrillation," *Circ Res.*, vol. 84, pp. 955–963, 1999.

[135] R. J. Selvaraj, P. Picton, K. Nanthakumar, and V. S. Chauhan, "Steeper restitution slopes across right ventricular endocardium in patients with cardiomyopathy at high risk of ventricular arrhythmias," *Am J Physiol Heart Circ Physiol*, vol. 292, pp. 1262–1268, 2007.

[136] A. M. Yue, M. R. Franz, P. R. Roberts, and J. M. Morgan, "Global endocardial electrical restitution in human right and left ventricles determined by noncontact mapping," *J. Am. Coll. Cardiol.*, vol. 46, p. 10671075, 2005.

[137] M. P. Nash, C. P. Bradley, P. M. Sutton, R. H. Clayton, P. Kallis, M. P. Hayward, D. J. Paterson, and P. Taggart, "Whole heart action potential duration restitution properties in cardiac patients: a combined clinical and modelling study," *Experimental physiology*, vol. 91, no. 2, pp. 339–54, 2006.

[138] K. R. Laurita, S. D. Girouard, and D. S. Rosenbaum, "Modulation of ventricular repolarization by a premature stimulus: Role of epicardial dispersion of repolarization kinetics demonstrated by optical mapping of the intact guinea pig heart," *Circ Res*, vol. 79, pp. 493–503, 1996.

[139] R. F. Gilmour, A. R. Gelzer, and N. F. Otani, "Cardiac electrical dynamics: maximizing dynamical heterogeneity," *Journal of Electrocardiology*, vol. 40, no. 6, Supplement 1, pp. S51 – S55, 2007.

[140] R. H. Clayton and P. Taggart, "Regional differences in APD restitution can initiate wavebreak and re-entry in cardiac tissue: a computational study," *Biomed Eng Online*, vol. 4, no. 54, 2005.

[141] H. Pak, S. Hong, G. Hwang, H. Lee, S. Park, J. Ahn, Y. Moo Ro, , and Y. Kim, "Spatial dispersion of action potential duration restitution kinetics is associated with induction of ventricular tachycardia/fibrillation in humans," *Journal of cardiovascular electrophysiology*, vol. 15, no. 12, pp. 1357–63, 2004.

[142] K. Ten Tusscher and A. Panfilov, "Alternans and spiral breakup in a human ventricular tissue model," *Am J Physiol Heart Circ Physiol.*, vol. 291, no. 3, pp. H1088–H1100, 2006.

[143] Z. Qu, J. N. Weiss, and A. Garfinkel, "Cardiac electrical restitution properties and stability of reentrant spiral waves: a simulation study," *Am J Physiol Heart Circ Physiol*, vol. 276, pp. 269–283, 1999.

[144] E. Heidenreich, J. M. Ferrero, M. Doblaré, and J. F. Rodríguez, "Adaptive macro finite elements for the numerical solution of monodomain equations in cardiac electrophysiology," *Annals of Biomedical Engineering*, vol. 38, pp. 2331–2345, 2010.

[145] G.-X. Yan, W. Shimizu, and C. Antzelevitch, "Characteristics and distribution of M cells in arterially perfused canine left ventricular wedge preparations," *Circulation*, vol. 98, pp. 1921–1927, 1998.

[146] D. D. Streeter, H. M. Spotnitz, D. P. Patel, J. Ross, and E. H. Sonnenblick, "Fiber Orientation in the Canine Left Ventricle during Diastole and Systole," *Circ. Res.*, vol. 24, pp. 339–347, 1969.

[147] A. V. Glukhov, V. V. Fedorov, Q. Lou, V. K. Ravikumar, P. W. Kalish, R. B. Schuessler, N. Moazami, and I. R. Efimov, "Transmural dispersion of repolarization in failing and nonfailing human ventricle," *Circ. Res.*, vol. 106, no. 5, pp. 981–991, 2010.

[148] E. Drouin, F. Charpentier, C. Gauthier, K. Laurent, and H. Le-Marec, "Electrophysiologic characteristics of cells spanning the left ventricular wall of human heart: Evidence for presence of M cells," *Am J Physiol Heart Circ Physiol*, vol. 26, no. 1, pp. 185–192, 1995.

[149] K. Gima and Y. Rudy, "Ionic Current Basis of Electrocardiographic Waveforms: A Model Study," *Circ. Res.*, vol. 90, pp. 889–896, 2002.

[150] J. M. Ferrero, *Bioelectrónica: señales bioeléctricas.* Univ. Politéc. Valencia, 1994.

[151] K. Ten Tusscher, D. Noble, P. J. Noble, and A. Panfilov, "A model for human ventricular tissue," *Am J Physiol Heart Circ Physiol*, vol. 286, pp. H1573–H1589, 2004.

[152] J. P. Couderc, S. Kaab, M. Hinterseer, S. McNitt, X. Xia, A. Fossa, B. M. Beckmann, S. Polonsky, and W. Zareba, "Baseline values and sotalol-induced changes of ventricular repolarization duration, heterogeneity, and instability in patients with a history of drug-induced torsades de pointes," *Journal of clinical pharmacology*, vol. 49, no. 1, pp. 6–16, 2009.

[153] A. Corrias, X. Jie, L. Romero, M. Bishop, M. Bernabeu, E. P. Paules, and B. Rodríguez, "Arrhythmic risk biomarkers for the assessment of drug cardiotoxicity: from experiments to computer simulations," *Philosophical Transactions of the Royal Society - A*, vol. 368, pp. 3001–3025, 2010.

[154] L. Romero, J. M. Ferrero (Jr), J. Sáiz, B. Trénor, and M. Monserrat, "Effects of acute ischemia on the restitution curves of myocardial tissue: A simulation study," pp. 525–528, Computers in Cardiology, 2004.